



UNIVERSIDADE ESTADUAL DE CAMPINAS
FACULDADE DE ENGENHARIA MECÂNICA
E INSTITUTO DE GEOCIÊNCIAS

DIEGO FERNANDO BARRERA PACHECO

**CONVOLUTION AND CORRELATION-BASED
INTERFEROMETRIC REDATUMING**

**REDATUMAÇÃO INTERFEROMETRICA
BASEADA EM CONVOLUÇÃO E CORRELAÇÃO**

CAMPINAS, SP
2017

DIEGO FERNANDO BARRERA PACHECO

**CONVOLUTION AND CORRELATION-BASED
INTERFEROMETRIC REDATUMING**

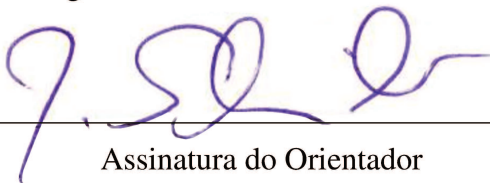
**REDATUMAÇÃO INTERFEROMETRICA
BASEADA EM CONVOLUÇÃO E CORRELAÇÃO**

Thesis presented to the Mechanical Engineering Faculty and Geosciences Institute of the University of Campinas in partial fulfillment of the requirements for the degree of Doctor in Petroleum Sciences and Engineering in the area of Reservoirs and Management.

Tese apresentada à Faculdade de Engenharia Mecânica e Instituto de Geociências da Universidade Estadual de Campinas como parte dos requisitos exigidos para a obtenção do título de Doutor em Ciências e Engenharia de Petróleo na área de Reservatórios e Gestão.

Orientador: Prof. Dr. Joerg Dietrich Wilhelm Schleicher

Este exemplar corresponde à versão final do trabalho de Tese definida pelo aluno Diego Fernando Barrera Pacheco, e orientada pelo Prof. Dr. Joerg Dietrich Wilhelm Schleicher.



Assinatura do Orientador

**CAMPINAS, SP
2017**

Agência(s) de fomento e nº(s) de processo(s): CNPq, 573890/2008-0

Ficha catalográfica
Universidade Estadual de Campinas
Biblioteca da Área de Engenharia e Arquitetura
Luciana Pietrosanto Milla - CRB 8/8129

B274c Barrera Pacheco, Diego Fernando, 1984-
Convolution and correlation-based interferometric redatuming / Diego
Fernando Barrera Pacheco. – Campinas, SP : [s.n.], 2017.

Orientador: Joerg Dietrich Wilhelm Schleicher.
Tese (doutorado) – Universidade Estadual de Campinas, Faculdade de
Engenharia Mecânica.

1. Interferometria. 2. Teoremas de reciprocidade. 3. Operadores de
convolução. I. Schleicher, Joerg Dietrich Wilhelm, 1964-. II. Universidade
Estadual de Campinas. Faculdade de Engenharia Mecânica. III. Título.

Informações para Biblioteca Digital

Título em outro idioma: Redatumação interferométrica baseada em convolução e correlação

Palavras-chave em inglês:

Interferometry

Reciprocity theorems

Convolution operators

Área de concentração: Reservatórios e Gestão

Titulação: Doutor em Ciências e Engenharia de Petróleo

Banca examinadora:

Joerg Dietrich Wilhelm Schleicher [Orientador]

Lúcio Tunes dos Santos

Ricardo Caetano Azevedo Biloti

Jessé Carvalho Costa

Reynam da Cruz Pestana

Data de defesa: 17-03-2017

Programa de Pós-Graduação: Ciências e Engenharia de Petróleo

UNIVERSIDADE ESTADUAL DE CAMPINAS
FACULDADE DE ENGENHARIA MECÂNICA
E INSTITUTO DE GEOCIÊNCIAS

TESE DE DOUTORADO

**CONVOLUTION AND CORRELATION-BASED
INTERFEROMETRIC REDATUMING**

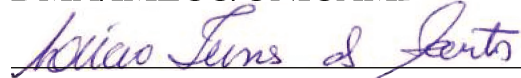
Autor: Diego Fernando Barrera Pacheco

Orientador: Prof. Dr. Joerg Dietrich Wilhelm Schleicher

A banca examinadora composta pelos membros abaixo aprovou esta tese:



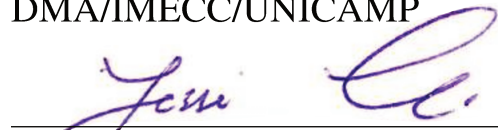
Prof. Dr. Joerg Dietrich Wilhelm Schleicher
DMA/IMECC/UNICAMP



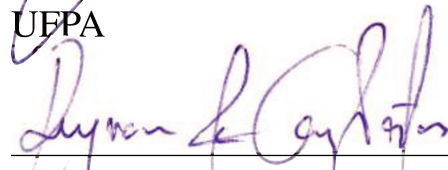
Prof. Dr. Lucio Tunes dos Santos
DMA/IMECC/UNICAMP



Prof. Dr. Ricardo Caetano Azevedo Biloti
DMA/IMECC/UNICAMP



Prof. Dr. Jessé Carvalho Costa
UFPA



Prof. Dr. Reynam da Cruz Pestana
UFBA

Campinas, 17 de março de 2017

Acknowledgements

Firstly I want to thank to God for give me the courage and faith to believe in myself and finish my work satisfactorily. Thanks to my mother Gloria Isabel Pacheco, my father Gustavo Barrera and my daughter Amy Alejandra Barrera R. for inspire me during my PhD adventure. Thanks to the people that in any way contribute to conclude this work. To my advisor Joerg Schleicher in UNICAMP and my mentors Kees Wapenaar, Joost van der Neut in TuDelft and Lucio Tunes in UNICAMP. To they, my more deeper grateful for believe in me and teach me how be a researcher. To the Ph.D student Axandre Camargo for the great discussions in the LGC and to my colombian friends in Brazil Edwin Fagua and Dany Rueda for the friendship.

Resumo

A interferometria sísmica é uma metodologia que permite calcular as funções de Green para fontes (ou receivers) onde só temos receptores (ou fontes, respectivamente). Isto pode ser feito com métodos baseados em correlação ou convolução. Neste trabalho nós apresentamos uma nova abordagem para reposicionar o arranjo sísmico desde a superfície da terra num datum arbitrário em profundidade, onde são usados os teoremas de reciprocidade unidireccionais tipo correlação e convolução. O processo de redatumação pode ser feito em três passos: (a) cálculo a função de Green descendente para fontes na superfície da terra e receptores no datum, (b) cálculo da correspondente função de Green ascendente, e (c) cálculo do campo de onda completo com o arranjo sísmico reposicionado no datum. Para calcular os passos (a) e (b) nós precisamos como dados de entrada o arranjo sísmico na superfície da terra e campos de onda modelados com as velocidades do meio acima do datum. Já para o cálculo do passo (c) é necessário conhecer as respostas dos passos (a) e (b), os quais serão usados como dados conhecidos na equação de interferometria baseada em convolução. O método leva em consideração a não homogeneidade do meio acima do datum, reduzindo os eventos anti-causais e artefactos, quando é comparado com métodos baseados puramente em correlação.

Palavras chave: Interferometria sísmica, teoremas de reciprocidade unidireccionais, convolução and correlação.

Abstract

Seismic interferometry is a method to retrieve Green's functions for sources (or receivers) where there are only receivers (or sources, respectively). This can be done by correlation- or convolution-based methods. In this work we present a new approach to reposition the seismic array from the earth's surface to an arbitrary datum at depth using the one-way reciprocity theorems of convolution and correlation type. The redatuming process is done in three steps: (a) retrieving the downward Green's function for sources at the earth's surface and receivers at the datum, (b) retrieving the corresponding upward Green's function, and (c) retrieving the reflected upward wavefield for sources and receivers at the datum. Input for steps (a) and (b) are the surface data and wavefields simulated in a velocity model of the datum overburden. Step (c) uses the responses of steps (a) and (b) as input data in the convolution-based interferometric equation. The method accounts for inhomogeneities in the overburden medium, thus reducing anticausal events and artefacts as compared to a purely correlation-based procedure.

Key words: Seismic interferometry, one-way reciprocity theorems, convolution and correlation.

List of Figures

1.1	Representation of a volume V with surface S , \hat{n} is a surface normal versor.	21
1.2	Representation of a volume V with surface S , the points A and B are inside V and \hat{n} is the surface normal vector.	22
2.1	Cylinder divided in three different surfaces, S_1 , S_2 and S_3	26
2.2	Sketch of two sources at positions x^A and x^B inside a volume V with receivers along the closed surface S with position x . The positions x are the directions of the incoming waves from x^A and x^B and their angles θ^A and θ^B with respect to the unit normal versor \hat{n} to the surface.	28
2.3	Sketch of a source at position x^A with a receiver at position x^B , where l is the representation of a wave path from x^A to x^B	32
3.1	Two-dimensional sketch of two sources at positions x_A and x_B inside a volume V with receivers along the closed surface S of V . Indicated at position x are the propagation directions of the incoming waves from x_A and x_B , and their angles θ_A and θ_B with respect to the unit normal vector \hat{n} to the surface.	35
3.2	Two-dimensional sketch of a source at positions x^S outside the surface S , with receivers along and inside the position x and x^B , respectively, at the closed surface S of volume V . Where \hat{n} is the unit normal vector at the surface S	38
3.3	Two states with the same inhomogeneous medium between surfaces S_1 and S_2 . State A describes the transmitted wavefield from S_1 to S_2 and its scattered response recorded at S_1 if the medium is homogeneous above S_1 and below S_2 . State B describes the corresponding wavefields if the medium is also inhomogeneous below S_2 . The dotted line indicates the volume V	41
3.4	Sketch with a cylindrical closed surface S , decomposed into three surfaces S_1 , S_2 and S_3 . At surface S_1 there is a seismic array, which with interferometric redatuming will be redatumed to the datum in the surface S_2	44

3.5	Sketch that shows the redatuming of a seismic survey to a new datum in two steps: (a) virtual receivers and (b) virtual sources.	46
3.6	Sketch that shows the redatuming equations of a seismic array on the earth's and at datum the (a) virtual receivers and (b) virtual sources.	49
4.1	Two wavefield states in an inhomogeneous overburden. State A is used to describe the transmitted wavefield from the surface and its response recorded at the datum and at the surface. State B describe the total wavefield propagation taking into account all events propagating in the medium.	52
4.2	Sketch with the linear problem inversion. Where we have the one-way Green's functions responses at the focus datum calculated by inversion and the reflection at the datum to be calculated by inversion.	56
5.1	Ray paths of P , where we show only three possible crosscorrelations, without regard second, third and high multiple order. Black lines represent positive times and red lines represent negative times. $P(x', \omega; x'')$ have two nonphysical responses with positive and negative signal, and a point at datum corresponding to the unique physical event retrieved when used the expression (5.1).	59
6.1	Modeling seismic data considering: (a) array of sources and receivers at the surface, (b) array of shots at the surface and receivers at 500 m depth and (c) both arrays positioned at 500 m depth.	73
6.2	Redatuming using seismic direct-wave interferometry with the numerical model of Figure 6.1. Step 1: Redatuming the receivers. (a) Redatumed data, and (b) modeled data for sources at the surface and receivers at the datum.	74
6.3	Redatuming using seismic direct-wave interferometry with the numerical model of Figure 6.1. Step 1: Redatuming the receivers. Comparison of the central trace (green line) to the modeled data with the same configuration (solid red line).	74
6.4	Redatuming using seismic direct-wave interferometry with the numerical model of Figure 6.1. Step 1: Redatuming the receivers. Comparison of the trace at 1000 m offset obtained from receivers redatuming in Figure 6.2.	75
6.5	Redatuming using seismic direct-wave interferometry with the numerical model of Figure 6.1. Step 1: Redatuming the receivers. Black lines represent causal wavefields, i.e., positive times and the white lines represent anticausal wavefields, i.e., negative times in the wavefield propagation.	76

6.6	Redatuming using seismic direct-wave interferometry with the numerical model of Figure 6.1. Step 2: Redatuming the sources. Where (a) is the output response of the source redatuming and (b) is the exact model	77
6.7	Comparison of the normalized central trace of the fully redatumed shot gather of Figure (6.6a) (green line) with the corresponding traces obtained from modeling (green line) and from redatuming the gather modeled with the receivers at the datum (red line).	77
6.8	Redatuming using seismic direct-wave interferometry with the numerical model of Figure 6.1. Step 2: Redatuming the sources. Comparison of the trace at 1000 m offset obtained from sources redatuming in Figure 6.6.	78
6.9	Redatuming using seismic direct-wave interferometry with the numerical model of Figure 6.1. Step 2: Redatuming the sources.	78
6.10	Seismic array on surface considering a inhomogeneous overburden, where we describe: (a) primary reflection events and (b) multiple events visible in the data.	79
6.11	Models used for direct-wavefield modeling in the redatuming procedure. (a) Exact overburden. (b) Smoothed overburden. (c) Constant velocity from average slowness. Also shown are possible ray paths connecting sources at the datum to receivers at the surface.	80
6.12	Result of redatuming with the (a) full wave train from the exact inhomogeneous overburden velocity model, (b) direct wave from the exact model, (c) direct wave from the smoothed model, and (d) direct wave from the constant-velocity model. The resulting redatumed events are labeled with numbers for further discussion.	81
6.13	Comparison of the central trace obtained from redatuming using the full wave train in the exact overburden and the direct wave in the exact, smoothed and constant-velocity models.	82
6.14	Comparison of the trace at 500 m offset obtained from redatuming using the full wave train in the exact overburden and the direct wave in the exact, smoothed and constant-velocity models.	82
6.15	Ray paths for the surface events, crosscorrelation operator, and redatuming response, for events 1, 2 and 3 of Figure (6.12).	84
6.16	Ray paths for the surface events, crosscorrelation operator, and redatuming response, for unphysical events 5, 6, 7, and 8 of Figure 6.12. Ray paths contributing negatively to the traveltimes are shown in white.	85
6.17	Ray paths for the surface events, crosscorrelation operator, and redatuming response, for unphysical events 9 and 10 of Figure 6.12a. Ray paths contributing negatively to the traveltimes are shown in white.	86

6.18	Anticausal part of the redatuming result using the full wave train from the exact overburden velocity model. The labeled events are explained in the text. The anticausal results was using (a) full wave train from the exact inhomogeneous overburden velocity model, (b) direct wave from the exact model, (c) direct wave from the smoothed model, and (d) direct wave from the constant-velocity model.	87
6.19	Trace at the zero offset corresponding to the anticausal part in Figures 6.18.	88
6.20	Ray paths for the surface events, crosscorrelation operator, and redatuming response, for events 12, 13, 14, and 15 of Figure (6.18). Ray paths contributing negatively to the traveltimes are shown in white.	89
6.21	Upgoing Green's functions retrieved using the inverse operator in equation (5.9) with different values for the regularization parameter in the PSF^{-1} : (a) 1%, (b) 0.1%, (c) 0.01% and (d) 0.001% of the maximum absolute value of the PSF	91
6.22	Central traces of the receiver redatuming responses at the datum.	92
6.23	Comparison of the traces at 1000 m offset of the receiver redatuming responses at the datum.	92
6.24	Sketch that describes the ray path in the inverse operator expression (5.9), where from the seismic data at the earth's surface, the model of the incident Green's function and the inverse of the PSF , the receivers can be repositioned at the datum.	93
6.25	Central shot of the Green's functions with source and receivers at datum using the inverse operator in equation (5.13), as obtained using four different regularization percentages: (a) 1%, (b) 0.1%, (c) 0.01% and (d) 0.001% of the maximum absolute value of the PSF	94
6.26	Central traces of the redatuming responses in Figure (6.25) compares with the central trace of the exact model.	95
6.27	Comparison of the traces at 1000 m offset of the redatuming responses in Figure (6.25) compares with the central trace of the exact model.	95
6.28	Sketch that explains the process to retrieve the total Green's function at datum using the inverse operator deduced in equation (5.15).	96
6.29	Upward causal responses obtained by the PSF inversion according to equation (5.9) with different values of ϵ : (a) 1%, (b) 0.1%, (c) 0.01% and (d) 0.001%.	98
6.30	Upward anticausal responses obtained by the PSF inversion according to equation (5.9) with different values of ϵ : (a) 1%, (b) 0.1%, (c) 0.01% and (d) 0.001%.	99
6.31	Sketch of the equation (5.9) that explains the process to retrieve the (a) primary reflections and (b-c) events associated to reverberations in the overburden.	100

6.32	Causal redatuming responses obtained by the <i>PSF</i> inversion according to equation (5.9) with different values of ϵ : (a) 1%, (b) 0.1%, (c) 0.01% and (d) 0.001%.	101
6.33	Anticausal redatuming responses obtained by the <i>PSF</i> inversion according to equation (5.9) with different values of ϵ : (a) 1%, (b) 0.1%, (c) 0.01% and (d) 0.001%. . .	102
6.34	Sketch of the equation (5.15) that explains the process to retrieve the (a) primary reflections and (b) events associated to reverberations in the overburden with sources and receivers at datum	103
6.35	(a) Full synthetic seismic wavefield with its up- and downgoing constituents labeled, obtained using a source array at the surface and receivers at the datum at 500 m in depth in the horizontally layer, where was recorded the (b) downward and (c) upward wavefield constituents.	104
6.36	Down-ward Green's function retrieved by inversion using equation (5.32), where we test five different values to ϵ , where: (a) 1%, (b)0.1%, (c) 0.01% and (d) 0.001%. The percentage above is with reference to the <i>PSF</i> maximum value	105
6.37	Central traces of the downgoing Green's functions sections in Figure (6.36) (coloured lines) compared to the wavefield simulated with sources at the surface and receivers at the datum (black line). (a) First part of the traces. (b) Later portion at a different scale.	106
6.38	Comparison of the traces at 500 m offset of the downgoing Green's functions sections in Figure (6.36) (coloured lines) compared to the wavefield simulated with sources at the surface and receivers at the datum (black line). (a) First part of the traces. (b) Later portion at a different scale.	106
6.39	Upward Green's function retrieved with equation (5.22), where we has tested five different values to ϵ , where: (a)1%, (b) 0.1% (c) 0.01% and (d) 0.001%.	108
6.40	Redatuming using inversion in the case of inhomogeneous overburden with the model of Figure (6.10). Comparison of the central trace between the responses of the Figure (6.39)	109
6.41	Redatuming using inversion in the case of inhomogeneous overburden with the model of Figure (6.10). Comparison of traces at 500 m offset between the responses of Figure (6.42)	110
6.42	Redatuming of source and receivers at 500m at depth retrieved by inversion using the equation (5.41), where we test five different values to ϵ , where: (a) 1%, (b)0.1%, (c) 0.01% and (d) 0.001%. The percentage above is with reference to the <i>PSF</i> maximum value. Up- and down-ward Green's functions used here was retrieved by inversion in above steps.	111

6.43	Redatuming using inversion in the case of inhomogeneous overburden with the model of Figure (6.10). Comparison of the central trace between the responses of Figure (6.42)	112
6.44	Sketch of the equation (5.15) that explains the process to retrieve the (a) primary reflections 1, 2 and 3, and (b) the event 4 that is associated to the reverberation of the transmitted wavefield in the overburden.	112
6.45	Modeling of the seismic input data considering: (a) array of sources and receivers at the surface, (b) array of shots and receivers at the earth's surface considering only information of the overburden (truncated wavefield) and (c) array of shots at the earth's surface and receivers at the datum (transmitted wavefield).	113
6.46	(a) Full synthetic seismic wavefield with its up- and downgoing constituents labeled, obtained using a source array at the surface and receivers at the datum at 500 m in depth in the horizontally layer, where was recorded the (b) downward and (c) upward wavefield constituents.	114
6.47	Shot 150 of the downward wavefields retrieved with the inverse operator (5.32), where we test four different values to ϵ : (a) 1%, (b)0.1%, (c) 0.01% and (d) 0.001%.	115
6.48	Shot 150 of the upward wavefield retrieved with the inverse operator (5.22), where we test four different values to ϵ : (a) 1%, (b)0.1%, (c) 0.01% and (d) 0.001%.	116
6.49	Shot 150 of the redatuming of source and receivers at 1.2 km in depth retrieved by inversion using the equation (5.41), where we test four different values to ϵ to retrieve the <i>PSF</i> inverse: (a) 1%, (b)0.1%, (c) 0.01% and (d) 0.001%.	117
6.50	Stacking responses correspond to the complete shot gathers in Figure (6.49) using four percentages to ϵ : (a) 1%, (b)0.1%, (c) 0.01% and (d) 0.001%, while the (e) is the stack response of the shot gathers corresponding to the exact model.	118
6.51	Redatuming using inversion in the case of inhomogeneous overburden with the model of Figure (6.10). Comparison of the central trace between the responses of the Figure (6.39)	119
6.52	Modeling of the seismic input data considering: (a) array of sources and receivers at the surface, (b) array of shots and receivers at the earth's surface considering only information of the overburden (truncated wavefield) and (c) array of shots at the earth's surface and receivers at the datum (transmitted wavefield).	120
6.53	(a) Smooth of the velocity model in Figure (6.52a) with a filter length of 5 x 5 and (b) eikonal-based Kirchhoff depth migration of the seismic model with the array on surface.	121

6.54	Downward Green's function retrieved by inversion using the equation (4.8) in the shot 125, where we test four different values to ϵ : (a) 1%, (b)0.1%, (c) 0.01% and (d) 0.001%.	122
6.55	Upward Green's function retrieved by inversion using the equation (4.3) in the shot 125, where we test four different values to ϵ : (a) 1%, (b)0.1%, (c) 0.01% and (d) 0.001%.	123
6.56	Redatuming of seismic data using the inverse of the <i>PSF</i> corresponding to the auto-correlation of the downgoing Green's function in Figure (6.54d) in equation (4.10). We show the redatuming responses corresponding at the shot 125, where we test four different values of ϵ : (a) 1%, (b)0.1%, (c) 0.01% and (d) 0.001%.	124
6.57	Redatuming using inversion in the case of inhomogeneous overburden with the model of Figure (6.52). Comparison of the central traces (zero-offset) between the responses of the Figure (6.56).	124
6.58	Redatuming using inversion in the case of inhomogeneous overburden with the model of Figure (6.52). Comparison of the traces at 100 m offset between the responses of the Figure (6.56).	125
6.59	(a) Smooth of the velocity model below the datum at 1 km in depth in Figure (6.52a) with a filter length of 5 x 5 and (b) is the exact migration response of the seismic data below the datum.	126
6.60	Eikonal-based pre-stack Kirchhoff depth migration of the redatuming responses using four percentages to ϵ : (a) 1%, (b)0.1%, (c) 0.01% and (d) 0.001%.	127
C.1	Results of forwards (a) and inverse (b) wavefield extrapolation of a point source response recorded on a finite aperture. On other hand we have the results of forward (c) and inverse (d) wavefield extrapolation of a point source response recorded on an infinite aperture. Note that the inverse extrapolation result contains artefacts, despite the infinite aperture (Wapenaar and Fokkema, 1997).	143

List of Tables

4.1	Analysis of the up- and downgoing wavefields at surfaces ∂D_1 and ∂D_2 in states A and B , respectively.	52
-----	--	----

Contents

Acknowledgements	5
Resumo	6
Abstract	7
List of Figures	8
List of Tables	15
1 Introduction	18
1.1 Acoustic wave equation	20
1.2 Gauss's Theorem	21
2 Reciprocity Theorems	23
2.1 Reciprocity theorem of the convolution type	23
2.2 Reciprocity theorem of correlation type	24
2.3 Surface decomposition of reciprocity theorems	26
2.4 One-way reciprocity theorems	28
2.5 Source-receiver reciprocity	31
3 Interferometric Redatuming	34
3.1 Interferometric equation with correlation-based expressions	34
3.1.1 Correlation-based Green's function approximation	36
3.2 Interferometric equation with convolution-based expressions	37
3.2.1 Convolution-based Green's function approximation	39
3.3 Correlation-based interferometric redatuming	40
3.4 Convolution-based interferometric redatuming	46

4	Interferometric redatuming by focusing	50
4.1	Wavefield decomposition	51
4.2	Convolution-based interferometric redatuming	54
5	Inverse functions of the interferometric redatuming expressions	57
5.1	Inversion of interferometric redatuming by convolution-based	57
5.2	Interferometric redatuming by focusing	63
5.3	Least squares	70
6	Numerical Examples	72
6.1	Interferometric redatuming: Correlation-based method	72
6.2	Interferometric redatuming: Convolution-based method	90
6.3	Interferometric redatuming by focusing	103
7	Conclusions	128
	References	130
A	Appendix A	133
B	Appendix B	140
C	Appendix C	142

1. Introduction

The redatuming of seismic data is a classic technique in the repertoire of seismic processing. Its purpose is to simulate data as if it were acquired from a new datum, i.e., a different measurement surface (Berryhill, 1979, 1984). The redatuming technique's principal applications are the correction of seismic data for the effects of an acquisition at an irregular surface and for the effects of complex geological structures in the overburden such as low-velocity layers or strong lateral variations. The objective is to focus the seismic data processing closer to the target in a specific subsurface region (Wapenaar et al., 1992).

In recent years there has been a growing interest to improve petroleum exploration and processing of seismic data using interferometric techniques. Seismic interferometry is a technique based on optical physics. It allows us to use parts of the information contained in the seismic data that are not taken into account in conventional processing. Its basic principle allows us to generate new seismic responses or virtual sources where only receivers were placed (Wapenaar et al., 2010a). In seismic exploration, authors like Claerbout (1968) and Scherbaum (1978) were the first to make use of interferometric techniques. Claerbout (1968) showed that the Green's function for reflections recorded at the Earth's surface could be obtained by the autocorrelation of the data generated by buried sources in a 1D medium, while Scherbaum (1978), constructed geological structure based on the properties of the Green's functions, using information of microquakes. Other authors as Wiggins (1984) and Wapenaar (1993) have been discussed about other interferometric methods, i.e., the Kirchhoff integral, and nowadays the discussion have included amplitude correction (Tegtmeyer et al., 2004). Another line of research is dedicated to wave-equation-based redatuming (Yilmaz and Lucas, 1986; Bevc, 1995; Schneider et al., 1995). More information on redatuming can be found in Schuster and Zhou (2006).

The classical redatuming procedure correlates surface seismic data with those acquired at depth as was mentioned before. This correlation-based method has been well studied in the literature, by Xiao and Schuster (2006), Schuster and Zhou (2006), Dong et al. (2007), Lu et al. (2008), Wapenaar et al. (2008), Schuster (2009), Curtis (2009), Wapenaar et al. (2010a), van der Neut et al. (2011), van der

Neut (2012), and many others. They attempt to use the techniques with the objective of improving the seismic sections and reducing the uncertainty in hydrocarbon exploration in regions of high structural and sedimentological complexity. Recently authors like Slob et al. (2007) and Wapenaar et al. (2008) extend the interferometric definition including not only crosscorrelation, but also crossconvolution inside of the technique.

Seismic interferometry by convolution is an alternative to the classical correlation-based scheme. There are many situations where the convolutional form is more convenient than the correlation-based methods. One of the main advantages of the convolution-based procedure is its inherent compensation for the properties of the source wavelet. Another important advantage is that the underlying theory does not require the assumption of a lossless medium (Slob and Wapenaar, 2007).

In this work we proposed a methodology that considers the properties of both convolution and correlation methods to solve the limitation of each when considered separately. We deduced similar equations to van der Neut et al. (2015a), where we used the one-way reciprocity theorems of correlation and convolution type to calculate expressions to retrieve the up- and downward wavefields constituents. Using both up- and downward wavefield as input data, is possible do the reposition of the seismic array from the earth's surface at an arbitrary datum in depth. This could be done considering two interpretations: convolution and correlation methods. To retrieve the up- and downward wavefields constituents and the complete wavefield at the datum, we calculated the inverse functions to retrieve them.

In the first chapter we deduced the Helmholtz wave equation starting from the movement and deformation expressions. In the second chapter we deduced the reciprocity theorems of convolution and correlation type in the complete and the one-way wavefields. In the chapter three we deduced the interferometric redatuming methods with correlation and convolution-based. In the chapter four we showed our expressions to calculate the up- and downward wavefield constituents by inversion and we presented two interpretations to calculate the complete wavefield at datum using as input above wavefields in expressions with convolution and correlation-based. In chapter five we deduced the inverse functions to solve the expressions in chapter four. Finally, in chapter six we showed the numerical experiments to validate our expressions to calculate the up- and downward with source at the earth's surface and receivers at datum, and the complete wavefield redatumed using the expressions from chapter three, four and five.

1.1 Acoustic wave equation

The Fourier transform of a time-dependent function $d(t)$ is defined as $\hat{d}(\omega) = \int_{-\infty}^{\infty} d(t) \exp(-i\omega t) dt$, where i is the imaginary unit and ω denotes the angular frequency. And the inverse Fourier transform, is defined as $d(t) = \frac{1}{2\pi} \int_{-\infty}^{\infty} \hat{d}(\omega) \exp(i\omega t) d\omega$. From the Fourier definition we can noticed that the limits of the integration can be decomposed in two time intervals, $(-\infty, 0]$ and $[0, \infty)$. According with Bleistein et al. (2001) the first interval corresponds to the physical condition of *anticausality*, i.e., the wavefield described at some time in the past implodes towards a source at time zero. The second interval corresponds to the physical condition of *causality*, that is, the source is initiated at some finite time, which can be taken at $t = 0$, before the wavefield is recorded. Having a clear definition of the Fourier transforms, and in order to deduce the Helmholtz wave equation, we define the acoustic wave equations for movement and deformation in frequency domain, respectively, as

$$\nabla \hat{p}(x, \omega) + i\omega \rho(x) \hat{v}(x, \omega) = \hat{f}, \quad (1.1)$$

$$\nabla \cdot \hat{v}(x, \omega) + i\omega \kappa(x) \hat{p}(x, \omega) = \hat{q}, \quad (1.2)$$

where $x = (x_1, x_2, x_3)$ and the subscripts are the axis coordinates, $\hat{p}(x, \omega)$ is the acoustic pressure (Pa), i is the imaginary part, ω is the angular frequency, ρ is the volume density of mass (kg/m^3), $v(x, \omega)$ is the particle velocity (m/s), κ is the compressibility (Pa^{-1}), f is the volume source density of volume force (N/m^3) and q is the volume density of injection rate (s^{-1}).

Multiplying equation (1.1) by $\frac{1}{\rho(x)}$, applying the divergent and multiplying by $\rho(x)$, respectively, we have

$$\rho(x) \nabla \cdot \left[\frac{1}{\rho(x)} \nabla \hat{p}(x, \omega) \right] + i\omega \rho(x) \nabla \cdot \hat{v}(x, \omega) = \rho(x) \nabla \cdot \left[\frac{1}{\rho(x)} \hat{f} \right]. \quad (1.3)$$

Multiplying (1.2) by $i\omega \rho(x)$, yields

$$i\omega \rho(x) \nabla \cdot \hat{v}(x, \omega) - \omega^2 \rho(x) \kappa(x) \hat{p}(x, \omega) = i\omega \rho(x) \hat{q}. \quad (1.4)$$

Subtracting equation (1.3) with (1.4), and taking into account that $\kappa = \frac{1}{c^2 \rho(x)}$, we have

$$\rho(x) \nabla \cdot \left[\frac{1}{\rho(x)} \nabla \hat{p}(x, \omega) \right] + \frac{\omega^2}{c^2} \hat{p}(x, \omega) = -\frac{\nabla \rho(x)}{\rho^2(x)} \hat{f} + \frac{1}{\rho(x)} \nabla \cdot \hat{f} - i\omega \rho(x) \hat{q}, \quad (1.5)$$

where c is the wave velocity. This expression is the inhomogeneous Helmholtz wave equation. We

define the source term of right-hand side of Equation (1.5) as

$$\hat{F} = -\frac{\nabla \rho(x)}{\rho^2(x)} \hat{f} + \frac{1}{\rho(x)} \nabla \cdot \hat{f} - i\omega \rho(x) \hat{q}. \quad (1.6)$$

We choose impulsive point sources of volume injection rate, according to $\hat{F} = -\delta(x - x^s)$. This is a Dirac delta source in the position x^s . Considering the above situation, the wavefield of equation (1.5) can be expressed in terms of acoustic Green's function, according to

$$\rho(x) \nabla \cdot \left[\frac{1}{\rho(x)} \nabla \hat{G}(x, \omega; x^s) \right] + \frac{\omega^2}{c^2(x)} \hat{G}(x, \omega; x^s) = -\delta(x - x^s). \quad (1.7)$$

1.2 Gauss's Theorem

The basis for all seismic interferometry is the Gauss's theorem, which relates an integral over a closed surface S of an arbitrary vector field to an integral over the enclosed volume V of the divergence of the vector field, this is written as:

$$\oint_S \mathbb{F} \cdot \hat{n} dS = \iiint_V \nabla \cdot \mathbb{F} dV, \quad (1.8)$$

where \mathbb{F} is a continuously differentiable vector field defined on a neighborhood of V . The left side of equation (1.8) is a surface integral over the surface S and the right side is a volume integral over the volume V (Figure 1.1).

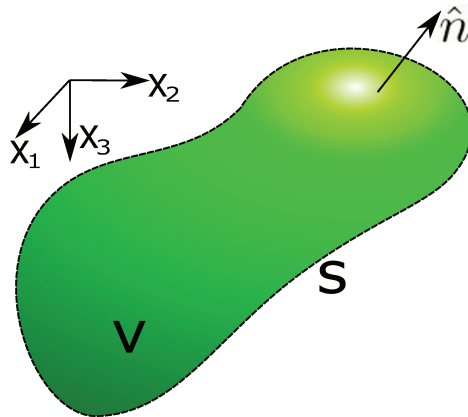


Figure 1.1: Representation of a volume V with surface S , \hat{n} is a surface normal vector.

To deduce the reciprocity theorems of convolution and correlation types, we start considering a

closed surface (Figure 1.2). On the surface we have sources and inside there are two receivers in the positions x_A and x_B , respectively. The medium in- and outside the surface S can be anything. This is the classical configuration to deduce the reciprocity theorems.

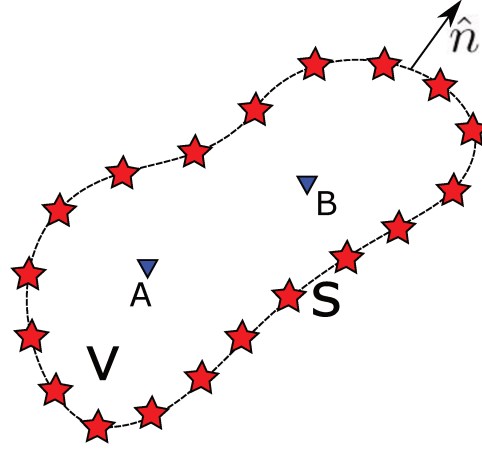


Figure 1.2: Representation of a volume V with surface S , the points A and B are inside V and \hat{n} is the surface normal vector.

In the next chapter we will deduce the reciprocity theorems, to both, full and one-way wavefield at cases of convolution and correlation type. Which we will have as a base the Gauss's theorem to make our deductions. There we will see that using conveniently this theorem we can make deductions in order to calculate the reciprocity theorems previously cited.

2. Reciprocity Theorems

In this chapter, we will derive the reciprocity theorems using the Helmholtz wave equation with velocity and density variation. These deductions allows us to discuss the limitations of the geometric distribution of the surface within the reciprocity theorems. Also, it is possible to analyze, how the surfaces geometric distribution can be influencing problems, i.g., interferometry, redatuming, focusing functions, etc. That is possible because the reciprocity theorems have as principal base the Gauss's theorem, which in the most basic essence consider a closed surface. We will do especial focus in the one-way reciprocity theorems of correlation and convolution type, which are the basis to the main contribution of this research work.

2.1 Reciprocity theorem of the convolution type

Considering $\hat{F}(x, \omega)$ in equation (1.6) as a monopole, where $\hat{f}(x, \omega) = 0$ and $\hat{q}(x, \omega; x^s) = \hat{q}(x, \omega)\delta(x - x^s)$. Following Wapenaar et al. (2010a,b), we consider two states A and B in the Helmholtz equation in order to calculate the reciprocity theorem of the convolution type. We assume both states to have the same properties, i.e., $\rho^A(x) = \rho^B(x) = \rho(x)$ and $c^A(x) = c^B(x) = c(x)$. Moreover, we assume that wavefields in both states have causal sources inside volume V . Since the states differ only in the source, the corresponding wavefields $\hat{p}(x, \omega; x^A) = \hat{p}^A$ and $\hat{p}(x, \omega; x^B) = \hat{p}^B$ must satisfy

$$\rho(x)\nabla \cdot \left[\frac{1}{\rho(x)} \nabla \hat{p}^A \right] + \frac{\omega^2}{c^2(x)} \hat{p}^A = -\hat{F}^A, \quad (2.1)$$

$$\rho(x)\nabla \cdot \left[\frac{1}{\rho(x)} \nabla \hat{p}^B \right] + \frac{\omega^2}{c^2(x)} \hat{p}^B = -\hat{F}^B, \quad (2.2)$$

Note that equations (2.1) and (2.2) show us that the difference between the state A and B is in the source distribution and the wavefield, the other properties remain the same. Multiplying equation (2.1) by $\hat{p}(x, \omega; x^B)$ and equation (2.2) by $\hat{p}(x, \omega; x^A)$, we have

$$\rho(x)\hat{p}^B \nabla \cdot \left[\frac{1}{\rho(x)} \nabla \hat{p}^A \right] + \frac{\omega^2}{c^2(x)} \hat{p}^B \hat{p}^A = -\hat{p}^B \hat{F}^A, \quad (2.3)$$

$$\rho(x)\hat{p}^A\nabla\cdot\left[\frac{1}{\rho(x)}\nabla\hat{p}^B\right]+\frac{\omega^2}{c^2(x)}\hat{p}^A\hat{p}^B=-\hat{p}^A\hat{F}^B. \quad (2.4)$$

Subtracting equations (2.3) with (2.4), we have

$$\rho(x)\hat{p}^B\nabla\cdot\left[\frac{1}{\rho(x)}\nabla\hat{p}^A\right]-\rho(x)\hat{p}^A\nabla\cdot\left[\frac{1}{\rho(x)}\nabla\hat{p}^B\right]=-\hat{p}^B\hat{F}^A+\hat{p}^A\hat{F}^B. \quad (2.5)$$

Reorganizing factors in the left-hand side of equation (2.5), we obtain

$$\rho(x)\left[\frac{\nabla\rho(x)}{\rho^2(x)}(\hat{p}^B\nabla\hat{p}^A-\hat{p}^A\nabla\hat{p}^B)+\frac{1}{\rho(x)}(\hat{p}^B\Delta\hat{p}^A-\hat{p}^A\Delta\hat{p}^B)\right]=\hat{p}^A\hat{F}^B-\hat{p}^B\hat{F}^A. \quad (2.6)$$

Then, equation (2.6) can be written as

$$\nabla\cdot\left[\frac{1}{\rho(x)}(\hat{p}^B\nabla\hat{p}^A-\hat{p}^A\nabla\hat{p}^B)\right]=\frac{1}{\rho(x)}(\hat{p}^A\hat{F}^B-\hat{p}^B\hat{F}^A). \quad (2.7)$$

After integration over an arbitrary volume V , equation (2.7) has an appropriate form to apply Gauss's theorem (equation 1.8). The result is the reciprocity theorem of convolution type, which we can represent as

$$\oint_S \frac{1}{\rho(x)}(\hat{p}^B\nabla\hat{p}^A-\hat{p}^A\nabla\hat{p}^B)\cdot\hat{n}dS=\iiint_V \frac{1}{\rho(x)}(\hat{p}^A\hat{F}^B-\hat{p}^B\hat{F}^A)dV. \quad (2.8)$$

Finally, equation (2.8) is the reciprocity theorem of the convolution type with density and velocity variation. This is because the operations in the frequency domain i.e., $\hat{p}^B\nabla\hat{p}^A$ are convolutions in the time domain. According with Bleistein et al. (2001) the integral over the closed surface S in equation (2.8) could be approached to zero, using the "Sommerfeld radiation conditions". Then, expression (2.8) can be written as

$$\oint_S \frac{1}{\rho(x)}(\hat{p}^B\nabla\hat{p}^A-\hat{p}^A\nabla\hat{p}^B)\cdot\hat{n}dS=0. \quad (2.9)$$

2.2 Reciprocity theorem of correlation type

A completely analogous analysis can be carried out starting at the complex conjugate of equation (2.1) together with expression (2.2). Replacing the wavefield \hat{p}^A and the source term \hat{F}^A in the above derivations by \hat{p}^{A*} and \hat{F}^{A*} , where the superscript $*$ denotes complex conjugate. Rewriting

expressions (2.1) and (2.2) for this analysis case, we have

$$\rho(x) \nabla \cdot \left[\frac{1}{\rho(x)} \nabla \hat{p}^{A*} \right] + \frac{\omega^2}{c^2(x)} \hat{p}^{A*} = -\hat{F}^{A*}, \quad (2.10)$$

$$\rho(x) \nabla \cdot \left[\frac{1}{\rho(x)} \nabla \hat{p}^B \right] + \frac{\omega^2}{c^2(x)} \hat{p}^B = -\hat{F}^B, \quad (2.11)$$

As the previous analysis, again we can verify that the difference between states A and B are in the source distribution and in the wavefield. Multiplying equations (2.10) by \hat{p}^B and (2.11) by \hat{p}^{A*} , we have

$$\rho(x) \hat{p}^B \nabla \cdot \left[\frac{1}{\rho(x)} \nabla \hat{p}^{A*} \right] + \frac{\omega^2}{c^2(x)} \hat{p}^B \hat{p}^{A*} = -\hat{p}^B \hat{F}^{A*}, \quad (2.12)$$

$$\rho(x) \hat{p}^{A*} \nabla \cdot \left[\frac{1}{\rho(x)} \nabla \hat{p}^B \right] + \frac{\omega^2}{c^2(x)} \hat{p}^{A*} \hat{p}^B = -\hat{p}^{A*} \hat{F}^B. \quad (2.13)$$

Subtracting equation (2.13) from (2.12), we have

$$\rho(x) \hat{p}^B \nabla \cdot \left[\frac{1}{\rho(x)} \nabla \hat{p}^{A*} \right] - \rho(x) \hat{p}^{A*} \nabla \cdot \left[\frac{1}{\rho(x)} \nabla \hat{p}^B \right] = -\hat{p}^B \hat{F}^{A*} + \hat{p}^{A*} \hat{F}^B. \quad (2.14)$$

Reorganizing factors in the left-hand side of equation (2.14), we obtain

$$\rho(x) \left[\frac{\nabla \rho(x)}{\rho^2(x)} (\hat{p}^{B*} \nabla \hat{p}^A - \hat{p}^A \nabla \hat{p}^{B*}) + \frac{1}{\rho(x)} (\hat{p}^B \Delta \hat{p}^{A*} - \hat{p}^{A*} \Delta \hat{p}^B) \right] = \hat{p}^{A*} \hat{F}^B - \hat{p}^B \hat{F}^{A*}. \quad (2.15)$$

Equation (2.15) can be written as

$$\nabla \cdot \left[\frac{1}{\rho(x)} (\hat{p}^B \nabla \hat{p}^{A*} - \hat{p}^{A*} \nabla \hat{p}^B) \right] = \frac{1}{\rho(x)} (\hat{p}^{A*} \hat{F}^B - \hat{p}^B \hat{F}^{A*}). \quad (2.16)$$

After integration over an arbitrary volume V , equation (2.16) has an appropriate form to apply the Gauss's theorem (equation 1.8). The result can be written as

$$\oint_S \frac{1}{\rho(x)} (\hat{p}^B \nabla \hat{p}^{A*} - \hat{p}^{A*} \nabla \hat{p}^B) \cdot \hat{n} dS = \iiint_V \frac{1}{\rho(x)} (\hat{p}^{A*} \hat{F}^B - \hat{p}^B \hat{F}^{A*}) dV. \quad (2.17)$$

Equation (2.17) is the reciprocity theorem of the correlation type with density and velocity variation. This is because the operations in the frequency domain i.e. $\hat{p}^B \nabla \hat{p}^{A*}$ are correlations in the time domain. According with Wapenaar and Berkhout (1989) the integral over the closed surface S in equation (2.17) could be approached to zero, using the "Wapenaar anti-ratiation conditions". Then,

expression (2.17) can be written as

$$\oint_S \frac{1}{\rho(x)} (\hat{p}^B \nabla \hat{p}^{A*} - \hat{p}^{A*} \nabla \hat{p}^B) \cdot \hat{n} dS = 0. \quad (2.18)$$

2.3 Surface decomposition of reciprocity theorems

In this section we will analyze the closed surface at the area integrals in the reciprocity theorems of convolutions and correlations type, previously deduced. The integral over the closed surface in equations (2.9) and (2.18) can be treated conveniently if is considered a cylindrical section of the wave-propagation medium, while the geometric restriction remains that the surface has to be closed. Now we show that the integrals in equations (2.9) and (2.18) can not only represent closed surfaces, but can also depict open surface integrals, simplifying the reciprocity theorem expressions above. This simplification is the fundamental basis to deduce the basic theory of interferometric redatuming methods. Surface S in equation (2.9) and (2.18) may be represented geometrically by a cylinder, composed of three surfaces defined as $S_1 = \{(x_1, x_2, x_3) \in \mathbb{R}^3 | x_3 = x_3^1\}$, $S_2 = \{(x_1, x_2, x_3) \in \mathbb{R}^3 | x_3 = x_3^2\}$ and $S_3 = \{(x_1, x_2, x_3) \in \mathbb{R}^3 | x_3 = x_3^3\}$, with the versors $\hat{n}_1 = (0, 0, -1)$, $\hat{n}_2 = (0, 0, 1)$ and $\hat{n}_3 = (x_1, x_2, 0)$, respectively (Figure 2.1).

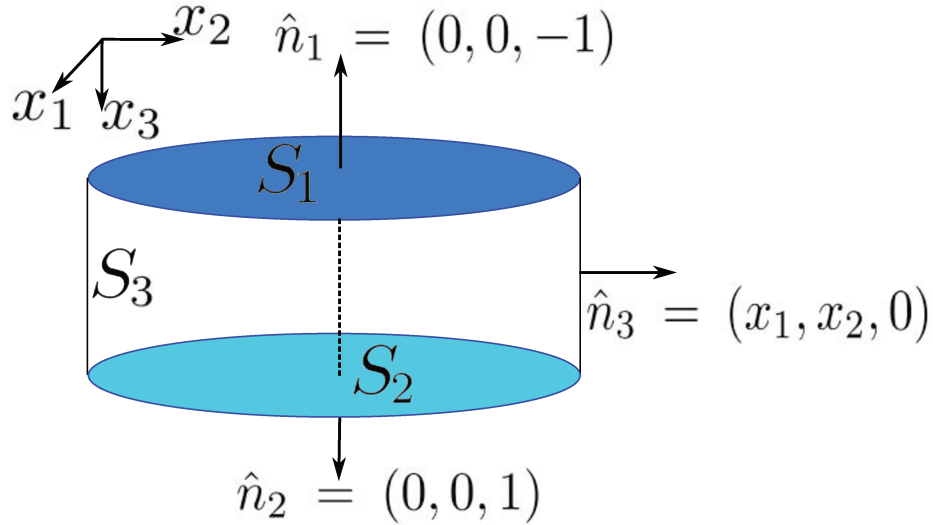


Figure 2.1: Cylinder divided in three different surfaces, S_1 , S_2 and S_3 .

Reciprocity theorem of convolution type

In order to decompose the closed surface in equation (2.9) to express the integral over a closed surface as an integral of open surface, as we can see in the next deduction, we write equation (2.9) as

$$\begin{aligned} & \iint_{S_1} \frac{1}{\rho(x)} (\hat{p}^B \nabla \hat{p}^A - \hat{p}^A \nabla \hat{p}^B) \cdot \hat{n}_1 dx_1 dx_2 + \iint_{S_2} \frac{1}{\rho(x)} (\hat{p}^B \nabla \hat{p}^A - \hat{p}^A \nabla \hat{p}^B) \cdot \hat{n}_2 dx_1 dx_2 + \\ & \iint_{S_3} \frac{1}{\rho(x)} (\hat{p}^B \nabla \hat{p}^A - \hat{p}^A \nabla \hat{p}^B) \cdot \hat{n}_3 dx_1 dx_2 = 0. \end{aligned} \quad (2.19)$$

According with Bleistein et al. (2001), the integral over the surface S_3 is zero when this surface is extended at the infinite. Then, equation (2.19) we can express the reciprocity theorem of convolution type as

$$\iint_{S_1} \frac{1}{\rho(x)} (\hat{p}^B \nabla \hat{p}^A - \hat{p}^A \nabla \hat{p}^B) \cdot \hat{n}_1 dx_1 dx_2 = - \iint_{S_2} \frac{1}{\rho(x)} (\hat{p}^B \nabla \hat{p}^A - \hat{p}^A \nabla \hat{p}^B) \cdot \hat{n}_2 dx_1 dx_2, \quad (2.20)$$

where S_1 and S_2 now denote the complete horizontal planes at $x_3 = x_3^1$ and $x_3 = x_3^2$, respectively. To derive equation (2.20), no assumptions regarding the nature of the medium inside and outside the surface S were necessary. In other words, this equation is valid for general inhomogeneous media, as long as the sources are outside volume V and the medium properties in both states are the same inside the volume V .

Reciprocity theorem of correlation type

In this section, we will simplify the reciprocity theorem of correlation type, decomposing the closed surface in equation (2.18), analogous to convolution type deduction. knowing the procedure, we write equation (2.18) as

$$\begin{aligned} & \iint_{S_1} \frac{1}{\rho(x)} (\hat{p}^B \nabla \hat{p}^{A*} - \hat{p}^{A*} \nabla \hat{p}^B) \cdot \hat{n}_1 dx_1 dx_2 + \iint_{S_2} \frac{1}{\rho(x)} (\hat{p}^B \nabla \hat{p}^{A*} - \hat{p}^{A*} \nabla \hat{p}^B) \cdot \hat{n}_2 dx_1 dx_2 + \\ & \iint_{S_3} \frac{1}{\rho(x)} (\hat{p}^B \nabla \hat{p}^{A*} - \hat{p}^{A*} \nabla \hat{p}^B) \cdot \hat{n}_3 dx_1 dx_2 = 0. \end{aligned} \quad (2.21)$$

Then form of the integral over the surface S_3 in equation (2.21) does not allow for the application of the Sommerfeld radiation conditions. However, using the ‘‘Wapenaar anti-radiation conditions’’ (Wapenaar and Berkhout, 1989), we can also justify that this integral tends to zero when the surface S_3

tends to infinity. In effect, these conditions state that there should be no contributions from infinity to this integral in an inhomogeneous medium with sufficient scattering. Hence, the reciprocity theorem of correlation type can be written as

$$\iint_{S_1} \frac{1}{\rho(x)} (\hat{p}^B \nabla \hat{p}^{A*} - \hat{p}^{A*} \nabla \hat{p}^B) \cdot \hat{n}_1 dx_1 dx_2 = - \iint_{S_2} \frac{1}{\rho(x)} (\hat{p}^B \nabla \hat{p}^{A*} - \hat{p}^{A*} \nabla \hat{p}^B) \cdot \hat{n}_2 dx_1 dx_2. \quad (2.22)$$

Again with S_1 and S_2 denoting the complete horizontal planes at $x_3 = x_3^1$ and $x_3 = x_3^2$, respectively. Equation (2.22) is valid for general inhomogeneous media inside and outside surface S . This theorem is valid if the media inside at surface S is scattering enough to satisfy the ‘‘Wapenaar anti-radiation conditions’’.

2.4 One-way reciprocity theorems

To derive the one-way forms of the above reciprocity theorems, we consider the two states, A and B , in the situation depicted in Figure (2.2). The surfaces S_1 and S_2 have now been extended to cover full horizontal planes, i.e., they are now defined as $S_1 = \{(x_1, x_2, x_3) \in \mathbb{R}^3 | x_3 = x_3^1\}$ and $S_2 = \{(x_1, x_2, x_3) \in \mathbb{R}^3 | x_3 = x_3^2\}$. Both states A and B have a source positions at surface S_1 , in x^A and x^B , respectively, and the receivers are distributed over both surfaces. Note that we do not consider S_1 to be a free surface.

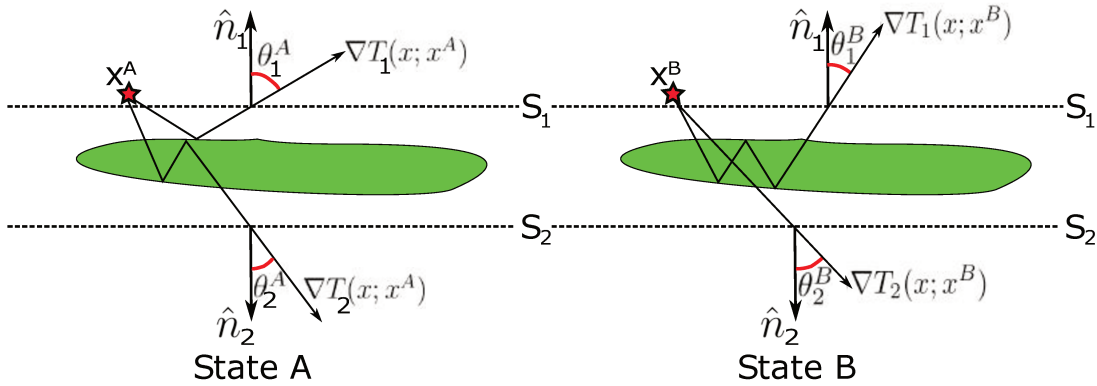


Figure 2.2: Sketch of two sources at positions x^A and x^B inside a volume V with receivers along the closed surface S with position x . The positions x are the directions of the incoming waves from x^A and x^B and their angles θ^A and θ^B with respect to the unit normal vector \hat{n} to the surface.

According with Wapenaar and Berkhout (1989) the total wavefield $\hat{p}(x, \omega)$ at the receiver can be

decomposed in up- (−) and downgoing (+) constituents, i.e.,

$$\hat{p}(x, \omega) = \hat{p}_+(x, \omega) + \hat{p}_-(x, \omega). \quad (2.23)$$

Equation (2.23) is important, because this decomposition allows to derive the one-way reciprocity theorems of convolution and correlation type. These, in turn, are the basis for the retrieval of the up- and downgoing Green's functions using least squares inversion.

At this point, we suppose that the sources are delta functions in space and time, and the velocity field is sufficiently smooth in a small region around both surfaces S_1 and S_2 . Under these assumptions, we can express the up- and downgoing pressure fields $\hat{p}(x, \omega; x^s)$ as the ray-theoretical approximation of the Green' function, which form is given by the following expression

$$\hat{p}_\pm(x, \omega; x^s) = A(x; x^s) \exp [\mp i\omega T(x; x^s)], \quad (2.24)$$

where T is the travelttime function that satisfies the eikonal equation $\|\nabla T(x; x^s)\|^2 = \frac{1}{c^2(x)}$, the subscript \pm in equation (2.24) is the down- and upgoing wavefield direction, respectively, and $A(x; x^s)$ amplitude, mainly determined by the geometrical-spreading factor. Signs (−) and (+) in the exponential factor in equation (2.24) are refer to causal and anticausal responses in time domain, respectively. In order to calculate the gradient of the pressure field, we does the derivative of equation (2.24), yields us

$$\nabla \hat{p}_\pm = \nabla A(x; x^s) \exp [\mp i\omega T(x; x^s)] \mp i\omega A(x; x^s) \nabla T(x; x^s) \exp [\mp i\omega T(x; x^s)]. \quad (2.25)$$

When the expression (2.25) is evaluated with high values of frequency, the term $\mp i\omega T(x; x^s)$ could be depressed because the term $\mp i\omega A(x; x^s) \nabla T(x; x^s) \exp [\mp i\omega T(x; x^s)]$ in high frequency values is dominant respect the other term, this case is called as “high-frequency approximation”. At that case, the gradient of equation (2.25) can be represented as

$$\nabla \hat{p}_\pm \approx \mp i\omega \hat{p}_\pm \nabla T(x; x^s), \quad (2.26)$$

where the amplitude variation has been neglected.

One-way reciprocity theorem of convolution type

In this section, we derive the one-way reciprocity theorems of convolution type using the above wavefield decomposition. This theorem is helpful to extract detailed information about the waves and

their behavior as a function of the propagation direction. When the wavefield is decomposed into up- and downgoing components, the gradients of these individual wavefield components depend on the propagation direction.

We start our derivation at the one-way reciprocity theorem of convolution type, replacing equation (2.23) in the expression (2.20), we obtain

$$\begin{aligned} & \iint_{S_1} \frac{1}{\rho(x)} [(\hat{p}_+^B + \hat{p}_-^B) \nabla (\hat{p}_+^A + \hat{p}_-^A) - (\hat{p}_+^A + \hat{p}_-^A) \nabla (\hat{p}_+^B + \hat{p}_-^B)] \cdot \hat{n}_1 dx_1 dx_2 = \\ & - \iint_{S_2} \frac{1}{\rho(x)} [(\hat{p}_+^B + \hat{p}_-^B) \nabla (\hat{p}_+^A + \hat{p}_-^A) - (\hat{p}_+^A + \hat{p}_-^A) \nabla (\hat{p}_+^B + \hat{p}_-^B)] \cdot \hat{n}_2 dx_1 dx_2. \end{aligned} \quad (2.27)$$

Assuming that the medium is smooth in a small region around S_1 and S_2 the gradient of pressure fields can be approximated in high frequency with the expression (2.26). Still upon high-frequency arguments, the main contributions to the integrals in equation (2.27) come from stationary points on surfaces S_1 and S_2 . At those stationary points \hat{p}^A and \hat{p}^B are identical. This implies, for example, that the terms $\hat{p}_+^B \nabla \hat{p}_-^A$ and $-\hat{p}_-^A \nabla \hat{p}_+^B$ give equal contribution to the integral, whereas the contributions of $-\hat{p}_+^B \nabla \hat{p}_+^A$ and $\hat{p}_+^A \nabla \hat{p}_+^B$ cancel each other (Wapenaar and Fokkema, 2006). Hence, we can rewrite equation (2.27) as

$$\iint_{S_1} \frac{1}{\rho(x)} (\hat{p}_+^B \nabla \hat{p}_-^A + \hat{p}_-^B \nabla \hat{p}_+^A) \cdot \hat{n}_1 dx_1 dx_2 \approx - \iint_{S_2} \frac{1}{\rho(x)} (\hat{p}_+^B \nabla \hat{p}_-^A + \hat{p}_-^B \nabla \hat{p}_+^A) \cdot \hat{n}_2 dx_1 dx_2. \quad (2.28)$$

Considering that surfaces S_1 and S_2 have the geometrical configuration as we show in the Figure (2.2), the normal vectors at the surfaces S_1 and S_2 in equation (2.28) can be expressed as $\hat{n}_1 = (0, 0, -1)$ and $\hat{n}_2 = (0, 0, 1)$, respectively, allowing us to express equation (2.28) as

$$\iint_{S_1} \frac{1}{\rho(x)} (\hat{p}_-^B \partial_3 \hat{p}_+^A - \hat{p}_-^A \partial_3 \hat{p}_+^B) dx_1 dx_2 \approx \iint_{S_2} \frac{1}{\rho(x)} (\hat{p}_+^B \partial_3 \hat{p}_-^A + \hat{p}_-^B \partial_3 \hat{p}_+^A) dx_1 dx_2. \quad (2.29)$$

We write in the left-hand side of the equation (2.29) the term $\hat{p}_+^B \partial_3 \hat{p}_-^A$ as $-\hat{p}_-^A \partial_3 \hat{p}_+^B$, that is the most convenient form for our deductions in future sections of this work. Equation (2.29) is the most common form to write the one-way reciprocity theorem of convolution type.

One-way reciprocity theorem of correlation type

In this section we will deduce the one-way reciprocity theorem of correlation type, in which we consider the state A as a complex conjugate, denoting this with an asterisk (*). Considering equation (2.23) in its complex conjugate form, we replace it into the equation (2.22), obtaining

$$\begin{aligned} \iint_{S_1} \frac{1}{\rho(x)} [(\hat{p}_+^B + \hat{p}_-^B) \nabla (\hat{p}_+^{A*} + \hat{p}_-^{A*}) - (\hat{p}_+^{A*} + \hat{p}_-^{A*}) \nabla (\hat{p}_+^B + \hat{p}_-^B)] \cdot \hat{n}_1 dx_1 dx_2 = \\ - \iint_{S_2} \frac{1}{\rho(x)} [(\hat{p}_+^B + \hat{p}_-^B) \nabla (\hat{p}_+^{A*} + \hat{p}_-^{A*}) - (\hat{p}_+^{A*} + \hat{p}_-^{A*}) \nabla (\hat{p}_+^B + \hat{p}_-^B)] \cdot \hat{n}_2 dx_1 dx_2. \end{aligned} \quad (2.30)$$

As previous analysis, the principal contributions to the integrals in equation (2.30) comes from the stationary points on surfaces S_1 and S_2 . This implies, for example, that the terms $\hat{p}_+^B \nabla \hat{p}_+^{A*}$ and $-\hat{p}_+^{A*} \nabla \hat{p}_+^B$ give equal contribution to the integral, whereas the contributions of $\hat{p}_+^B \nabla \hat{p}_-^{A*}$ and $-\hat{p}_-^{A*} \nabla \hat{p}_+^B$ cancel each other (Wapenaar and Fokkema, 2006). After that, we can write equation (2.30) as

$$\iint_{S_1} \frac{1}{\rho(x)} (\hat{p}_+^B \nabla \hat{p}_+^{A*} + \hat{p}_-^B \nabla \hat{p}_-^{A*}) \cdot \hat{n}_1 dx_1 dx_2 \approx - \iint_{S_2} \frac{1}{\rho(x)} (\hat{p}_+^B \nabla \hat{p}_+^{A*} + \hat{p}_-^B \nabla \hat{p}_-^{A*}) \cdot \hat{n}_2 dx_1 dx_2. \quad (2.31)$$

Similar to previous analysis we consider the normal vectors at surfaces S_1 and S_2 as $\hat{n}_1 = (0, 0, -1)$ and $\hat{n}_2 = (0, 0, 1)$, respectively, to deduce the following expression

$$\iint_{S_1} \frac{1}{\rho(x)} (\hat{p}_-^B \partial_3 \hat{p}_-^{A*} - \hat{p}_+^{A*} \partial_3 \hat{p}_+^B) dx_1 dx_2 \approx \iint_{S_2} \frac{1}{\rho(x)} (\hat{p}_+^B \partial_3 \hat{p}_+^{A*} + \hat{p}_-^B \partial_3 \hat{p}_-^{A*}) dx_1 dx_2. \quad (2.32)$$

Again we write the equation (2.32) as the most convenient form to our future deductions in this work, we rewrite the term $\hat{p}_+^B \partial_3 \hat{p}_+^{A*}$ to $-\hat{p}_+^{A*} \partial_3 \hat{p}_+^B$ in the left-hand side of equation (2.32). Equation (2.32) is the most common form to write the one-way reciprocity theorem of correlation type.

2.5 Source-receiver reciprocity

In this section we will deduce the reciprocity theorem between the Green's functions, where we also consider a especial conditions in the medium where the wavefield is propagated. In this case, the medium between x^A and x^B in the Figure (2.3) is inhomogeneous. Through the use of Gauss' theorem with the vector field appropriately chosen, we will deduce the Green's functions reciprocity theorem for points x^A and x^B in a variable-density medium.

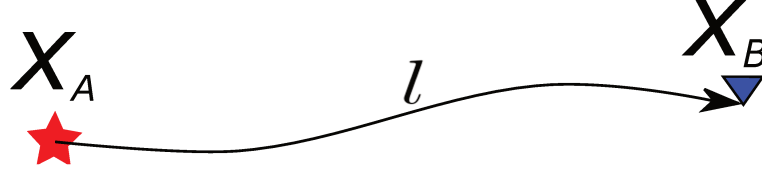


Figure 2.3: Sketch of a source at position x^A with a receiver at position x^B , where l is the representation of a wave path from x^A to x^B .

We start from equations (1.5) and (1.7). For simplicity, we write $\hat{G}^A = \hat{G}(x, \omega; x^A)$. Multiplying Equation (1.5) by \hat{G}^A , we obtain

$$\rho(x)\hat{G}^A \nabla \cdot \left[\frac{1}{\rho(x)} \nabla \hat{p} \right] + \frac{\omega^2}{c^2(x)} \hat{G}^A \hat{p} = -\hat{F}(x, \omega) \hat{G}^A, \quad (2.33)$$

and multiplying the equation (1.7) at the position x^A by \hat{p} , yields

$$\rho(x)\hat{p} \nabla \cdot \left[\frac{1}{\rho(x)} \nabla \hat{G}^A \right] + \frac{\omega^2}{c^2(x)} \hat{p} \hat{G}^A = -\delta(x - x^A) \hat{p}. \quad (2.34)$$

Subtracting Equations (2.33) and (2.34), integrating over an arbitrary volume V , and applying Gauss's theorem show in Equation (1.8), we find

$$\oint_S \frac{1}{\rho(x)} \left(\hat{p} \nabla \hat{G}^A - \hat{G}^A \nabla \hat{p} \right) \cdot \hat{n} dS = \iiint_V \frac{1}{\rho(x)} \left[\hat{F}(x, \omega) \hat{G}^A - \delta(x - x^A) \hat{p} \right] dV. \quad (2.35)$$

An analogous analysis as done to obtain equation (2.9), expression (2.35) can be written as

$$\oint_{\partial S} \frac{1}{\rho(x)} \left(\hat{p} \nabla \hat{G}^A - \hat{G}^A \nabla \hat{p} \right) \cdot \hat{n} dS = 0. \quad (2.36)$$

Using equation (2.36) in expression (2.35) and solving the volume integral of the Dirac delta at a point x^A of the function \hat{p} , yields

$$\hat{p}(x^A, \omega) = \rho(x^A) \iiint_V \frac{1}{\rho(x)} \hat{F}(x, \omega) \hat{G}^A dV. \quad (2.37)$$

Considering another stage, where the source term is in the position x^B , then we have $\hat{F}(x, \omega) = \delta(x - x^B)$, replacing this in the equation (2.37), yields

$$\hat{G}(x^A, \omega; x^B) = \rho(x^A) \iiint_V \frac{1}{\rho(x)} \delta(x - x^B) \hat{G}(x, \omega; x^A) dV, \quad (2.38)$$

which results is the identity

$$\frac{\hat{G}(x^A, \omega; x^B)}{\rho(x^A)} = \frac{\hat{G}(x^B, \omega; x^A)}{\rho(x^B)}. \quad (2.39)$$

From equation (2.39), we see that the Green' function between points x^A and x^B is not reciprocal, if the values of the densities at these points are different. However, a density-scaled Green's function (Bleistein et al., 2001) is reciprocal as can be seen, if we multiplied each side of equation by a density factor $\sqrt{\rho(x^A)\rho(x^B)}$, as

$$\left[\frac{\hat{G}(x^A, \omega; x^B)}{\rho(x^A)} \right] \sqrt{\rho(x^A)\rho(x^B)} = \left[\frac{\hat{G}(x^B, \omega; x^A)}{\rho(x^B)} \right] \sqrt{\rho(x^A)\rho(x^B)}. \quad (2.40)$$

Therefore, the density-scaled Green's function can then be defined as

$$\hat{g}(x, \omega; x^s) = \sqrt{\frac{\rho(x^s)}{\rho(x)}} \hat{G}(x, \omega; x^s), \quad (2.41)$$

where x_s is the source position. Conversely, the Green' function can be recovered from its density-scaled version by

$$\hat{G}(x, \omega; x^s) = \sqrt{\frac{\rho(x)}{\rho(x^s)}} \hat{g}(x, \omega; x^s). \quad (2.42)$$

We can note that in the case of constant density the density-scaled Green's function $\hat{g}(x, \omega; x^s)$ reduces to the Green's function $\hat{G}(x, \omega; x^s)$ itself. With definition (2.41), the reciprocity relation is

$$\hat{g}(x^A, \omega; x^B) = \hat{g}(x^B, \omega; x^A). \quad (2.43)$$

3. Interferometric Redatuming

In this chapter, we deduce the basic interferometry equations based on the reciprocity theorem of correlation type in order to apply this theory as a way to focus seismic imaging below geologically complex bodies or structures. Redatuming is a technique that seeks to correct seismic data for effects of an irregular surface acquisition (land seismic data) and effects of complex geological structures in the overburden. Interferometric methods can be used to relocate sources where only receivers are available and have been used to move acquisition geometries to the ocean bottom or transform data between surface seismic and velocity seismic profiles. By combining modeling with interferometry and correlating the modeled direct wave with seismic surface data, we can relocate the acquisition system to an arbitrary datum in the subsurface, in which the propagation of direct waves can be modeled with sufficient accuracy. In this way, we can carry the seismic acquisition geometry from the surface to geologic horizons of interest. Specifically, we show the derivation and approximation of the seismic interferometry equation, conveniently using Green's theorem for the Helmholtz equation with density variation.

3.1 Interferometric equation with correlation-based expressions

We start with a review of the basic interferometry equation (see, e.g., Wapenaar et al., 2010a). We consider the case where we have a closed surface S with receivers located on it. Inside the enclosed volume V , we have two sources located in positions x_A and x_B , where $x = (x_1, x_2, x_3)$ (see Figure 3.1). Considering the form of the wave equation (1.7) we define two expressions with the same form but evaluated at different source position x^A and x^B , respectively, as

$$\rho(x) \nabla \cdot \left[\frac{1}{\rho(x)} \nabla \hat{G}^*(x, \omega; x^A) \right] + \frac{\omega^2}{c^2(x)} \hat{G}^*(x, \omega; x^A) = -\delta(x - x^A), \quad (3.1)$$

and

$$\rho(x) \nabla \cdot \left[\frac{1}{\rho(x)} \nabla \hat{G}(x, \omega; x^B) \right] + \frac{\omega^2}{c^2(x)} \hat{G}(x, \omega; x^B) = -\delta(x - x^B). \quad (3.2)$$

In equation (3.1) the superscript $*$ denotes the complex conjugate.

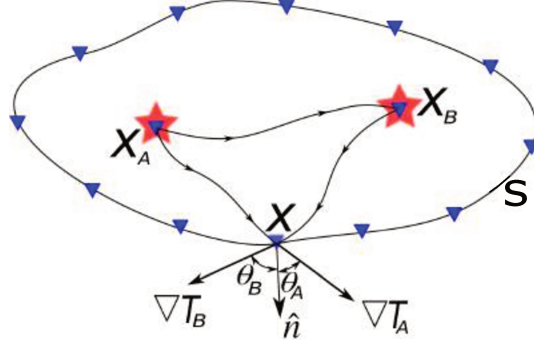


Figure 3.1: Two-dimensional sketch of two sources at positions x_A and x_B inside a volume V with receivers along the closed surface S of V . Indicated at position x are the propagation directions of the incoming waves from x_A and x_B , and their angles θ_A and θ_B with respect to the unit normal vector \hat{n} to the surface.

Multiplying equations (3.1) by $\hat{G}(x, \omega; x^B)$ and equation (3.2) by $\hat{G}^*(x, \omega; x^A)$, and subtracting the results, we can write, in analogy to the analysis of the source-receiver reciprocity theorem

$$\nabla \cdot \left\{ \frac{1}{\rho(x)} \left[\hat{G}(x, \omega; x^B) \nabla \hat{G}^*(x, \omega; x^A) - \hat{G}^*(x, \omega; x^A) \nabla \hat{G}(x, \omega; x^B) \right] \right\} = \frac{1}{\rho(x)} \left[\delta(x - x^B) \hat{G}^*(x, \omega; x^A) - \delta(x - x^A) \hat{G}(x, \omega; x^B) \right]. \quad (3.3)$$

Integrating equation (3.3) over an arbitrary volume V with surface S and applying Gauss' theorem

$$\oint_S \frac{1}{\rho(x)} \left[\hat{G}(x, \omega; x^B) \nabla \hat{G}^*(x, \omega; x^A) - \hat{G}^*(x, \omega; x^A) \nabla \hat{G}(x, \omega; x^B) \right] \cdot \hat{n} \, dS = \iiint_V \frac{1}{\rho(x)} \left[\delta(x - x^B) \hat{G}^*(x, \omega; x^A) - \delta(x - x^A) \hat{G}(x, \omega; x^B) \right] dV. \quad (3.4)$$

The volume integral on the right-hand side of equation (3.4) can be explicitly solved. This yields

$$\oint_S \frac{1}{\rho(x)} \left[\hat{G}(x, \omega; x^B) \nabla \hat{G}^*(x, \omega; x^A) - \hat{G}^*(x, \omega; x^A) \nabla \hat{G}(x, \omega; x^B) \right] \cdot \hat{n} \, dS = \frac{1}{\rho(x^B)} \hat{G}^*(x^B, \omega; x^A) - \frac{1}{\rho(x^A)} \hat{G}(x^A, \omega; x^B). \quad (3.5)$$

The reciprocity of Green's functions, as seen above have the following relation

$$\frac{1}{\rho(x^B)} \hat{G}(x^B, \omega; x^A) = \frac{1}{\rho(x^A)} \hat{G}(x^A, \omega; x^B). \quad (3.6)$$

Replacing relation (3.6) in equation (3.5) we have

$$\begin{aligned} \oint_S \frac{1}{\rho(x)} \left[\hat{G}(x, \omega; x^B) \nabla \hat{G}^*(x, \omega; x^A) - \hat{G}^*(x, \omega; x^A) \nabla \hat{G}(x, \omega; x^B) \right] \cdot \hat{n} dS = \\ \frac{1}{\rho(x^B)} \left[\hat{G}^*(x^B, \omega; x^A) - \hat{G}(x^B, \omega; x^A) \right]. \end{aligned} \quad (3.7)$$

On the right-hand side of equation (3.7) the real part of $\hat{G}(x^B, \omega; x^A)$ cancels. Thus, we obtain the general interferometry relation that is

$$\begin{aligned} \oint_S \frac{1}{\rho(x)} \left[\hat{G}(x, \omega; x^B) \nabla \hat{G}^*(x, \omega; x^A) - \hat{G}^*(x, \omega; x^A) \nabla \hat{G}(x, \omega; x^B) \right] \cdot \hat{n} dS = \\ - \frac{2i}{\rho(x^B)} \text{Im} \left[\hat{G}(x^B, \omega; x^A) \right], \end{aligned} \quad (3.8)$$

or

$$\begin{aligned} \oint_S \frac{1}{\rho(x)} \left[\hat{G}(x, \omega; x^B) \nabla \hat{G}^*(x, \omega; x^A) - \hat{G}^*(x, \omega; x^A) \nabla \hat{G}(x, \omega; x^B) \right] \cdot \hat{n} dS = \\ - \frac{2i}{\rho(x^A)} \text{Im} \left[\hat{G}(x^A, \omega; x^B) \right]. \end{aligned} \quad (3.9)$$

This is the fundamental relationship for all interferometry techniques with correlation, because it proves that the Green's function of the propagation from x^A to x^B can be obtained with information about the wavefield propagating from x^A and from x^B to (all) receivers on the closed surface. This only is possible if x^A and x^B are inside the closed surface.

3.1.1 Correlation-based Green's function approximation

For the following considerations, we refer to Figure (3.1). In high-frequency approximation, the Green's function's gradients satisfy

$$\nabla \hat{G}(x, \omega; x^s) \approx -i\omega \hat{G}(x, \omega; x^s) \nabla T(x; x^s). \quad (3.10)$$

The complex conjugate of equation (3.10) reads

$$\nabla \hat{G}^*(x, \omega; x^s) \approx i\omega \hat{G}^*(x, \omega; x^s) \nabla T(x; x^s). \quad (3.11)$$

Substituting equations (3.10) and (3.11) in (3.8), and simplifying the imaginary terms on both sides, we have

$$\begin{aligned} -i\omega \rho(x^B) \oint_S \frac{1}{\rho(x)} \left[\hat{G}(x, \omega; x^B) \nabla T(x; x^A) \hat{G}^*(x, \omega; x^A) + \right. \\ \left. \hat{G}^*(x, \omega; x^A) \nabla T(x; x^B) \hat{G}(x, \omega; x^B) \right] \cdot \hat{n} dS \approx 2i \text{Im} \left[\hat{G}(x^B, \omega; x^A) \right]. \end{aligned} \quad (3.12)$$

At the stationary point (Bleistein et al., 2001) it is satisfied that $\nabla T(x; x^A) = \nabla T(x; x^B) = \nabla T(x)$. This implies that both terms in the left-hand side of equation (3.12) have the same contribution at the stationary point. Then is possible to rewrite equation (3.12) as

$$-i\omega \rho(x^B) \oint_S \frac{1}{\rho(x)} \hat{G}(x, \omega; x^B) \nabla T(x) \hat{G}^*(x, \omega; x^A) \cdot \hat{n} dS \approx i \text{Im} \left[\hat{G}(x^B, \omega; x^A) \right]. \quad (3.13)$$

Considering expression (3.11) is possible rewrite equation (3.13) as

$$\oint_S \frac{1}{\rho(x)} \hat{G}(x, \omega; x^B) \nabla \hat{G}^*(x, \omega; x^A) \cdot \hat{n} dS \approx -i \text{Im} \left[\frac{\hat{G}(x^B, \omega; x^A)}{\rho(x^B)} \right]. \quad (3.14)$$

Equation (3.14) allows us to calculate the Green' function between the source points x^A and x^B , only multiplying in the frequency domain the Green' functions with source in x^B and receivers varying in x by the gradient of the complex conjugate Green' function with source in x^A and receivers varying in x . This is a particular and important result in the literature i.e., Wapenaar et al. (2010a), because with a simple multiplication in the frequency domain allows us to retrieve Green's functions for source positions where we only have receivers.

3.2 Interferometric equation with convolution-based expressions

In this section, we will present the seismic interferometry by convolution-based, that is an alternative to the classical correlation-based scheme. According with Wapenaar et al. (2010b) in many situations is most convenient to make interferometry by convolution-based than by correlation-based. One of the main advantages of the convolution-based procedure is its inherent compensation for the properties of the source wavelet. Another important advantage is that the underlying theory does not

require the assumption of a lossless medium (Slob and Wapenaar, 2007). To deduce the convolution-based type expressions, we consider that outside at the closed surface S we have a point source denoted as x^S (Figure 3.2). At this point, we define two Helmholtz equations, where equation (3.15) have a point source at the position x^S and the second equation is (3.16) which the source term is zero, this equation have virtual sources over the closed surface S denoted as x which correspond to the stationary points between x^S and x^B (see Figure 3.2)

$$\rho(x)\nabla \cdot \left[\frac{1}{\rho(x)} \nabla \hat{G}(x, \omega; x^S) \right] + \frac{\omega^2}{c^2(x)} \hat{G}(x, \omega; x^S) = -\delta(x - x^S). \quad (3.15)$$

and

$$\rho(x)\nabla \cdot \left[\frac{1}{\rho(x)} \nabla \hat{G}(x^B, \omega; x) \right] + \frac{\omega^2}{c^2(x)} \hat{G}(x^B, \omega; x) = 0. \quad (3.16)$$

The geometrical configuration for the convolution-type method is described in Figure (3.2)

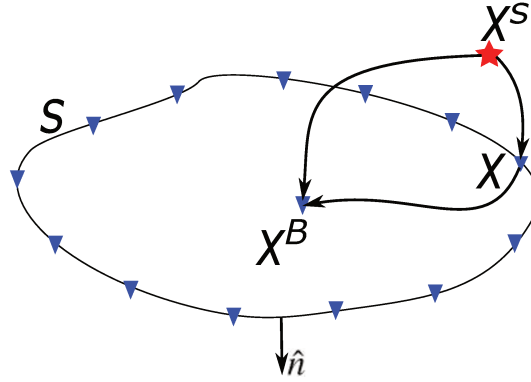


Figure 3.2: Two-dimensional sketch of a source at positions x^S outside the surface S , with receivers along and inside the position x and x^B , respectively, at the closed surface S of volume V . Where \hat{n} is the unit normal vector at the surface S .

Multiplying equations (3.15) by $\hat{G}(x^B, \omega; x)$ and equation (3.16) by $\hat{G}(x, \omega; x^S)$, and subtracting the results, respectively, analogous to the analysis of the source-receiver reciprocity theorem, this operation can be expressed as

$$\begin{aligned} \nabla \cdot \left\{ \frac{1}{\rho(x)} \left[\hat{G}(x^B, \omega; x) \nabla \hat{G}(x, \omega; x^S) - \hat{G}(x, \omega; x^S) \nabla \hat{G}(x^B, \omega; x) \right] \right\} = \\ - \frac{1}{\rho(x)} \left[\delta(x - x^S) \hat{G}(x^B, \omega; x) \right], \end{aligned} \quad (3.17)$$

applying Gauss' theorem making integration over an arbitrary surface S and an arbitrary volume V ,

respectively, we have

$$\begin{aligned} \oint_S \frac{1}{\rho(x)} \left[\hat{G}(x^B, \omega; x) \nabla \hat{G}(x, \omega; x^S) - \hat{G}(x, \omega; x^S) \nabla \hat{G}(x^B, \omega; x) \right] \cdot \hat{n} dS = \\ - \iiint_V \frac{1}{\rho(x)} \left[\delta(x - x^S) \hat{G}(x^B, \omega; x) \right] dV, \end{aligned} \quad (3.18)$$

solving the volume integral of right-hand side of equation (3.18) we obtain

$$\begin{aligned} \oint_S \frac{1}{\rho(x)} \left[\hat{G}(x^B, \omega; x) \nabla \hat{G}(x, \omega; x^S) - \hat{G}(x, \omega; x^S) \nabla \hat{G}(x^B, \omega; x) \right] \cdot \hat{n} dS = \\ - \frac{1}{\rho(x^S)} \hat{G}(x^B, \omega; x^S). \end{aligned} \quad (3.19)$$

This is the fundamental relationship for all convolution based interferometry techniques, because it proves that the Green' function of the propagation from x^S to x^B can be obtained with information about the wavefield propagating from x^S to (all) receivers on the closed surface.

3.2.1 Convolution-based Green's function approximation

In this section we will simplify the term evaluated in equation (3.19). The right-hand side of equation (3.19) contains a combination of two convolution products in the frequency domain. To start we observe that $\hat{G}(x, \omega; x^S)$ is the superposition of an inward and outward propagating field, denoted with the subscripts $+$ and $-$, respectively, which is written as $\hat{G}(x, \omega; x^S) = \hat{G}_+(x, \omega; x^S) + \hat{G}_-(x, \omega; x^S)$ (Wapenaar et al., 2010b). In the high frequency regime the derivatives in equation (3.19) can be approximated in correspondence to the expression (2.26). The main contribution to integral 3.19 comes from the stationary points on surface S . However, the stationary points are different for terms containing \hat{G}_+ than for those containing \hat{G}_- . Considering the wavefield decomposition of the Green's function $\hat{G}(x, \omega; x^S)$ is possible rewrite equation (3.19) as a coupled system, as we show in equations (3.20) and (3.21). For terms containing \hat{G}_+ in the expression evaluated in the closed surface integral in equation (3.19), we have at the stationary points

$$\begin{aligned} \oint_S \frac{1}{\rho(x)} \left[\hat{G}(x^B, \omega; x) \nabla \hat{G}_+(x, \omega; x^S) - \hat{G}_+(x, \omega; x^S) \nabla \hat{G}(x^B, \omega; x) \right] \cdot \hat{n} dS = \\ i\omega \oint_S \frac{1}{\rho(x)} \left[-\hat{G}(x^B, \omega; x) \nabla T \hat{G}_+(x, \omega; x^S) + \hat{G}_+(x, \omega; x^S) \nabla T \hat{G}(x^B, \omega; x) \right] \cdot \hat{n} dS, \end{aligned} \quad (3.20)$$

whereas for terms containing \hat{G}_- we have

$$\begin{aligned} & \oint_S \frac{1}{\rho(x)} \left[\hat{G}(x^B, \omega; x) \nabla \hat{G}_-(x, \omega; x^S) - \hat{G}_-(x, \omega; x^S) \nabla \hat{G}(x^B, \omega; x) \right] \cdot \hat{n} dS = \\ & i\omega \oint_S \frac{1}{\rho(x)} \left[\hat{G}(x^B, \omega; x) \nabla T \hat{G}_-(x, \omega; x^S) + \hat{G}_-(x, \omega; x^S) \nabla T \hat{G}(x^B, \omega; x) \right] \cdot \hat{n} dS. \end{aligned} \quad (3.21)$$

Considering the gradient of in- and outward constituents of the Green's functions, we can rewrite the right-hand side expressions of equations (3.20) and (3.21) as, respectively

$$\oint_S \frac{1}{\rho(x)} \left[\hat{G}(x^B, \omega; x) \nabla \hat{G}_+(x, \omega; x^S) - \hat{G}_+(x, \omega; x^S) \nabla \hat{G}(x^B, \omega; x) \right] \cdot \hat{n} dS, \quad (3.22)$$

and

$$- \oint_S \frac{1}{\rho(x)} \left[\hat{G}(x^B, \omega; x) \nabla \hat{G}_-(x, \omega; x^S) + \hat{G}_-(x, \omega; x^S) \nabla \hat{G}(x^B, \omega; x) \right] \cdot \hat{n} dS. \quad (3.23)$$

According with Wapenaar and Fokkema (2006) at the stationary point over the surface S , the term $\hat{G}(x^B, \omega; x) \nabla \hat{G}_+(x, \omega; x^S)$ can be expressed as $-\hat{G}_+(x, \omega; x^S) \nabla \hat{G}(x^B, \omega; x)$, the in equation (3.23) the terms have contribution among them. On the other hand the term $\hat{G}(x^B, \omega; x) \nabla \hat{G}_-(x, \omega; x^S)$ can be expressed as $-\hat{G}_-(x, \omega; x^S) \nabla \hat{G}(x^B, \omega; x)$, then the terms in equation (3.23) cancel each other. Taking into account the above observations, we can rewrite the equation (3.19) as

$$2\rho(x^S) \oint_S \frac{1}{\rho(x)} \hat{G}(x^B, \omega; x) \nabla \hat{G}_+(x, \omega; x^S) \cdot \hat{n} dS = \hat{G}(x^B, \omega; x^S). \quad (3.24)$$

Equation (3.24) allows us to calculate the Green' function between x and x^B , which represents the wavefield inside the surface S , if we know the gradient of the reference wavefield $\nabla \hat{G}_+(x, \omega; x^S)$ and the Green's function between x^S and x^B . Knowing this, it is possible retrieve $\hat{G}(x^B, \omega; x)$ using any numerical inversion technique.

3.3 Correlation-based interferometric redatuming

For practical purposes, equation (3.8) is still inadequate, because it is extremely rare for closed surface data to be available. Moreover, the Green' functions' gradients generally are unknown. Therefore, the quantities in equation (3.8) need to be approximated by practically available data. In this section we will consider the theory of correlation-based interferometry considering a seismic array

over the earth's surface, we will show that it is possible to relocate this seismic array to an arbitrary position at depth that we call datum. To start the analysis of both correlation and convolution-based the interferometric methods (next section), we consider two states A and B , just as we show in Figure (3.3). We consider state A to represent the background (or unperturbed) medium and B the perturbed medium.

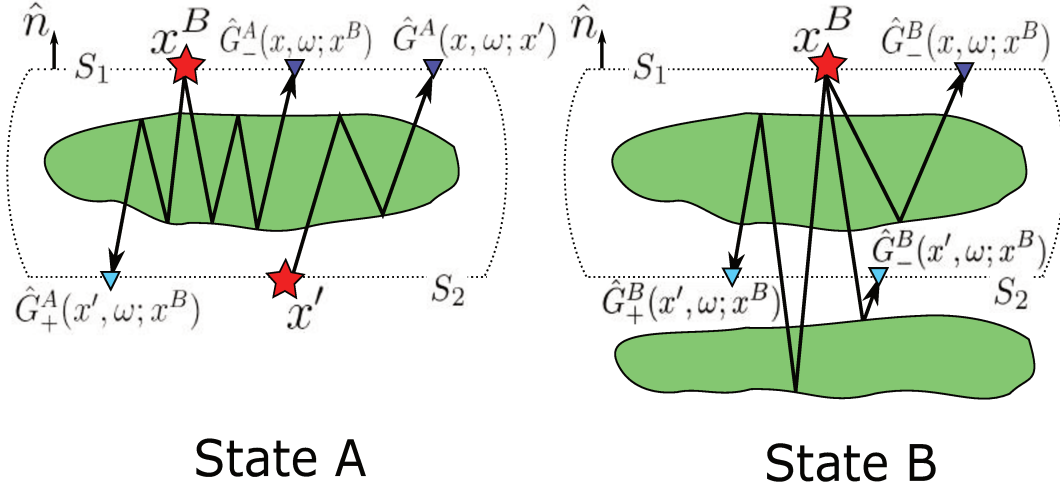


Figure 3.3: Two states with the same inhomogeneous medium between surfaces S_1 and S_2 . State A describes the transmitted wavefield from S_1 to S_2 and its scattered response recorded at S_1 if the medium is homogeneous above S_1 and below S_2 . State B describes the corresponding wavefields if the medium is also inhomogeneous below S_2 . The dotted line indicates the volume V .

Interferometric methods based on correlation could be a initial tool to retrieve the Green' functions in depth and try to focus the seismic image in the area of interest. The Helmholtz equations describing the wavefields for a point source at x^B in states A and B are

$$\mathcal{L}^A \hat{G}^{A*}(x, \omega; x^B) = -\delta(x - x^B), \quad (3.25)$$

and

$$\mathcal{L}^B \hat{G}^B(x, \omega; x^B) = -\delta(x - x^B), \quad (3.26)$$

equations (3.25) and (3.26) are associated to the Helmholtz operators as

$$\mathcal{L}^A = \rho_A(x) \nabla \cdot \left[\frac{1}{\rho_A(x)} \nabla \right] + \frac{\omega^2}{c_A^2(x)}, \quad (3.27)$$

and

$$\mathcal{L}^B = \rho_B(x) \nabla \cdot \left[\frac{1}{\rho_B(x)} \nabla \right] + \frac{\omega^2}{c_B^2(x)}. \quad (3.28)$$

Here $\rho_A(x)$, $\rho_B(x)$ and $c_A(x)$ and $c_B(x)$ are the density and velocity in the unperturbed and perturbed media, respectively. There is a unique difference wavefield $\hat{G}^s(x, \omega; x^B)$, conventionally also known as scattered (Bleistein et al., 2001) that allows to relate the two Green's functions of the states A and B as

$$\hat{G}^B(x, \omega; x^B) = \hat{G}^A(x, \omega; x^B) + \hat{G}^s(x, \omega; x^B). \quad (3.29)$$

It is our objective to determine this scattered wavefield due to the presence of inhomogeneities below S_2 as if recorded with sources and receivers at S_2 . Upon the use of the general form of the *perturbation operator* or *scattering potential*, defined as (Rodberg and Thaler, 1967)

$$\mathcal{V} = \mathcal{L}^B - \mathcal{L}^A, \quad (3.30)$$

and using the wavefield decomposition (3.29), equation (3.26) can be written as

$$(\mathcal{L}^A + \mathcal{V}) \left[\hat{G}^A(x, \omega; x^B) + \hat{G}^s(x, \omega; x^B) \right] = -\delta(x - x^B). \quad (3.31)$$

Together with equation (3.25), this leads to

$$\mathcal{L}^A \hat{G}^s(x, \omega; x^B) = -\mathcal{V} \left[\hat{G}^A(x, \omega; x^B) + \hat{G}^s(x, \omega; x^B) \right]. \quad (3.32)$$

At this point, we consider a Green's function $\hat{G}^{A*}(x, \omega; x')$, which satisfies a Helmholtz equation similar to expression (3.25), however with a point source at x' positioned slightly above the datum in depth. Multiplying in both sides of the complex conjugate of this Helmholtz equation by $\hat{G}^s(x, \omega; x^B)$ we find

$$\begin{aligned} \rho_A(x) \hat{G}^s(x, \omega; x^B) \nabla \cdot \left[\frac{1}{\rho_A(x)} \nabla \hat{G}^{A*}(x, \omega; x') \right] + \frac{\omega^2}{c_A^2(x)} \hat{G}^s(x, \omega; x^B) \hat{G}^{A*}(x, \omega; x') = \\ - \hat{G}^s(x, \omega; x^B) \delta(x - x'). \end{aligned} \quad (3.33)$$

Correspondingly, multiplying in both sides of equation (3.32) by $\hat{G}^{A*}(x, \omega; x')$, we can explicitly write

$$\begin{aligned} \rho_A(x) \hat{G}^{A*}(x, \omega; x') \nabla \cdot \left[\frac{1}{\rho_A(x)} \nabla \hat{G}^s(x, \omega; x^B) \right] + \frac{\omega^2}{c_A^2(x)} \hat{G}^{A*}(x, \omega; x') \hat{G}^s(x, \omega; x^B) = \\ - \hat{G}^{A*}(x, \omega; x') \mathcal{V} \left[\hat{G}^A(x, \omega; x^B) + \hat{G}^s(x, \omega; x^B) \right]. \end{aligned} \quad (3.34)$$

Subtracting equation (3.33) from (3.34) and rewriting the terms, we have

$$\begin{aligned} \nabla \cdot \left\{ \frac{1}{\rho_A(x)} \left[\hat{G}^{A*}(x, \omega; x') \nabla \hat{G}^s(x, \omega; x^B) - \hat{G}^s(x, \omega; x^B) \nabla \hat{G}^{A*}(x, \omega; x') \right] \right\} = \\ \frac{1}{\rho_A(x)} \left[\hat{G}^{A*}(x, \omega; x') \mathcal{V} \hat{G}^B(x, \omega; x^B) - \hat{G}^s(x, \omega; x^B) \delta(x - x') \right]. \end{aligned} \quad (3.35)$$

After application of Green's theorem, solving the volume integral of the term with the delta function and reorganizing the expression (3.35), we arrive at

$$\begin{aligned} \hat{G}^s(x', \omega; x^B) = \rho_A(x') \left\{ \iiint_V \frac{1}{\rho_A(x)} \hat{G}^{A*}(x, \omega; x') \mathcal{V} \hat{G}^B(x, \omega; x^B) dV - \right. \\ \left. \oint_S \frac{1}{\rho_A(x)} \left[\hat{G}^{A*}(x, \omega; x') \nabla \hat{G}^s(x, \omega; x^B) - \hat{G}^s(x, \omega; x^B) \nabla \hat{G}^{A*}(x, \omega; x') \right] \cdot \hat{n} dS \right\}. \end{aligned} \quad (3.36)$$

Equation (3.36) represents the scattered Green's function with source in x^B and receiver in x' , whose results are given by the sum of a volume and a closed surface integrals, multiplied by the unperturbed density in x^A . It is given by the sum of a volume and a closed-surface integral, multiplied by the unperturbed density in x' . Considering that in both states A and B the overburden between the surfaces S_1 and S_2 is the same, the scattering potential satisfies $\mathcal{V} = 0$ inside V . Thus,

$$\iiint_V \frac{1}{\rho_A(x)} \hat{G}^{A*}(x, \omega; x') \mathcal{V} \hat{G}^B(x, \omega; x^B) dV = 0. \quad (3.37)$$

Equation (3.37) allows us to simplify the correlation-based interferometric expression (3.36) as an integral evaluated over the closed surface S . Analogous to section (2.4), the closed surface integral in the reciprocity theorem of correlation type is divided in three surfaces S_1 , S_2 and S_3 , respectively, as we can see in the Figure (3.4). Again, according to Schuster (2009) the Sommerfeld radiation conditions guarantee that the integral over S_3 vanishes at infinity.

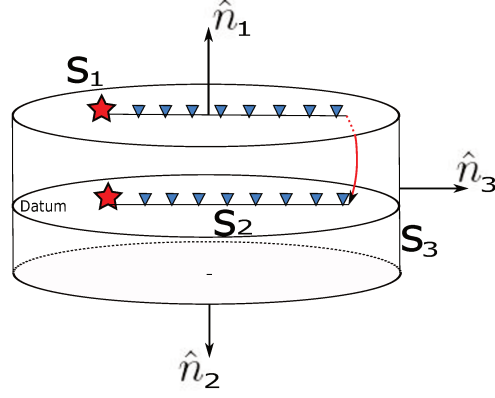


Figure 3.4: Sketch with a cylindrical closed surface S , decomposed into three surfaces S_1 , S_2 and S_3 . At surface S_1 there is a seismic array, which with interferometric redatuming will be redatumed to the datum in the surface S_2 .

With the remaining integrals over surfaces S_1 and S_2 in equation (3.36), we have

$$\begin{aligned} \hat{G}^s(x', \omega; x^B) \approx & \rho_A(x') \left\{ \iint_{S_1} \frac{1}{\rho_A(x)} \left[\hat{G}^{A*}(x, \omega; x') \nabla \hat{G}^s(x, \omega; x^B) - \hat{G}^s(x, \omega; x^B) \nabla \hat{G}^{A*}(x, \omega; x') \right] \cdot \hat{n}_1 dx_1 dx_2 + \right. \\ & \left. \iint_{S_2} \frac{1}{\rho_A(x)} \left[\hat{G}^{A*}(x, \omega; x') \nabla \hat{G}^s(x, \omega; x^B) - \hat{G}^s(x, \omega; x^B) \nabla \hat{G}^{A*}(x, \omega; x') \right] \cdot \hat{n}_2 dx_1 dx_2 \right\}. \end{aligned} \quad (3.38)$$

Integrals over surfaces S_1 and S_2 will be simplified to obtain an expression that allow us to relocate the seismic array at the surface to an aleatory datum at depth (see Figure 3.4). To simplify it, in the equation (3.38) we write the Green' function with source in x^B and receiver at x^A as

$$\hat{G}^s(x', \omega; x^B) = \rho_A(x') \left[\hat{I}_1 + \hat{I}_2 \right], \quad (3.39)$$

where the factors \hat{I} are defined respectively as

$$\hat{I}_1 = \iint_{S_1} \frac{1}{\rho_A(x)} \left[\hat{G}^{A*}(x, \omega; x') \nabla \hat{G}^s(x, \omega; x^B) - \hat{G}^s(x, \omega; x^B) \nabla \hat{G}^{A*}(x, \omega; x') \right] \cdot \hat{n}_1 dx_1 dx_2, \quad (3.40)$$

and

$$\hat{I}_2 = \iint_{S_2} \frac{1}{\rho_A(x)} \left[\hat{G}^{A*}(x, \omega; x') \nabla \hat{G}^s(x, \omega; x^B) - \hat{G}^s(x, \omega; x^B) \nabla \hat{G}^{A*}(x, \omega; x') \right] \cdot \hat{n}_2 dx_1 dx_2. \quad (3.41)$$

Correlation-based redatuming equation

According with the analysis corresponding to correlation-based in appendix A, only the integral over the surface S_1 contributes in equation (3.38). This implies that to all contributions $\hat{G}_-^s(x, \omega; x^B)$ originate below this surface. Thus, the Green's function $\hat{G}_-^s(x, \omega; x^B)$ measured at the surface S_1 in equation (3.38) can be interpreted as $\hat{G}_-^B(x, \omega; x^B)$ (Vasconcelos et al., 2009). Hence, equation (3.38) can be written as

$$\hat{G}^s(x', \omega; x^B) \approx 2\rho_A(x') \iint_{S_1} \frac{1}{\rho_A(x)} \left[\partial_3 \hat{G}_-^{A*}(x, \omega; x') \right] \hat{G}_-^B(x, \omega; x^B) dx_1 dx_2, \quad (3.42)$$

where x' is an auxiliary variable that represent a coordinate at the datum (see Figure 3.5). Expression (3.42) is an equation that allows us to relocate the receivers to an arbitrary datum using correlation-based interferometric redatuming (see Figure 3.5a). It is possible retrieve the scattered wavefield $\hat{G}^s(x', \omega; x^B)$ just evaluating the crosscorrelation represented by the product $\partial_3 \hat{G}_-^{A*}(x, \omega; x') \hat{G}_-^s(x, \omega; x^B)$ and integrating it over the surface S_1 .

The input data to retrieve the redatumed Green's functions are the complete seismic data $\hat{G}_-^s(x, \omega; x^B)$ over the surface S_1 and the vertical derivative of the complex conjugate of the Green's function $\partial_3 \hat{G}_-^{A*}(x', \omega; x^B)$ which is the transmitted wavefield from the surface S_1 until the datum at S_2 . Figure (3.5) is a sketch that show us intuitively the process of redatuming in two steps: (1) receiver redatuming (equation 3.42) and (2) source redatuming that is possible to do with the following expression

$$\hat{G}^s(x', \omega; x'') \approx 2\rho_A(x') \iint_{S_1} \frac{1}{\rho_A(x)} \left[\partial_3 \hat{G}_-^{A*}(x, \omega; x') \right] \hat{G}_-^s(x', \omega; x^B) dx_1 dx_2, \quad (3.43)$$

where x'' is an auxiliary variable that represents a coordinate at the datum. The input terms in equation (3.43) are the Green's function with redatumed receiver $\hat{G}_-^s(x', \omega; x^B)$, retrieved in expression (3.42), and again the vertical derivative of the complex conjugate incident Green's function $\partial_3 \hat{G}_-^{A*}(x', \omega; x^A)$. In this way it is possible to retrieve a seismic array at the datum $\hat{G}_-^s(x', \omega; x'')$, where both x' and x'' are the virtual receiver and source positions at datum, respectively.

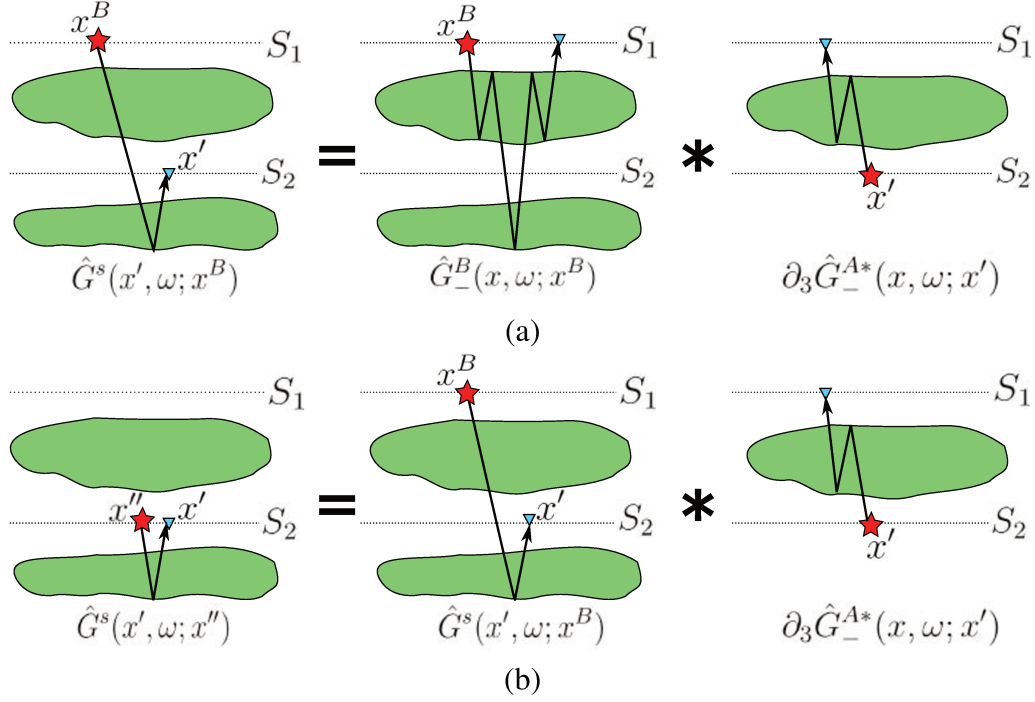


Figure 3.5: Sketch that shows the redatuming of a seismic survey to a new datum in two steps: (a) virtual receivers and (b) virtual sources.

3.4 Convolution-based interferometric redatuming

In this section, we deduce an expression using seismic interferometry by convolution, that is an alternative to the classical correlation-based scheme, explained in the previous section. According to Wapenaar et al. (2010b), there are many situations where it is more convenient. One of the main advantages of the convolution-based procedure is its inherent compensation for the properties of the source wavelet. Another important advantage is that the underlying theory does not require the assumption of a lossless medium. The analysis is very much analogous to the one for the correlation-based equations. As before, we consider two states A and B for the analysis, representing the perturbed and unperturbed media, that are defined by the expressions (3.15) and (3.16), respectively. The Helmholtz equation describing the wavefield for a point source just below the earth's surface at x^A and receiver at x , both of these in state A , just as we show in Figure (3.3), is

$$\mathcal{L}^A \hat{G}^A(x, \omega; x^A) = -\delta(x - x^A), \quad (3.44)$$

where this equation makes use of the Helmholtz operator in expression (3.27). We multiply both sides of equation (3.44) by $\hat{G}^s(x', \omega; x^B)$ to find

$$\begin{aligned} \rho_A(x) \hat{G}^s(x, \omega; x^B) \nabla \cdot \left[\frac{1}{\rho_A(x)} \nabla \hat{G}^A(x, \omega; x^A) \right] + \frac{\omega^2}{c_A^2(x)} \hat{G}^s(x, \omega; x^B) \hat{G}^A(x, \omega; x^A) = \\ - \hat{G}^s(x, \omega; x^B) \delta(x - x^A), \end{aligned} \quad (3.45)$$

Correspondingly, we multiply both sides of equation (3.32) by $\hat{G}^A(x', \omega; x^A)$ to find

$$\begin{aligned} \rho_A(x) \hat{G}^A(x, \omega; x^A) \nabla \cdot \left[\frac{1}{\rho_A(x)} \nabla \hat{G}^s(x, \omega; x^B) \right] + \frac{\omega^2}{c_A^2(x)} \hat{G}^A(x, \omega; x^A) \hat{G}^s(x, \omega; x^B) = \\ - \hat{G}^A(x, \omega; x^A) \mathcal{V} \left[\hat{G}^A(x, \omega; x^B) + \hat{G}^s(x, \omega; x^B) \right]. \end{aligned} \quad (3.46)$$

Subtracting equation (3.46) from (3.45) and rewriting it in a convenient form, we have

$$\begin{aligned} \nabla \cdot \left\{ \frac{1}{\rho_A(x)} \left[\hat{G}^A(x, \omega; x^A) \nabla \hat{G}^s(x, \omega; x^B) - \hat{G}^s(x, \omega; x^B) \nabla \hat{G}^A(x, \omega; x^A) \right] \right\} = \\ \frac{1}{\rho_A(x)} \left[\hat{G}^A(x, \omega; x^A) \mathcal{V} \hat{G}^B(x, \omega; x^B) - \hat{G}^s(x, \omega; x^B) \delta(x - x^A) \right]. \end{aligned} \quad (3.47)$$

After application of Green's theorem, solution of the volume integral over the term with the delta function and reorganization, we have

$$\begin{aligned} \hat{G}^s(x^A, \omega; x^B) = \rho_A(x^A) \left\{ \iiint_V \frac{1}{\rho_A(x)} \hat{G}^A(x, \omega; x^A) \mathcal{V} \hat{G}^B(x, \omega; x^B) dV - \right. \\ \left. \oint_S \frac{1}{\rho_A(x)} \left[\hat{G}^A(x, \omega; x^A) \nabla \hat{G}^s(x, \omega; x^B) - \hat{G}^s(x, \omega; x^B) \nabla \hat{G}^A(x, \omega; x^A) \right] \cdot \hat{n} dS \right\}. \end{aligned} \quad (3.48)$$

Equation (3.48) represents the scattering Green' function with source in x^B and receiver in x^A , given by the sum of a volume and a closed surface integrals, multiplied by the density at the receivers in the state A . Considering again that in both states A and B the overburden in between surfaces S_1 and S_2 is the same (Figure 3.3), the scattering potential satisfies $\mathcal{V} = 0$ inside V . Thus, the volume integral satisfies

$$\iiint_V \frac{1}{\rho_A(x)} \hat{G}^A(x, \omega; x^A) \mathcal{V} \hat{G}^B(x, \omega; x^B) dV = 0. \quad (3.49)$$

Equation (3.49) allows us to simplify the convolution-based interferometric expression (3.48) as an integral over the closed surface S . Analogous to section (3.3), the closed surface integral in the reciprocity theorem of correlation type is divided in three surfaces S_1 , S_2 and S_3 , previously defined (Figure 3.4). According to Schuster (2009) the integral over the surface S_3 vanishes by the Sommerfeld radiation conditions. Thus, we can rewrite equation (3.48) as

$$\begin{aligned} \hat{G}^s(x^A, \omega; x^B) \approx & \rho_A(x^A) \left\{ \iint_{S_1} \frac{1}{\rho_A(x)} \left[\hat{G}^A(x, \omega; x^A) \nabla \hat{G}^s(x, \omega; x^B) - \hat{G}^s(x, \omega; x^B) \nabla \hat{G}^A(x, \omega; x^A) \right] \cdot \hat{n}_1 dx_1 dx_2 + \right. \\ & \left. \iint_{S_2} \frac{1}{\rho_A(x)} \left[\hat{G}^A(x, \omega; x^A) \nabla \hat{G}^s(x, \omega; x^B) - \hat{G}^s(x, \omega; x^B) \nabla \hat{G}^A(x, \omega; x^A) \right] \cdot \hat{n}_2 dx_1 dx_2 \right\}. \end{aligned} \quad (3.50)$$

To simplify equation (3.50), we rewrite it as

$$\hat{G}^s(x^A, \omega; x^B) = \rho_A(x^A) \left[\hat{J}_1 + \hat{J}_2 \right]. \quad (3.51)$$

where

$$\hat{J}_1 = \iint_{S_1} \frac{1}{\rho_A(x)} \left[\hat{G}^A(x, \omega; x^A) \nabla \hat{G}^s(x, \omega; x^B) - \hat{G}^s(x, \omega; x^B) \nabla \hat{G}^A(x, \omega; x^A) \right] \cdot \hat{n}_1 dx_1 dx_2, \quad (3.52)$$

and

$$\hat{J}_2 = \iint_{S_2} \frac{1}{\rho_A(x)} \left[\hat{G}^A(x, \omega; x^A) \nabla \hat{G}^s(x, \omega; x^B) - \hat{G}^s(x, \omega; x^B) \nabla \hat{G}^A(x, \omega; x^A) \right] \cdot \hat{n}_2 dx_1 dx_2. \quad (3.53)$$

Convolution-based redatuming equation

According to the analysis corresponding to the convolution-based in appendix A, equation (3.50) only have contributions over the surface S_2 . The term $\hat{G}^s(x^A, \omega; x^B)$ in equation (3.50) can be interpreted as $\hat{G}^B(x^A, \omega; x^B)$, because positions x^A and x^B are over the earth's surface, as we showed in the Figure (3.3). Hence, equation (3.50) can be written as

$$\hat{G}^B(x^A, \omega; x^B) \approx -2\rho_A(x^A) \iint_{S_2} \frac{1}{\rho_A(x)} \hat{G}_-^s(x', \omega; x^B) \partial_3 \hat{G}_+^A(x', \omega, x^A) dx'_1 dx'_2. \quad (3.54)$$

The first step to make redatuming can be done using the expression (3.54), that allows us to relocate receivers by interferometric convolution-based methods, with the seismic array configuration of Fig-

ure (3.6a). With this equation it is possible retrieve the scattered Green's function $\hat{G}_{-}^s(x', \omega; x^B)$ by inversion, assuming that we know the vertical derivative of the transmitted wave field $\partial_3 \hat{G}_{+}^A(x', \omega; x^A)$ and the full seismic data at the earth's surface $\hat{G}^B(x^A, \omega; x^B)$. The second step allows us to retrieve the Green's function with sources and receiver at the datum. If we used the result of the expression (3.54) as an input, together with the vertical derivative of the transmitted wavefield, it is possible to complete the redatuming process. The equation that describe mathematically the second step is

$$\hat{G}_{-}^s(x', \omega; x^B) \approx -2\rho_A(x') \iint_{S_2} \frac{1}{\rho_A(x)} \hat{G}^s(x', \omega; x'') \partial_3 \hat{G}_{+}^A(x', \omega; x^A) dx'_1 dx'_2. \quad (3.55)$$

Equation (3.55) is the expression that describes convolution-based interferometric redatuming. If the Green's function with source at the earth's surface and receivers at datum $\hat{G}_{-}^s(x', \omega; x^B)$ is know, and we can model the vertical derivative of the incident Green's function $\partial_3 \hat{G}_{+}^A(x', \omega; x^A)$, it is possible to retrieve by inversion the upward component of the scattering Green's function $\hat{G}^s(x', \omega; x'')$ with source and receiver at datum. Here x'' is a virtual source at the datum, respectively.

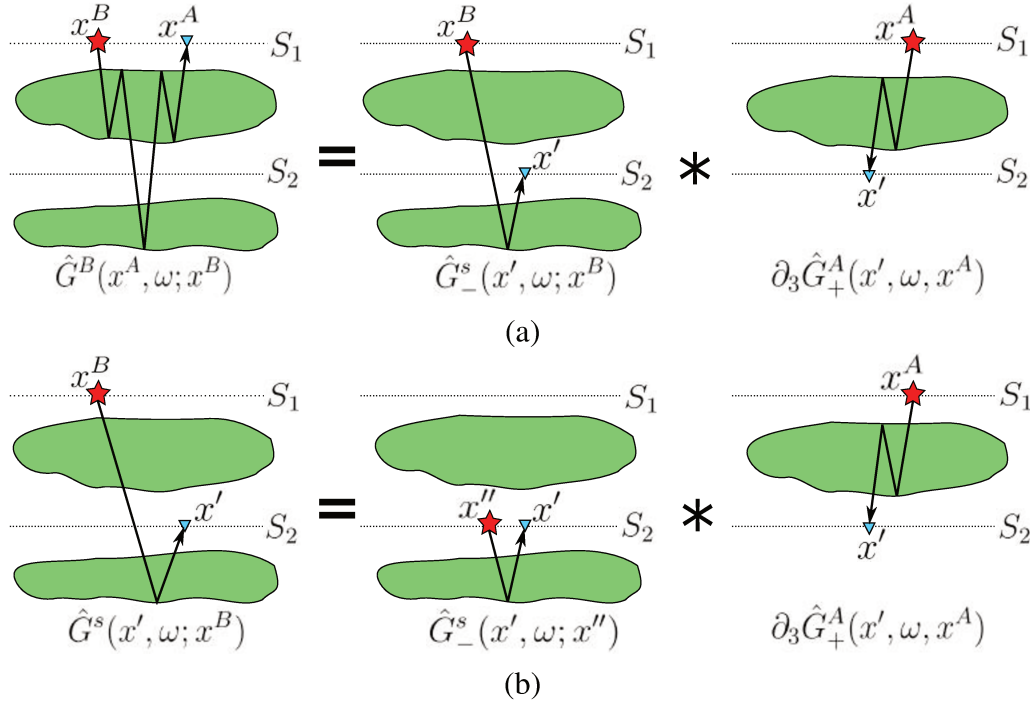


Figure 3.6: Sketch that shows the redatuming equations of a seismic array on the earth's and at datum the (a) virtual receivers and (b) virtual sources.

4. Interferometric redatuming by focusing

Inverse wavefield extrapolation is a term used to describe the process of recovering the wavefield somewhere in depth and from there to recorded it on the earth's surface, generally by retropropagation back into the earth (van der Neut et al., 2015b). This concept is used in many imaging schemes, e.g., RTM (Kosloff and Baysal, 1983), interferometric redatuming (Schuster, 2009), Marchenko imaging (Wapenaar et al., 2014) and others. Particularly, many works regarding the topic of Marchenko imaging, study and employ inverse wavefield extrapolation to recover so-called focusing functions, where the first iteration is based on the conventional wavefield extrapolation methods (van der Neut et al., 2015a). Interferometric redatuming methods could be classified as conventional wavefield extrapolation. But this classification can carry some problems, because this means that between surfaces S_1 and S_2 there is no presence of scatters in some input data at theoretical considerations, just as we shown in Figures (3.5) and (3.6) to redatuming by correlation and convolution based, respectively. This conventional techniques has a great limitation, because many of the artefacts are coming from inhomogeneities in the overburden (Vasconcelos et al., 2009).

In this chapter, we propose a simpler alternative to the estimation of focusing functions, which allows us to remove overburden multiples and spurious events from the Green's functions retrieved at a new datum in depth. The strength of the conventional procedure lies in the fact that it needs only an estimate of the transmitted wavefield from the earth's surface to the datum to recover the full wavefield there. However, this makes it a rather sophisticated method to retrieve the Green's functions at the datum. By using an additional wavefield estimated in the overburden, our procedure allows us to determine the up- and downgoing constituents of the Green's functions at depth by means of a least-squares inversion. Note, however, that this will generally require a better model of the overburden inhomogeneities. Retrieved the up- and downward constituents makes possible to make redatuming if we account a convolution operation in frequency domain between the downward constituent and the redatuming wavefield with seismic array at datum, this all equal to the upward wavefield constituent retrieved by inversion in above step.

The equations of our method are the one-way reciprocity theorems of convolution and correlation type. These two formulas can be reformulated in such a way that they allow us to express the data at the surface as integrals over wavefields, which propagate only in the overburden and the desired up- and downgoing wavefield constituents at the datum (van der Neut et al., 2015a). The two involved wavefields in the overburden are the transmitted wavefield from the surface to the datum, and the so-called truncated wavefield, i.e., the one reflected from the overburden scatterers only and recorded at the surface receivers. Both wavefields can be simulated in a reference model which is homogeneous below the datum.

4.1 Wavefield decomposition

To derive the relations deduced in this section, using our notation, we start with two states, A and B (indicated by superscripts A and B) in the frequency-space domain (Figure 4.1). To do wavefield decomposition in our proposed method, we defined that surfaces S_1 and S_2 have been extended to cover the complete horizontal planes, i.e., they are now defined as $\partial D_1 = \{(x_1, x_2, x_3) \in \mathbb{R}^3 | x_3 = x_3^1\}$ and $\partial D_2 = \{(x_1, x_2, x_3) \in \mathbb{R}^3 | x_3 = x_3^2\}$. In the state A, we considered a point source positioned immediately above surface ∂D_1 . In this situation, the vertical derivative of the downgoing wavefield at the surface can be expressed as $\partial_3 \hat{p}_+^A = -\frac{1}{2} \delta(x_1 - x_1^A) \delta(x_2 - x_2^A)$ (See demonstration in Appendix B). The validity region of this expression in state A is limited by surfaces ∂D_1 and ∂D_2 . Between these surfaces, the medium may be arbitrarily inhomogeneous. Above ∂D_1 and below ∂D_2 we considered homogeneous halfspaces without a free surface (Figure 4.1).

In state B, we considered the same inhomogeneous medium between surfaces ∂D_1 and ∂D_2 as in state A. Above ∂D_1 , we still considered a homogeneous medium halfspace without a free surface, but below ∂D_2 we considered a scattering body. The source in the state B is a point source immediately above surface ∂D_1 , such that the vertical derivative of the downgoing wavefield can be represented as $\partial_3 \hat{p}_+^B = -\frac{1}{2} \delta(x - x^B) \delta(x_2 - x_2^B)$ (see Appendix B). In both states A and B, we considered the wavefield decomposition into up- and downgoing constituents in analogy to equation (2.23). An analysis of the physical situation in both states allows an interpretation of all propagation events at each surface in Figure 4.1, resulting in Table (4.1).

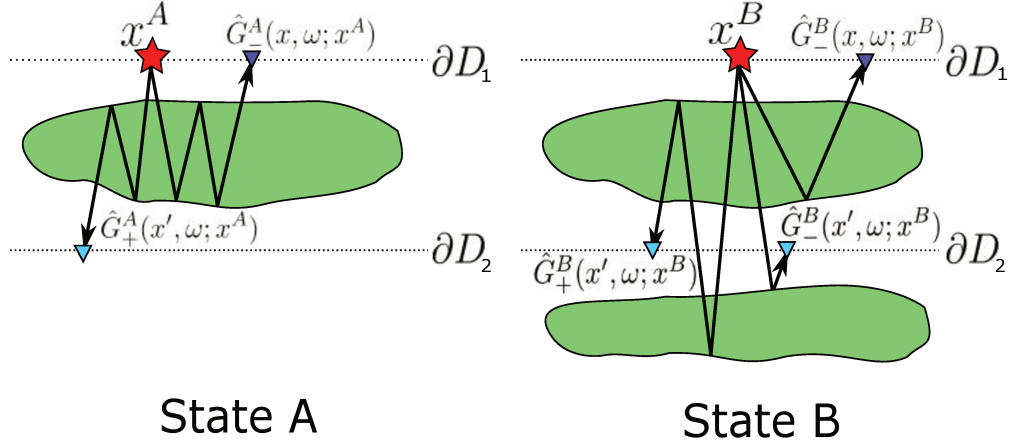


Figure 4.1: Two wavefield states in an inhomogeneous overburden. State *A* is used to describe the transmitted wavefield from the surface and its response recorded at the datum and at the surface. State *B* describes the total wavefield propagation taking into account all events propagating in the medium.

Surface	Direction	State A	State B
∂D_1	+	point source in x^A	point source in x^B
∂D_1	-	$\hat{G}_-^A(x, \omega; x^A)$	$\hat{G}_-^B(x, \omega; x^B)$
∂D_2	+	$\hat{G}_+^A(x', \omega; x^A)$	$\hat{G}_+^B(x', \omega; x^B)$
∂D_2	-	0	$\hat{G}_-^B(x', \omega; x^B)$

Table 4.1: Analysis of the up- and downgoing wavefields at surfaces ∂D_1 and ∂D_2 in states *A* and *B*, respectively.

Upgoing Green's functions

In this section we will deduce an equation that allows us to retrieve the upgoing constituent of the total Green's function at datum, considering the model of Figure (4.1). Taking into account the relations of the states *A* and *B* and its interpretation wavefield decomposition in the Table (4.1), we substituted these terms in the one-way reciprocity theorem of convolution type that is shown in equation (2.29), to obtain

$$\begin{aligned}
 & \iint_{\partial D_1} \frac{1}{\rho(x)} \left[\hat{G}_-^B(x, \omega; x^B) \frac{1}{2} \delta(x_1 - x_1^A) \delta(x_2 - x_2^A) - \hat{G}_-^A(x, \omega; x^A) \frac{1}{2} \delta(x_1 - x_1^B) \delta(x_2 - x_2^B) \right] d^2x \approx \\
 & - \iint_{\partial D_2} \frac{1}{\rho(x)} \hat{G}_-^B(x', \omega; x^B) \partial_3 \hat{G}_+^A(x', \omega; x^A) d^2x'.
 \end{aligned} \tag{4.1}$$

Solving right-hand side of the equation (4.1) we have

$$\frac{1}{2\rho(x^A)}\hat{G}_-^B(x^A, \omega; x^B) - \frac{1}{2\rho(x^B)}\hat{G}_-^A(x^B, \omega; x^A) \approx - \iint_{\partial D_2} \frac{1}{\rho(x)}\hat{G}_-^B(x', \omega; x^B)\partial_3\hat{G}_+^A(x', \omega; x^A)d^2x'. \quad (4.2)$$

Equation (4.2) is the first of our main results. This expression allows us to invert for the upgoing Green's function $\hat{G}_-^B(x', \omega; x^B)$ at the datum ∂D_2 if we know the corresponding Green's functions $\hat{G}_-^B(x^A, \omega; x^B)$ at the surface ∂D_1 , as long as we have sufficient information on the inhomogeneous medium between the two surfaces to model the terms $\frac{1}{2\rho(x^B)}\hat{G}_-^A(x^B, \omega; x^A)$ and $\frac{1}{2\rho(x)}\partial_3\hat{G}_+^A(x', \omega; x^A)$. If we consider the particular case in equation (4.2) where the density constant we can simplify it equation as

$$\frac{1}{2}\hat{G}_-^B(x^A, \omega; x^B) - \frac{1}{2}\hat{G}_-^A(x^B, \omega; x^A) \approx - \iint_{\partial D_2} \hat{G}_-^B(x', \omega; x^B)\partial_3\hat{G}_+^A(x', \omega; x^A)d^2x'. \quad (4.3)$$

Equation (4.3) is a expression that allows us to retrieve $\hat{G}_-^B(x', \omega; x^B)$, knowing the transmitted wavefield $\partial_3\hat{G}_+^A(x', \omega; x^A)$ and the truncated wavefield at overburden $\hat{G}_-^A(x^B, \omega; x^A)$.

Downgoing Green's functions

In a procedure similar to the analysis before, in this section we will deduce the expression to obtain the downgoing constituent of the total Green's function at the datum. In the first place, we replace the expressions of Table (4.1) into the one-way reciprocity theorem of correlation type (equation 2.32), to obtain

$$\begin{aligned} \iint_{\partial D_1} \frac{1}{\rho(x)} \left[\hat{G}_-^B(x, \omega; x^B)\partial_3\hat{G}_-^{A*}(x, \omega; x^A) + \frac{1}{2}\hat{G}_+^{A*}(x, \omega; x^A)\delta(x_1 - x_1^B)\delta(x_2 - x_2^B) \right] d^2x \approx \\ \iint_{\partial D_2} \frac{1}{\rho(x)}\hat{G}_+^B(x', \omega; x^B)\partial_3\hat{G}_+^{A*}(x', \omega; x^A)d^2x'. \end{aligned} \quad (4.4)$$

Solving the left-hand side and rewriting the right-hand side of equation (4.4) , we have

$$\begin{aligned} \iint_{\partial D_1} \frac{1}{\rho(x)}\hat{G}_-^B(x, \omega; x^B)\partial_3\hat{G}_-^{A*}(x, \omega; x^A)d^2x + \frac{1}{2\rho(x^B)}\hat{G}_+^{A*}(x^B, \omega; x^A) \approx \\ - \iint_{\partial D_2} \frac{1}{\rho(x)}\hat{G}_+^{A*}(x', \omega; x^A)\partial_3\hat{G}_+^B(x', \omega; x^B)d^2x'. \end{aligned} \quad (4.5)$$

Due that states A and B have the same overburden medium, we can rewrite all terms of equation (4.5) as

$$\begin{aligned} \frac{1}{2\rho(x^B)}\hat{G}_+^{A*}(x^B, \omega; x^A) \approx & - \iint_{\partial D_1} \frac{1}{\rho(x)}\hat{G}_-^A(x, \omega; x^B)\partial_3\hat{G}_-^{A*}(x, \omega; x^A)d^2x - \\ & \iint_{\partial D_2} \frac{1}{\rho(x)}\hat{G}_+^{A*}(x', \omega; x^A)\partial_3\hat{G}_+^A(x', \omega; x^B)d^2x', \end{aligned} \quad (4.6)$$

replacing equation (4.6) in (4.5)

$$\begin{aligned} & - \iint_{\partial D_1} \frac{1}{\rho(x)}\hat{G}_-^A(x, \omega; x^B)\partial_3\hat{G}_-^{A*}(x, \omega; x^A)d^2x - \iint_{\partial D_2} \frac{1}{\rho(x)}\hat{G}_+^{A*}(x', \omega; x^A)\partial_3\hat{G}_+^A(x', \omega; x^B)d^2x' \\ & + \iint_{\partial D_1} \frac{1}{\rho(x)}\hat{G}_-^B(x, \omega; x^B)\partial_3\hat{G}_-^{A*}(x, \omega; x^A)d^2x \approx - \iint_{\partial D_2} \frac{1}{\rho(x)}\hat{G}_+^{A*}(x', \omega; x^A)\partial_3\hat{G}_+^B(x', \omega; x^B)d^2x'. \end{aligned} \quad (4.7)$$

Equation (4.7) allows us to calculate the vertical derivative of the downgoing Green's function defined as $\partial_3\hat{G}_+^B(x', \omega; x^B)$ at the datum. This is if we know the complex conjugate of the transmitted wavefield from the earth's surface until the datum $\frac{1}{\rho(x)}\hat{G}_+^{A*}(x', \omega; x^A)$. We also need to know the complex conjugate of the truncated wavefield $\frac{1}{\rho(x)}\hat{G}_-^{A*}(x^B, \omega; x^A)$ and its corresponding vertical derivative $\frac{1}{\rho(x)}\partial_3\hat{G}_-^{A*}(x, \omega; x^A)$. However, if we consider that the density is constant, we can simplify the expression (4.7) as follows

$$\begin{aligned} & - \iint_{\partial D_1} \hat{G}_-^A(x, \omega; x^B)\partial_3\hat{G}_-^{A*}(x, \omega; x^A)d^2x - \iint_{\partial D_2} \hat{G}_+^{A*}(x', \omega; x^A)\partial_3\hat{G}_+^A(x', \omega; x^B)d^2x' \\ & + \iint_{\partial D_1} \hat{G}_-^B(x, \omega; x^B)\partial_3\hat{G}_-^{A*}(x, \omega; x^A)d^2x \approx - \iint_{\partial D_2} \hat{G}_+^{A*}(x', \omega; x^A)\partial_3\hat{G}_+^B(x', \omega; x^B)d^2x'. \end{aligned} \quad (4.8)$$

Here if we know the same Green's functions listed to solve equation (4.8), as we mentioned above, but without density factors. We can retrieve the vertical derivative of the downgoing constituent $\partial_3\hat{G}_+^B(x', \omega; x^B)$ at the datum in equation (4.8).

4.2 Convolution-based interferometric redatuming

Having calculated the equations that allows us to retrieve the constituents up- and downgoing of the Green's functions at the datum, is possible to estimate an equation in order to retrieve a complete wavefield at datum. Considering that each trace in the output gather $\hat{G}_-^B(x', \omega; x^B)$ can be interpreted

as the stack of a convolution gather, which is obtained by crossconvolution of each trace in the reflection response $\hat{R}_n(x', \omega; x^d)$ at fixed source point x^d at datum with each trace of the vertical derivative of the downgoing constituent $\partial_3 \hat{G}_+^B(x', \omega; x^B)$ with fixed source position x^B at surface and receiver location in x' at the datum (Figure 4.2). According to Wapenaar et al. (2010b) in more situations it is most convenient to make interferometry by convolution-based than by correlation-based expressions. This is because in the convolution way, the processes to retrieve the interferometric responses are compensated by the properties of the source wavelet. Another advantage is that it is unnecessary to assume that the medium is lossless, as we mentioned previously in the section (3.4). Therefore, because of the benefits of the convolution-based methods we focused our work in this method with the numerical examples at Chapter 6. Expressions (4.2) and (4.8) ensure the presence of the complete wavefield up- and downward constituents, respectively, with information of the medium in- and outside at the surfaces ∂D_1 and ∂D_2 , without free-surface. This allows us to express as a complete form the convolution-based equation deduced in expression (3.55), then the redatuming equation by convolution-based can be expressed in the case of variable density as

$$\hat{G}_-^B(x'', \omega, x^B) = -2\rho(x') \iint_{\partial D_2} \frac{1}{\rho(x)} \hat{R}_n(x', \omega; x^d) \partial_3 \hat{G}_+^B(x', \omega; x^B) d^2 x'. \quad (4.9)$$

Equation (4.9) is the main result of this work, with this equation it is possible to retrieve the total wavefield at the datum $\hat{R}_n(x', \omega; x^d)$ using any inversion method (at the case of this work we used least-squares), if we know the up- and downward Green's function constituents $\frac{1}{\rho(x')} \hat{G}_-^B(x'', \omega, x^B)$ and $\frac{1}{\rho(x)} \partial_3 \hat{G}_+^B(x', \omega; x^B)$. This is an alternative to approach the redatuming problem, as we can see in the Figure (4.2). In the case that the density is considered smooth enough laterally, equation (4.9) can be expressed as

$$\hat{G}_-^B(x'', \omega, x^B) = -2 \iint_{\partial D_2} \hat{R}_n(x', \omega; x^d) \partial_3 \hat{G}_+^B(x', \omega; x^B) d^2 x'. \quad (4.10)$$

With the equation (4.10) it is possible to retrieve the total Green's functions at datum $\hat{R}_n(x', \omega; x^d)$ if we know the up- and downward Green's functions constituents, using any numerical inversion methods.

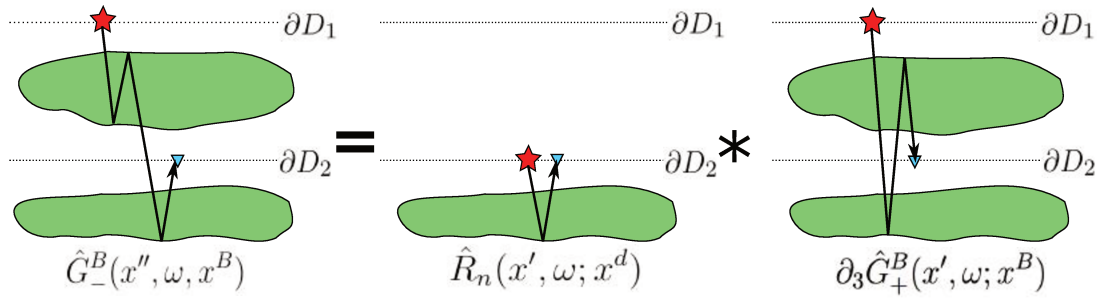


Figure 4.2: Sketch with the linear problem inversion. Where we have the one-way Green's functions responses at the focus datum calculated by inversion and the reflection at the datum to be calculated by inversion.

5. Inverse functions of the interferometric redatuming expressions

In this chapter, we will deduce the inverse functions of the previously raised linear problems that involve convolution and correlation based methods. The solutions to the inverse problems shown here will be addressed in the continuum. Expressions proposed in this chapter have the introduction of the point spread functions (PSF) that allows us to solve the integral expressions and calculate the desired Green's functions. The PSF have the inconvenient that carry non-physical information, then, to attenuate this kind of signals in the interferometric redatuming responses we introduce the inverse of the point spread function (PSF^{-1}). Other problem appear in the implementation of the inversion methods because the space limitation of the seismic array. This was discussed by Wapenaar and Fokkema (1997) (see Appendix C), where is commented about the limitations between inverse wavefield extrapolation operators, where in spite of the time-symmetry of acoustic wave equation, inverse wavefield extrapolation operators is not exact, even for the simple situation of a homogeneous medium and an infinite aperture. On the other hand for strongly inhomogeneous media the kinematic aspects of multi-valued events are handled correctly, but angle-dependent errors occur in their dynamical behavior. Computational implementation of inverse operators also has limitations in the point of surfaces coverage, because it involves discretization of the inverse problem, making laterally that the solved integral surfaces truncated. Numerically the inverse problem will be solved by least-squares inversion method.

5.1 Inversion of interferometric redatuming by convolution-based

In previous chapter, we mentioned that the interferometry by convolution methods is an inverse linear problem that could be solved by any inversion of the numerical method. In this section, we show a general methodology to calculate the inverse functions to retrieve the unknown Green's function from equations (3.54) and (3.55), in order to calculate the upward and redatuming Green's functions, respectively. To start, we will calculate the inverse function from equation (3.54), which result will

be the input for the expression (3.55) in order to complete the redatuming of the total seismic array at datum in depth.

Upward Green's function

We start defining a point spread function (*PSF*), that represents the blurring function of a delta (Hansen et al., 2006; van der Neut and Wapenaar, 2015). The *PSF* in this case will be used to help us to solve equation (4.3). To simplify the way of writing we denoted the *PSF* as a function P and we define it as

$$\iint_{S_1} \partial_3 \hat{G}_+^A(x', \omega; x^A) \partial_3 \hat{G}_+^{A*}(x^A, \omega; x'') d^2 x^A = P(x', \omega; x''). \quad (5.1)$$

Equations (5.1) represent the function $P(x', \omega; x'')$ that is composed by the autocorrelation between the vertical derivative of the transmitted wavefield in state A in Figure (4.1) with source in x^A and receiver in x' with the complex conjugate of itself with receiver in x^A and source in x'' . Here, we denoted x' and x'' as auxiliary variables that represents different positions of sources and receivers or vice versa over the surface ∂D_2 (datum). Multiplying both sides of (3.54) by $\partial_3 \hat{G}_+^{A*}(x^A, \omega; x'')$ and integrating it over the surface S_1 , yields

$$\begin{aligned} & \iint_{S_1} \hat{G}^B(x^A, \omega; x^B) \partial_3 \hat{G}_+^{A*}(x^A, \omega; x'') d^2 x^A \approx \\ & - 2\rho_A(x^A) \iint_{S_1} \left[\iint_{S_2} \frac{1}{\rho_A(x)} \hat{G}_-^s(x', \omega; x^B) \partial_3 \hat{G}_+^A(x', \omega; x^A) d^2 x' \right] \partial_3 \hat{G}_+^{A*}(x^A, \omega; x'') d^2 x^A. \end{aligned} \quad (5.2)$$

Reorganizing equation (5.2), we have

$$\begin{aligned} & \iint_{S_1} \hat{G}^B(x^A, \omega; x^B) \partial_3 \hat{G}_+^{A*}(x^A, \omega; x'') d^2 x^A \approx \\ & - 2\rho_A(x^A) \iint_{S_2} \left[\iint_{S_1} \partial_3 \hat{G}_+^A(x', \omega; x^A) \partial_3 \hat{G}_+^{A*}(x^A, \omega; x'') dx^A \right] \frac{1}{\rho_A(x)} \hat{G}_-^s(x', \omega; x^B) d^2 x'. \end{aligned} \quad (5.3)$$

Replacing equation (5.1) in (5.3), we obtain

$$\iint_{S_1} \hat{G}^B(x^A, \omega; x^B) \partial_3 \hat{G}_+^{A*}(x^A, \omega; x'') d^2 x^A \approx -2\rho_0(x^A) \iint_{S_2} \frac{1}{\rho_A(x)} P(x', \omega; x'') \hat{G}_-^s(x', \omega; x^B) d^2 x'. \quad (5.4)$$

In the homogeneous case $P(x', \omega; x'')$ could be a good approximation to a delta function, because only physical events in the PSF would be retrieved. In the inhomogeneous case, if we consider in state A all events in the overburden, then we obtain many artefacts from nonphysical events in the function P (Figure 5.1).

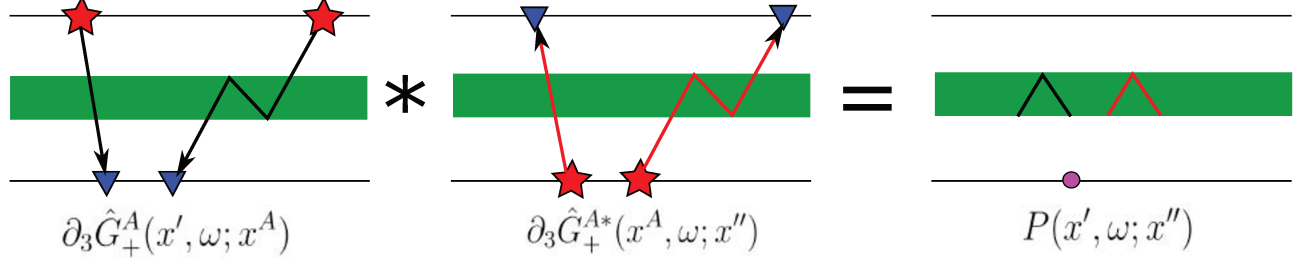


Figure 5.1: Ray paths of P , where we show only three possible crosscorrelations, without regard second, third and high multiple order. Black lines represent positive times and red lines represent negative times. $P(x', \omega; x'')$ have two nonphysical responses with positive and negative signal, and a point at datum corresponding to the unique physical event retrieved when s used the expression (5.1).

An alternative to attenuate the non-physical events that come from the function P in expression (5.4) is computing the inverse of the function P and apply it in equation (5.4) to retrieve the upward Green's function $\hat{G}_-^s(x', \omega; x'')$. Supposing that we know the inverse function of P , that we denoted as P^{-1} , we multiply in both sides of equation (5.1) by $P^{-1}(x', \omega; x'')$ and integrating over the surface S_2 , we obtain

$$\iint_{S_2} \left[\iint_{S_1} \partial_3 \hat{G}_+^A(x'', \omega; x^A) \partial_3 \hat{G}_+^{A*}(x^A, \omega; x') d^2 x^A \right] P^{-1}(x', \omega, x'') d^2 x' = \iint_{S_2} P(x', \omega; x'') P^{-1}(x', \omega, x'') d^2 x' \approx \delta(x'_1 - x''_1) \delta(x'_2 - x''_2). \quad (5.5)$$

Applying the inverse function $P^{-1}(x', \omega, x'')$ in equation (5.4), we have

$$\iint_{S_2} \left[\iint_{S_1} \hat{G}^B(x^A, \omega; x^B) \partial_3 \hat{G}_+^{A*}(x^A, \omega; x'') d^2 x^A \right] P^{-1}(x', \omega, x'') d^2 x' \approx -2\rho_A(x^A) \iint_{S_2} \left[\iint_{S_2} \frac{1}{\rho_A(x)} P(x'', \omega; x') \hat{G}_-^s(x', \omega; x^B) d^2 x' \right] P^{-1}(x', \omega, x'') d^2 x'. \quad (5.6)$$

Rewriting the right-hand side of equation (5.6), we have

$$\begin{aligned} & \iint_{S_2} \left[\iint_{S_1} \hat{G}^B(x^A, \omega; x^B) \partial_3 \hat{G}_+^{A*}(x^A, \omega; x'') d^2 x^A \right] P^{-1}(x', \omega, x'') d^2 x' \approx \\ & - 2\rho_A(x^A) \iint_{S_2} \left[\iint_{S_2} P(x', \omega; x'') P^{-1}(x'', \omega, x') d^2 x' \right] \frac{1}{\rho_A(x)} \hat{G}_-^s(x', \omega; x^B) d^2 x'. \end{aligned} \quad (5.7)$$

Replacing equation (5.5) in the right-hand side of expression (5.7), we have

$$\begin{aligned} & \iint_{S_2} \left[\iint_{S_1} \hat{G}^B(x^A, \omega; x^B) \partial_3 \hat{G}_+^{A*}(x^A, \omega; x'') d^2 x^A \right] P^{-1}(x', \omega, x'') d^2 x' \approx \\ & - 2\rho_A(x^A) \iint_{S_2} \delta(x'_1 - x''_1) \delta(x'_2 - x''_2) \frac{1}{\rho_A(x)} \hat{G}_-^s(x', \omega; x^B) d^2 x'. \end{aligned} \quad (5.8)$$

Solving right-hand side of equation (5.8) we obtain

$$\begin{aligned} & \hat{G}_-^s(x'', \omega; x^B) \approx \\ & - \frac{\rho_A(x'')}{2\rho_A(x^A)} \iint_{S_2} \left[\iint_{S_1} \hat{G}^B(x^A, \omega; x^B) \partial_3 \hat{G}_+^{A*}(x^A, \omega; x'') d^2 x^A \right] P^{-1}(x', \omega, x'') d^2 x'. \end{aligned} \quad (5.9)$$

Equation (5.9) is a expression that allows us to retrieve the up-ward Green's function. Actually, this equation is more exact than the first approximation to obtain $\hat{G}_-^s(x'', \omega; x^B)$ in equation (5.4). This is because expression (5.4) have a *PSF* that is a blurring of delta function and this is not appropriate. However, equation (5.9) considers the delta function definition in expression (5.5), which allows us to obtain a equation (5.9) to retrieve $\hat{G}_-^s(x'', \omega; x^B)$ more accurately.

Redatuming

In this section, we will deduce a function to complete the redatuming at datum in depth with equation (3.55) using as input data the upward Green's function $\hat{G}_-^s(x'', \omega; x^B)$ calculated previously in expression (5.9). To find the function to solve equation (3.55) we consider the same expression to P in equation (5.1) but at difference of it, here we consider the source position at x^B and receivers at x'' . Multiplying equation (3.55) in both sides by $\partial_3 \hat{G}_+^{A*}(x^B, \omega; x'')$ and integrating over the surface

S_1 , we have

$$\begin{aligned} \iint_{S_1} \hat{G}^s(x'', \omega; x^B) \partial_3 \hat{G}_+^{A*}(x^B, \omega; x'') d^2 x^B \approx \\ - 2\rho_A(x^A) \iint_{S_1} \left[\iint_{S_2} \frac{1}{\rho_A(x)} \hat{G}_-^s(x'', \omega; x^d) \partial_3 \hat{G}_+^A(x', \omega; x^B) dx' \right] \partial_3 \hat{G}_+^{A*}(x^B, \omega; x'') d^2 x^B. \end{aligned} \quad (5.10)$$

Reorganizing equation (5.10), we have

$$\begin{aligned} \iint_{S_1} \hat{G}^s(x'', \omega; x^B) \partial_3 \hat{G}_+^{A*}(x^B, \omega; x'') d^2 x^B \approx \\ - 2\rho_A(x^A) \iint_{S_2} \left[\iint_{S_1} \partial_3 \hat{G}_+^{A*}(x^B, \omega; x'') \partial_3 \hat{G}_+^A(x', \omega; x^B) dx^B \right] \frac{1}{\rho_A(x)} \hat{G}_-^s(x'', \omega; x^d) d^2 x'. \end{aligned} \quad (5.11)$$

The integral over the surface S_1 in the right-hand side of equation (5.11) is P as we show in equation (5.1), then expression (5.11) can be rewritten as

$$\iint_{S_1} \hat{G}^s(x'', \omega; x^B) \partial_3 \hat{G}_+^{A*}(x^B, \omega; x'') d^2 x^B \approx -2\rho_A(x^A) \iint_{S_2} \frac{1}{\rho_A(x)} P(x', \omega; x'') \hat{G}_-^s(x'', \omega; x^d) d^2 x'. \quad (5.12)$$

As previous analysis we also could have a redatuming expression with equation (5.12), considering that P come from an inhomogeneous medium, the blurring function will have nonphysical events as we showed in Figure (5.1). Analogous to equation (5.5), supposing that we know the inverse of the function P , we applied it in both sides of expression (5.12) and make integration over the surface S_2 , to obtain

$$\begin{aligned} \iint_{S_2} \left[\iint_{S_1} \hat{G}^s(x'', \omega; x^B) \partial_3 \hat{G}_+^{A*}(x^B, \omega; x'') d^2 x^B \right] P^{-1}(x'', \omega; x') d^2 x'' \approx \\ - 2\rho_A(x^A) \iint_{S_2} \left[\iint_{S_2} \frac{1}{\rho_A(x)} P(x', \omega; x'') \hat{G}_-^s(x'', \omega; x^d) d^2 x'' \right] P^{-1}(x'', \omega; x') d^2 x'', \end{aligned} \quad (5.13)$$

rewriting the right-hand side of equation (5.13) we have

$$\begin{aligned} & \iint_{S_2} \left[\iint_{S_1} \hat{G}^s(x'', \omega; x^B) \partial_3 \hat{G}_+^{A*}(x^B, \omega; x'') d^2 x^B \right] P^{-1}(x'', \omega; x') d^2 x'' \approx \\ & - 2\rho_A(x^A) \iint_{S_2} \left[\iint_{S_2} P(x', \omega; x'') P^{-1}(x'', \omega; x') d^2 x'' \right] \frac{1}{\rho_A(x)} \hat{G}_-^s(x'', \omega; x^d) d^2 x''. \end{aligned} \quad (5.14)$$

Similar to expression (5.5), the inner integral of the right-hand side of equation (5.14) can be interpreted as a delta at position the x' , this allows us rewrite equation (5.14) as

$$\begin{aligned} & \iint_{S_2} \left[\iint_{S_1} \hat{G}^s(x'', \omega; x^B) \partial_3 \hat{G}_+^{A*}(x^B, \omega; x'') d^2 x^B \right] P^{-1}(x'', \omega; x') d^2 x'' \approx \\ & - 2\rho_A(x^A) \iint_{S_2} \delta(x''_1 - x'_1) \delta(x''_2 - x'_2) \frac{1}{\rho_A(x)} \hat{G}_-^s(x'', \omega; x^d) d^2 x'', \end{aligned} \quad (5.15)$$

Finally, solving right-hand side of equation (5.15) we have

$$\begin{aligned} & \hat{G}_-^s(x', \omega; x^d) \approx \\ & - \frac{\rho_A(x')}{2\rho_A(x^A)} \iint_{S_2} \left[\iint_{S_1} \hat{G}_-^s(x'', \omega; x^B) \partial_3 \hat{G}_+^{A*}(x^B, \omega; x'') d^2 x^B \right] P^{-1}(x'', \omega; x') d^2 x''. \end{aligned} \quad (5.16)$$

Equation (5.16) is an expression that allows us to make redatuming at datum in depth. This equation is evaluated over the surfaces S_1 and S_2 , and only needs as input a model of the vertical derivative of the complex conjugate of the Green's function from the earth's surface until the datum at depth $\partial_3 \hat{G}_+^{A*}(x^B, \omega; x'')$, the upward Green's function retrieved in equation (5.9) $\hat{G}_-^s(x'', \omega; x^B)$ and $P^{-1}(x'', \omega; x')$. At homogeneous case is relatively easy to make a model like this, because the background velocity is constant and supposed an approach of the model does not require great effort. But things change when we consider an inhomogeneous overburden, because the background would be more complex, and many events would be part of the data, causing presence of artefacts, doing it more difficult when we try to retrieve the total Green's function at datum. It is the case that we will study in the next section, where we will retrieve the up- and downward Green's functions at depth. It will be the input that allows us to retrieve the total Green's function at datum, when is account homogeneity and inhomogeneities at the overburden.

5.2 Interferometric redatuming by focusing

Now we have another system of equations to solve. This approach consider inhomogeneities at the medium between surfaces ∂D_1 and ∂D_2 (Figure 4.1). In this case we will find expressions to retrieve by inversion the up- and downgoing Green's functions $\hat{G}_-^B(x', \omega; x^B)$ and $\partial_3 \hat{G}_+^B(x', \omega; x^B)$ which are expressed in equations (4.3) and (4.8), respectively. After calculating of the inverse operators to retrieve the up- and downward Green's functions at datum, we will use this as input data in expression (4.10) to calculate the inverse operator that allows us to make relocate of source and receivers at datum retrieving the response $\hat{R}_n(x'', \omega; x')$ by inversion. To express the inverse operators in the most simple form, we will assume that the medium has no high density contrasts.

Upgoing Green's function

To start, we make use of the operator P defined in equation (5.1). Again, the operator P will bring us information about the inhomogeneities in the overburden (Figure 5.1). Multiplying in both sides of equation (4.2) by the complex conjugate of the vertical derivative of the transmitted wavefield with source at the datum in x'' and receiver at the earth's surface in x^A $\partial_3 \hat{G}_+^{A*}(x^A, \omega; x'')$, we obtain

$$\begin{aligned} & \iint_{\partial D_1} \left[\frac{1}{2} \hat{G}_-^B(x^A, \omega; x^B) - \frac{1}{2} \hat{G}_-^A(x^B, \omega; x^A) \right] \partial_3 \hat{G}_+^{A*}(x^A, \omega; x'') d^2 x^A \approx \\ & - \iint_{\partial D_1} \left[\iint_{\partial D_2} \hat{G}_-^B(x', \omega; x^B) \partial_3 \hat{G}_+^A(x', \omega; x^A) dx' \right] \partial_3 \hat{G}_+^{A*}(x^A, \omega; x'') d^2 x^A. \end{aligned} \quad (5.17)$$

Rewriting the right-hand side of equation (5.17), yields

$$\begin{aligned} & \iint_{\partial D_1} \left[\frac{1}{2} \hat{G}_-^B(x^A, \omega; x^B) - \frac{1}{2} \hat{G}_-^A(x^B, \omega; x^A) \right] \partial_3 \hat{G}_+^{A*}(x^A, \omega; x'') d^2 x^A \approx \\ & - \iint_{\partial D_2} \left[\iint_{\partial D_1} \partial_3 \hat{G}_+^A(x', \omega; x^A) \partial_3 \hat{G}_+^{A*}(x^A, \omega; x'') dx^A \right] \hat{G}_-^B(x', \omega; x^B) d^2 x'. \end{aligned} \quad (5.18)$$

In the integral over the surface S_1 in the right-hand side of equation (5.18) can be interpreted as the operator P in equation (5.1), then, expression (5.18) can be written as

$$\begin{aligned} & \iint_{\partial D_1} \left[\frac{1}{2} \hat{G}_-^B(x^A, \omega; x^B) - \frac{1}{2} \hat{G}_-^A(x^B, \omega; x^A) \right] \partial_3 \hat{G}_+^{A*}(x^A, \omega; x'') d^2 x^A \approx \\ & - \iint_{\partial D_2} P(x', \omega; x'') \hat{G}_-^B(x', \omega; x^B) d^2 x'. \end{aligned} \quad (5.19)$$

Analogous to equation (5.5) we suppose that is know the operator inverse P^{-1} , then applying it in equation (5.19) we obtain the following expression

$$\begin{aligned} & \iint_{\partial D_2} \left\{ \iint_{\partial D_1} \left[\frac{1}{2} \hat{G}_-^B(x^A, \omega; x^B) - \frac{1}{2} \hat{G}_-^A(x^B, \omega; x^A) \right] \partial_3 \hat{G}_+^{A*}(x^A, \omega; x'') d^2 x^A \right\} P^{-1}(x', \omega; x'') d^2 x' \approx \\ & - \iint_{\partial D_2} \left[\iint_{\partial D_2} P(x', \omega; x'') P^{-1}(x', \omega; x'') d^2 x' \right] \hat{G}_-^B(x', \omega; x^B) d^2 x', \end{aligned} \quad (5.20)$$

as we mentioned previously, the inner integral over the surface ∂D_2 in the right-hand side of equation (5.20) is a two-dimensional delta at position x'' , then, equation (5.20) can be rewritten as

$$\begin{aligned} & \iint_{\partial D_2} \left\{ \iint_{\partial D_1} \left[\frac{1}{2} \hat{G}_-^B(x^A, \omega; x^B) - \frac{1}{2} \hat{G}_-^A(x^B, \omega; x^A) \right] \partial_3 \hat{G}_+^{A*}(x^A, \omega; x'') d^2 x^A \right\} P^{-1}(x', \omega; x'') d^2 x' \approx \\ & - \iint_{\partial D_2} \delta(x' - x'') \delta(x' - x'') \hat{G}_-^B(x', \omega; x^B) d^2 x', \end{aligned} \quad (5.21)$$

solving the right-hand side of equation (5.21) we obtain the expression

$$\begin{aligned} & \hat{G}_-^B(x'', \omega; x^B) \approx \\ & - \iint_{\partial D_2} \left\{ \iint_{\partial D_1} \left[\frac{1}{2} \hat{G}_-^B(x^A, \omega; x^B) - \frac{1}{2} \hat{G}_-^A(x^B, \omega; x^A) \right] \partial_3 \hat{G}_+^{A*}(x^A, \omega; x'') d^2 x^A \right\} P^{-1}(x', \omega; x'') d^2 x', \end{aligned} \quad (5.22)$$

Equation (5.22) is an expression that allows us to calculate the upward constituent of the Green's function with source over the earth's surface and receiver at datum. We can note that the integral is evaluated over surface ∂D_1 , where the input data is the original seismic array $\hat{G}_-^B(x^A, \omega; x^B)$ at the earth's surface, the model of the overburden truncated with source and receivers on surface $\hat{G}_-^A(x^B, \omega; x^A)$ and a model of the transmitted wave field from the surface at datum $\hat{G}_+^{A*}(x^A, \omega; x'')$.

Downgoing Green's function inversion

In this section we will deduce an inverse operator to retrieve the downward wavefield constituent of equation (4.8). To start our analysis we define the auxiliary term $\hat{B}(x^A, \omega; x^B)$ in equation (4.8) as

$$\begin{aligned} \hat{B}(x^A, \omega; x^B) = & - \iint_{\partial D_1} \hat{G}_-^A(x, \omega; x^B) \partial_3 \hat{G}_-^{A*}(x, \omega; x^A) d^2x - \iint_{\partial D_2} \hat{G}_+^{A*}(x', \omega; x^A) \partial_3 \hat{G}_+^A(x', \omega; x^B) d^2x' \\ & + \iint_{\partial D_1} \hat{G}_-^B(x, \omega; x^B) \partial_3 \hat{G}_-^{A*}(x, \omega; x^A) d^2x \end{aligned} \quad (5.23)$$

Replacing expression (5.23) in (4.8) we obtain

$$\hat{B}(x^A, \omega; x^B) \approx - \iint_{\partial D_2} \hat{G}_+^{A*}(x', \omega; x^A) \partial_3 \hat{G}_+^B(x', \omega; x^B) d^2x'. \quad (5.24)$$

In order to deduce an inverse operator to retrieve the vertical derivative of the downward wavefield $\partial_3 \hat{G}_-^B(x', \omega; x^B)$ in equation (5.24) we define a new *PSF* as

$$\iint_{\partial D_1} \hat{G}_+^{A*}(x', \omega; x^A) \hat{G}_+^A(x^A, \omega; x'') d^2x^A = S(x', \omega; x''). \quad (5.25)$$

Where S is the *PSF* operator that is composed by the autocorrelation between the downward wavefield constituent in state A with source in x^A and receiver x' with the complex conjugate of itself with receiver in x^A and source x'' . Multiplying in both sides of equation (5.25) by the term $\hat{G}_+^A(x^A, \omega; x'')$ we have

$$\begin{aligned} \iint_{\partial D_1} \hat{B}(x^A, \omega; x^B) \hat{G}_+^A(x^A, \omega; x'') d^2x^A \approx \\ - \iint_{\partial D_1} \left[\iint_{\partial D_2} \hat{G}_+^{A*}(x', \omega; x^A) \partial_3 \hat{G}_+^B(x', \omega; x^B) d^2x' \right] \hat{G}_+^A(x^A, \omega; x'') d^2x^A. \end{aligned} \quad (5.26)$$

Rewriting the right-hand side of equation (5.26) we have

$$\begin{aligned} \iint_{\partial D_1} \hat{B}(x^A, \omega; x^B) \hat{G}_+^A(x^A, \omega; x'') d^2x^A \approx \\ - \iint_{\partial D_2} \left[\iint_{\partial D_1} \hat{G}_+^{A*}(x', \omega; x^A) \hat{G}_+^A(x^A, \omega; x'') d^2x^A \right] \partial_3 \hat{G}_+^B(x', \omega; x^B) d^2x'. \end{aligned} \quad (5.27)$$

Replacing the definition in equation (5.25) in (5.27), we have

$$\iint_{\partial D_1} \hat{B}(x^A, \omega; x^B) \hat{G}_+^A(x^A, \omega; x'') d^2 x^A \approx - \iint_{\partial D_2} S(x', \omega; x'') \partial_3 \hat{G}_+^B(x', \omega; x^B) d^2 x'. \quad (5.28)$$

Equation (5.28) is the first approximation to the inverse operator for the vertical derivative of the downward Green's function with sources at the earth's surface and receiver at datum $\partial_3 \hat{G}_+^B(x', \omega; x^B)$. Regarding that the operator S contains non-physical events, similar to the operator P , as we discussed previously. Therefore, to improve the inverse operator in expression (5.28) we carry out in the same procedure as the previous section, supposing that is know the inverse of the operator S , that we denoted as S^{-1} . Multiplying the function inverse S^{-1} in both sides of expression (5.25) and integrating it over the surface S_2 , we have

$$\begin{aligned} \iint_{\partial D_2} \left[\iint_{\partial D_1} \hat{G}_+^{A*}(x', \omega; x^A) \hat{G}_+^A(x^A, \omega; x'') d^2 x^A \right] S^{-1}(x', \omega; x'') dx' = \\ \iint_{\partial D_2} S(x', \omega; x'') S^{-1}(x', \omega; x'') d^2 x' \approx \delta(x'_1 - x''_1) \delta(x'_2 - x''_2). \end{aligned} \quad (5.29)$$

Multiplying in both sides of equation (5.28) by the inverse function $S^{-1}(x', \omega; x'')$ and integrate it over the surface S_2 , we obtain

$$\begin{aligned} \iint_{\partial D_2} \left[\iint_{\partial D_1} \hat{B}(x^A, \omega; x^B) \hat{G}_+^A(x^A, \omega; x'') d^2 x^A \right] S^{-1}(x', \omega; x'') d^2 x' \approx \\ - \iint_{\partial D_2} \left[\iint_{\partial D_2} S(x', \omega; x'') \partial_3 \hat{G}_+^B(x', \omega; x^B) d^2 x' \right] S^{-1}(x', \omega; x'') d^2 x', \end{aligned} \quad (5.30)$$

rewriting the right-hand side of equation (5.30) we have

$$\begin{aligned} \iint_{\partial D_2} \left[\iint_{\partial D_1} \hat{B}(x^A, \omega; x^B) \hat{G}_+^A(x^A, \omega; x'') d^2 x^A \right] S^{-1}(x', \omega; x'') d^2 x' \approx \\ - \iint_{\partial D_2} \left[\iint_{\partial D_2} S(x', \omega; x'') S^{-1}(x', \omega; x'') d^2 x' \right] \partial_3 \hat{G}_+^B(x', \omega; x^B) d^2 x', \end{aligned} \quad (5.31)$$

Using the expression (5.29) in the inner integral over the surface ∂D_2 of the right-hand side of equation (5.31) we have

$$\begin{aligned} & \iint_{\partial D_2} \left[\iint_{\partial D_1} \hat{B}(x^A, \omega; x^B) \hat{G}_+^A(x^A, \omega; x'') d^2 x^A \right] S^{-1}(x', \omega; x'') d^2 x' \approx \\ & - \iint_{\partial D_2} \delta(x'_1 - x''_1) \partial(x'_2 - x''_2) \partial_3 \hat{G}_+^B(x', \omega; x^B) d^2 x'. \end{aligned} \quad (5.32)$$

Solving the right-hand side of equation (5.32) we have

$$\begin{aligned} & \partial_3 \hat{G}_+^B(x'', \omega; x^B) \approx \\ & - \iint_{\partial D_2} \left[\iint_{\partial D_1} \hat{B}(x^A, \omega; x^B) \hat{G}_+^A(x^A, \omega; x'') d^2 x^A \right] S^{-1}(x', \omega; x'') d^2 x'. \end{aligned} \quad (5.33)$$

Equation (5.33) is an expression that allows us to retrieve the vertical derivative of the downgoing Green's functions $\partial_3 \hat{G}_+^B(x'', \omega; x^B)$ with source position in x^B at the earth's surface and the receiver in x'' at the datum. For the purpose of this work, we need above deductions for up- and downward wavefield constituents to complete the redatuming process make reposition of source and receiver at datum. To do it, we will use the interferometric redatuming by convolution method in expression (4.10).

Redatuming

In this section we deduce an inverse operator to retrieve the total wavefield at the datum. Having calculated the up- and downward Green's functions constituents at datum, it is possible to relocate the sources and the receivers at the surface ∂D_2 . To start the analysis, we define a new *PSF* operator that we denoted as T . Different to the operator P in expression (5.1) that is composed by the autocorrelation between the transmitted wavefield in the state A . Here, the operator T is composed by the autocorrelation between the downward wavefield constituent in the state B with source position in x^B and receiver in x' , with the complex conjugate of itself with source position at x'' and receiver at x^B , this is defined as

$$\iint_{\partial D_1} \partial_3 \hat{G}_+^B(x', \omega; x^B) \partial_3 \hat{G}_+^{B*}(x^B, \omega; x'') d^2 x^B = T(x', \omega; x''), \quad (5.34)$$

The definition of the operator T considers all of the events between scatters above and below the datum with downward wavefield component with source at the earth's surface and receiver at the datum. Continuing with our deductions, we apply the expression (5.34) in equation (4.10), multiplying it in both sides by $\partial_3 \hat{G}_+^{B*}(x^B, \omega; x')$, which yields

$$\begin{aligned} & \iint_{\partial D_1} \hat{G}_-^B(x'', \omega; x^B) \partial_3 \hat{G}_+^{B*}(x^B, \omega; x'') d^2 x^B \approx \\ & -2 \iint_{\partial D_1} \left[\iint_{\partial D_2} \hat{R}_n(x', \omega; x^d) \partial_3 \hat{G}_+^B(x', \omega; x^B) d^2 x' \right] \partial_3 \hat{G}_+^{B*}(x^B, \omega; x'') d^2 x^B, \end{aligned} \quad (5.35)$$

rewriting right-hand side of equation (5.35), we obtain

$$\begin{aligned} & \iint_{\partial D_1} \hat{G}_-^B(x'', \omega; x^B) \partial_3 \hat{G}_+^{B*}(x^B, \omega; x'') d^2 x^B \approx \\ & -2 \iint_{\partial D_2} \left[\iint_{\partial D_1} \partial_3 \hat{G}_+^B(x', \omega; x^B) \partial_3 \hat{G}_+^{B*}(x^B, \omega; x'') d^2 x^B \right] \hat{R}_n(x', \omega; x^d) d^2 x'. \end{aligned} \quad (5.36)$$

substituting expression (5.34) in equation (5.36), we have

$$\iint_{\partial D_1} \hat{G}_-^B(x'', \omega; x^B) \partial_3 \hat{G}_+^{B*}(x^B, \omega; x'') d^2 x^B \approx -2 \iint_{\partial D_2} T(x', \omega; x'') \hat{R}_n(x', \omega; x^d) d^2 x'. \quad (5.37)$$

As previous analysis, we know that the operator T have non-physical events. Then, supposing that is know the inverse operator of T , denoted as T^{-1} , we apply it in equation (5.34) to obtain the following expression

$$\begin{aligned} & \iint_{\partial D_2} \left[\iint_{\partial D_1} \partial_3 \hat{G}_+^B(x'', \omega; x^B) \partial_3 \hat{G}_+^{B*}(x^B, \omega; x') d^2 x^B \right] T^{-1}(x', \omega; x'') d^2 x' = \\ & \iint_{\partial D_2} T(x', \omega; x'') T^{-1}(x', \omega; x'') d^2 x' \approx \delta(x'_1 - x''_1) \delta(x'_2 - x''_2), \end{aligned} \quad (5.38)$$

having defined above expression, we multiply in both sides of equation (5.37) by $T^{-1}(x', \omega; x'')$ and make integration over the surface S_2 , we obtain

$$\begin{aligned} & \iint_{\partial D_2} \left[\iint_{\partial D_1} \hat{G}_-^B(x'', \omega; x^B) \partial_3 \hat{G}_+^{B*}(x^B, \omega; x') d^2 x^B \right] T^{-1}(x', \omega; x'') d^2 x' \approx \\ & - 2 \iint_{\partial D_2} \left[\iint_{\partial D_2} T(x', \omega; x'') \hat{R}_n(x', \omega; x^d) d^2 x' \right] T^{-1}(x', \omega; x'') d^2 x', \end{aligned} \quad (5.39)$$

rewriting the right-hand side of equation (5.39) we have the following expression

$$\begin{aligned} & \iint_{\partial D_2} \left[\iint_{\partial D_1} \hat{G}_-^B(x'', \omega; x^B) \partial_3 \hat{G}_+^{B*}(x^B, \omega; x') d^2 x^B \right] T^{-1}(x', \omega; x'') d^2 x' \approx \\ & - 2 \iint_{\partial D_2} \left[\iint_{\partial D_2} T(x', \omega; x'') T^{-1}(x', \omega; x'') d^2 x'' \right] \hat{R}_n(x', \omega; x^d) d^2 x'. \end{aligned} \quad (5.40)$$

The inner integral over the surface ∂D_2 in the right-hand side of equation (5.40) can be substituted by expression (5.38), then (5.40) can be written as

$$\begin{aligned} & \iint_{\partial D_2} \left[\iint_{\partial D_1} \hat{G}_-^B(x'', \omega; x^B) \partial_3 \hat{G}_+^{B*}(x^B, \omega; x') d^2 x^B \right] T^{-1}(x', \omega; x'') d^2 x' \approx \\ & - 2 \iint_{\partial D_2} \delta(x'_1 - x''_1) \delta(x'_2 - x''_2) \hat{R}_n(x', \omega; x^d) d^2 x'. \end{aligned} \quad (5.41)$$

Solving the right-hand side of equation (5.41) we find the final expression to complete the redatuming process with sources and receivers at the datum $\hat{R}_n(x'', \omega; x^d)$

$$\begin{aligned} & \hat{R}_n(x'', \omega; x^d) \approx \\ & - \frac{1}{2} \iint_{\partial D_2} \left[\iint_{\partial D_1} \hat{G}_-^B(x'', \omega; x^B) \partial_3 \hat{G}_+^{B*}(x^B, \omega; x') d^2 x^B \right] T^{-1}(x', \omega; x'') d^2 x'. \end{aligned} \quad (5.42)$$

Equation (5.42) is the main result of this work, because with this expression it is possible to retrieve the total Green's function at datum in the surface ∂D_2 . Note that equation (5.41) is evaluated over surface ∂D_1 , that is the acquisition surface. Input data of equation (5.41) are the upward Green's function $\hat{G}_-^B(x'', \omega; x^B)$ calculated with the expression (5.22), the complex conjugate of the downward

Green's function $\hat{G}_+^B(x^B, \omega; x')$ calculated with the equation (5.32), and finally the *PSF* inverse defined in expression (5.34).

5.3 Least squares

Least squares is a standard approach in regression analysis to approximate solution of overdetermined systems, i.e., set of equations in which there are more equations than variables. "Least squares" means that the overall solution minimizes the sum of the squares of the errors made in the result of each single equation. To retrieve the Green's functions at datum end to avoid the presence of artefacts in the inhomogeneous case, as we discussed before, is necessary to calculate the inverse of the *PSF*, for that we will deduce an expression in order to invert it using Least square. We start defining equation (5.5) in a matrix form as

$$\mathbf{PSF}(x'_{ij}; x''_{ij}) \mathbf{PSF}^{-1}(x'_{ij}; x''_{ij}) = \mathbf{I}, \quad (i = 1, 2, \dots, m) \text{ and } (j = 1, 2, \dots, m), \quad (5.43)$$

where \mathbf{I} is the identity matrix, \mathbf{PSF} is the matrix form of the product in frequency domain between \hat{G}_+^A and \hat{G}_+^{A*} and \mathbf{PSF}^{-1} is the matrix inverse of the \mathbf{PSF} . Matrix system of equation (5.43) is solved for each column of $\mathbf{PSF}^{-1}(x'_{i,j}; x''_{i,j})$ and for each \mathbf{I} , where the terms for the first system to solve are

$$\mathbf{PSF} = \mathbf{P}_{m \times m} = \begin{bmatrix} P_{11} & P_{12} & P_{13} & \dots & P_{1m} \\ P_{21} & P_{22} & P_{23} & \dots & P_{2m} \\ \vdots & \vdots & \vdots & \ddots & \vdots \\ P_{m1} & P_{m2} & P_{m3} & \dots & P_{mm} \end{bmatrix}, \mathbf{D}_{m \times 1} = \begin{bmatrix} D_{11} \\ D_{21} \\ \vdots \\ D_{m1} \end{bmatrix}, \mathbf{I}_{m \times 1} = \begin{bmatrix} 1 \\ 0 \\ \vdots \\ 0 \end{bmatrix}.$$

Where \mathbf{P} is the *PSF* matrix, \mathbf{D} is the inverse of each column of \mathbf{P} and \mathbf{I} represent each column of the identity matrix. The principal goal of this kind of problems is to find the coefficients D that fit into the equations as best as possible in order to solve the quadratic minimization problem, where the objective function \mathbf{M} is given by

$$\mathbf{M}(\mathbf{S}) = \|\mathbf{P} \mathbf{S} - \mathbf{I}\|^2. \quad (5.44)$$

In equation (5.44) the expression \mathbf{S} represents the complete matrix with all inverted columns that are represented in \mathbf{D} , this equation is the standard approach to a linear regression with least squares. Usually, ordinary least squares estimation leads to solving an overdetermined problem if the matrix system have complete rank, then this solution will be of unique. On the other hand, If the matrix have a variety of magnitude values that involve hight differences between its terms is necessary make a regularization of it, then, in order to make this regularization to solve in equation (5.44) we include

term ϵ as

$$\mathbf{M}(\mathbf{S}) = \|\mathbf{P} \mathbf{S} - \mathbf{I}\|^2 + \epsilon \|\mathbf{S}\|^2. \quad (5.45)$$

Where ϵ is the regularization factor, that improves the conditioning of the problem. The solution to expression (5.45) is given by i.e., Watkins (2010) and is written as

$$\mathbf{S} = (\mathbf{P}^T \mathbf{P} + \epsilon)^{-1} \mathbf{P}^T. \quad (5.46)$$

Expression (5.46) allows us to calculate the PSF^{-1} solving equation (5.45). Depending of the regularization parameter to solve the inverse problem in expression (5.46), we will stabilize the computational implementation. In theory, this parameter would be small enough for the system to be independent of it.

6. Numerical Examples

In this chapter, we will exemplify the main deductions performed at previous sections, using the appropriate numerical examples to explain the main physical phenomena involved specially, in methods of inverse wavefield extrapolation for overburden with both homogeneous and inhomogeneous media. Also, we will test the interferometry with correlation and convolution based methods. These methods are conventional approaches to make redatuming in the classics methods i.e., Schuster (2009), Wapenaar et al. (2010a), etc.

6.1 Interferometric redatuming: Correlation-based method

To numerically validate the interferometric redatuming equations (3.42) and (3.43) to test its limitations due to the use of the direct wave instead of the full reference wavefield, we applied interferometric methods of convolution and correlation-type in a few simple numerical experiments.

Datum below a homogeneous layer

In our first test, we used a horizontally-layered velocity model with a width of 8 km and a depth of 3 km containing velocities between 1.8 km/s and 2.5 km/s (Figure 6.1). The datum is located 500 m below the surface within the first homogeneous layer with velocity 1.8 km/s. This experiment represents the ideal theoretically situation, where the reference wavefield consists only of a direct wave.

We simulated synthetic data with a marine acquisition geometry considering three situations: (1) Shots and receivers are located at the surface (Figure 6.1a). These are the data to be redatumed. (2) Shots are located at the surface and receivers at 500 m depth (Figure 6.1b) and (3) shots and receiver are located at 500 m depth (Figure 6.1c). The data of the latter two simulations are used for comparison to the redatuming results.

All three seismic arrays consisted of 201 sources spaced at 25 m, horizontally located between

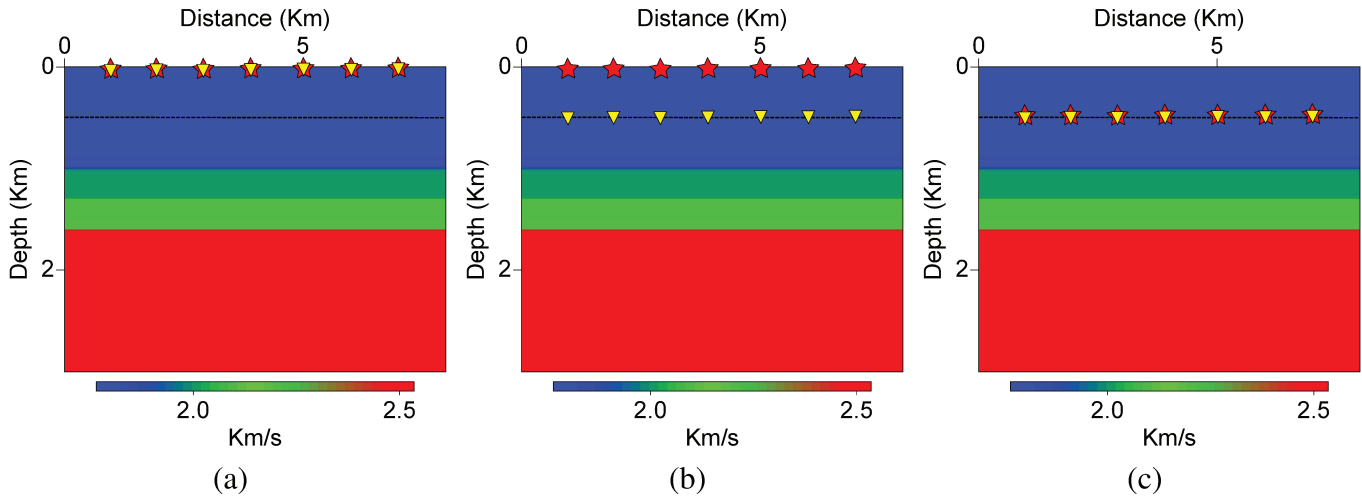


Figure 6.1: Modeling seismic data considering: (a) array of sources and receivers at the surface, (b) array of shots at the surface and receivers at 500 m depth and (c) both arrays positioned at 500 m depth.

coordinates 1 km and 6 km, and the same number of receivers for each shot, located at the same horizontal positions (Figure 6.1). The wavelet used for the numerical modeling was a Ricker wavelet with 25 Hz peak frequency. For simplicity, we considered the density in all layers constant.

Receiver redatuming

The first step of redatuming the complete seismic array from the surface to the datum consisted of redatuming the receivers, i.e., transforming the configuration of Figure (6.1a) into the geometry of Figure (6.1b). The seismic data recorded with the surface array contain three reflections. Their two-way times at zero offset are: event 1 at $t = 1.1$ s, event 2 at $t = 1.4$ s and event 3 at $t = 1.67$ s (Figure 6.2). To carry out the redatuming, we modeled all direct waves from all desired receiver positions at depth to all true receiver positions at the surface (Figure 6.1b) and crosscorrelated them with the surface data according to equation (3.42). Here, we used the same wavelet as in the original data, assumed to be known. This first step yields the redatumed data for receivers at the datum at 500 m in depth. The theoretical zero-offset times of the three reflection events 1, 2, and 3 are $t = 0.82$ s, $t = 1.12$ s and $t = 1.39$ s, respectively (Figure 6.2a). The events are correctly positioned at the times calculated from the model parameters.

Figure 6.2 shows the resulting common-shot gather with the receivers at the new depth in comparison to the modeled data with the same configuration. We see that the kinematic properties of the data are nicely matched. For a more detailed inspection, Figure 6.3 shows a comparison of the

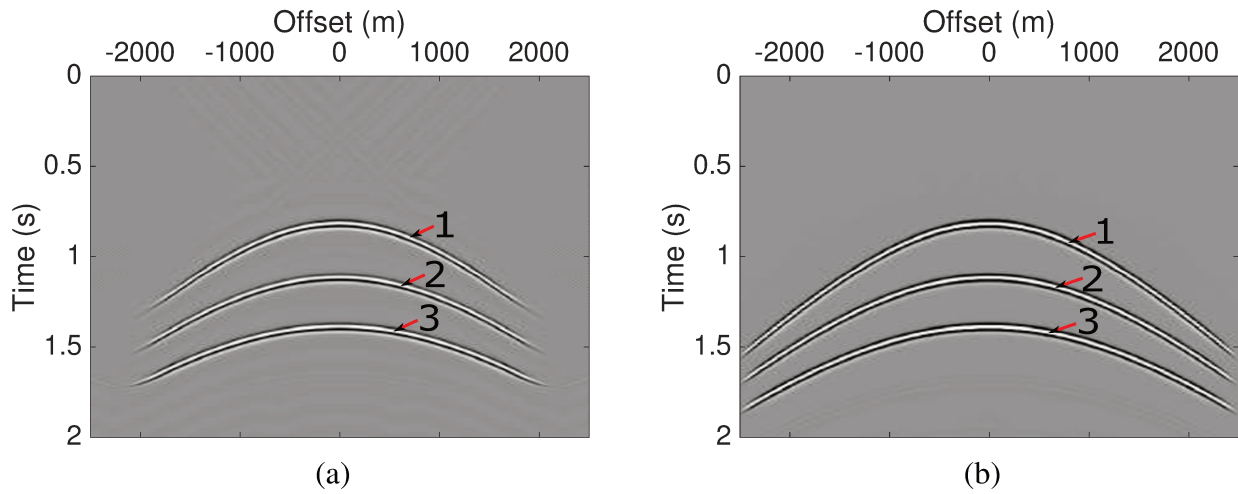


Figure 6.2: Redatuming using seismic direct-wave interferometry with the numerical model of Figure 6.1. Step 1: Redatuming the receivers. (a) Redatumed data, and (b) modeled data for sources at the surface and receivers at the datum.

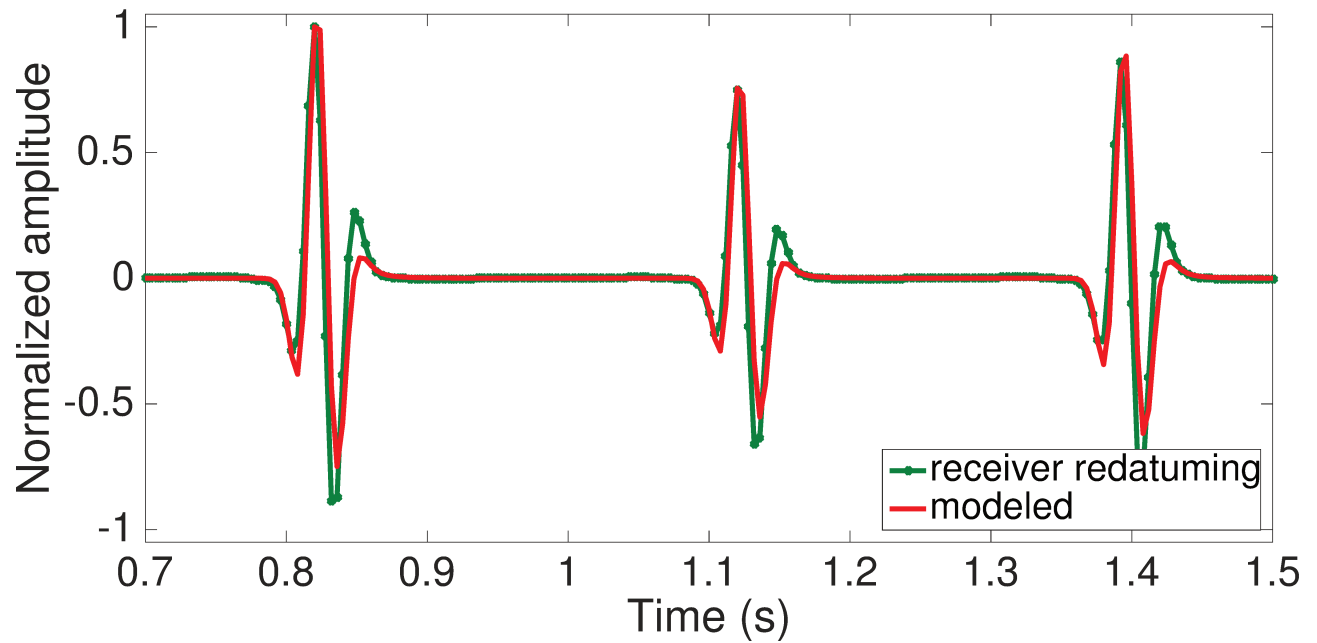


Figure 6.3: Redatuming using seismic direct-wave interferometry with the numerical model of Figure 6.1. Step 1: Redatuming the receivers. Comparison of the central trace (green line) to the modeled data with the same configuration (solid red line).

central trace of the redatumed data (green line) to corresponding trace of the modeled data (red line). Because the absolute amplitudes of the crosscorrelation are unreliable because of the presence of the wavelet in the data, we normalized the traces to the amplitude of the first redatumed primary reflection. We see that the redatuming has positioned all three reflection events at their correct arrival times

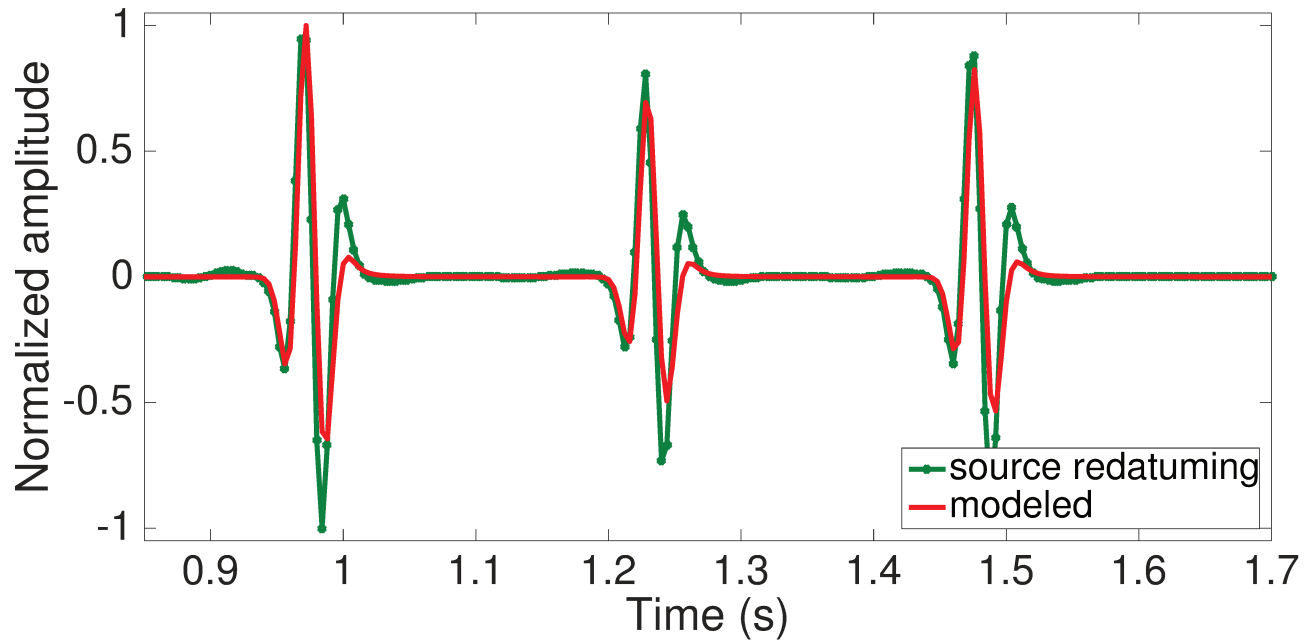


Figure 6.4: Redatuming using seismic direct-wave interferometry with the numerical model of Figure 6.1. Step 1: Redatuming the receivers. Comparison of the trace at 1000 m offset obtained from receivers redatuming in Figure 6.2.

and that their relative amplitudes are correctly recovered. Note that the wavelets in the redatumed trace are stretched in comparison to the modeled trace. The reason is that the crosscorrelations with the modeled data wavelet slightly reduce the frequency content.

Figure 6.4 shows the normalized traces at offset 1000 m of the redatumed data corresponding to the shot 101 in Figure 6.2. The three primary events are correctly positioned and their relative amplitudes are well preserved. Figure (6.5) shows us the interpretation that describe the process to retrieve the upgoing Green's functions with sources at the earth's surface and receivers at datum. Through the process of crosscorrelation between the seismic data at the earth's surface and the transmitted wavefield from the earth's surface until the datum it is possible make redatuming of the receivers.

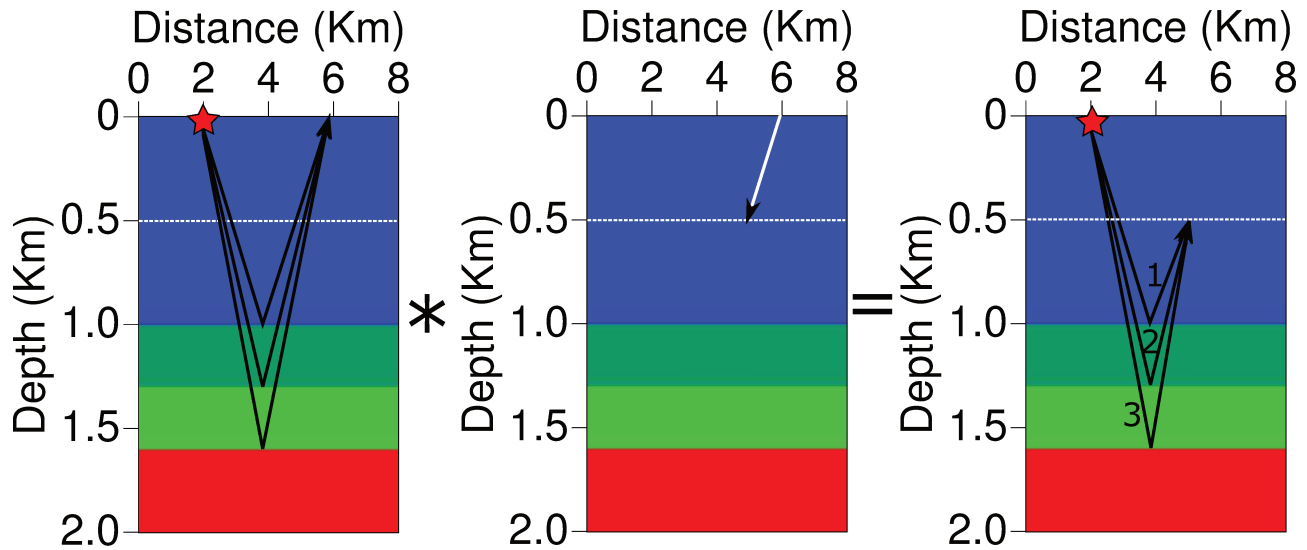


Figure 6.5: Redatuming using seismic direct-wave interferometry with the numerical model of Figure 6.1. Step 1: Redatuming the receivers. Black lines represent causal wavefields, i.e., positive times and the white lines represent anticausal wavefields, i.e., negative times in the wavefield propagation.

Source redatuming

The second step of the complete redatuming of the full survey consists of repositioning the sources at depth, i.e., transforming the configuration of experiment shown in Figure (6.1b) into the one shown in Figure (6.1c). For this purpose, we sort the data into common-receiver gathers. These can be redatumed using again equation (3.43) because of the reciprocity principle.

We used both data sets, the transmitted wavefield model and the upgoing Green's function retrieved in above step as input to this second redatuming step. We see that the positioning of the three reflections events in the two-step result (Figure 6.6a) matches when is compared with the exact model (Figure 6.6b).

The two-step redatuming of the surface data introduces some additional noise, particularly at the border of the events. These are boundary effects that result from the limited data aperture, as we mentioned in the previous chapter. These effects are restricted to the boundary zone and are of less importance if more input data are available.

For a more detailed analysis of the quality of the redatumed data, Figure (6.7) compares the normalized redatumed trace at the center of both the source and receiver arrays to the corresponding modeled one. As after receiver redatuming, all events are correctly positioned in time, and their rel-

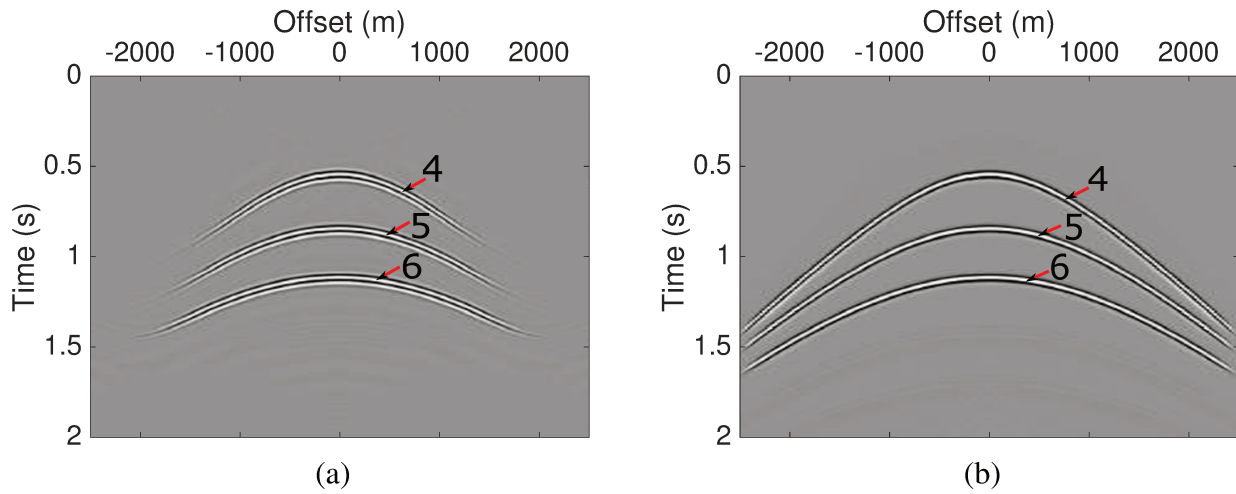


Figure 6.6: Redatuming using seismic direct-wave interferometry with the numerical model of Figure 6.1. Step 2: Redatuming the sources. Where (a) is the output response of the source redatuming and (b) is the exact model

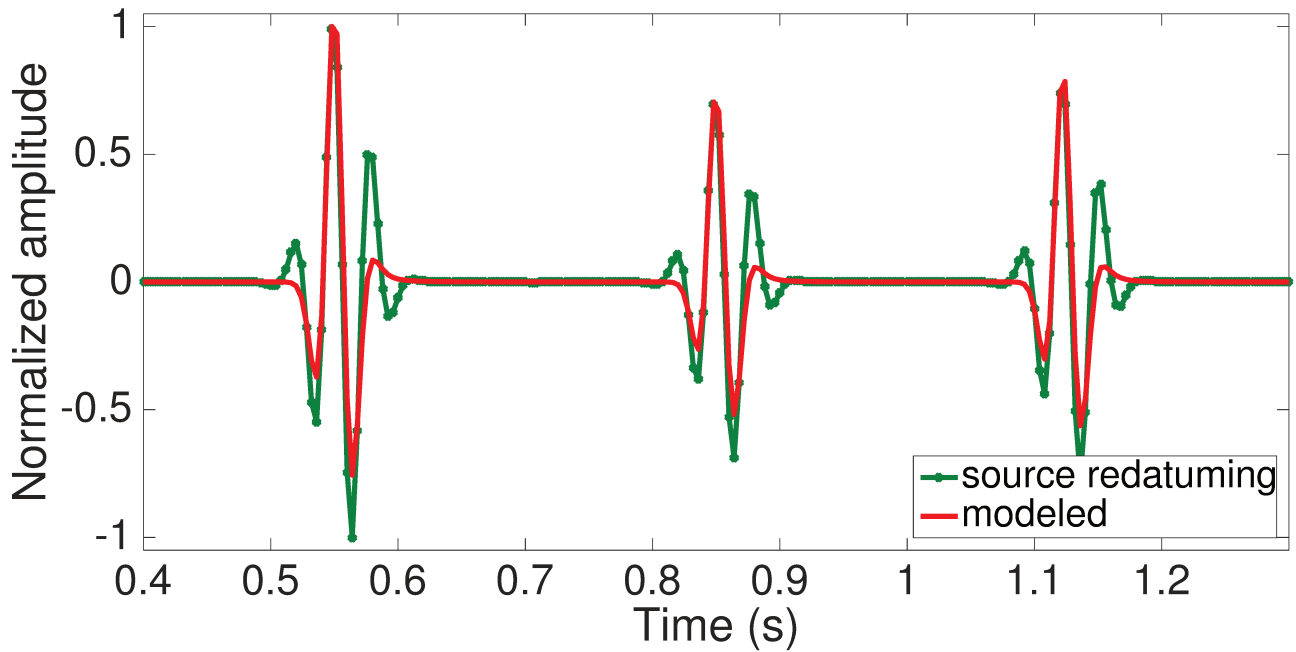


Figure 6.7: Comparison of the normalized central trace of the fully redatumed shot gather of Figure (6.6a) (green line) with the corresponding traces obtained from modeling (green line) and from redatuming the gather modeled with the receivers at the datum (red line).

active amplitudes are correctly recovered. We observe again that the redatuming has caused a certain wavelet deformation and stretch. Figure 6.8 shows the complete redatuming with sources and receivers at the datum in 500 m in depth at the central shot 101 at offset 1000 m in all responses in Figures 6.6. Figures 6.9 schematically explain the crosscorrelation between the output data of step 1

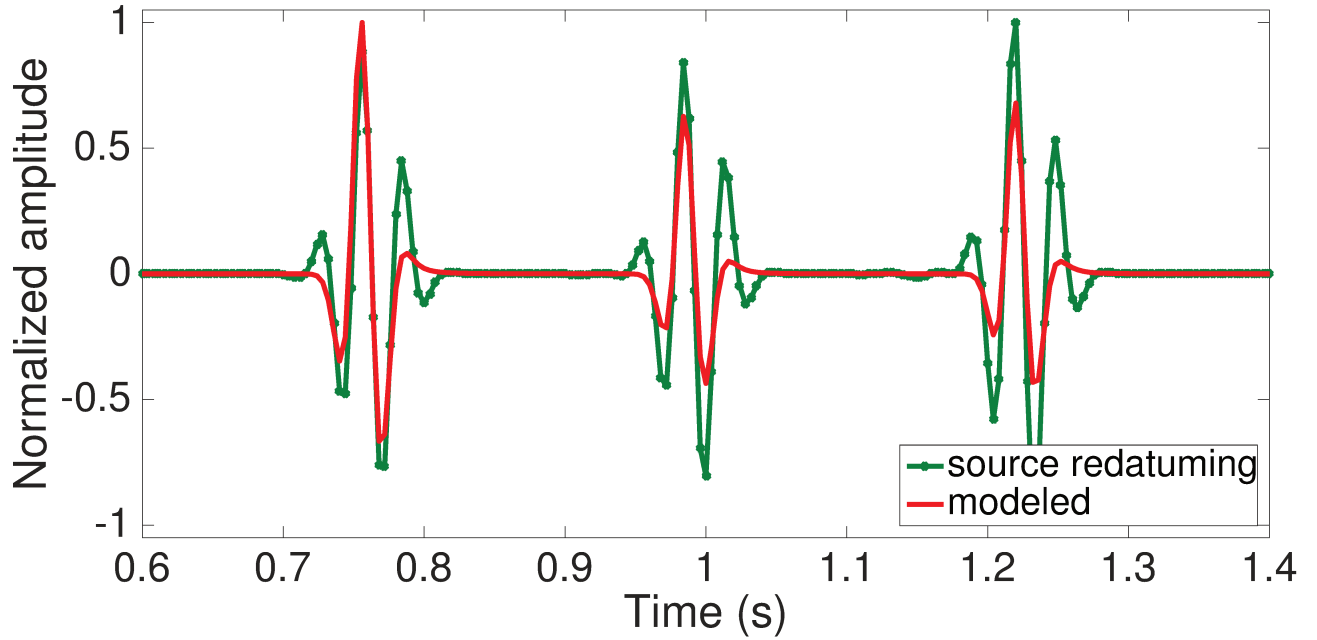


Figure 6.8: Redatuming using seismic direct-wave interferometry with the numerical model of Figure 6.1. Step 2: Redatuming the sources. Comparison of the trace at 1000 m offset obtained from sources redatuming in Figure 6.6.

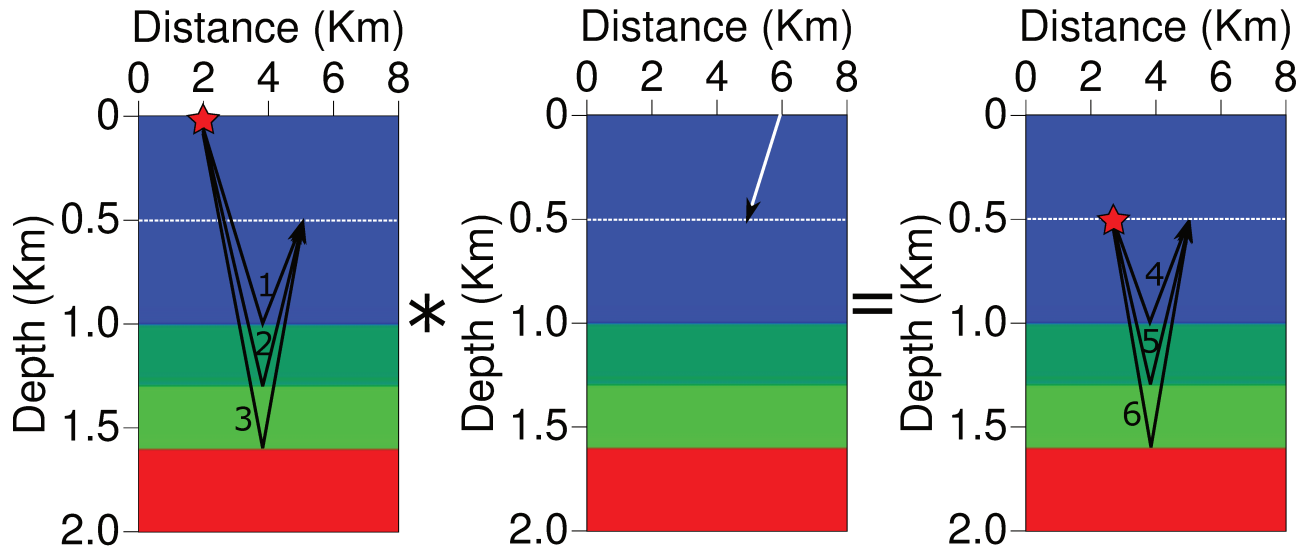


Figure 6.9: Redatuming using seismic direct-wave interferometry with the numerical model of Figure 6.1. Step 2: Redatuming the sources.

and the direct wave modeling at 500 m at depth. As result of the previous operation, we obtain the redatumed data with sources and receivers at the new datum (Figure 6.9).

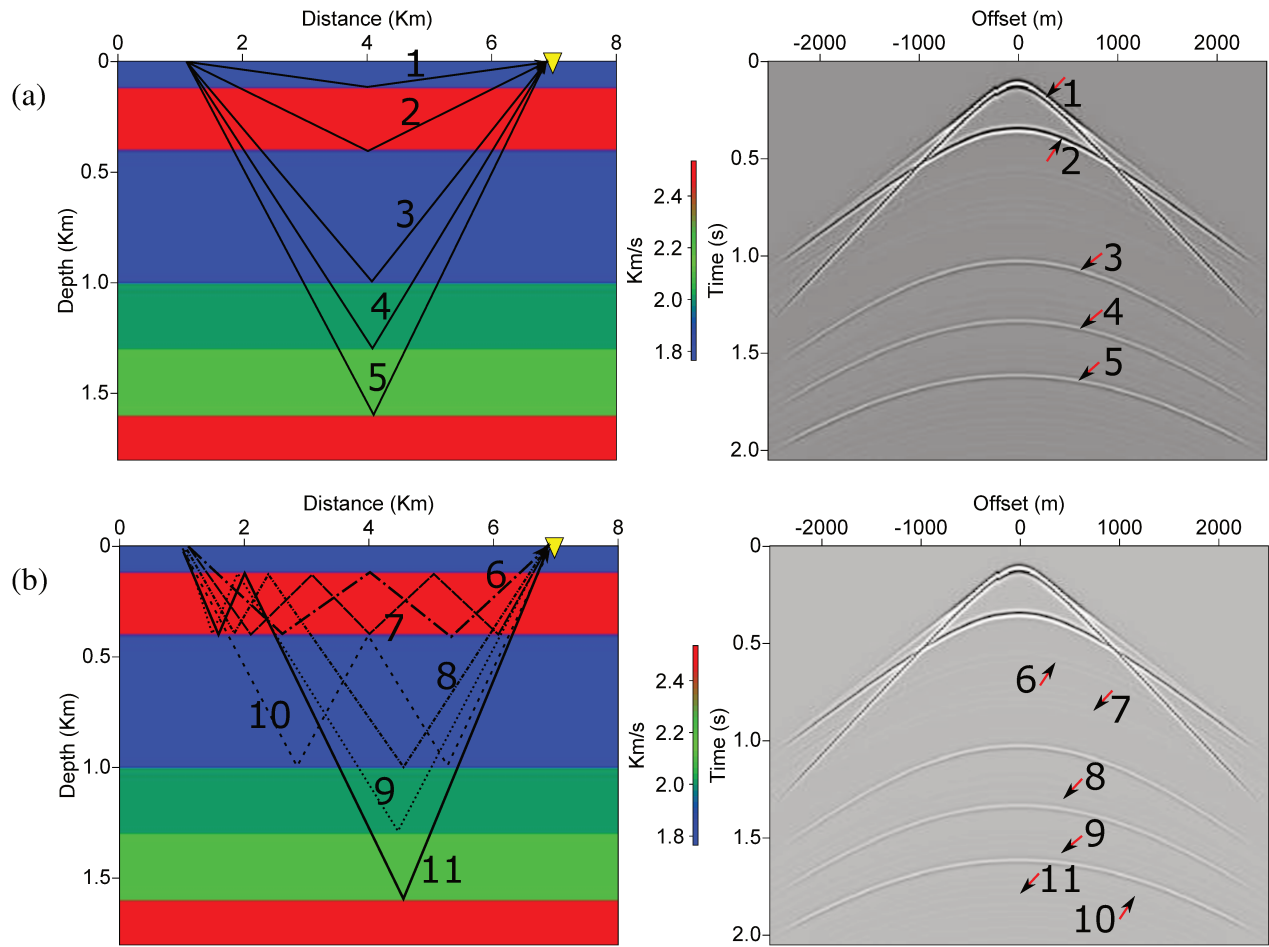


Figure 6.10: Seismic array on surface considering an inhomogeneous overburden, where we describe: (a) primary reflection events and (b) multiple events visible in the data.

Datum below a high-velocity layer: Correlation-based

In the second numerical experiment, we chose a model with a high-velocity layer (2.5 km/s) from 120 m to 400 m depth, between the original acquisition surface and the datum at 500 m depth. The lower part of the model is the same as before (Figure 6.10a). In this situation, the reference wavefield includes the direct wave and later arrivals due to scattering in the high-velocity layer. To restrict the number of visible multiples, we did not use a free boundary at the top of the model. Our purpose is to see how these later arrivals affect the quality of the redatumed data.

Figure (6.10) shows the modeled synthetic data with labeled events and ray-path sketches, separated in primary reflections (Figure 6.10a) and the most prominent multiples (Figure 6.10b). The zero-offset times of the primary reflections are: $t_1 = 0.133$ s, $t_2 = 0.357$ s, $t_3 = 1.024$ s, $t_4 = 1.324$ s and $t_5 = 1.597$ s (Figure 6.10a). The strongest multiples are: Events 6 and 10 are the first multiples

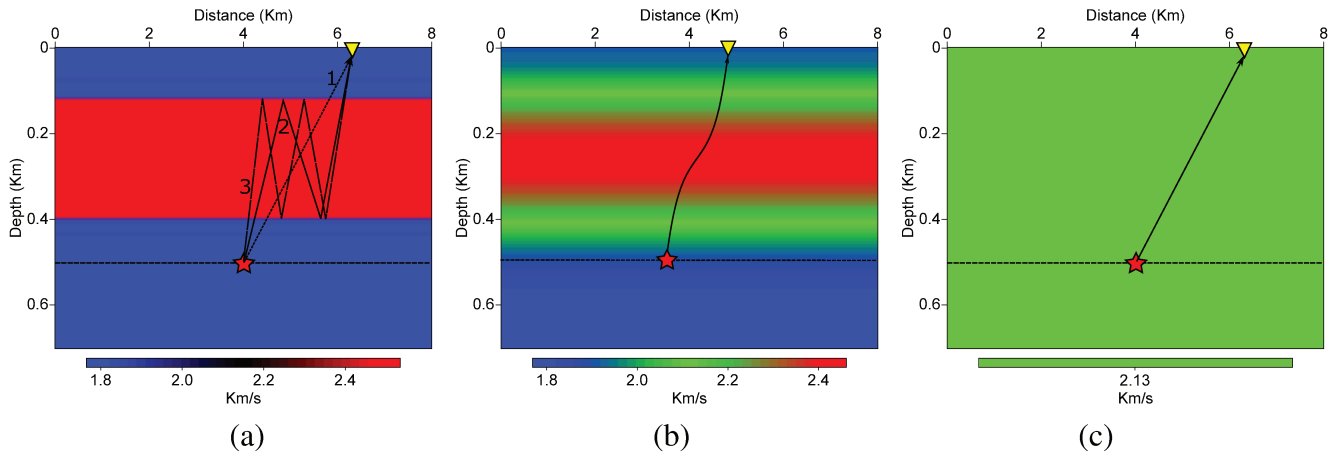


Figure 6.11: Models used for direct-wavefield modeling in the redatuming procedure. (a) Exact overburden. (b) Smoothed overburden. (c) Constant velocity from average slowness. Also shown are possible ray paths connecting sources at the datum to receivers at the surface.

in the second and third layers with zero-offset times $t_6 = 0.581$ s and $t_{10} = 1.690$ s; events 8, 9, and 11 are peg-leg multiples with $t_8 = 1.248$ s, $t_9 = 1.548$ s, and $t_{11} = 1.820$ s; and event 7 is a second-order multiple in the second layer with $t_7 = 0.805$ s (Figure 6.10b). Other higher-order multiples are present in the data but their amplitudes are too small to be visible. Not labeled is the head wave, which is the first event at offsets larger than 250 m.

Redatuming

The redatuming procedure is the same as detailed for the first example. Also as before, we modeled synthetic data for 201 sources and receivers, spaced at 25 m. For the wave modeling in our four test of the redatuming process, we used three different background models, shown in Figure (6.11). The first model uses the exact velocity model in the region between the surface and the datum (Figure 6.11a). With the exact model (Figure 6.11a), we carried out two experiments, one modeling the direct wave only by means of one-way wave propagation, and the other modeling the complete wave train. In the third test, we use a smoothed model (Figure 6.11b), and in the fourth test, we use a constant-velocity model with the correct average slowness (Figure 6.11c). To calculate the direct waves Figure (6.11) also shows ray paths associated with the modeled events in these overburden models.

The results of the crosscorrelations between the data of Figure (6.10) and the different transmitted waves using the models of Figure (6.11) are shown in Figure (6.12). As a first observation, we notice that redatuming using the full wave train in the inhomogeneous overburden between the surface and

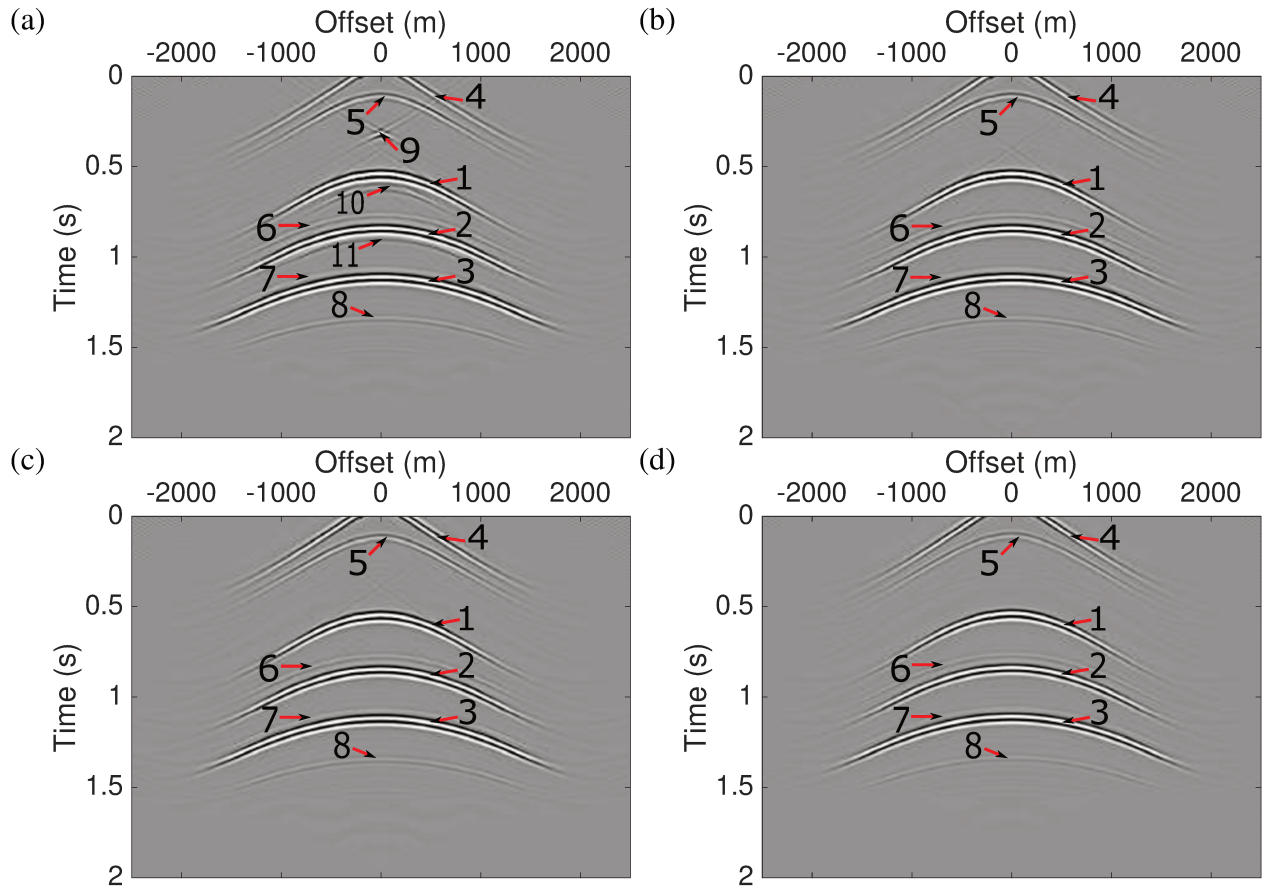


Figure 6.12: Result of redatuming with the (a) full wave train from the exact inhomogeneous overburden velocity model, (b) direct wave from the exact model, (c) direct wave from the smoothed model, and (d) direct wave from the constant-velocity model. The resulting redatumed events are labeled with numbers for further discussion.

the datum (Figure 6.12a) creates much more events than redatuming using the direct wave only (Figure 6.12b-d). A comparison with the desired result (Figure 6.6c) reveals that even the other results contain more events than they should. Moreover, we notice upon closer inspection that the kinematic behavior of the data redatumed using the constant-velocity model (Figure 6.12d) is slightly incorrect at non-zero offset.

The principal conclusion from this experiment is that it might not be convenient use equation (3.43) for redatuming in a strongly inhomogeneous overburden. As we can see in Figure (6.12), all ways of modeling the wavefield in the overburden produce unphysical events that should not be present in the redatumed data. In any case, using the direct wave only for redatuming is advantageous over using the full wave train, even if the overburden model is exactly known.

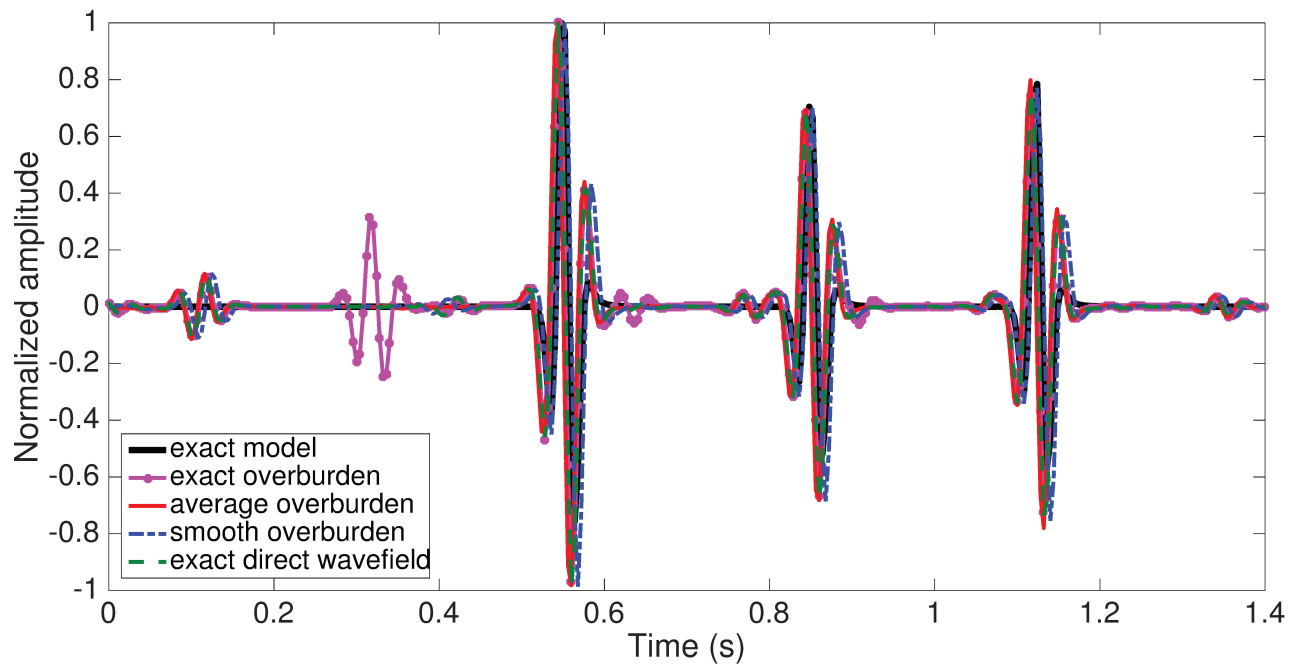


Figure 6.13: Comparison of the central trace obtained from redatuming using the full wave train in the exact overburden and the direct wave in the exact, smoothed and constant-velocity models.

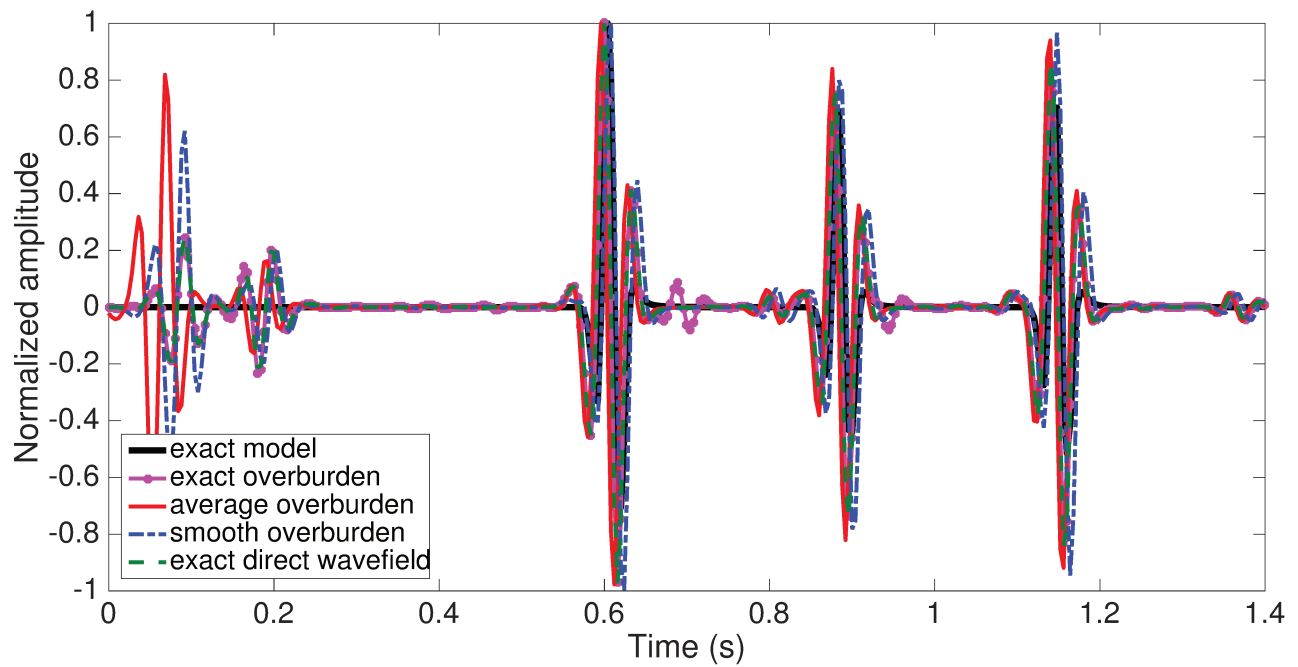


Figure 6.14: Comparison of the trace at 500 m offset obtained from redatuming using the full wave train in the exact overburden and the direct wave in the exact, smoothed and constant-velocity models.

For more detail we show in Figure (6.13) the normalized traces at zero offset, obtained using

the full wave train in the exact overburden and the direct wave in the exact, smoothed and constant-velocity models as compared to the data modeled at the datum. The three primary events are correctly positioned and their relative amplitudes are well preserved. In addition to these desired effects, we notice a number of events with smaller amplitudes. These are the unphysical events as discussed above. Note that the true internal multiples in the medium below the datum are of much smaller amplitude and cannot be seen at this scale. The traces obtained with the direct waves in the exact, smoothed, and average-velocity models are very similar to each other, with a very small kinematic error for the average-velocity model.

In Figure 6.14 we show the trace that corresponds to the offset 500 m in the redatuming responses in Figure 6.12. The three primary events are correctly positioned and their relative amplitudes are well preserved. In addition to these desired effects, we notice a number of events with smaller amplitudes. These are the unphysical events as discussed above. Note that the true internal multiples in the medium below the datum are of much smaller amplitude and cannot be seen at this scale

Event interpretation

To explain all events present in the parts of Figure (6.12), we have labeled them. In the next set of figures, we will discuss the ray paths associated to all (physical and unphysical) events. In this way, we will be able to better understand the shortcomings of each of the tested modeling approaches.

The events labeled 1, 2, and 3 are the desired primary reflections from the deeper reflectors after redatuming. The corresponding ray paths associated with the original surface events, the two-step redatuming operators (representing the convolution of the two one-step operators), and the redatumed events are depicted in Figure (6.15).

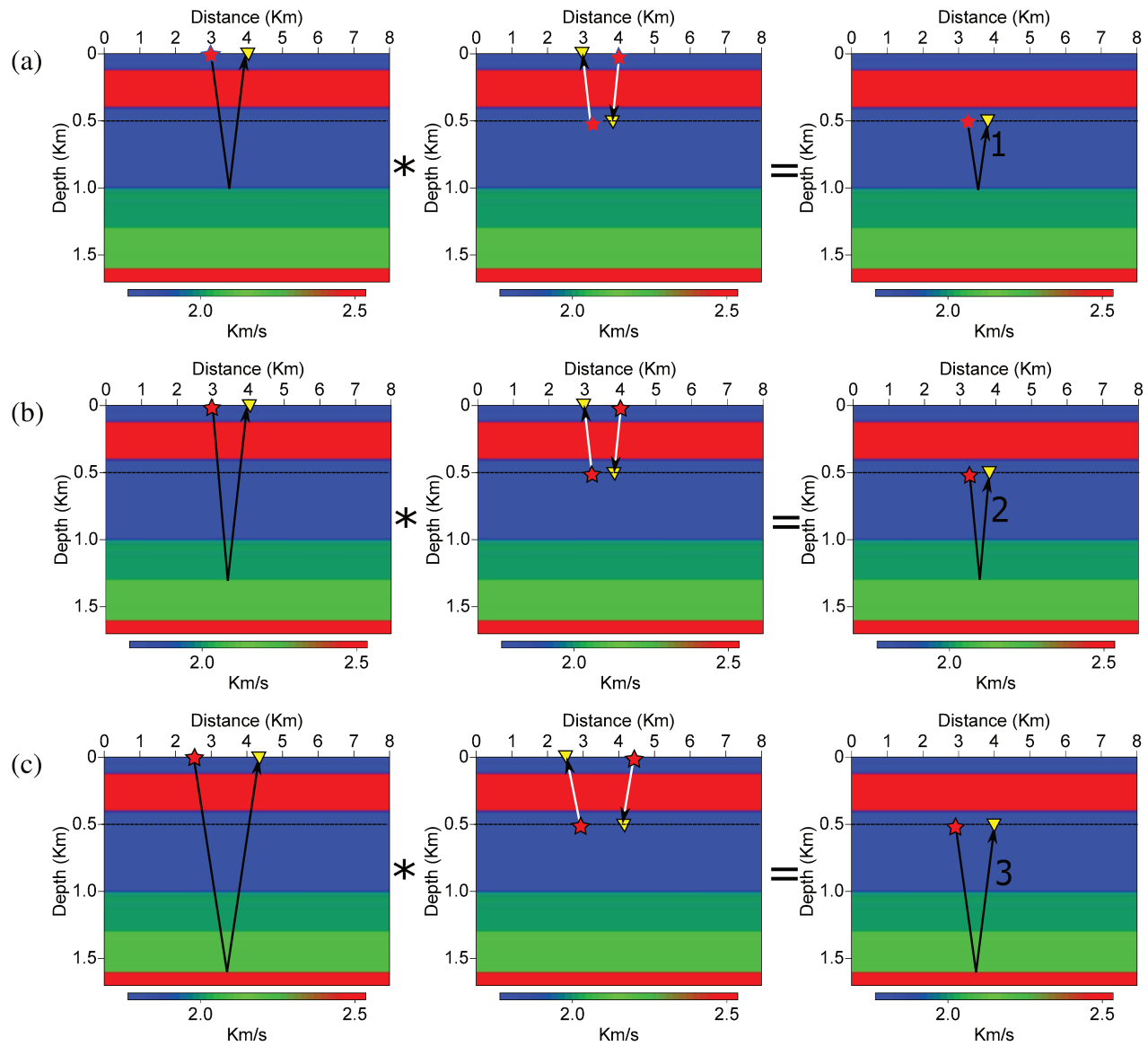


Figure 6.15: Ray paths for the surface events, crosscorrelation operator, and redatuming response, for events 1, 2 and 3 of Figure (6.12).

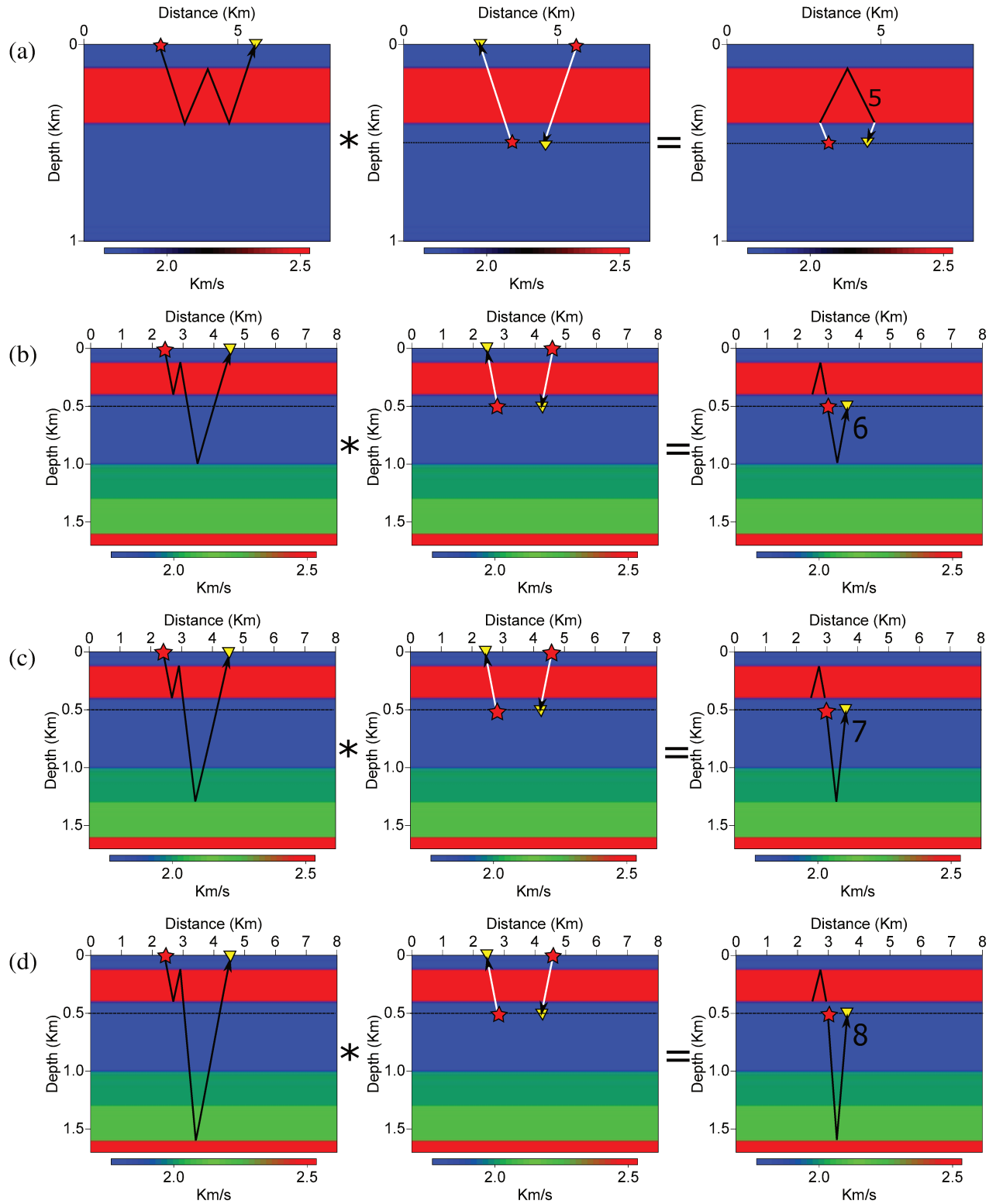


Figure 6.16: Ray paths for the surface events, crosscorrelation operator, and redatuming response, for unphysical events 5, 6, 7, and 8 of Figure 6.12. Ray paths contributing negatively to the traveltimes are shown in white.

Event 4 is a boundary effect of the redatuming of the primary reflection at the first interface in the overburden (see Appendix C). Events 5, 6, 7, and 8 (see ray paths in Figure 6.16) are unphysical events resulting from redatuming the multiples with a first leg in the high-velocity layer (events 6, 8, 9, and 11 in Figure 6.10b) with the direct wave.

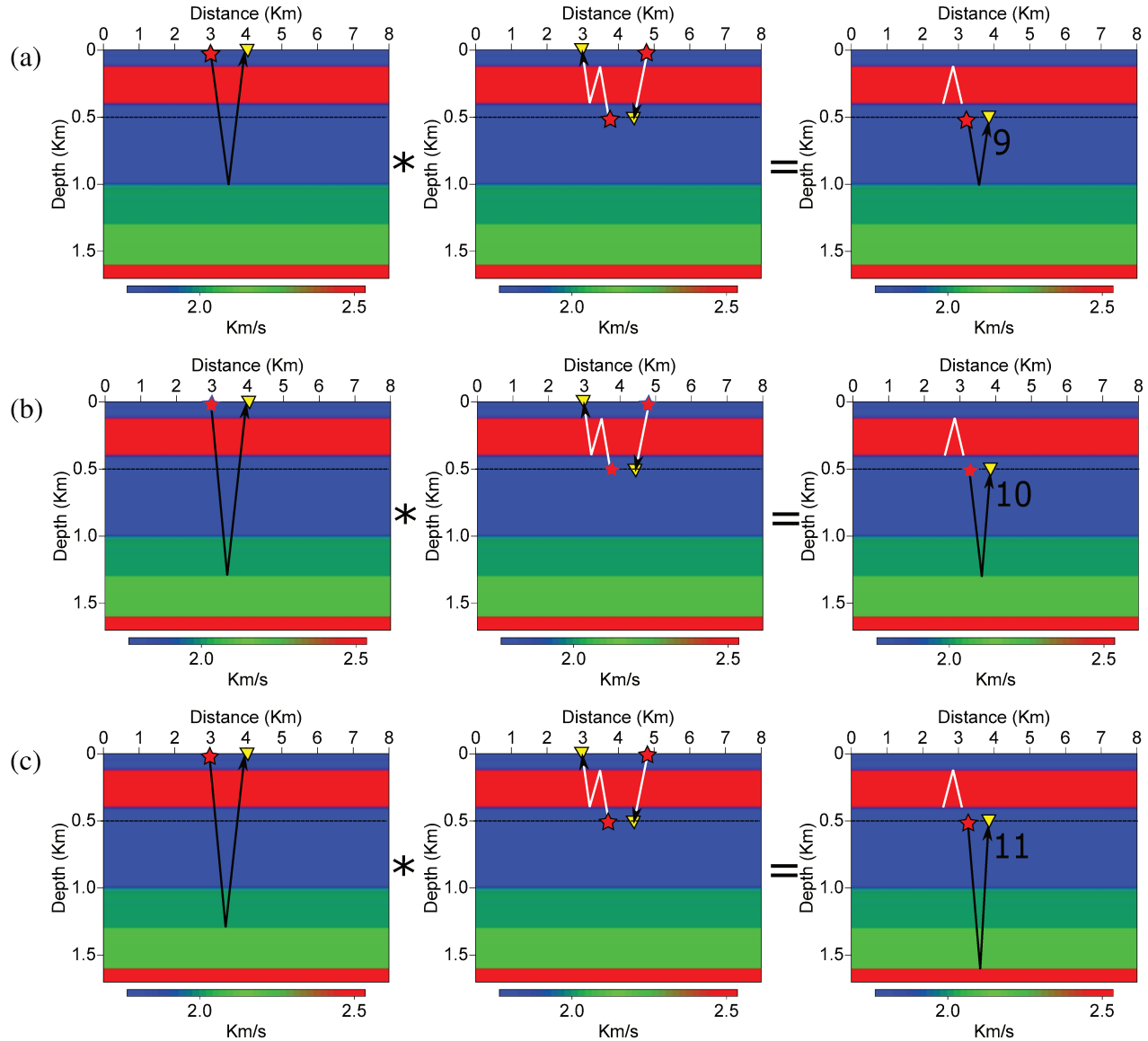


Figure 6.17: Ray paths for the surface events, crosscorrelation operator, and redatuming response, for unphysical events 9 and 10 of Figure 6.12a. Ray paths contributing negatively to the traveltimes are shown in white.

Events 9, 10 and 11 appear only in Figure (6.12a), because they are unphysical events caused by crosscorrelation of the data primaries with multiples in the modeled wave train. Specifically, these events are obtained from redatuming the primaries of the 3rd, 4th and 5th reflectors (events 3, 4 and

5 in Figure 6.10a) with the direct wave at the receiver side and with the first high-velocity-layer multiple at the source side or vice versa (see ray paths in Figure 6.17). A corresponding event generated from the primary at the deepest interface is present (but barely visible) immediately after event 2 in Figure 6.12a.

Finally, we can analyze the anticausal wavefield part of the redatumed wavefield generated by the correlation-based interferometric redatuming procedure. Here, we restrict ourselves to discussing the one obtained with the full wave train in the true overburden model (Figure 6.18a). The other three results are similar (Figure 6.18b-d), but do not contain the events obtained from crosscorrelation with the multiples. It should be kept in mind that the desired part of the redatumed wavefield is its causal part.

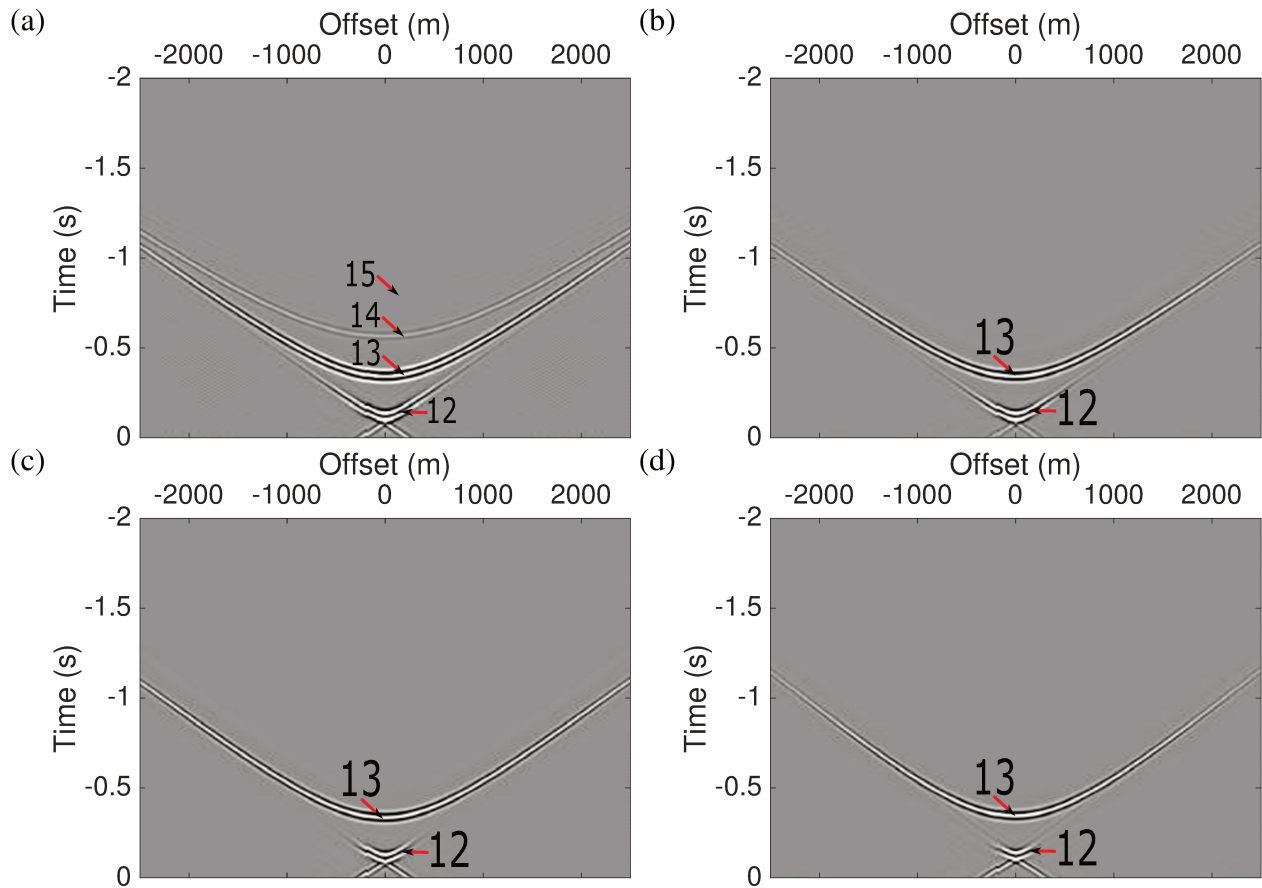


Figure 6.18: Anticausal part of the redatuming result using the full wave train from the exact overburden velocity model. The labeled events are explained in the text. The anticausal results was using (a) full wave train from the exact inhomogeneous overburden velocity model, (b) direct wave from the exact model, (c) direct wave from the smoothed model, and (d) direct wave from the constant-velocity model.

Events 12 and 13 are the primary reflections from the two interfaces in the overburden. Since they are above the datum, they appear in the redatumed data at negative traveltimes. Also visible is the initial part of the redatumed head wave (event 4 in Figure 6.12). Finally, events 14 and 15 are the events caused by redatuming these primaries with a direct wave and a multiple in the same way as explained for events 9, 10 and 11 in Figure (6.12a). The ray paths associated with these events at negative traveltimes are depicted in Figure 6.20.

For more detail, we show in Figure (6.19) the normalized traces at zero offset in the anticausal part of the redatumed response. In this case we see that events 12 and 13 retrieved by interferometry with correlation-based are matched with the exact model, which source and receivers are located at the datum. Also the event 14 can be seen in the Figure (6.19), but with a very low amplitude, and event 15 does not appear in the central traces analyzed here. Because their amplitudes are too attenuated by the propagation effects, they are almost invisible in the zero-offset trace. Actually, these events correspond to second and third order multiples, as we interpret in the Figure (6.20).

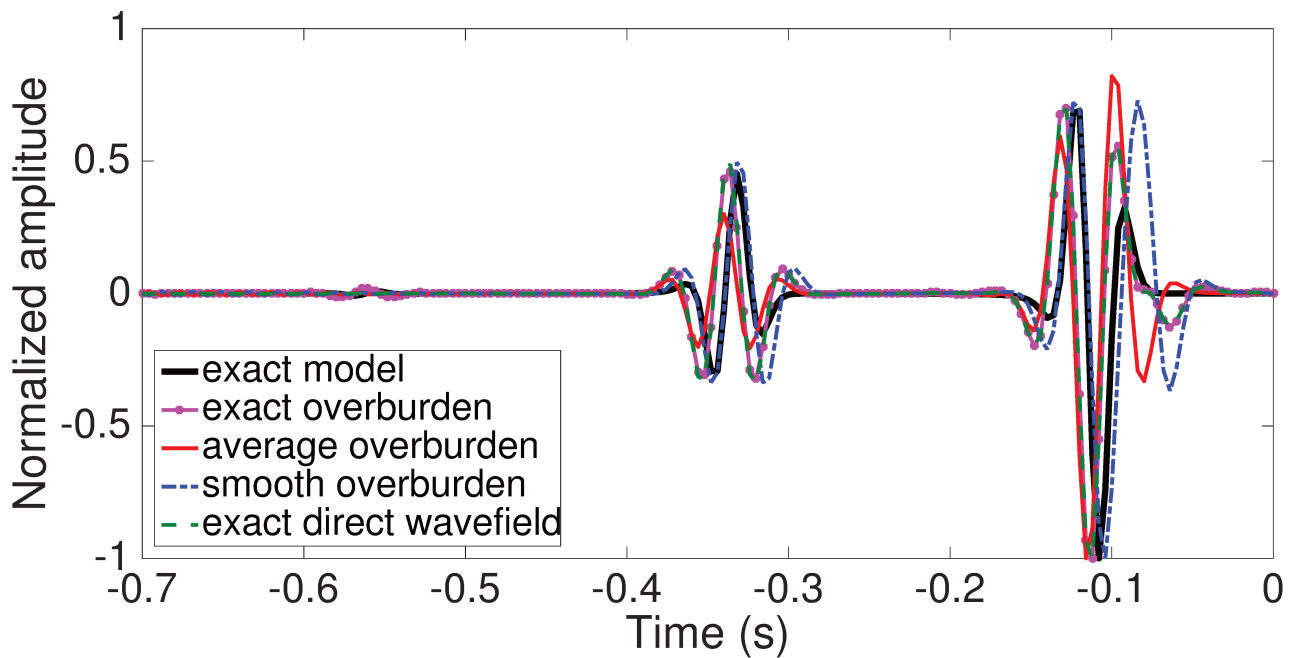


Figure 6.19: Trace at the zero offset corresponding to the anticausal part in Figures 6.18.

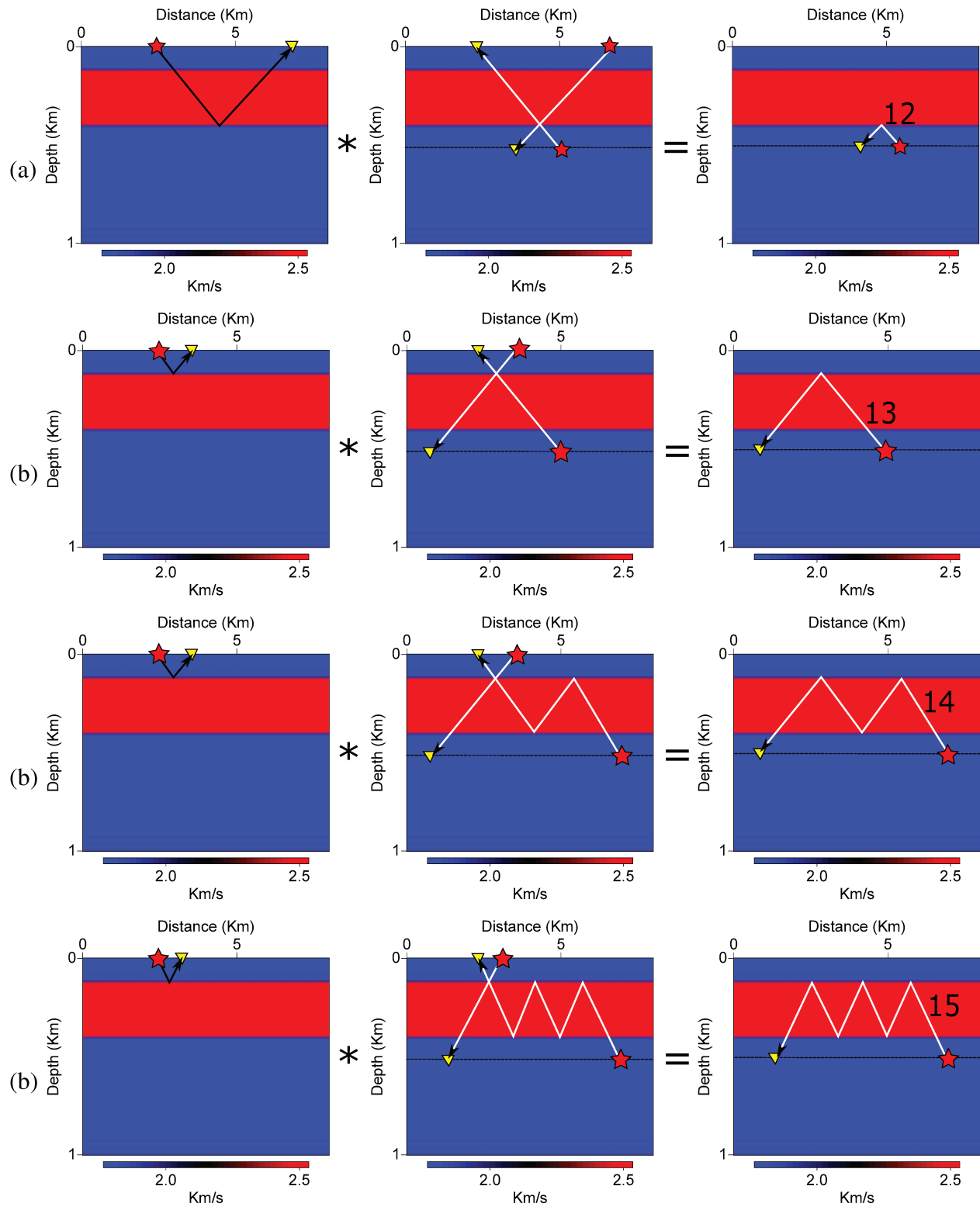


Figure 6.20: Ray paths for the surface events, crosscorrelation operator, and redatuming response, for events 12, 13, 14, and 15 of Figure (6.18). Ray paths contributing negatively to the traveltimes are shown in white.

6.2 Interferometric redatuming: Convolution-based method

As we mentioned in section (3.2), interferometry by convolution is an alternative to the classical correlation-based scheme and in many situations it is more convenient than the correlation methods (Wapenaar et al., 2010b). In this section we will validate the expressions (3.54) and (3.55) that also allow us to retrieve information of the wave propagation at the datum. As for the previous analysis in above section, we will make numerical experiments in the models of Figures (6.1) and (6.10) that consider homogeneous and inhomogeneous media, respectively, between the acquisition surface and the datum. In this numerical experiment, we will also see the principal limitations of the interferometric redatuming with convolution-based methods in an inhomogeneous medium. We note that many of the artefacts are coming from the overburden, just as we interpreted in the convolution-based interferometry in section (3.4), polluting the Green's functions results at the datum. To retrieve the responses in this section we use least-squares inversion methods to solve the equations (3.54) and (3.55) to do redatuming of receivers and sources, respectively.

Datum below a homogeneous layer

In this numerical example we used the horizontally-layer velocity model that we showed in Figure (6.1) with the same seismic array configuration explained in the model at the beginning of this chapter. In this section we will solve the equations (3.54) and (3.55), that represent ill-posed problems. We will solve these equations by least-squares inversion methods, which is necessary to stabilize them in order to obtain numerically stable results. Therefore, we opted for a simple regularization of the parameter ϵ as we showed in the section (5.3), and tested different values for the regularization parameter to study its influence on the inversion result.

Receiver redatuming

To start, we solved by least-squares inversion the equation (3.54) to retrieve the upward Green's function with source at the earth's surface and receivers at datum $\hat{G}_{-}^s(x', \omega; x^B)$. The goal of this experiment is to validate the behavior of least-squares inversion with stabilization to retrieve PSF^{-1} . To do this we will use directly the inverse operator deduced in Chapter (5), where from equation (3.54) we deduced the expression (5.9). For our tests to calculate the PSF^{-1} we used the following values for the stabilization parameter ϵ : (a) 1%, (b) 0.1%, (c) 0.01% and (d) 0.001%, with respect to the maximum absolute value of the PSF in equation (5.1). In Figure (6.21) we can see the responses for each value of ϵ . Events 1, 2 and 3 correspond to the primary reflections above the datum, as shown in Figure (6.1). We note that each event at the datum was positioned correctly (see Figure 6.21), com-

pared with the synthetic data modeled at the datum (Figure 6.6b).

We can see in Figure (6.21) increasing boundary effects in the retrieved Green's functions, just as we commented the Section (5.4). As explained previously, this kind of events occurs because the aperture of the seismic data is limited.

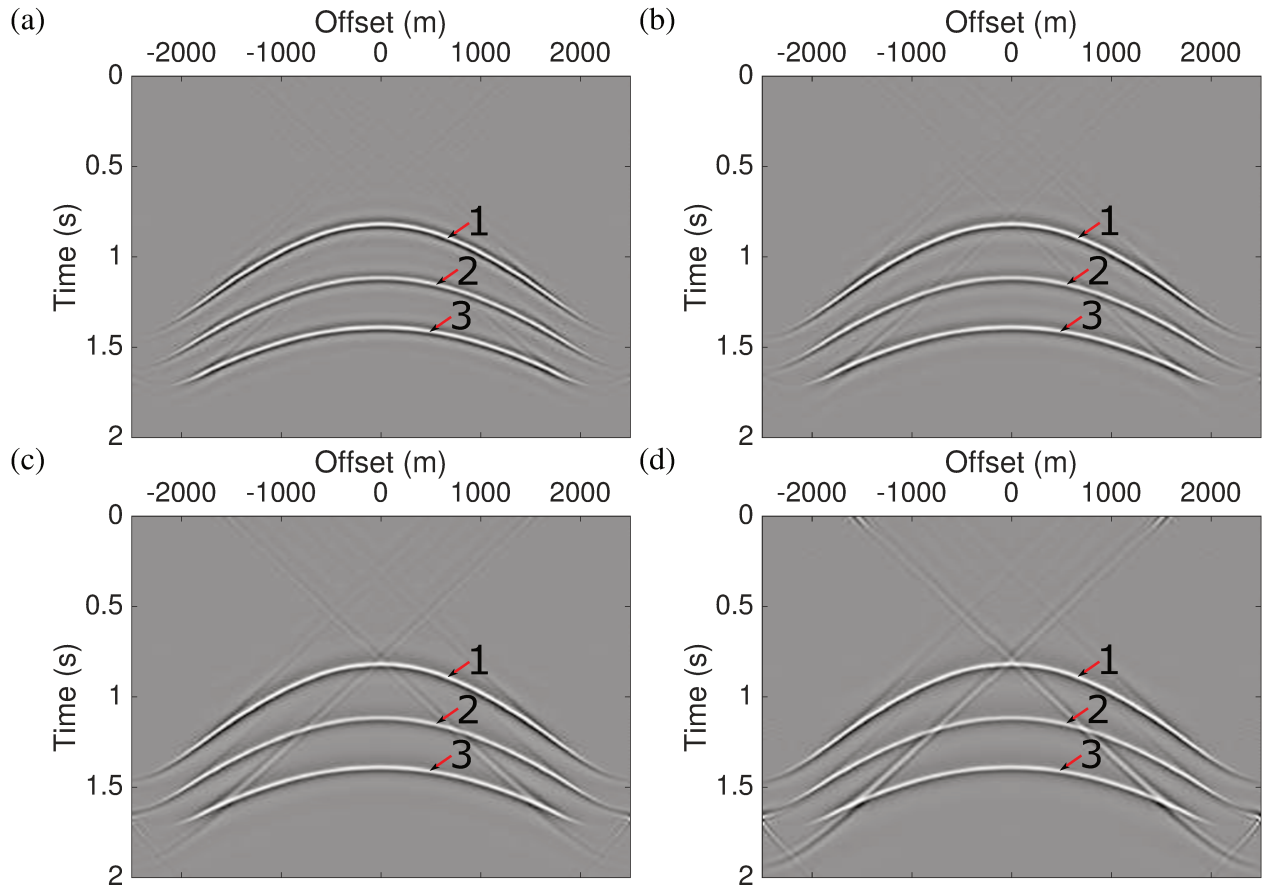


Figure 6.21: Upgoing Green's functions retrieved using the inverse operator in equation (5.9) with different values for the regularization parameter in the PSF^{-1} : (a) 1%, (b) 0.1%, (c) 0.01% and (d) 0.001% of the maximum absolute value of the PSF .

To verify if each event interpreted in Figure (6.21) is kinematically correct, we compare the central trace of each response with the exact receiver redatumed model in Figure (6.22). We note that in the zero-offset trace of the receiver-redatumed responses in Figure (6.21), the relative amplitudes have the correct proportions as compared to the corresponding data modeled at the datum in Figure (6.22). We see that the stabilization parameter with percentage 1% is the most stable, as compared to the smallest stabilization percentage 0.001% in Figure (6.22). This observation allows us to infer that the solution by inversion of this kind of problems is very sensitive to small variations.

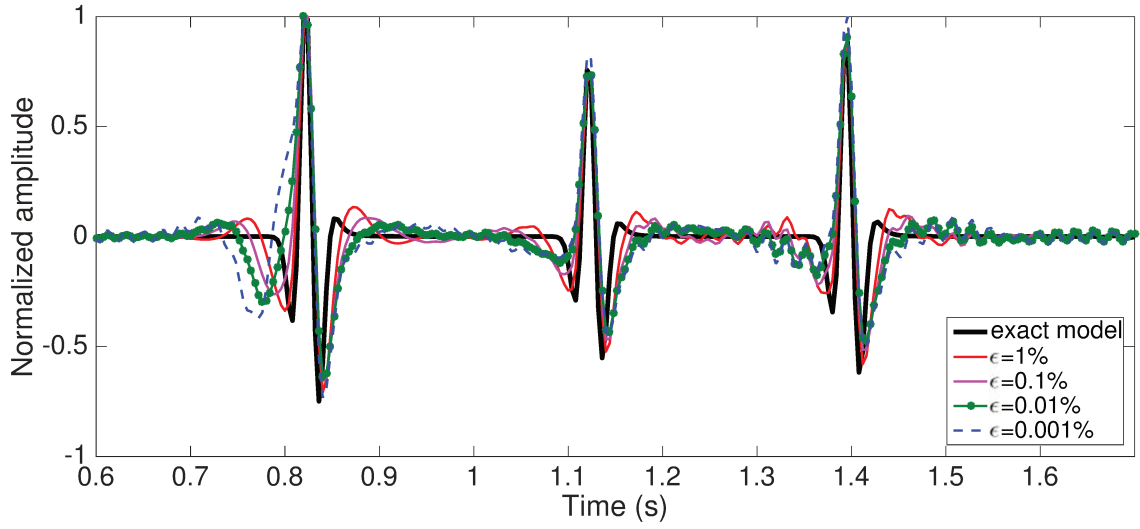


Figure 6.22: Central traces of the receiver redatuming responses at the datum.

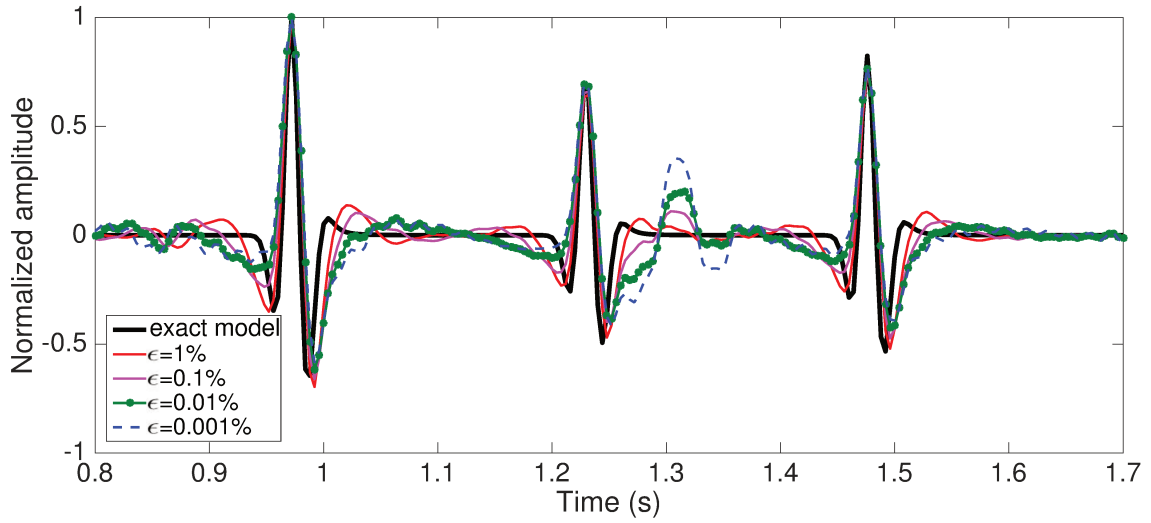


Figure 6.23: Comparison of the traces at 1000 m offset of the receiver redatuming responses at the datum.

Taking into account the inverse operator in the expression (5.9) and the events highlighted in the Figure (6.21), we can do an interpretation of the ray path propagation in Figure (6.24). As mentioned before, this is the most simple model to apply the interferometric convolution-based operator, because the *PSF* only contains one event in this response, because of the homogeneity of the overburden.

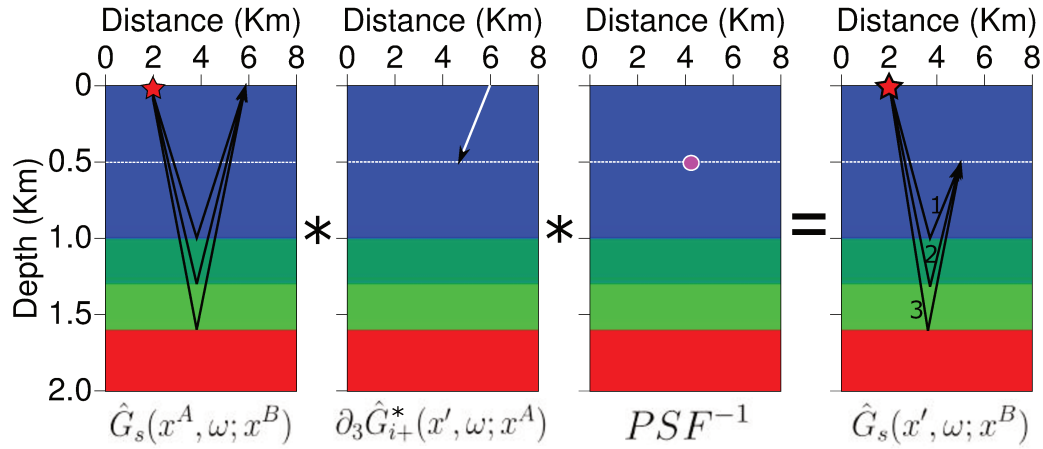


Figure 6.24: Sketch that describes the ray path in the inverse operator expression (5.9), where from the seismic data at the earth's surface, the model of the incident Green's function and the inverse of the PSF , the receivers can be repositioned at the datum.

Source redatuming

In this section, we will complete the redatuming. For that, we will use the data from the previous section as input data to reposition the sources at the datum. Using the inverse operator in equation (5.15) we can retrieve the complete Green's function at the datum considering a homogeneous overburden. Again, to retrieve the Green's functions, we did inversion of the PSF using four regularization percentages, measured from the maximum absolute value of the PSF . The different responses of the source redatuming with different values of the regularization percentages of ϵ are showed in Figure (6.25). As we mentioned in the previous step, the consequence of using the inverse operators is that it introduces artefacts in the Green's functions retrieved responses, just like we shown in the first step in Figure (6.21), most prominently the boundary effects.

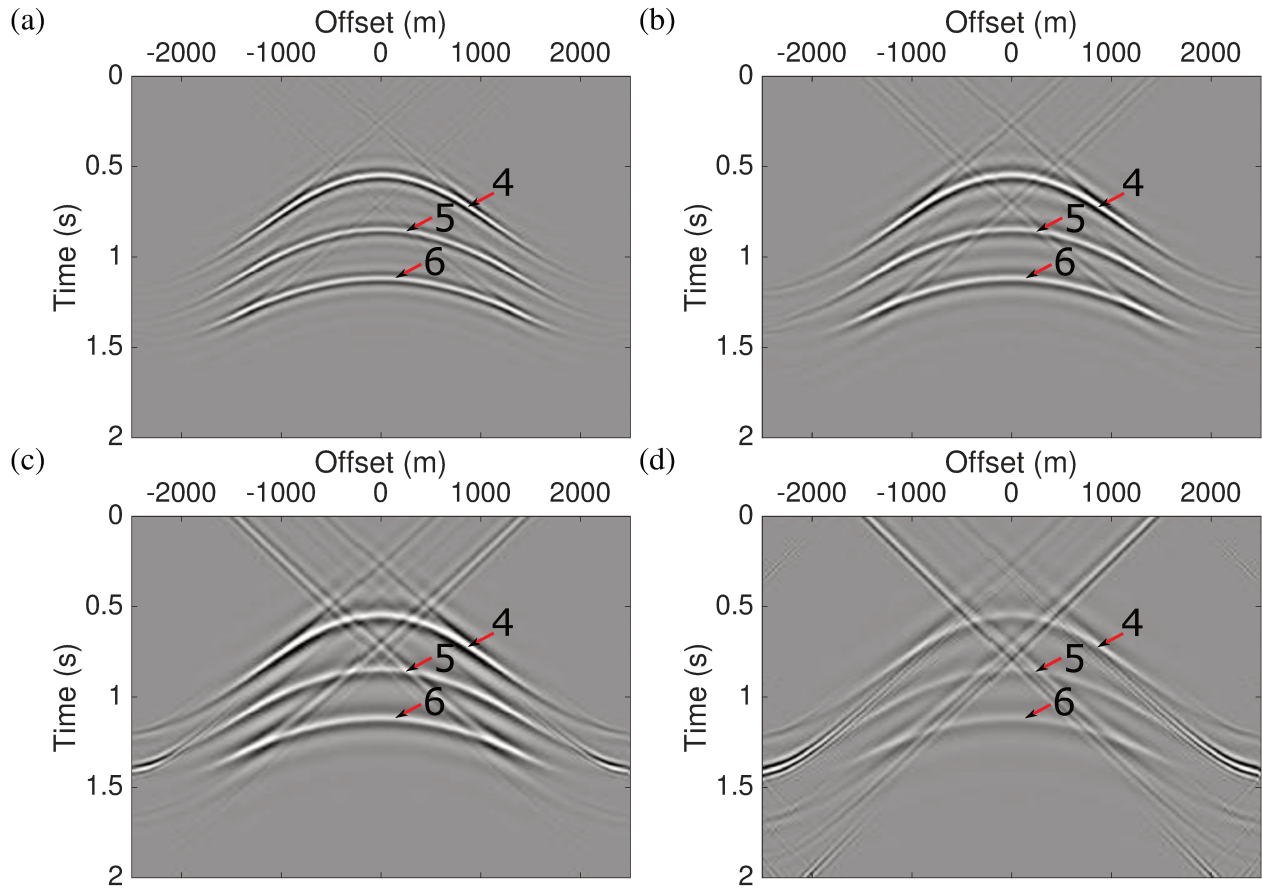


Figure 6.25: Central shot of the Green's functions with source and receivers at datum using the inverse operator in equation (5.13), as obtained using four different regularization percentages: (a) 1%, (b) 0.1%, (c) 0.01% and (d) 0.001% of the maximum absolute value of the PSF .

For more details we show the central trace of each responses in Figure (6.25), where we note that the three principal events are kinematically well positioned as compared to the modeled data in Figure (6.26). Regarding the different stabilization factors we note that the responses become more unstable with decreasing ϵ . The valleys strong artifact at 0.25 s is the boundary effect. It is particularly strong in the central trace because the effects of both boundaries enhance each other because of the symmetrical geometry. The same properties at the central trace are preserved along the offset, as we can see in Figure 6.27 that show the comparison of traces at 1000 m offset of the redatuming responses in Figure 6.25.

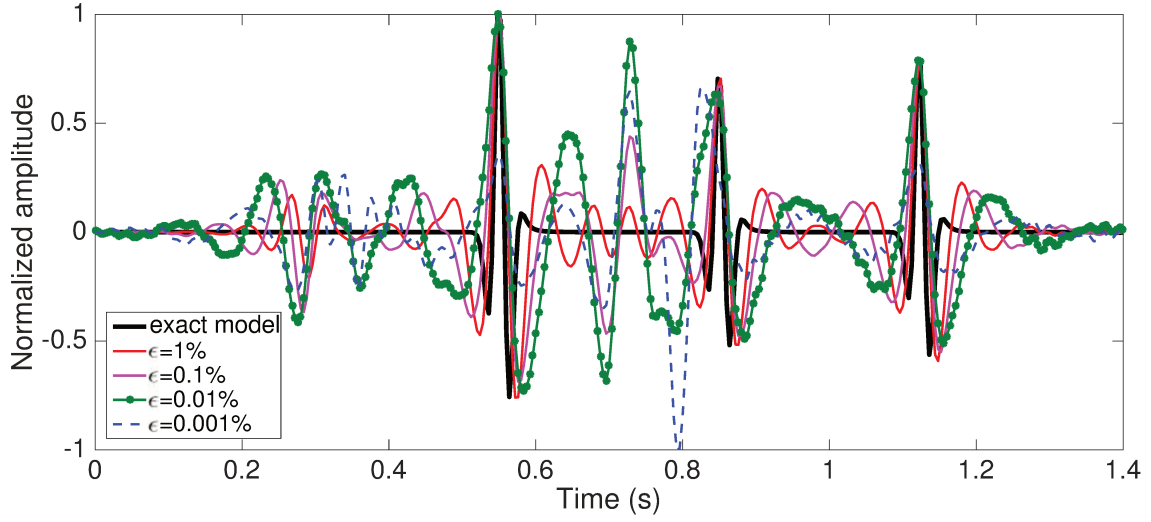


Figure 6.26: Central traces of the redatuming responses in Figure (6.25) compares with the central trace of the exact model.

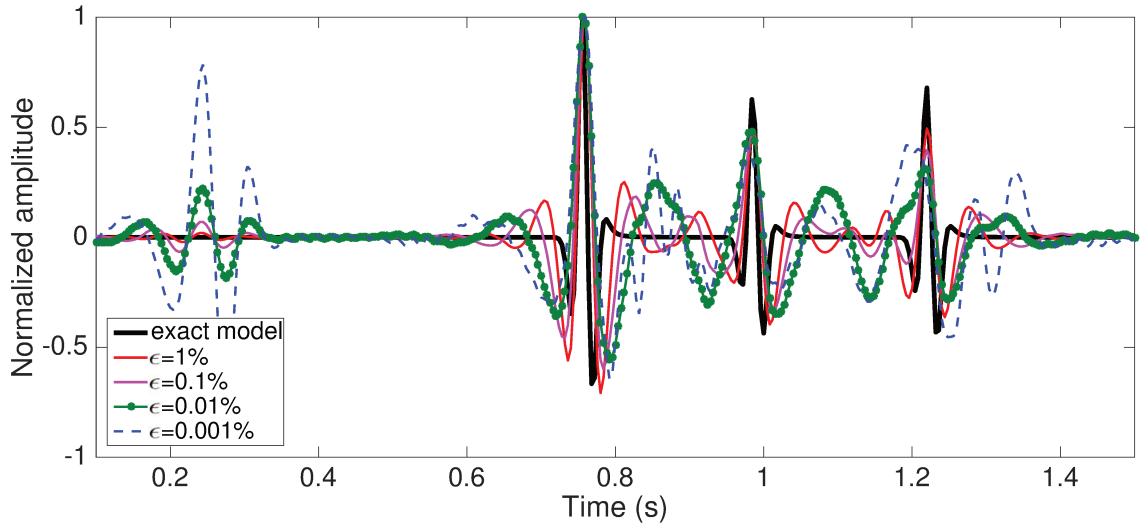


Figure 6.27: Comparison of the traces at 1000 m offset of the redatuming responses in Figure (6.25) compares with the central trace of the exact model.

Figure (6.28) schematically explains the inverse operator in equation (5.15) to retrieve the redatumed Green's functions. We note that the medium between the earth's surface and the datum is homogeneous. Then, the main limitation in this method is the aperture in the seismic acquisition and in the stabilization, regarding that here we solve an ill-posed problem, which is sensitive to small variations of the stabilization parameter ϵ .

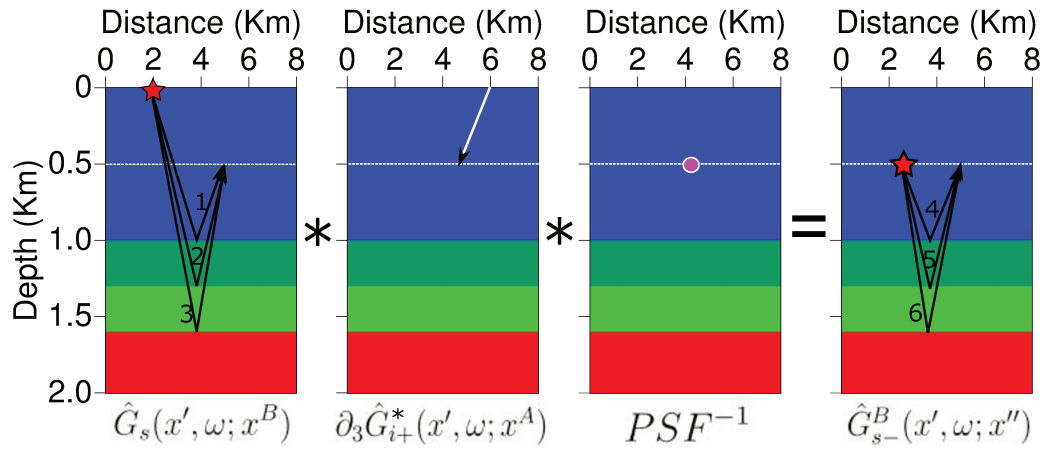


Figure 6.28: Sketch that explains the process to retrieve the total Green's function at datum using the inverse operator deduced in equation (5.15).

Datum below a high-velocity layer

In this numerical example, we will analyze the main limitations of the interferometric redatuming by convolution-based method when it accounts inhomogeneities in the media above the datum. To do that we used the models shown in Figures (6.10) and (6.11a). Similar to the numerical example of interferometric redatuming by correlation-based with inhomogeneous overburden, we will interpret all of the events that are retrieved using the appropriate inverse operators which solve the equations (3.54) and (3.55), that allow us to retrieve the upward and the complete redatuming of the Green's functions, respectively. To retrieve the total Green's functions at the datum with convolution-based methods, we only need as input the vertical derivative of the transmitted wavefield from the earth's surface at the datum, together with the complete seismic data at surface. It is possible to retrieve the Green's functions at the datum by convolution methods in two steps: (a) receivers repositioning using equation (5.9) and (b) source repositioning using as input the Green's function retrieved in step (a) in equation (5.15). The two steps consider the inverse operators that solve equations (3.54) and (3.55).

Receiver redatuming

In this section, we will interpret the upward Green's functions with sources at the earth's surface and receivers at the datum. We will analyze the causal and anticausal events in the responses retrieved using the inverse operator showed in equation (5.9). In the Figure (6.29) we shown the upward Green's function retrieved using the expression (5.9). Here, it was necessary to invert the PSF calculated with the vertical derivatives of the transmission wavefields, as shown in Chapter (5). In this inversion we used again four different percentages for the regularization parameter ϵ , with respect

to the maximum absolute value of the PSF . These parameters were: (a) 1%, (b) 0.1%, (c) 0.01% and (d) 0.001%. In Figure (6.29) we shown the causal result of having used the inverse operator (5.9) with the PSF^{-1} retrieved with the four percentages of ϵ . In this result we note that events 1, 2 and 3 are kinematically correct. On the other hand, we have the events that are coming from the overburden reflections, that we labeled as 4, 5, 6, 7 and 8. In Figure (6.29) we also note that when decreasing ϵ , there events coming from the overburden tend to vanish. The unique event that prevails is the boundary effect, which is coming from the anticausal events. Figures (6.29c-d) have attenuated the primary reflections too much, together with events 4, 5, 6 and 8. Also we note that in Figures (6.29c-d) instability begins to appear due to the sensitive of this inversion method, whose principal limitation is the problem that we try to solve here being ill-posed. According with van der Neut and Wapenaar (2015) the instability effects that come from PSF^{-1} can be attenuated using FK filters, but for our case this is not the objective, however if we consider the FK filters, Figures (6.29c-d) could be improved. All of the events interpreted in Figure (6.29) are explained in detail in Figure (6.31), where we showed each ray path that explains the corresponding event in the seismic response in Figure (6.29).

Continuing our analysis, in Figure (6.30) we have the anticausal events of the upward Green's function retrieved with equation (5.9). Each response in Figure (6.30) corresponds to the anticausal part of each response in Figure (6.29), respectively. We can see that the anticausal part only contains event 9, the ray path of which is interpreted in Figure (6.31). We also see that the anticausal response corresponds to each regularization parameter ϵ , where noted that the boundary effect is too strong, however in all responses is possible to recognize the presence of event 9. Some instabilities appear especially in the Figures (6.30c-d). These artefacts are coming from the ill-posedness which is very sensitive to small variations to the regularization parameter. As mentioned before, in Figure (6.31) we interpret each event in the causal and anticausal responses using the inverse operator in equation (5.9). We noted that all of the events retrieved are physical. Figures (6.31a-b) show the ray paths of the primary reflections of the layers below the datum and their delay because of reverberation in the overburden layer, respectively. Figures (6.31c-d) show the ray paths of events in the overburden, where only event 9 is anticausal. This interpretations are very important to take into account in the next step of the redatuming process, because we will understand the real importance of using the interferometry by convolution-based. Its importance lies in the many artefacts and nonphysical events that are too common in methods with correlation-based. Here these artefacts are attenuated by the effect of the PSF^{-1} , as we will show later.

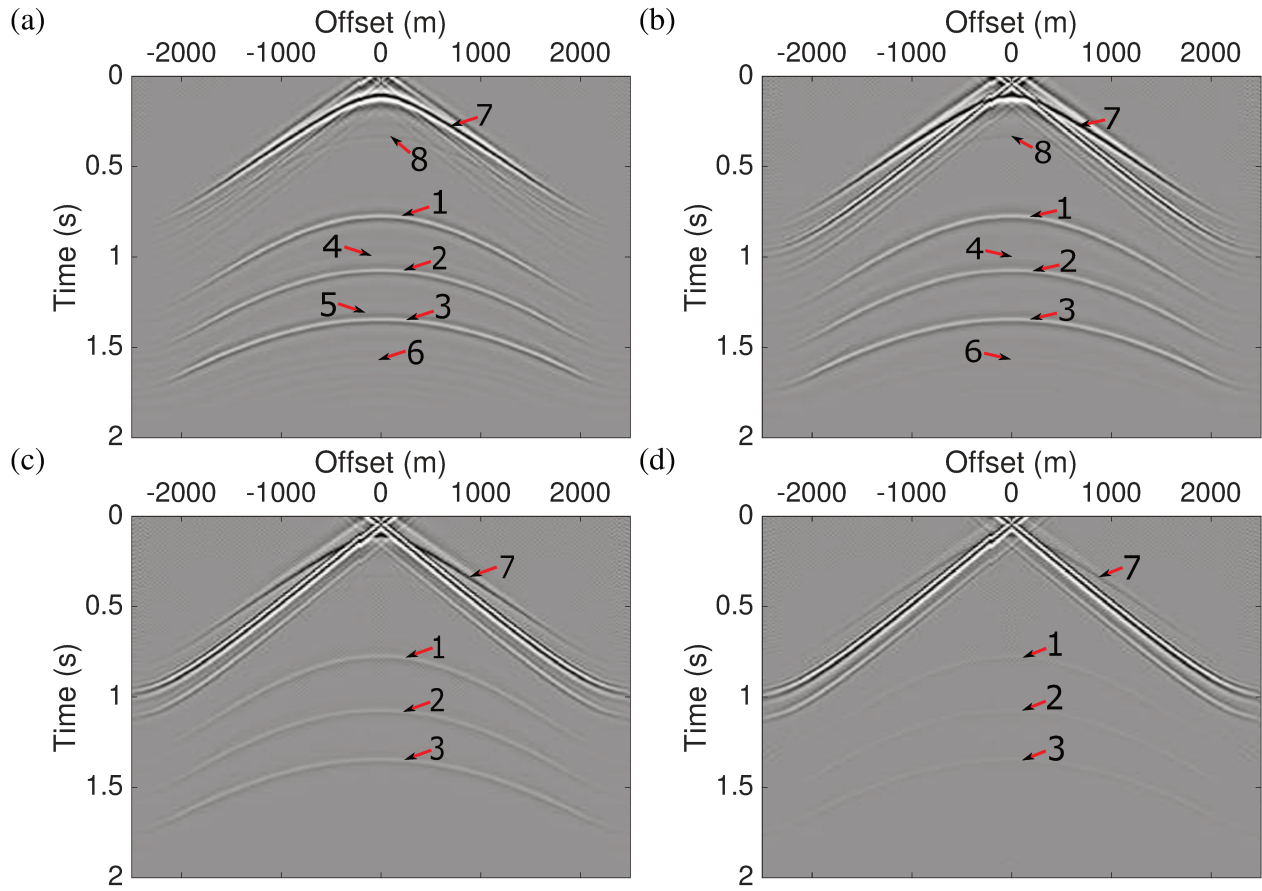


Figure 6.29: Upward causal responses obtained by the PSF inversion according to equation (5.9) with different values of ϵ : (a) 1%, (b) 0.1%, (c) 0.01% and (d) 0.001%.

Source redatuming

In this section, we will analyze the source redatuming, this step allows us to complete the reposition process of the seismic array at the datum. In Figure (6.32) we showed the results of the complete redatuming, where we used as input data the results in Figures (6.29) and (6.30), and with the vertical derivative of the transmitted wavefield from the earth's surface at the datum. This input data was used in equation (5.15), with the PSF^{-1} , that was retrieved by least-squares, similar to receiver redatuming step. We used four regularization percentages respect to the maximum absolute value of the PSF , which were: (a) 1%, (b) 0.1%, (c) 0.01% and (d) 0.001%. At this point, is important to regard the causal and anticausal redatuming results obtained with the correlation-base methods in Figures (6.12a) and (6.18). This, is because we will compare the results obtained with the interferometric redatuming by convolution-base with the correlation-base. The first point to compare between the two approaches is the non physical events. We can see in Figure (6.12a) that we interpreted many of the non physical events, that come from the reverberations in the overburden layer of the complete

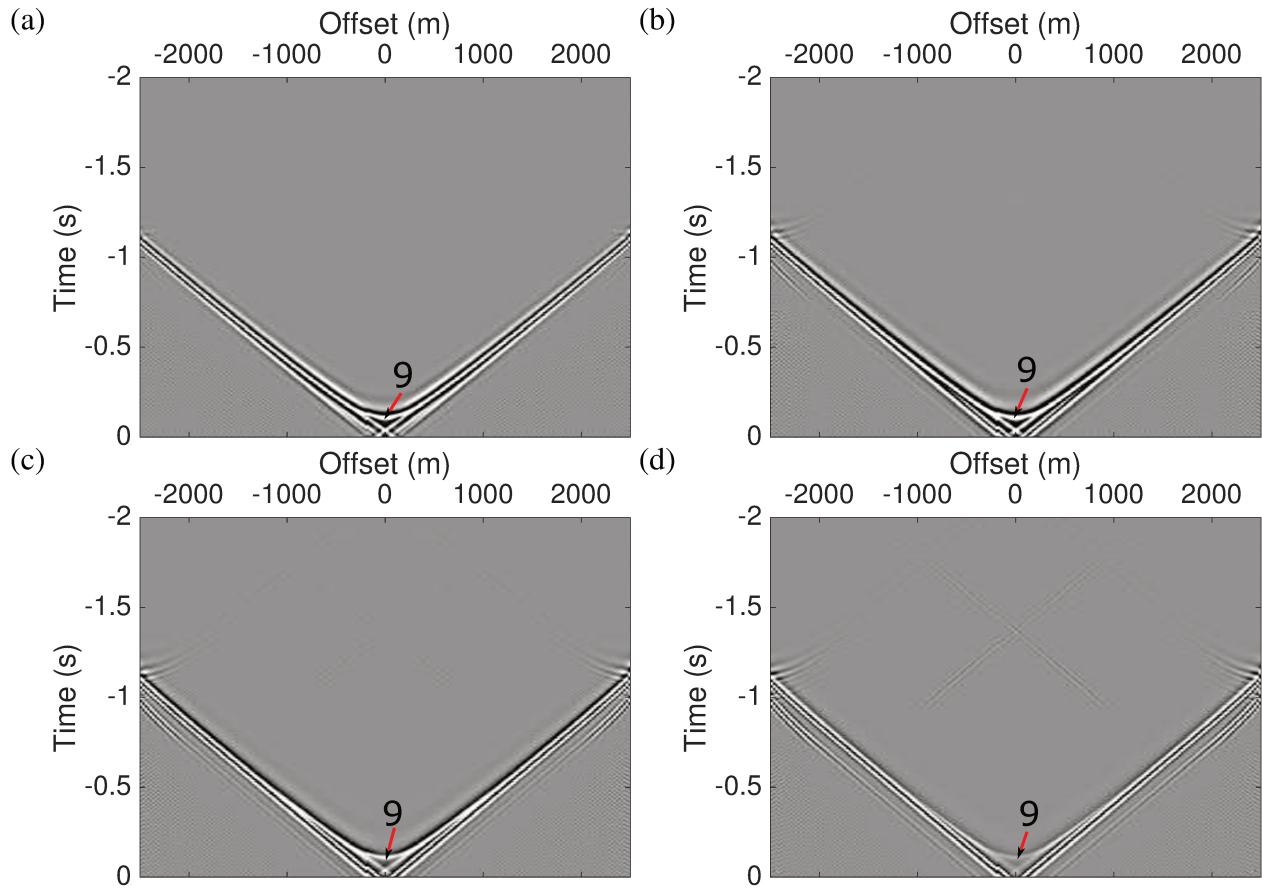


Figure 6.30: Upward anticausal responses obtained by the PSF inversion according to equation (5.9) with different values of ϵ : (a) 1%, (b) 0.1%, (c) 0.01% and (d) 0.001%.

seismic data at the earth's surface and the incident wavefield from the earth's surface at the datum. But, in Figure (6.32) all events are physical, which is the main and great difference between the interferometric methods with correlation and convolution based in the practical aspect.

If we compare the two expressions to obtain the redatuming results from the correlation (equation 3.43) and the convolution (equation 5.15) base, we noted that the main difference between the two expressions is the presence of the term PSF^{-1} in the convolution-based equation. This allows us to assign to the PSF^{-1} the attenuation of the non physical events in the convolution method, making it most convenient for this case than the correlation-base methods. Following with the interpretation of the redatuming results of the convolution-base method in Figure (6.32), we noted that at the top of these appears a lineal noise that is coming from the boundary artefacts of the anticausal responses (Figure 6.33). Events 1, 2 and 3 in Figure (6.32) correspond to the primary reflections, here we noted that when decrease the stabilization parameter ϵ the process to retrieve its responses is more unstable, and this events tend to vanish because of the boundary artefacts and noise that come from the

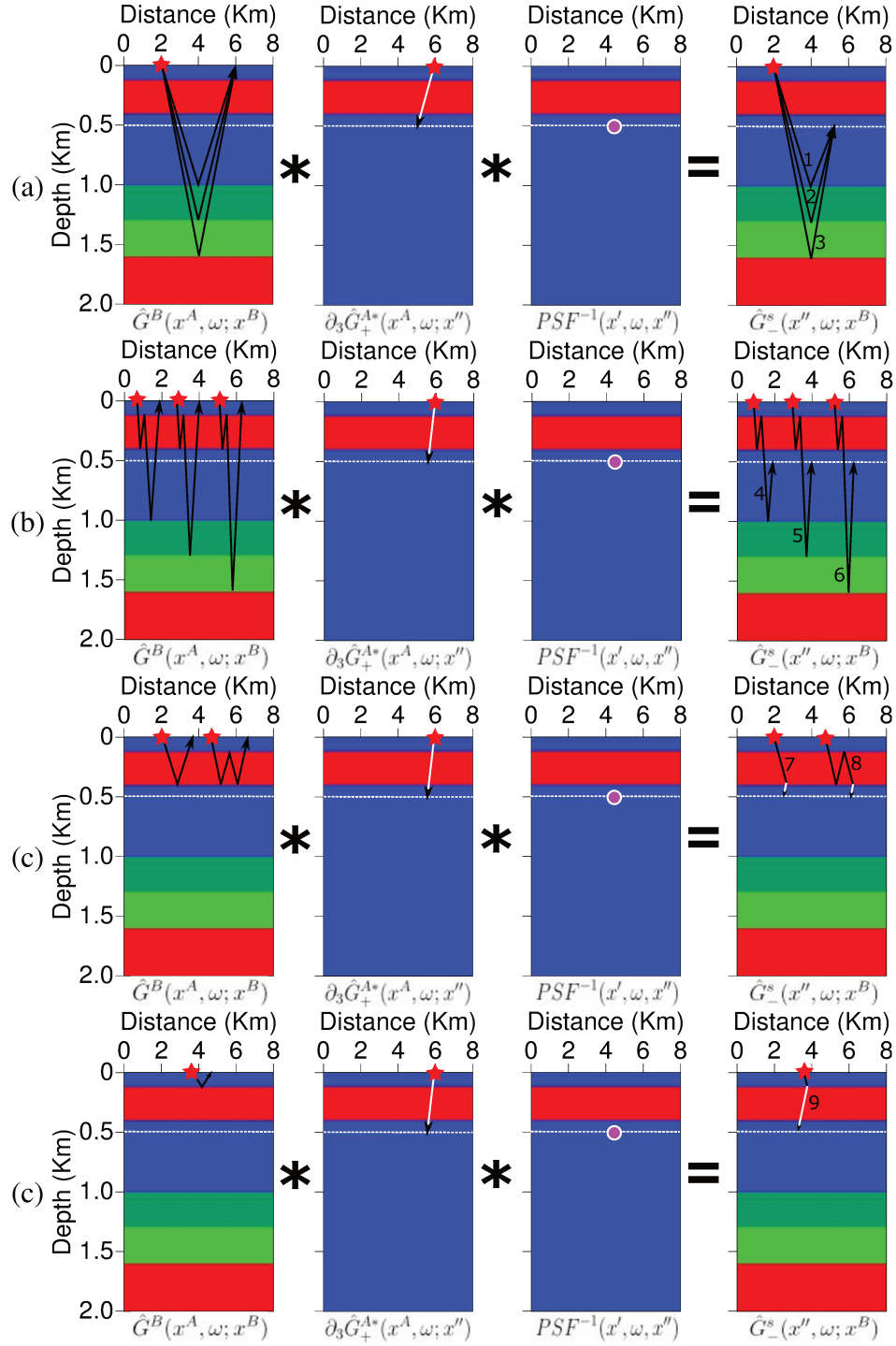


Figure 6.31: Sketch of the equation (5.9) that explains the process to retrieve the (a) primary reflections and (b-c) events associated to reverberations in the overburden.

instability of the inversion method. The event 8 is very especial, because it is composed by positive and negative signals, just as was interpreted in Figure (6.34), where this event represents a physical

trajectory in the layer above the datum.

Also we noted that the convolution-base results in Figure (6.32) become more unstable when decrease the percentage of the regularization parameter ϵ . Principally in $\epsilon = 0.01\%$ and $\epsilon = 0.001\%$, the primary reflections are too attenuated because of the influence of the boundary effects that come from the anticausal part (Figures 6.32c-d).

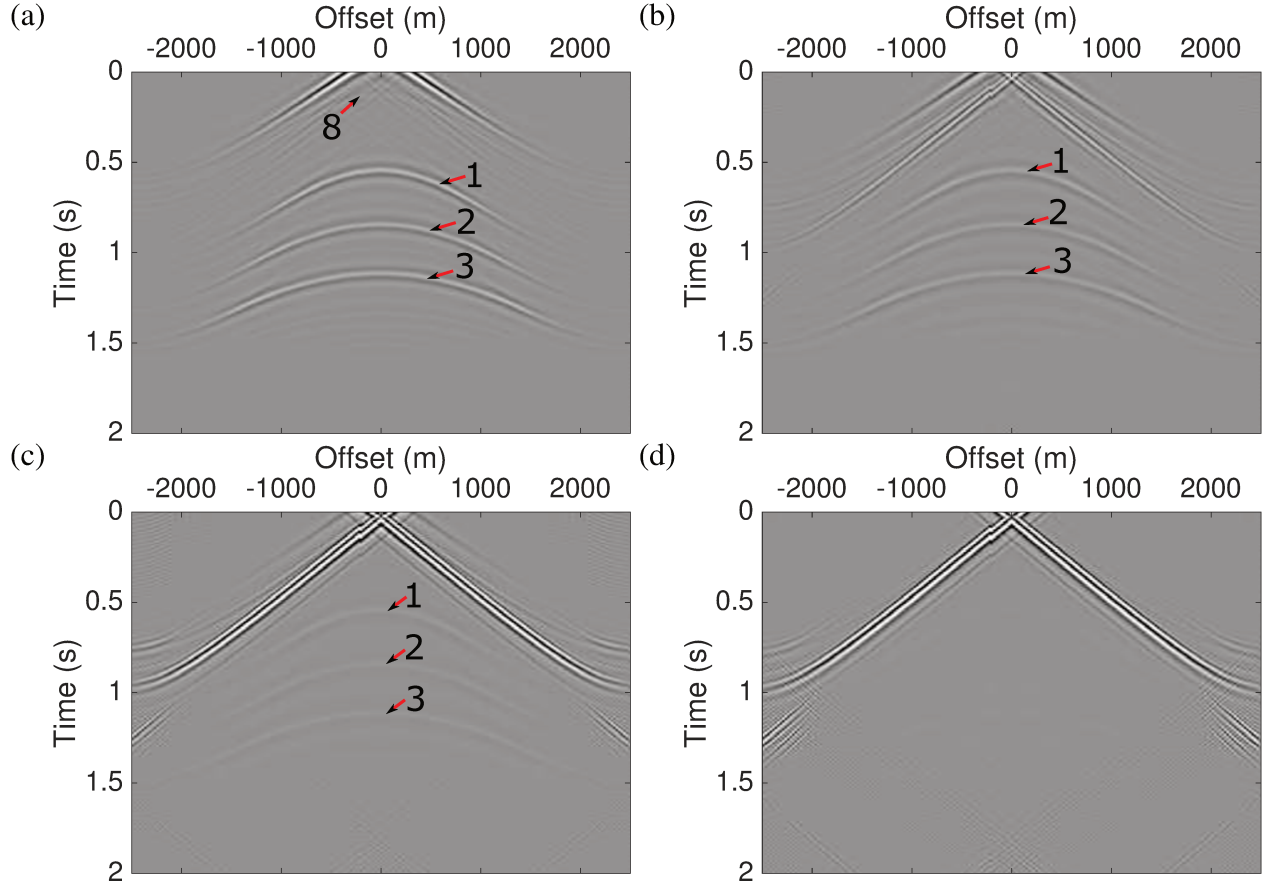


Figure 6.32: Causal redatuming responses obtained by the PSF inversion according to equation (5.9) with different values of ϵ : (a) 1%, (b) 0.1%, (c) 0.01% and (d) 0.001%.

On the other hand, in the Figure (6.33) we have the anticausal response corresponding to the classical approach of the interferometric redatuming by convolution-based. Here we noted that the events 7 and 9 comes from the primary responses that correspond to the illumination of the overburden interfaces from below. Similar to the anticausal response in the correlation-based method all of the events are physical.

The main difference between the anticausal responses of correlation and convolution methods

is the presence of internal multiples in the responses. Figure (6.18a) is the anticausal redatuming response by correlation-base with exact overburden, where appears first and second-order multiples. While in Figure (6.33) we showed the anticausal redatuming response by convolution-base which has the multiples too attenuated, and only primary reflections appear in these responses, which correspond to the events 7 and 9, interpreted in Figure (6.34).

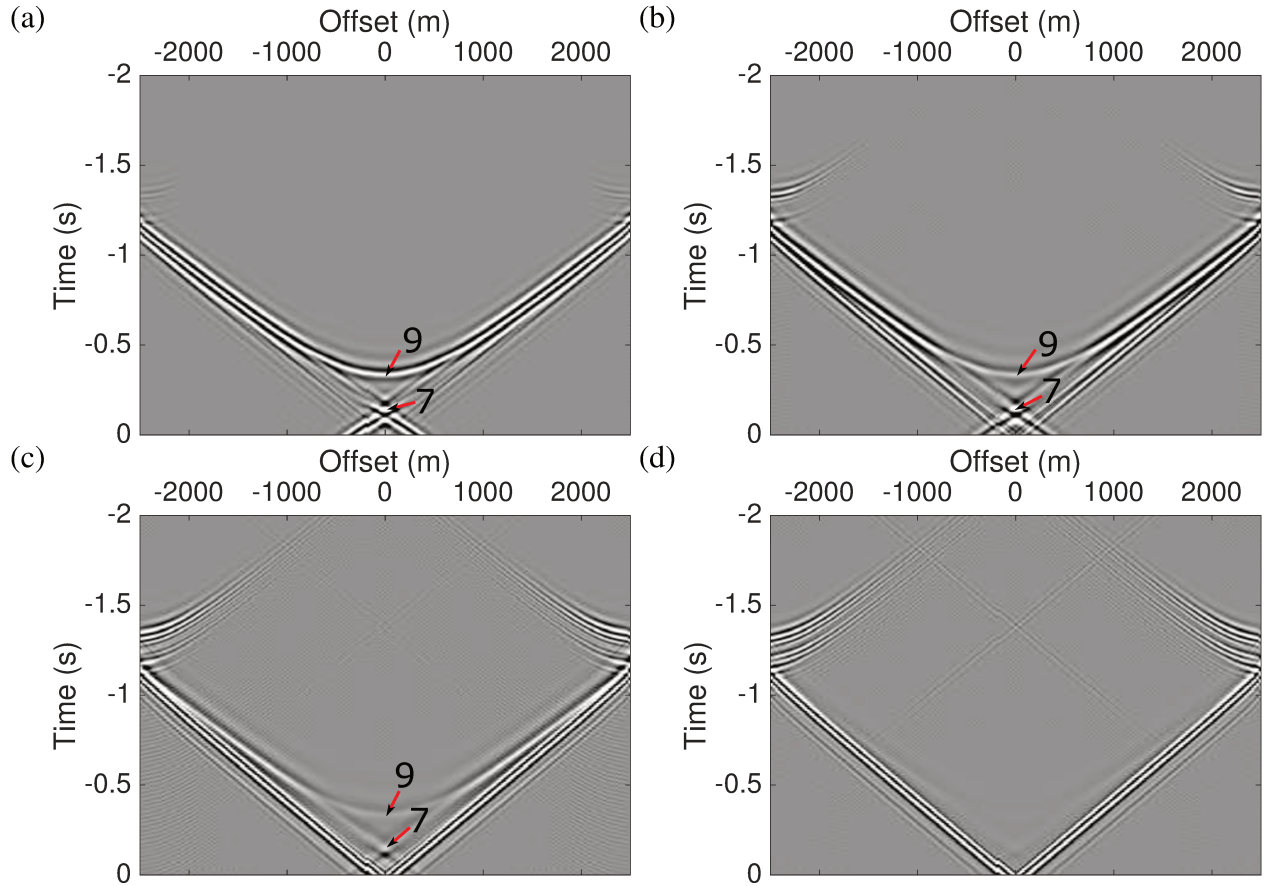


Figure 6.33: Anticausal redatuming responses obtained by the PSF inversion according to equation (5.9) with different values of ϵ : (a) 1%, (b) 0.1%, (c) 0.01% and (d) 0.001%.

Finally in Figure (6.34) we have the interpretation of the highlighted events presented in Figures (6.32) and (6.33). Where we noted that all of the events are physical. Also, all responses are coming from three croscorelations that correspond to the redatuming of the receivers at datum, the vertical derivative of the transmitted wavefield and the inverse of the PSF , just as we deduced in the equation (5.15). An interesting thing is that the vertical derivative of the transmitted wavefield from the earth's surface until the datum in all the events is direct, without internal multiples. We did such interpretation because the responses in Figures (6.32) and (6.33) have not artefacts or events that include this time of propagation. This observation help us to explain the artefact attenuation by the presence of the

PSF^{-1} . This because is the internal multiples of the transmitted wavefield could generate artefacts or non physical events, as we explained in the correlation-based interferometric redatuming, but the PSF^{-1} have the property of attenuate this kind of artefacts.

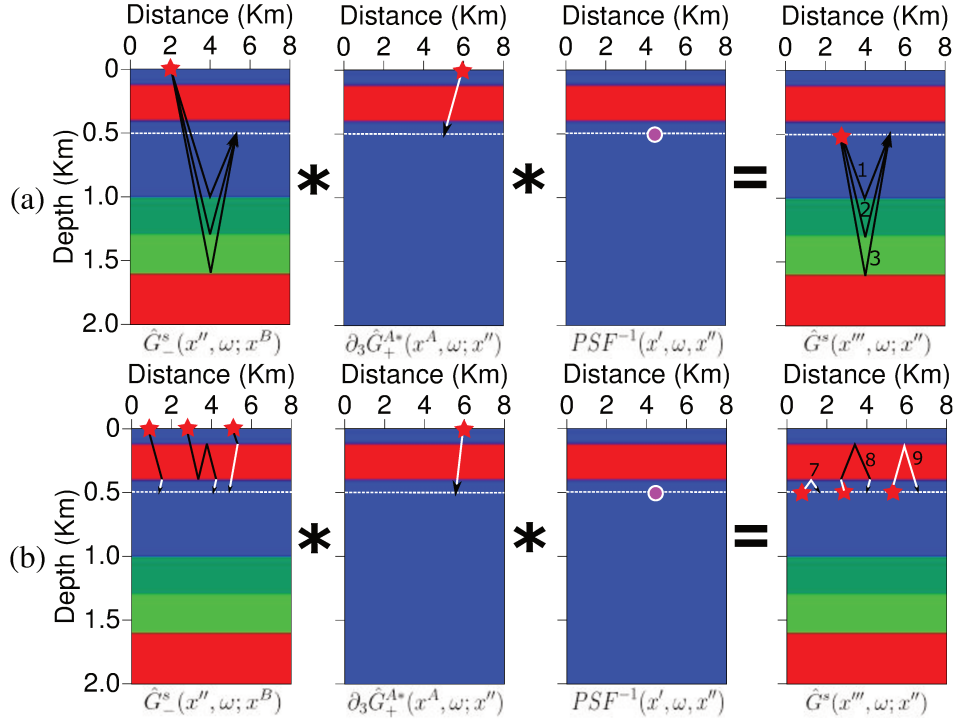


Figure 6.34: Sketch of the equation (5.15) that explains the process to retrieve the (a) primary reflections and (b) events associated to reverberations in the overburden with sources and receivers at datum

6.3 Interferometric redatuming by focusing

In this numerical example, we will demonstrate and interpret the main result in this thesis. We will use the model in Figure (6.10) in which we will make reposition of the sources and receivers at the datum at 500m in depth. In the first place, we separated the redatuming process in three steps, in three steps was used the deductions in chapter (5), the steps are: (1) Retrieve the down-ward Green's function using the inverse operator in the equation (5.32), (2) Retrieve the up-ward Green's function using the inverse operator in the equation (5.22) and (3) complete the redatuming of the seismic array using both previous results in the expression (5.41).

For comparison, we simulated the full wavefield (Figure 6.35a) with sources at the surface and receivers at the datum in 500 m of depth (Figures 6.35b-c). The visible events in the seismic section

of the Figure (6.35a) are labeled with numbers in order to identify and interpret them. To facilitate the interpretation, we used green arrows for downgoing events and red arrows for upgoing events. This will also help us to compare the respective events with the inverted up- and downgoing wavefields showed below.

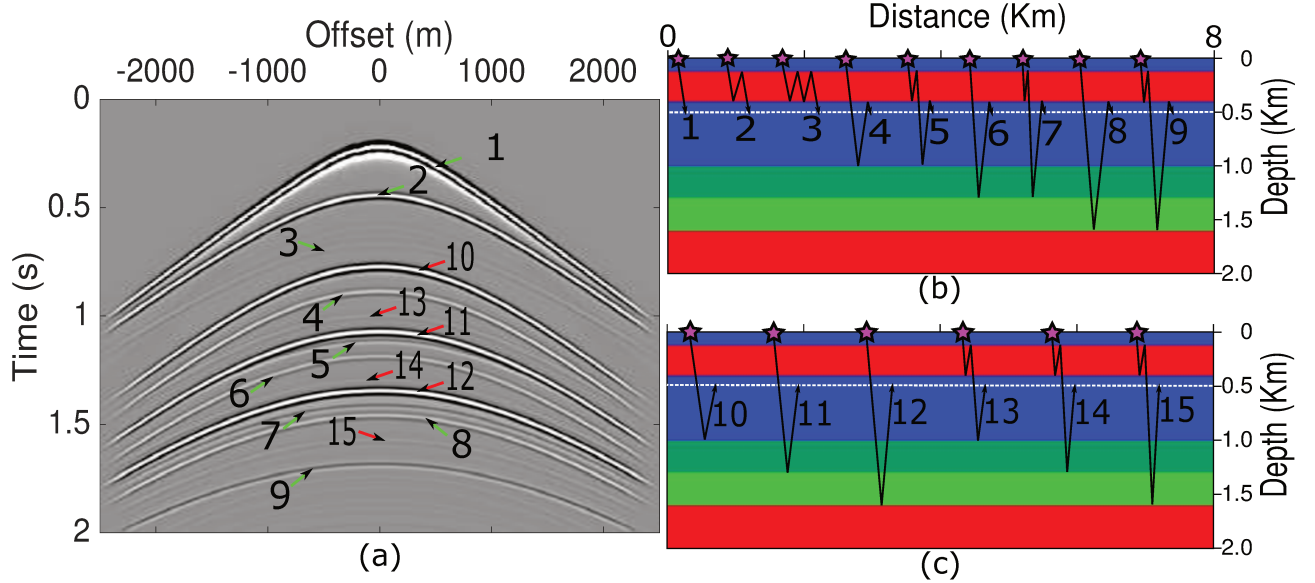


Figure 6.35: (a) Full synthetic seismic wavefield with its up- and downgoing constituents labeled, obtained using a source array at the surface and receivers at the datum at 500 m in depth in the horizontally layer, where was recorded the (b) downward and (c) upward wavefield constituents.

Downward wavefield constituent by focusing

As next step, we retrieved the downgoing constituents of the Green's function $\hat{G}_+^B(x', \omega; x^B)$ at the datum in 500 m at depth with the inverse operator in equation (5.32). For this purpose, we modeled the vertical derivative of the transmitted wavefield $\partial_3 \hat{G}_+^A(x', \omega; x^A)$, the vertical derivative of the truncated wavefield $\partial_3 \hat{G}_-^A(x, \omega; x^A)$ in the reference model without inhomogeneity below the datum and the inverse of the *PSF*, that we retrieve by least-squares inversion. As we mentioned in section (6.2), this inversion problem is ill-posed. Therefore, the least-squares inversion needs to be stabilized. For this purpose we will use four regularization percentages to stabilize the inversion method, these values of ϵ are: (a) 1%, (b) 0.1%, (c) 0.01% and (d) 0.001%, in order is to study its influence on the inversion result.

Figure (6.36) shows the inverted vertical derivative of the Green's function $\partial_3 \hat{G}_+^B(x', \omega; x^B)$ at the datum in 500 m at depth for the four values of the regularization parameter. In all four sections, the kinematic properties and the relative amplitudes correspond to the downward propagating events in

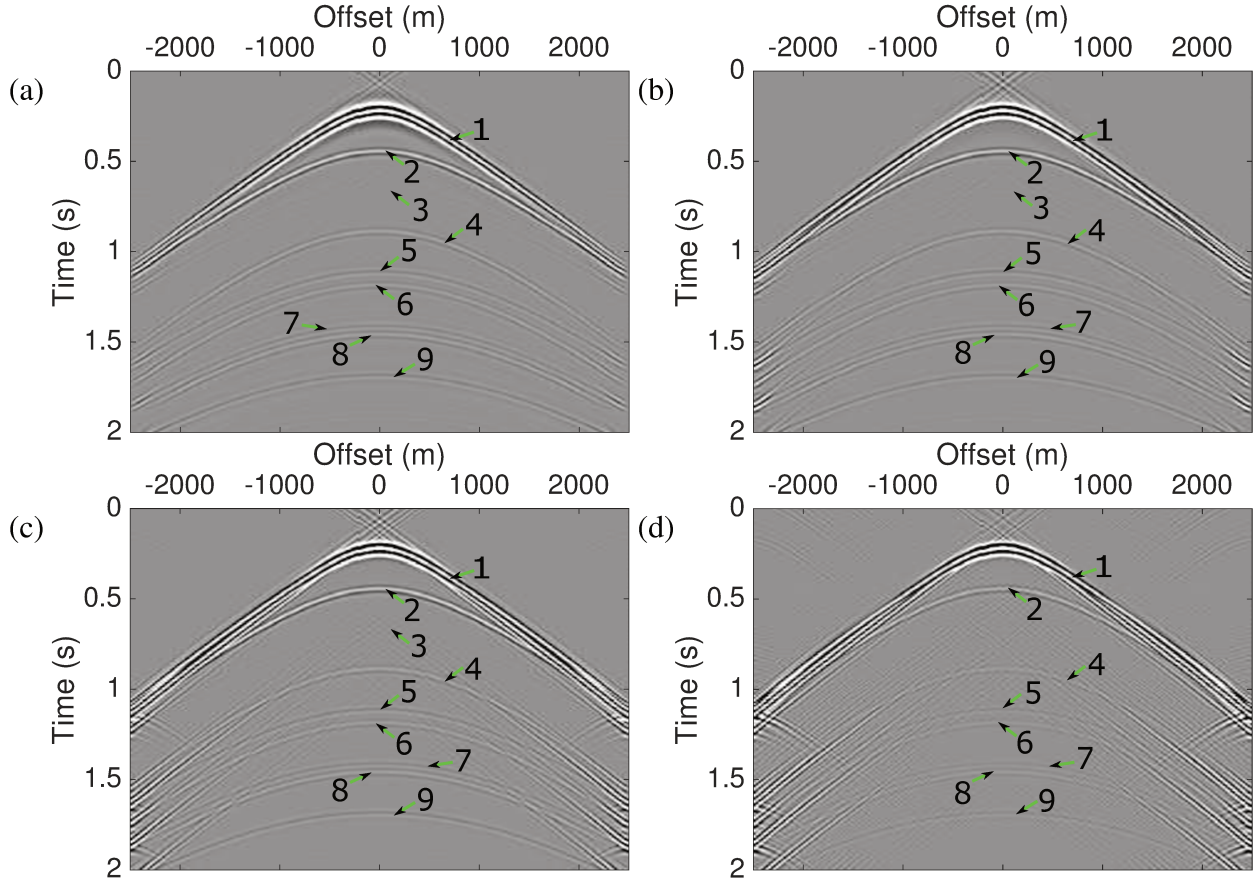


Figure 6.36: Down-ward Green's function retrieved by inversion using equation (5.32), where we test five different values to ϵ , where: (a) 1%, (b) 0.1%, (c) 0.01% and (d) 0.001%. The percentage above is with reference to the *PSF* maximum value

the Figure (6.35a). For more quantitative evaluation of the result, Figures (6.37) and (6.38) shows the central traces (zero-offset) and the traces at 500 m offset of the four downward wavefields of Figures (6.36), retrieved by differently regularized inversions. Moreover, the black line in Figure (6.37) is the result from synthetic modeling. We noticed again that the latter wavefield includes both up- and downward propagating events. For better visibility, Figure (6.37a) shows the first 0.75 s and Figure (6.37b) shows the part between 0.75 s and 1.9 s on a scale twenty times smaller. At this scale, numerical artefacts become visible. For the weakest regularization ($\epsilon = 0.001\%$), their amplitude is comparable to that of the smallest events. Then, a value of $\epsilon = 0.01\%$ is already sufficient to reduce them to an acceptable level.

Comparing the modeled trace with the inverted ones, we noticed that events 1, 2, 4, 5, 6, 7, 8 and 9 match nicely. On the other hand, events 10, 11 and 12 are only present in the modeled result, but they do not present a counterpart in the inverted traces. The reason is that events 10, 11 and 12

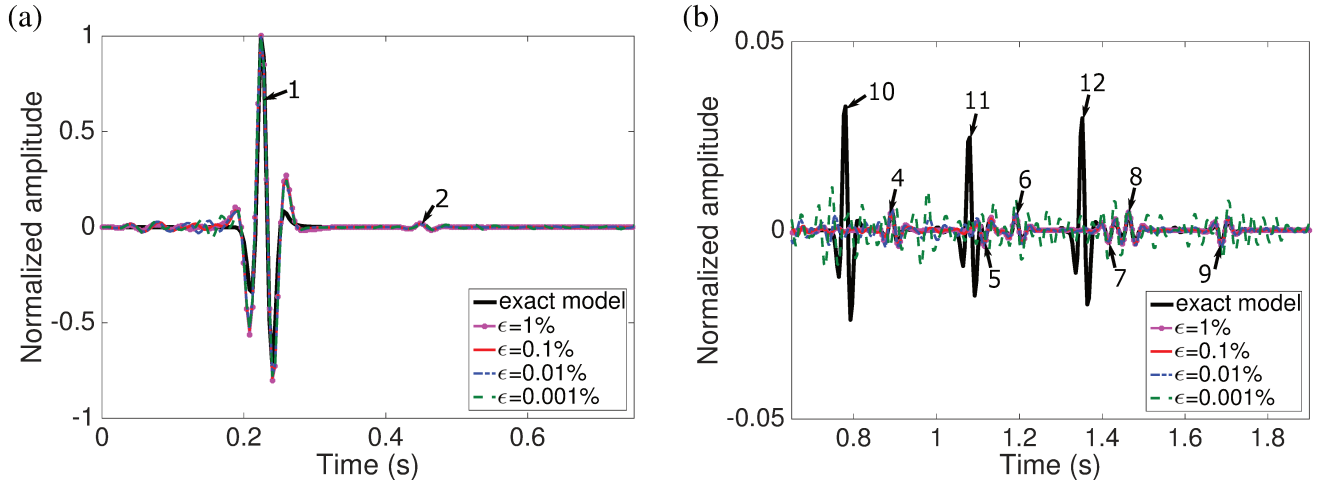


Figure 6.37: Central traces of the downgoing Green's functions sections in Figure (6.36) (coloured lines) compared to the wavefield simulated with sources at the surface and receivers at the datum (black line). (a) First part of the traces. (b) Later portion at a different scale.

belong to the upward propagating Green's function. Therefore, their absence in the counterpart is the desired behavior of the inversion. Event 3 does not appear in the central trace analyzed here, because its amplitude is highly attenuated by the propagation effects when it is compared at the same scale with the direct wavefield (event 1), making it almost invisible in the zero-offset trace.

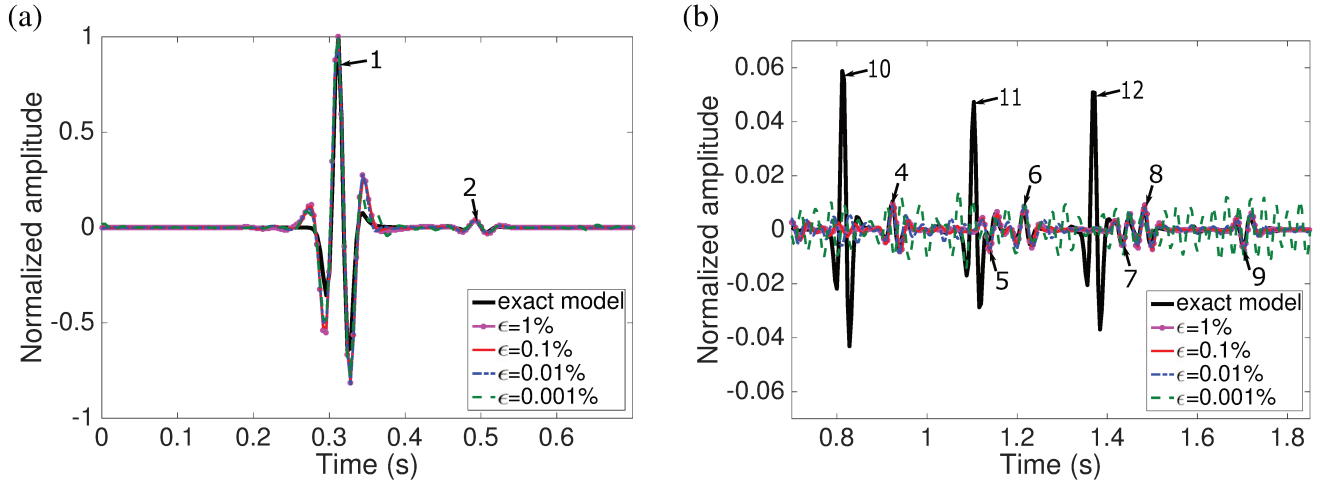


Figure 6.38: Comparison of the traces at 500 m offset of the downgoing Green's functions sections in Figure (6.36) (coloured lines) compared to the wavefield simulated with sources at the surface and receivers at the datum (black line). (a) First part of the traces. (b) Later portion at a different scale.

In summary, we see that all downward propagating events are correctly positioned in time and the amplitudes are comparable. Moreover and most importantly, the result does not exhibit strong

artefacts or non physical events. Our inversion response nicely recovers high-quality versions of the physical events just as interpreted in Figure (6.35b).

Upward wavefield constituent by focusing

Once worked the downward inverse extrapolation, now we will calculate the up-ward Green's functions using the inverse operator calculated in equation (5.22). To do that, we need three input data: (1) the model of the vertical derivative of the transmitted wavefield from the earth's surface until 500m at depth (datum of our numerical model), (2) the model of the truncated wavefield with sources and receivers at the earth's surface and (3) the PSF^{-1} retrieved by least-squares, to do that we tested four different values to the regularization parameter ϵ to invert the PSF : (1) 1%, (2) 0.1%, (3) 0.01% and (4) 0.001%. Using this results, we retrieved the upward Green's function with equation (5.22), where we showed that only the causal upward constituents are retrieved, these responses have not artefacts or non physical events. Figure (6.39) shows the upward Green's functions retrieved with different values to ϵ .

We observed in Figure (6.39) that, as desired, only upgoing Green's functions constituents were retrieved. A comparison with Figure (6.35a) reveals correct positioning. Also the dynamic properties of the inverted events largely correspond to those in the modeled section. Events 13, 14 and 5 correspond to a second order multiple and are the weakest events. Moreover, except for boundary effects, any non physical events appear in the inverted sections. Which is an important advantage over correlation-based redatuming techniques. We also have a fundamental difference regarding to the downgoing case, the effect of using different values for the regularization parameter is clearly visible. We noticed differences in relative amplitudes and, most important, in wavelet shape.

The more quantitative analysis of the zero-offset traces (Figure 6.40) reveals more details. We notice the overall good match between the inverted traces and the upgoing events in the modeled data, both in travel time and in amplitude. On the other hand, as desire the downgoing events are absent from the invert data. While increasing values of the regularization parameter help to better suppress the numerical artefacts, they also lead to broadened wavelets of the inverted events. Again, a value of $\epsilon = 0.001$ seems a good compromise between data quality and noise suppression. Once retrieved the up- and downward Green's functions constituents by inversion, we will complete the redatuming of the seismic array with sources and receiver at 500 m at depth. To do that, we will use the two interpretations named at section (4): (a) convolution-based and (b) correlation-based.

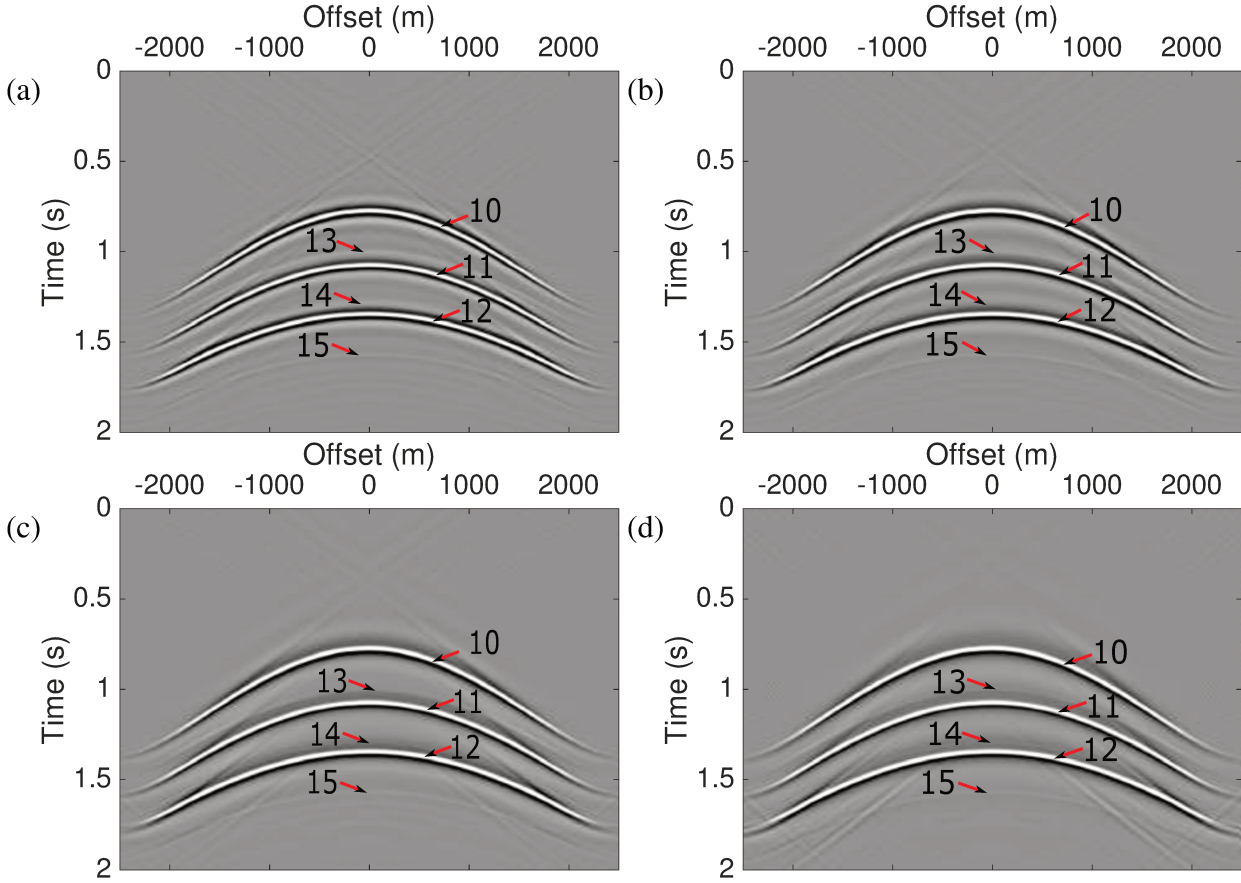


Figure 6.39: Upward Green's function retrieved with equation (5.22), where we have tested five different values to ϵ , where: (a) 1%, (b) 0.1% (c) 0.01% and (d) 0.001%.

Redatuming by inverse wavefield extrapolation: Convolution-based method

In this section, we will show the results to make reposition of sources and receivers at the datum with convolution-based interpretation obtained in section (4). In the Figure (6.42) we have four results that were retrieved using the inverse operator showed in expression (5.41). The input data to retrieve the complete Green's function at the datum in 500 m at depth are: (a) the downward wavefield extrapolation retrieved with the equation (5.32), which result was showed in Figure (6.36) and (b) the upward wavefield extrapolation retrieved with the equation (5.22), which result was showed in Figure (6.39). The interferometric redatuming by convolution-based interpretation using the equation (5.41) also needs as input data the PSF^{-1} , that is calculated multiplying in the frequency domain the vertical derivatives of the downward wavefield constituent $\partial_3 \hat{G}_+^B(x'', \omega; x^B)$ by the complex conjugate of itself $\partial_3 \hat{G}_+^{B*}(x'', \omega; x^B)$, just as we showed in the equation (5.34). Again, to retrieve the PSF^{-1} we used four regularization percentages measured from the maximum absolute value of the PSF , their percentages were: (a) 1%, (b) 0.1%, (c) 0.01% and (d) 0.001%. With each regularization value

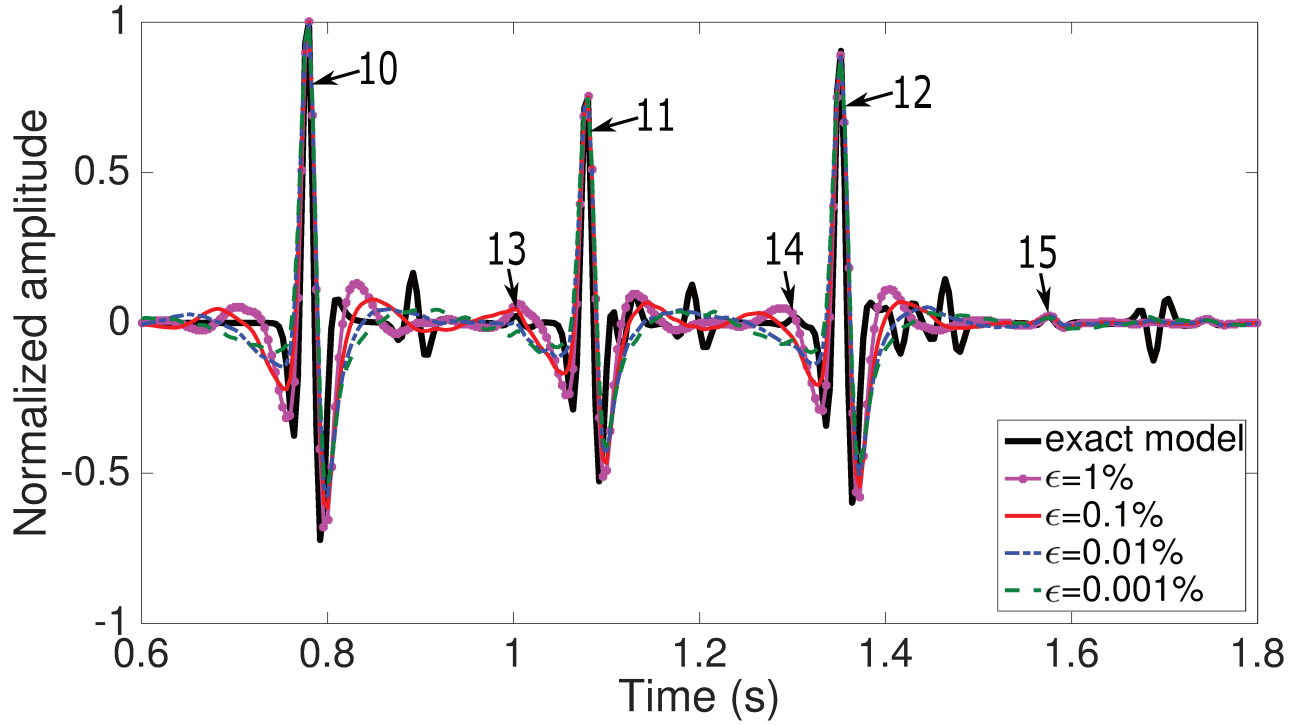


Figure 6.40: Redatuming using inversion in the case of inhomogeneous overburden with the model of Figure (6.10). Comparison of the central trace between the responses of the Figure (6.39)

we will retrieve the results of the Figure (6.42).

We noted that in the four results of the Figure (6.42), the primary reflection with sources and receivers at datum (500 m at depth), denoted as 1, 2 and 3 were retrieved correctly. In addition of this, we also retrieved the non physical event 4, which is coming from a reverberation of the transmitted wavefield at the overburden correlated with the upward constituent of the first reflector below the datum, just as we interpreted in Figure (6.44). While in Figures (6.42c-d) the event 4 was too attenuated. This was because the smallest percentages to retrieve the PSF^{-1} helps to attenuate the non physical events, just as we showed in the interferometric redatuming by convolution-based in the corresponding numerical example at section (6.2).

For more details of the analysis, we show the zero-offset traces (Figure 6.44) of the complete redatuming retrieved by inversion of each response in the Figure (6.42). We noticed that all responses that correspond to the primary reflections have a good match between the inverted traces and the exact model with sources and receivers at 500 m of depth, both in travel time and in amplitude.

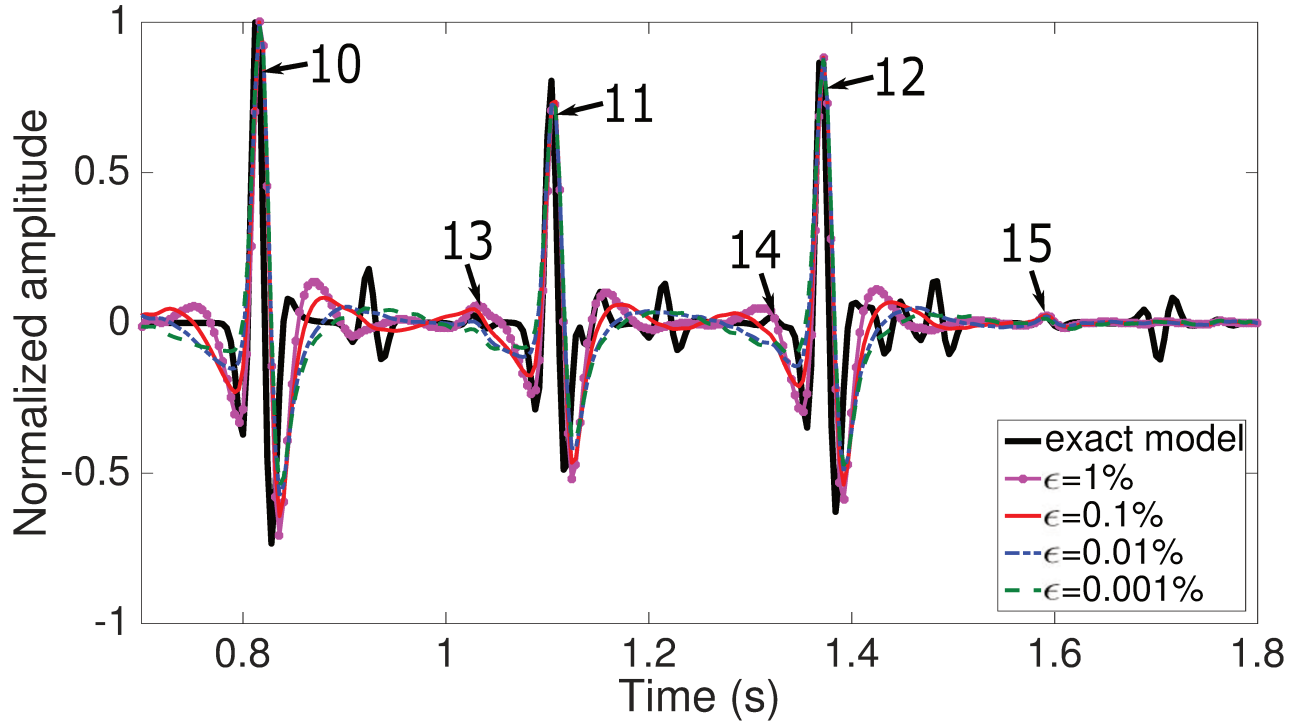


Figure 6.41: Redatuming using inversion in the case of inhomogeneous overburden with the model of Figure (6.10). Comparison of traces at 500 m offset between the responses of Figure (6.42)

Each event that appears in the results of Figures (6.42) and (6.43) was interpreted in the next set of figures, where we will discuss the ray path associated to the physical and non physical events. As we mentioned before, events 1, 2 and 3 are the primary reflections after redatuming. The Figure (6.44a) shows a ray path that explains the origin of the primary reflections using the inverse operator in the expression (5.41). In this figure we showed the most simple possibility to retrieve the primary reflections, but we know that many of other ray path combinations contribute to retrieve the Green's function at the datum. On the other hand we have the non physical event 4 that is coming from a reverberation of the downward wavefield constituent. This artefact is too attenuated with low values of ϵ in the inversion process, just as we showed in Figures (6.42c-d).

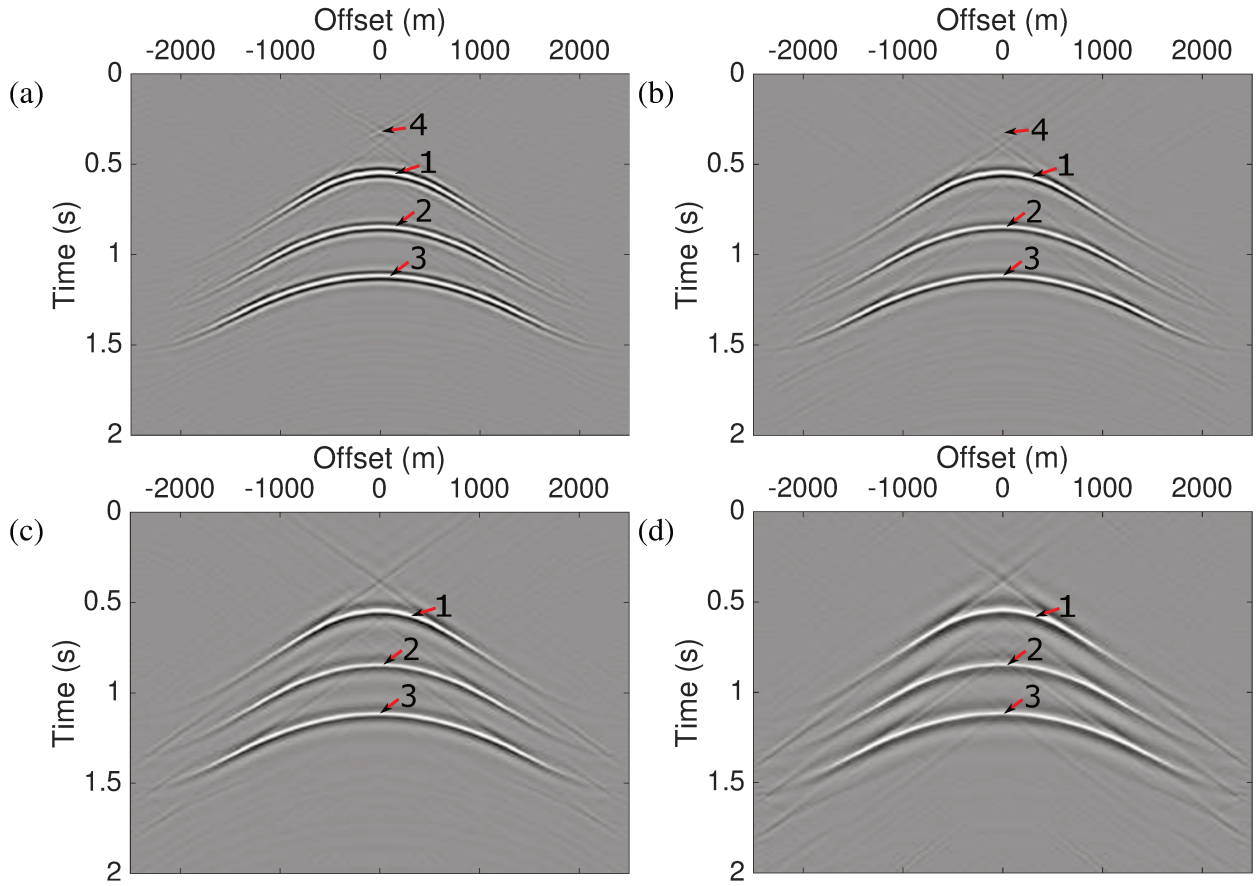


Figure 6.42: Redatuming of source and receivers at 500m at depth retrieved by inversion using the equation (5.41), where we test five different values to ϵ , where: (a) 1%, (b) 0.1%, (c) 0.01% and (d) 0.001%. The percentage above is with reference to the *PSF* maximum value. Up- and down-ward Green's functions used here was retrieved by inversion in above steps.

Convolution-based redatuming with inverse wavefield extrapolation: Dip layer model

In this numerical example, we will modify lightly the geological structure of the previous model, in which we will consider a dipper layer in the overburden medium. We will make redatumation with the expectation of testing the influence of our methodology to make reposition of sources and receivers at an arbitrary datum in depth by inverse wavefield extrapolation with the convolution-based interpretation in structures different to flat layers, as we showed in previous numerical examples. We will apply the inverse operators in equations (5.22) and (5.32) to calculate the up- and downward wavefields constituents, respectively. After retrieve up- and downward wavefield constituents we use them as input data in the inverse operator at equation (5.41) to retrieve the complete wavefield with sources and receivers at datum.

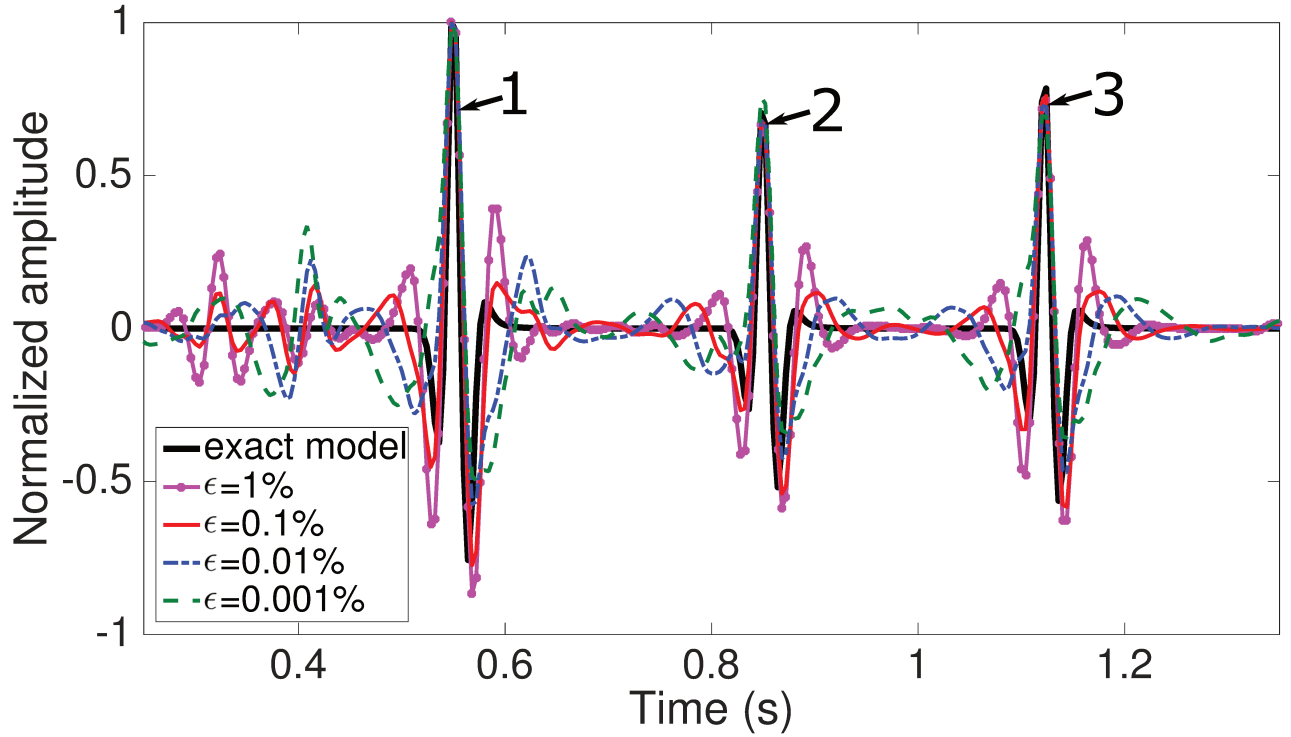


Figure 6.43: Redatuming using inversion in the case of inhomogeneous overburden with the model of Figure (6.10). Comparison of the central trace between the responses of Figure (6.42)

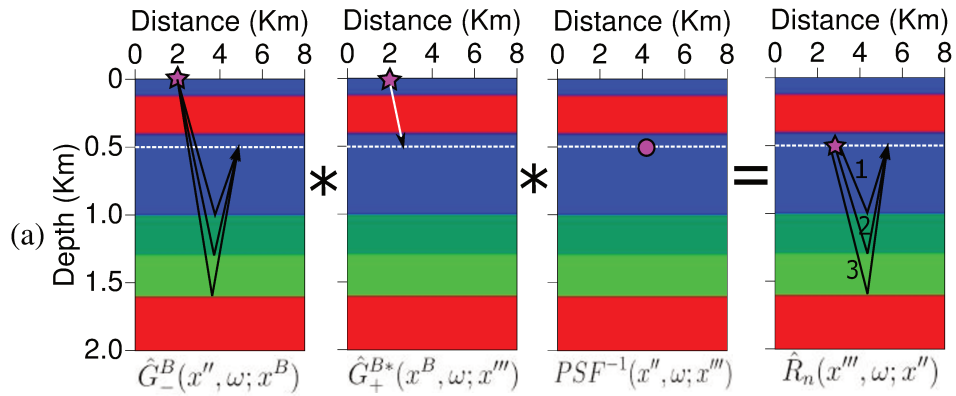


Figure 6.44: Sketch of the equation (5.15) that explains the process to retrieve the (a) primary reflections 1, 2 and 3, and (b) the event 4 that is associated to the reverberation of the transmitted wavefield in the overburden.

Model

In first place we will describe the model that we will analyze. In this model we have a source and receivers distribution with a width at the earth's surface of 5 km and depth of 2 km. The datum is located at 1.2 km below the earth's surface, in Figure (6.45) all three seismic arrays consisted of

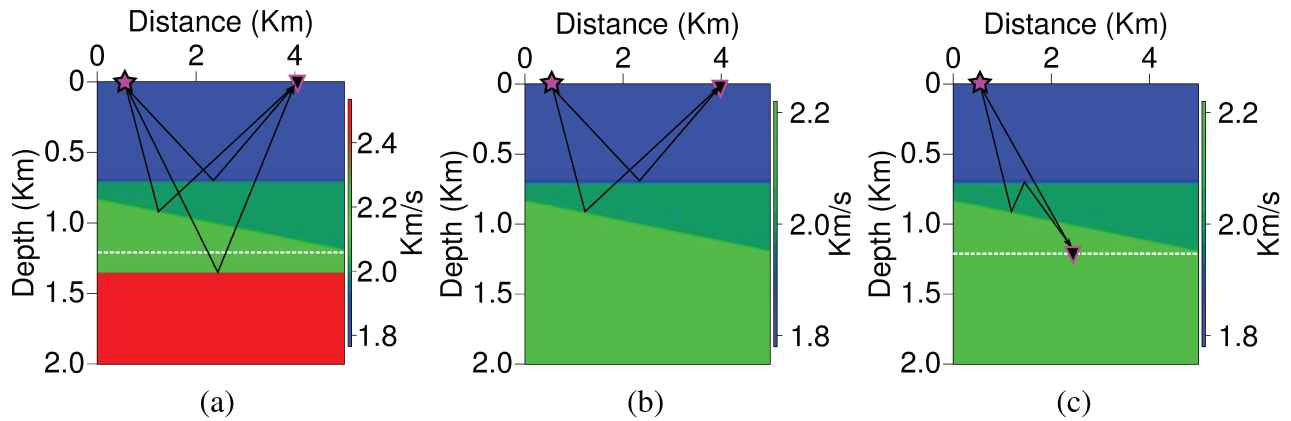


Figure 6.45: Modeling of the seismic input data considering: (a) array of sources and receivers at the surface, (b) array of shots and receivers at the earth's surface considering only information of the overburden (truncated wavefield) and (c) array of shots at the earth's surface and receivers at the datum (transmitted wavefield).

201 sources spaced at 25 m, horizontally located between coordinates 0 km and 5 km, and the same number of receivers for each shot, located at the same horizontal position. The wavelet used for the numerical modeling was a Ricker wavelet with 25 Hz peak frequency. For simplicity, we considered the density in all layers constant.

Interpretation of down- and upward wavefield constituents

In this section, for comparison we simulated the full wavefield with sources and receivers at the datum in 1.2 km of depth (Figure 6.46). The events that appear in the seismic section of the Figure (6.46a) are labeled with numbers in order to identify and interpret them. In this model we have 7 events, where 1 – 4 corresponds to the downward wavefield constituents (Figure 6.46b) and 5 – 7 corresponds to upward wavefield constituents (Figure 6.46c). In the Figure (6.46a), events 6 and 7 are not visible, because correspond to second order multiples.

Downward Green's functions

Once we have simulated the full wavefield, we will retrieve the down- and upward wavefields. We will start with the downward wavefield constituent using the inverse operator in equation (5.32). In Figure (6.45) we show the sketches that represent the input data models required to calculate the up- and downgoing wavefield constituents. This input data are: (a) the complete seismic data with source and receivers at the earth's surface (Figure 6.46a), (b) the truncated model with its respectively vertical derivative (Figure 6.46b) and (c) the transmitted wavefield with sources at the earth's surface

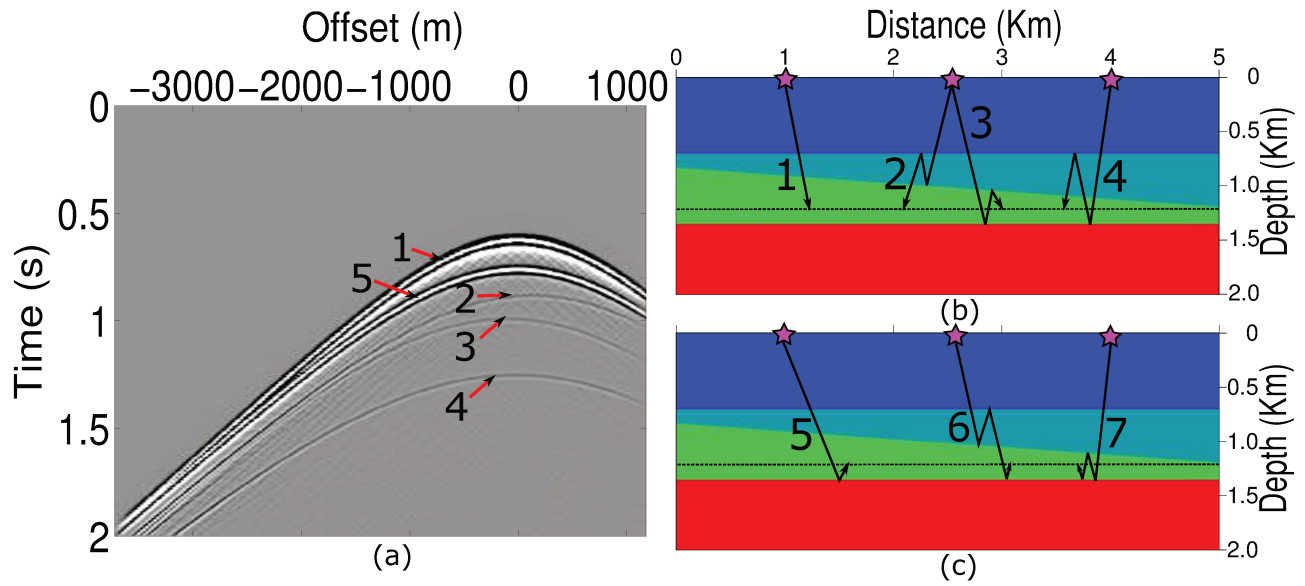


Figure 6.46: (a) Full synthetic seismic wavefield with its up- and downgoing constituents labeled, obtained using a source array at the surface and receivers at the datum at 500 m in depth in the horizontally layer, where was recorded the (b) downward and (c) upward wavefield constituents.

and receivers at the datum in 1.2km in depth and its corresponding vertical derivative.

In Figure (6.47) we have the inversion responses of the downward Green's functions retrieved considering four different percentages of the regularization parameter ϵ to invert the PSF : (a) 1%, (b) 0.1%, (c) 0.01%, (d) 0.001%. Each response in Figure (6.47) corresponds to the shot 150 and have their corresponding interpretation in Figure (6.46b). In this case we denoted with numbers 1 – 4 the physical events and the non physical event was marked with the capital letter A . We noticed in Figure (6.47) that the event 1 is present in all of the responses of this figure, while events 2, 3 and 4 appear only in the inversion responses with $\epsilon = 1\%$ and $\epsilon = 0.1\%$ (Figure 6.47a-b). The attenuation of events 2, 3 and 4 in Figures (6.47c-d) is because the instability of the inversion process when is considered smaller values to the regularization parameter ϵ . We noted that specially in Figures (6.47b-d) appear a linear noise at the right boundary of the shot figure, that we associated to the instability of the inversion process, also for having consider smaller values of ϵ . In Figures (6.47a-b) appear a non physical event that we denoted as A , this event corresponds to the delay of the event 1 because of the reverberation of the complex conjugate of the model of the transmitted wavefield from the earth's surface at the datum in 1.2 km in depth. The non physical event also is attenuated because of the inversion process with smaller values of ϵ .

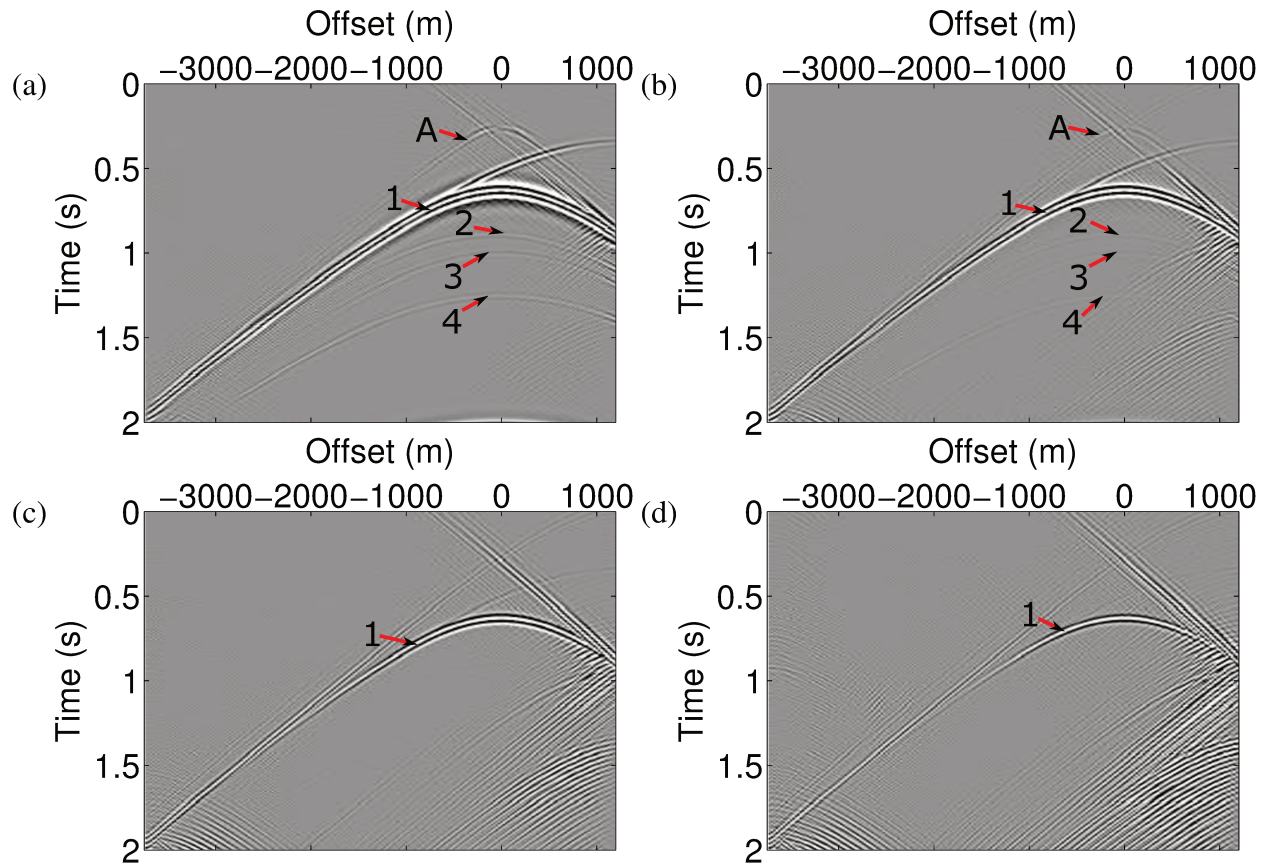


Figure 6.47: Shot 150 of the downward wavefields retrieved with the inverse operator (5.32), where we test four different values to ϵ : (a) 1%, (b) 0.1%, (c) 0.01% and (d) 0.001%.

Upward Green's functions

Now, we will calculate the upward Green's functions using the inverse operator in equation (5.22), the corresponding input data is showed as sketch form in the Figure (6.45) and represents: (a) complete seismic data at the earth's surface (Figure 6.45a), (b) the truncated wavefield above the datum (Figure 6.45b) and (c) the vertical derivative of the transmitted wavefield from the earth's surface at the datum in 1.2 km at depth. Again we considered four percentages of the regularization parameter ϵ to invert the *PSF*: (a) 1%, (b) 0.1%, (c) 0.01%, (d) 0.001%. In Figure (6.48) we show the upward wavefields retrieved for each percentage of ϵ in the shot gather 150, where their events are interpreted in the Figure (6.46c). We noticed that all of the events responses in Figure (6.48) are physical, the event 5 appears in all responses and the events 6 and 7 correspond to second order multiples, that specially in Figures (6.48b-c) are too attenuated because of the effects of the inversion. Again we have a lot of lineal noise at the boundaries of Figure (6.48), also attributed to the instability of the inversion.

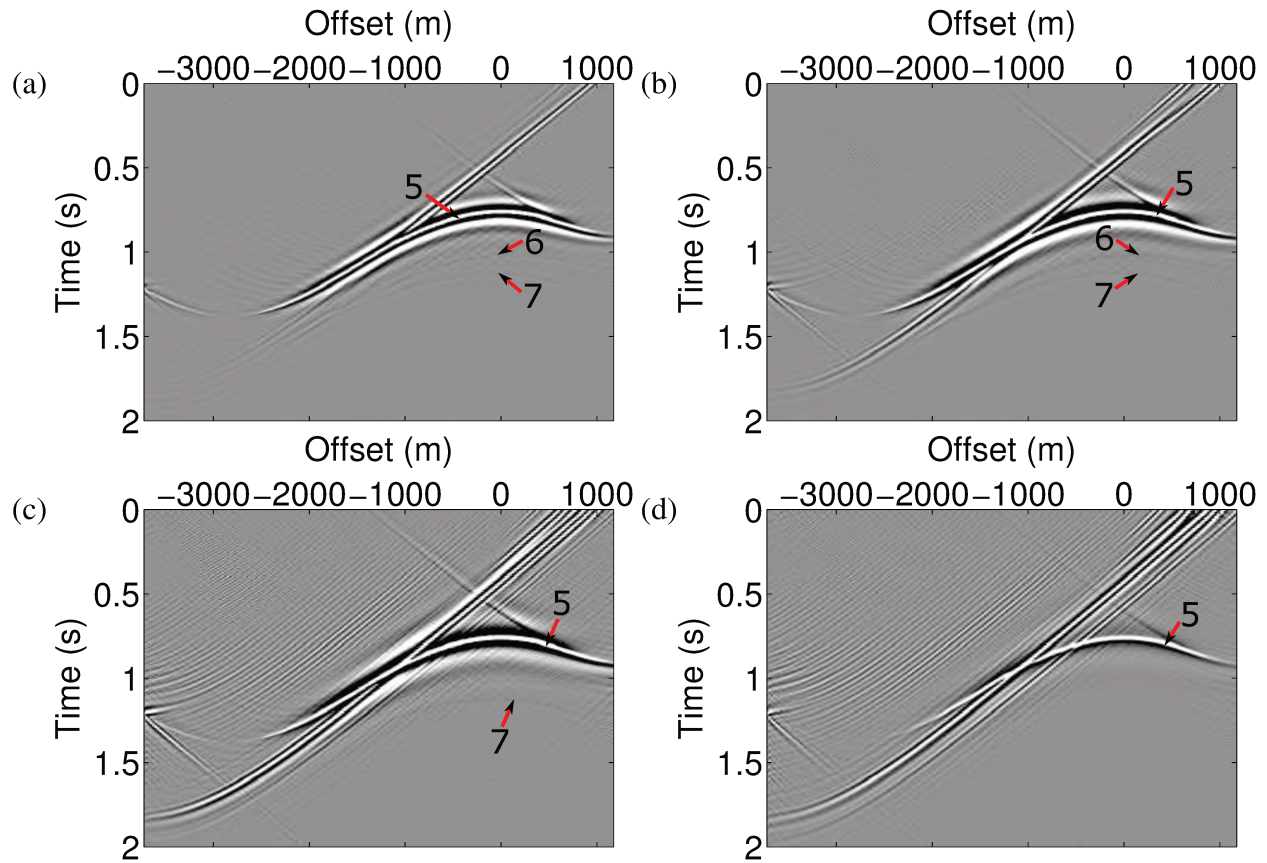


Figure 6.48: Shot 150 of the upward wavefield retrieved with the inverse operator (5.22), where we test four different values to ϵ : (a) 1%, (b) 0.1%, (c) 0.01% and (d) 0.001%.

Redatuming

Finally, we will complete the redatuming process, using as input data the up- and downward wavefields retrieved previously. To do this we used the inverse operator in equation (5.41), where we retrieved different responses varying the percentage of ϵ to calculate the *PSF* inverse, these percentages were: (a) 1%, (b) 0.1%, (c) 0.01%, (d) 0.001%. In Figure (6.49) we showed each result corresponding to each percentage of ϵ at the shot gather 150. We noticed that in shot 150 of Figure (6.49) the event corresponding to the layer below the datum at the new acquisition horizon that we denoted as 1 was retrieved. In Figures (6.49a-c) we noticed that the responses are too clean, without non physical events and inversion artefacts. While in Figure (6.49d) we showed that the inversion with $\epsilon = 0.001\%$ is the most instable, where appear linear noise at the top of figure, masking the event corresponding to the redatumed layer. In seismic processing a natural form to clean noise is stacking the gathers if we know the velocity field. In Figure (6.50) we showed the stack of the complete redatuming shot gathers corresponding to each inversion showed in Figure (6.49). We noticed that all of the stacking responses in Figure (6.50) are too cleaned, including the most instable inverse

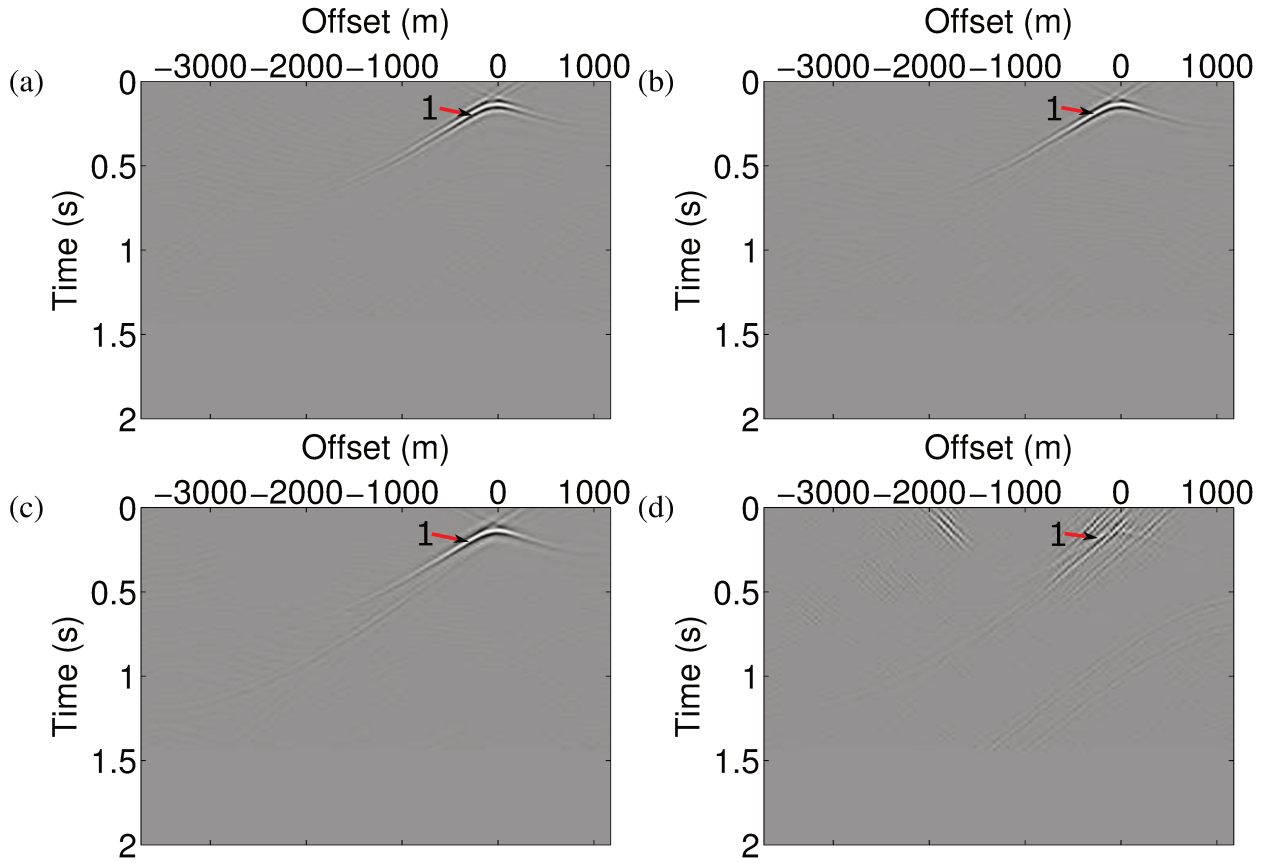


Figure 6.49: Shot 150 of the redatuming of source and receivers at 1.2 km in depth retrieved by inversion using the equation (5.41), where we test four different values to ϵ to retrieve the *PSF* inverse: (a) 1%, (b) 0.1%, (c) 0.01% and (d) 0.001%.

response in Figure (6.49d). This is because we did a normal moveout (NMO) in the shot gathers with the exact velocity corresponding to the redatumed event, then we did the stacking process that added coherent information and discarded incoherent information. Also we noticed that all of the redatumed events are well positioned when are compared with the exact model with sources and receivers at the datum in Figure (6.50). For more details of the analysis, we show the zero-offset traces (Figure 6.51) of the complete redatuming process retrieved by inversion of each response corresponding to shot gather 101. We noticed that all of the responses that correspond to the redatumed event have a good match between the inverted traces and the exact model with sources and receivers at 1.2 mk in depth, both in travel time and in amplitude.

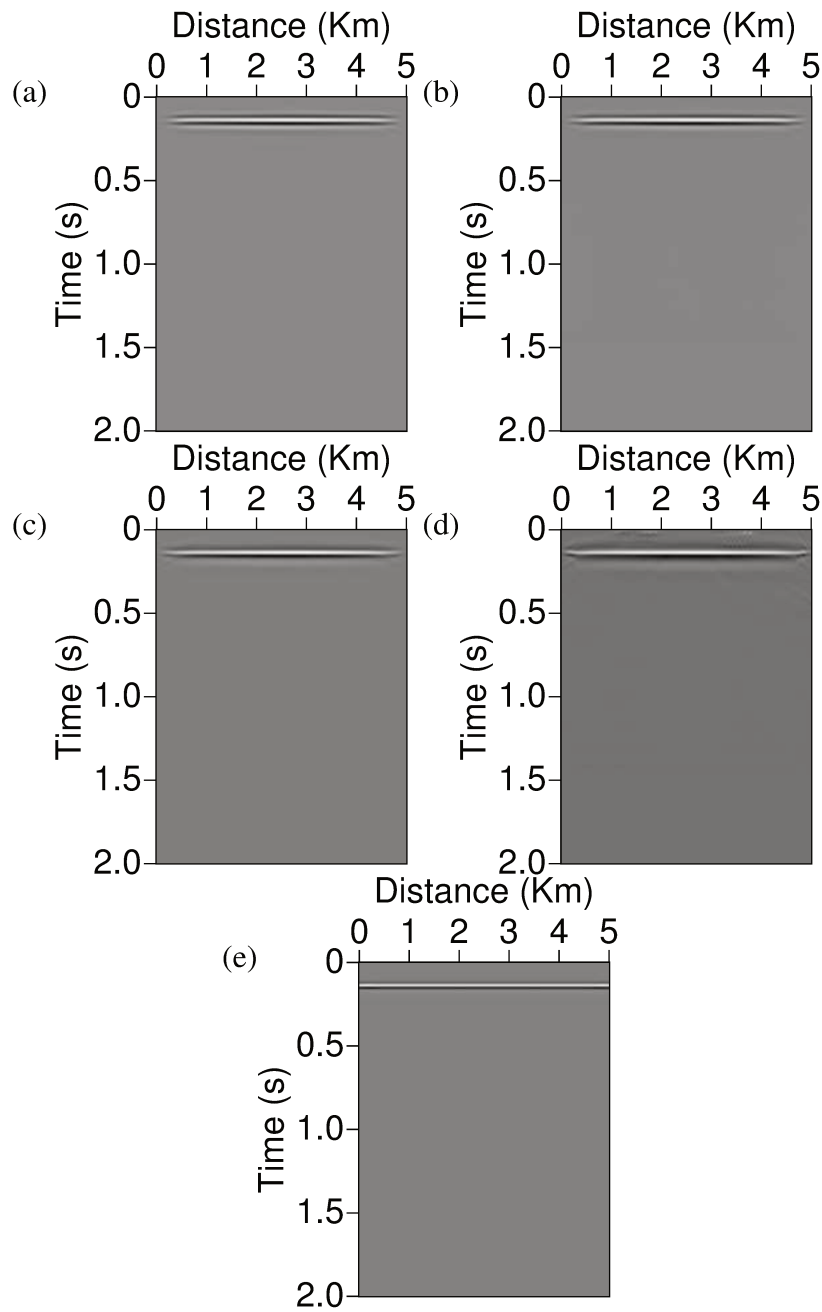


Figure 6.50: Stacking responses correspond to the complete shot gathers in Figure (6.49) using four percentages to ϵ : (a) 1%, (b) 0.1%, (c) 0.01% and (d) 0.001%, while the (e) is the stack response of the shot gathers corresponding to the exact model.

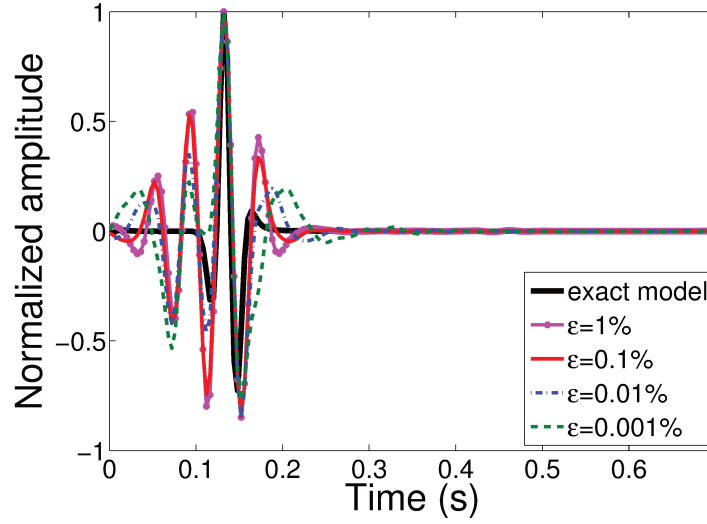


Figure 6.51: Redatuming using inversion in the case of inhomogeneous overburden with the model of Figure (6.10). Comparison of the central trace between the responses of the Figure (6.39)

Convolution-based interferometric redatuming by focusing: Syncline model

In this numerical example, we will address a model that considers a structure with relative geological complexity, because we will include in the model a syncline with a velocity inversion. Including this we have two classical problems in the seismic imaging: (1) the syncline, which depending of the structural deformation could generate artefacts in the seismic data, especially in the time domain i.e., caustics, sideswipes, etc, and (2) the velocity inversion, which can generate pulldowns, this means that the seismic structures are pushed down by the presence of a low velocity body above them. An alternative to solve this kind of problem is: (a) to work in depth domain (migration), (b) to make redatuming of the seismic data below the complex structure or (c) combining (a) and (b). This is because is possible to avoid the complexity of geological structures, by simplifying the seismic data to better focus the wanted target.

As we concluded in above examples, the convolution-based redatuming with inverse wavefield extrapolation is the most appropriate method to solve problems with any structural and stratigraphic complexity. Here we will apply equations (4.8) and (4.3) to retrieve the down- and upward Green's functions and use these results in equation (4.10) to retrieve the complete wavefield with sources and receivers at datum in 1 km in depth in the model of Figure (6.52). Each response obtained in above steps was retrieved for different values of ϵ , following the same way of all previous numerical examples.

Model

The model considered in this section have a width of 12 km and depth of 3 Km, containing velocities between 1.8 km/s and 3 km/s (Figure 6.52). The datum is located at 1 km in depth, just below the bottom of the syncline structure in the model. Below the datum we have two horizontal structures to control and between them a corrugated layer, which we want to retrieve with a correct kinematic in depth. All three seismic arrays in Figure (6.52) consisted of 250 sources spaced at 16 m, horizontally located between coordinates 4 km and 8 km, and the same number of receivers for each shot, located at the same horizontal positions (Figure 6.52). The wavelet used for the numerical modeling was a Ricker wavelet with 25 Hz peak frequency. For simplicity, we have considered the density in all layers constant.

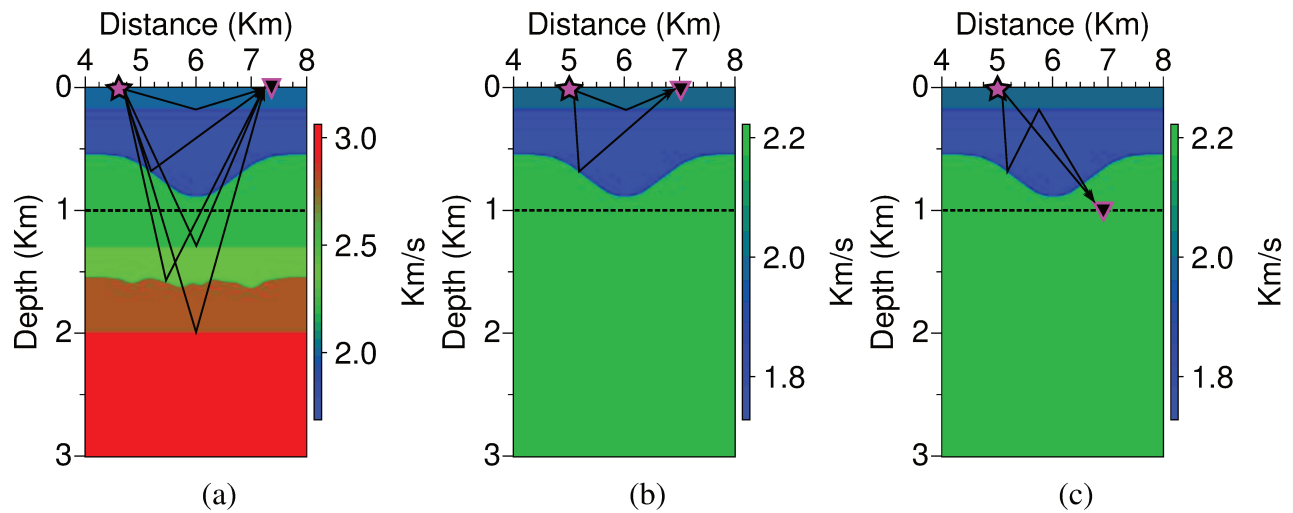


Figure 6.52: Modeling of the seismic input data considering: (a) array of sources and receivers at the surface, (b) array of shots and receivers at the earth's surface considering only information of the overburden (truncated wavefield) and (c) array of shots at the earth's surface and receivers at the datum (transmitted wavefield).

To validate our redatuming results (knowing the exact model) we will compare depth migration responses in order to check if the reflectors are in the correct position in depth. To do this, we used a Kirchhoff depth migration where the travel times are computed with the eikonal equation (Li and Fomel, 2013). This migration method has proved, in the literature that makes reposition of the reflectors in the true position. However, when is required the preservation of the dynamic properties in the seismic responses, is not a good method (Li and Fomel, 2013). We noticed that in Figure (6.53), when the first reflector obey to a inversion velocity. In our migration response (Figure 6.53b) we noticed that the phase did not respond to the dynamic property of the media.

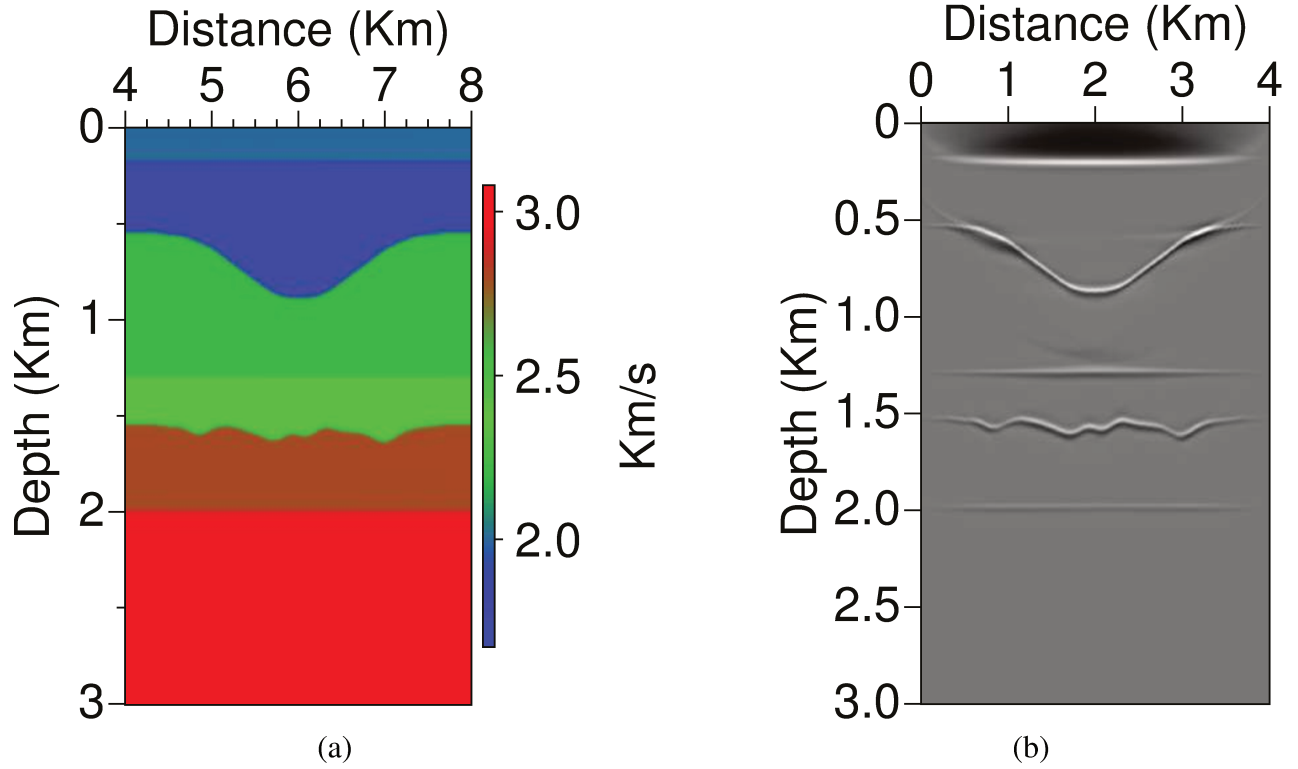


Figure 6.53: (a) Smooth of the velocity model in Figure (6.52a) with a filter length of 5 x 5 and (b) eikonal-based Kirchhoff depth migration of the seismic model with the array on surface.

Downward Green's functions

In this section, we retrieved the vertical derivative of the downward Green's functions, where was considered as input data: (a) the complete seismic data at the earth's surface (Figure 6.52a), (b) the truncated wavefield and its respectively vertical derivative (Figure 6.52b) and (c) the transmitted wavefield and its respectively vertical derivative (Figure 6.52c). Using equation (4.8) we retrieved the vertical derivative of the downward constituent for different values of ϵ in the least-squares inversion scheme. Figure (6.54) shows the inverted Green's function $\partial_3 \hat{G}_+^B(x', \omega; x^B)$ with sources at the earth's surface and receivers at the datum in 1 km in depth, for the values of regularization parameter ϵ : (a) 1%, (b) 0.1%, (d) 0.01% and 0.001%. We noticed that in Figure (6.54) when decrease the factor ϵ the responses are more unstable (Figure 6.54c-d). The noise that appears in the most unstable responses are coming from the PSF^{-1} as we interpreted in previous numerical examples. The noise in Figures (6.54b-d) could be removed with FK filters according with van der Neut and Wapenaar (2015). In Figure (6.54) we retrieved all downward train wavefield constituents that come directly from the overburden and the mixed between propagation below the datum and the overburden.

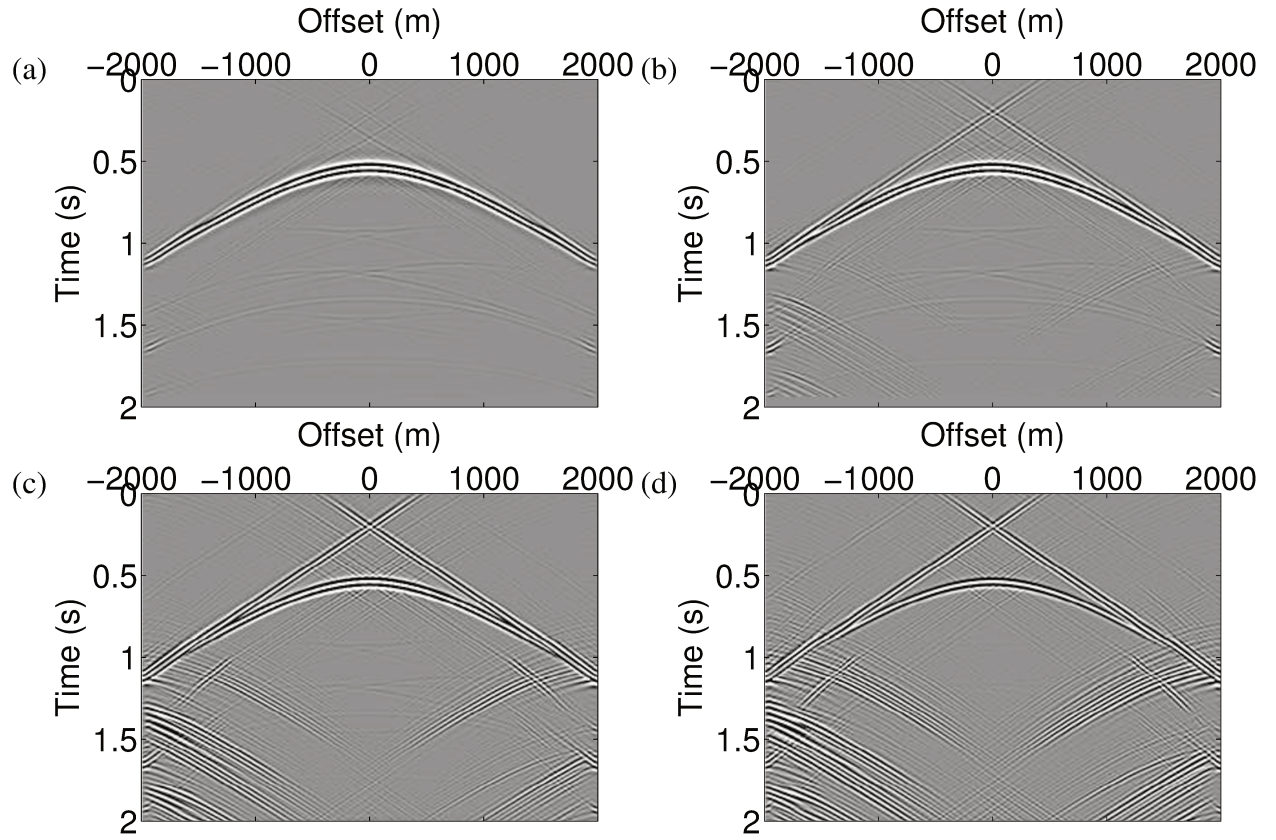


Figure 6.54: Downward Green's function retrieved by inversion using the equation (4.8) in the shot 125, where we test four different values to ϵ : (a) 1%, (b) 0.1%, (c) 0.01% and (d) 0.001%.

Upward Green's functions

In this section we show the responses of the upward Green's functions retrieved with equation (5.22). To do this we used as input data: (a) the complete seismic data at the earth's surface (Figure 6.52a), (b) the truncated wavefield (Figure 6.52b) and (c) the vertical derivative of the transmitted wavefield from the earth's surface until the datum at 1 km in depth (Figure 6.52c). Again we tested four values of ϵ to retrieve each response in Figure (6.55) using least-squares scheme: (a) 1%, (b) 0.1%, (d) 0.01% and 0.001%. We noticed that the instability of the inverse responses increase when the stabilization factor ϵ decrease. This behavior was observed in all responses retrieved by inversion in previous numerical examples. As we mentioned above, the noise that appears in the inversion responses could be attenuated using FK filters (van der Neut and Wapenaar, 2015). For our proposal is not necessary remove the noise, but is necessary to reposition all the events in the true position when the seismic array is moved from the earth's surface until the datum. In this way we will use the responses of the upward Green's functions together with the downgoing constituent retrieved above to complete the redatuming in the next section.

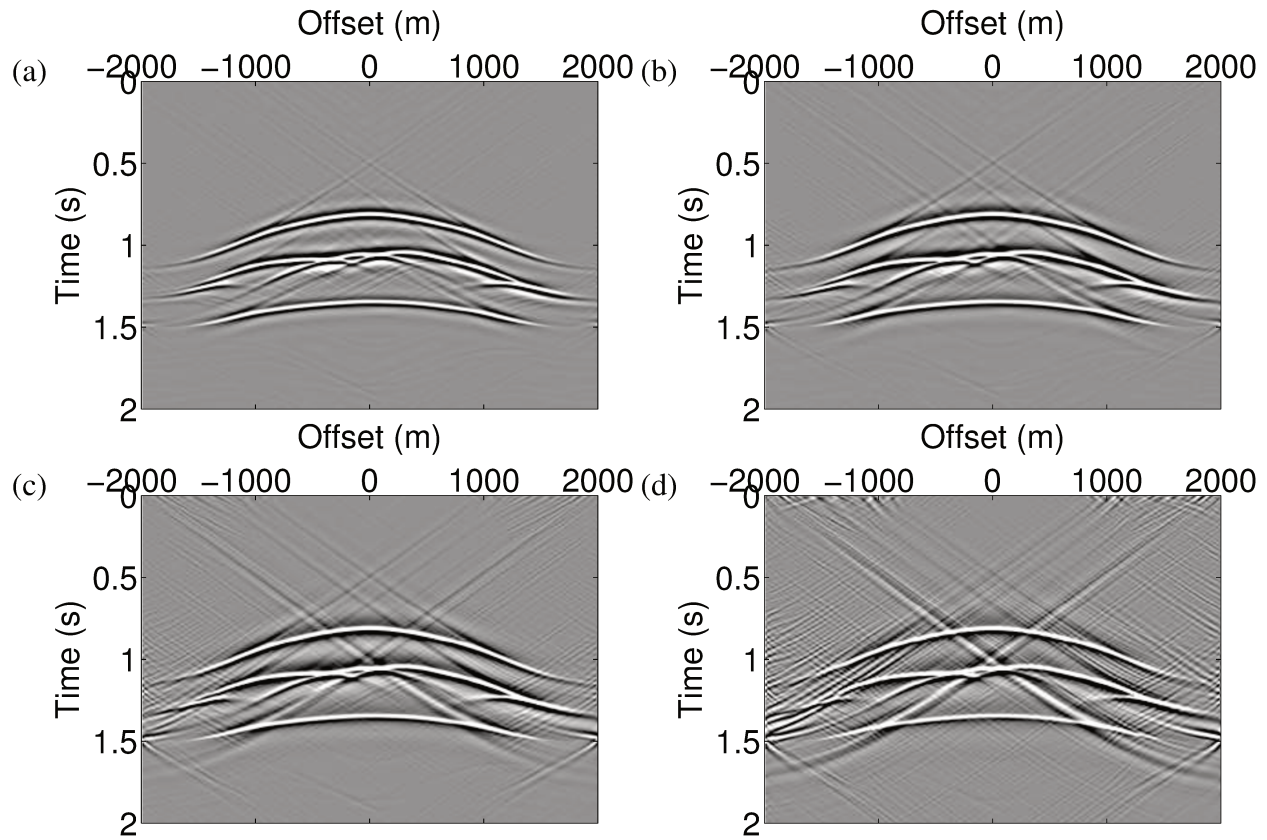


Figure 6.55: Upward Green's function retrieved by inversion using the equation (4.3) in the shot 125, where we test four different values to ϵ : (a) 1%, (b) 0.1%, (c) 0.01% and (d) 0.001%.

Redatuming

In this section we complete the redatuming process using as input data the two previous results, both down- and upward Green's functions, respectively, in equation (4.10). In Figure (6.56) we showed the responses of the complete redatuming, in which are repositioned the sources and receivers at 1 km in depth, considering the model of Figure (6.52). We noticed that the redatuming responses have less noise than the corresponding inversions in previous responses. To retrieve each redatuming response in Figure (6.56) we used four different values to ϵ in the least-squares inversion scheme: (a) 1%, (b) 0.1%, (c) 0.01% and (d) 0.001%.

In Figures (6.57) and (6.58) we see the central trace and the trace at 500 m offset of the response. There we noticed in detail that all of the events are correctly positioned kinematically, when compared with the exact model. The main difference between the redatumed responses and the exact model is in the relative amplitudes, specially in the traces at 100 m offset.

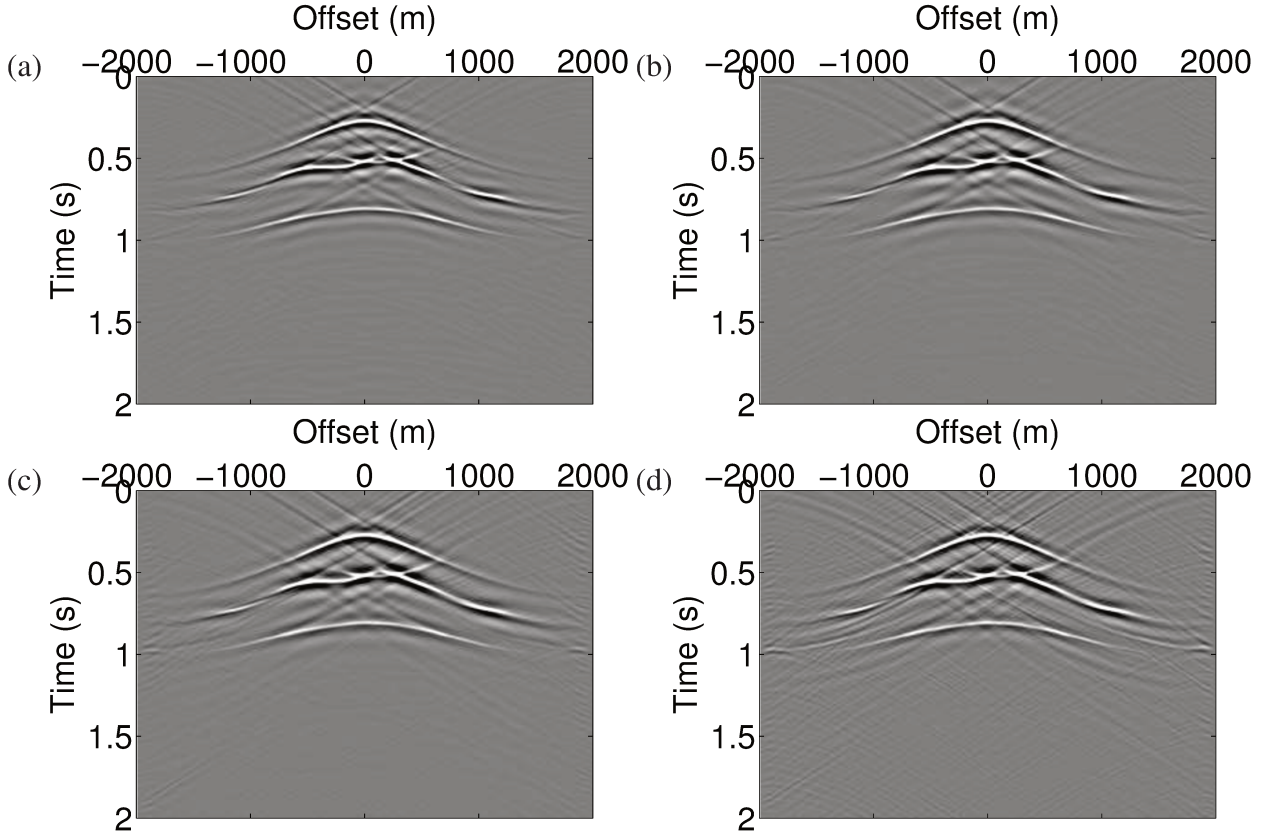


Figure 6.56: Redatuming of seismic data using the inverse of the PSF corresponding to the auto-correlation of the downgoing Green's function in Figure (6.54d) in equation (4.10). We show the redatuming responses corresponding at the shot 125, where we test four different values of ϵ : (a) 1%, (b) 0.1%, (c) 0.01% and (d) 0.001%.

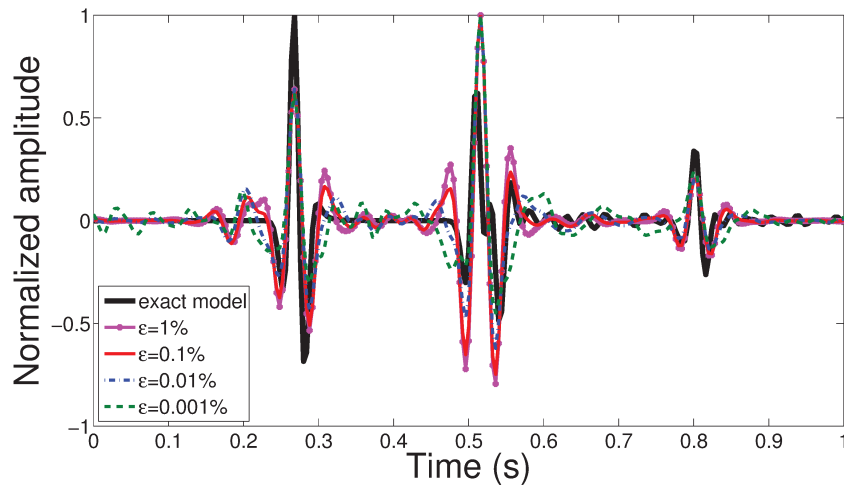


Figure 6.57: Redatuming using inversion in the case of inhomogeneous overburden with the model of Figure (6.52). Comparison of the central traces (zero-offset) between the responses of the Figure (6.56).

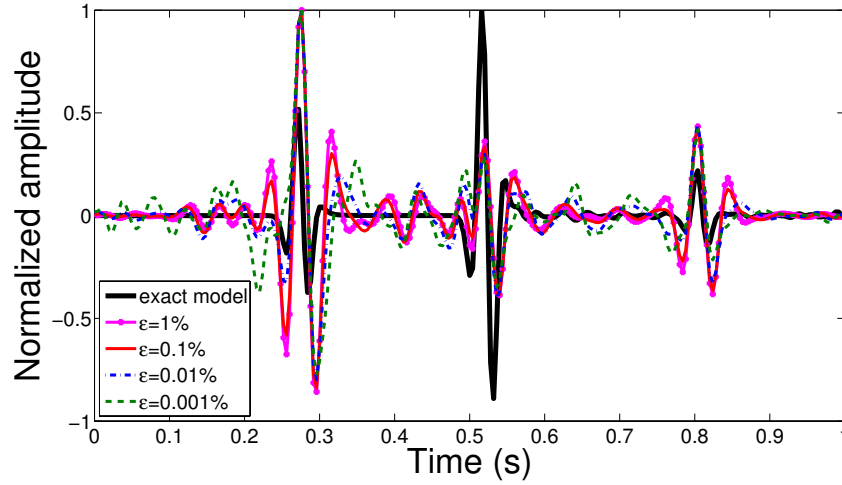


Figure 6.58: Redatuming using inversion in the case of inhomogeneous overburden with the model of Figure (6.52). Comparison of the traces at 100 m offset between the responses of the Figure (6.56).

Pre-stack depth migration of the redatuming results

Finally, we will validate our redatuming results. As we mentioned before, we applied eikonal-based pre-stack Kirchhoff depth migration method (Li and Fomel, 2013) to show the geological structure and demonstrate that the redatuming events are well positioned, when compared with the exact model. As we know the true velocity of the model below the datum we can use it in our migrations and retrieve the seismic sections of the redatuming responses (Figure 6.60) and compare it with the exact model in Figure (6.59a).

In Figure (6.60) we show that all of the events below the datum at 1 km in depth in the model (6.52) were retrieved in the true position when we applied the eikonal-based pre-stack Kirchhoff depth migration (Li and Fomel, 2013). We see that the migration results was too clean, which means that many of the noise coming from the PSF^{-1} in the down- and upward Green's functions and also from the inverse process that allows us to complete the redatuming method vanishes. We noticed that Figure (6.60d) was the most unstable response.

Also we noticed in the migration responses in Figure (6.60) that the irregular event between the horizontal reflectors is not well continuous, specially in the valleys and crests of geological structures. This is because we have bad sampling at the datum, meaning that we have a spatial aliasing, because we tried to repositioned the same source-receiver distribution over the earth's surface in the datum. This loss of resolution is because many of the stationary events at the lateral seismic array distribution are lost when the seismic array is repositioned at a new surface in depth.

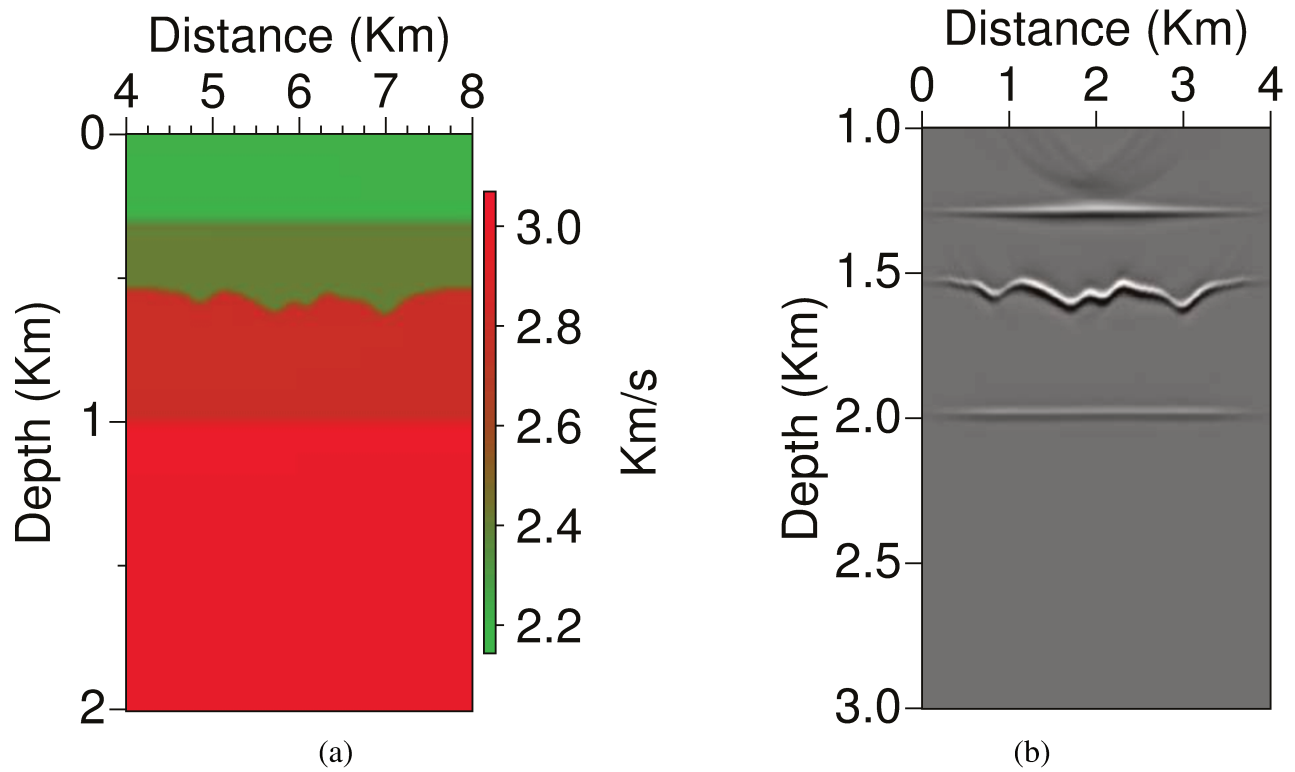


Figure 6.59: (a) Smooth of the velocity model below the datum at 1 km in depth in Figure (6.52a) with a filter length of 5 x 5 and (b) is the exact migration response of the seismic data below the datum.

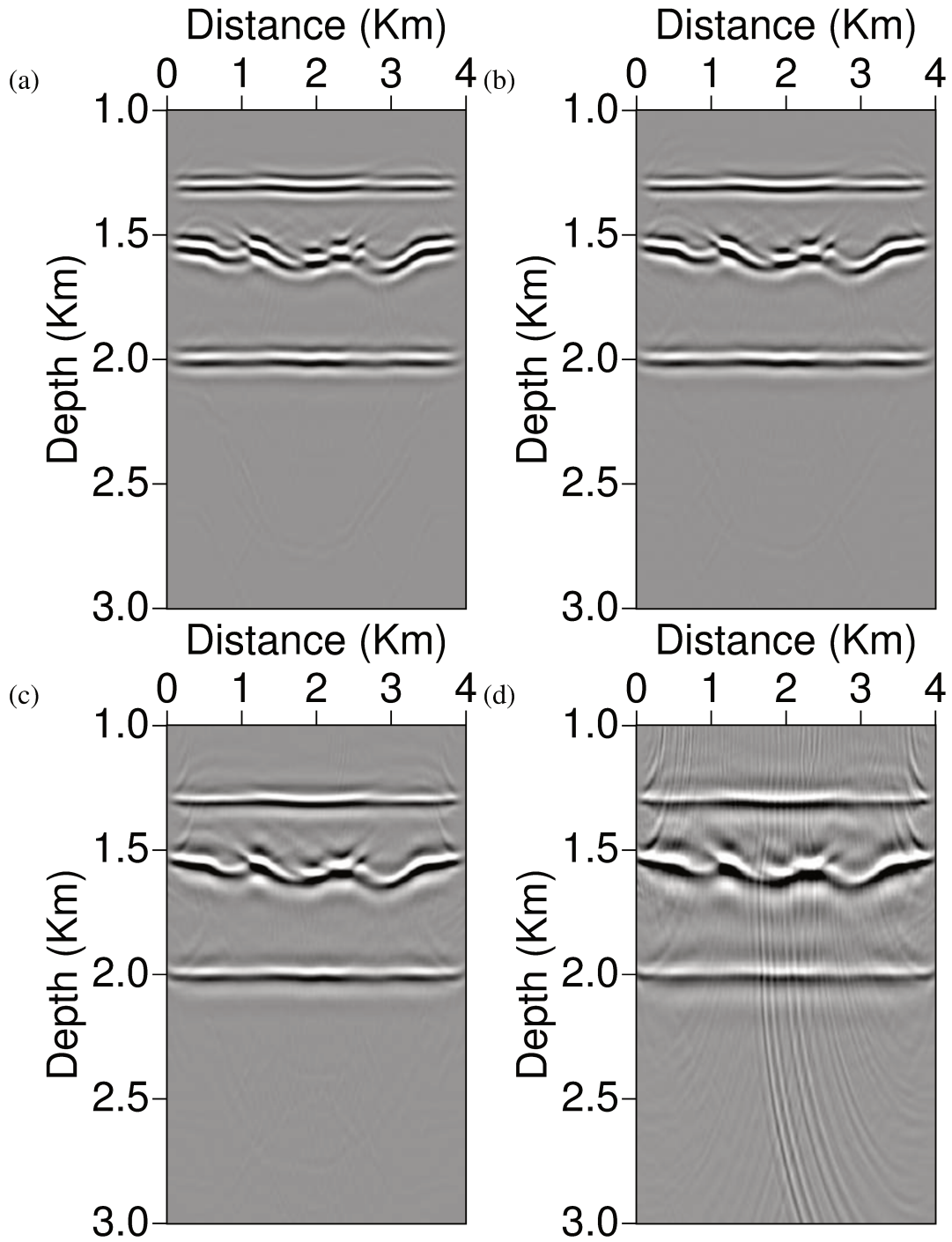


Figure 6.60: Eikonal-based pre-stack Kirchhoff depth migration of the redatuming responses using four percentages to ϵ : (a) 1%, (b) 0.1%, (c) 0.01% and (d) 0.001%.

7. Conclusions

In this work we deduced the classical interferometric expressions with convolution and correlation-based. These equations allows us to reposition the seismic array over the earth's surface to an arbitrary datum at depth in two steps: (a) redatuming of receivers and (b) redatuming of sources. To do this, we needed as input data the vertical derivative of the transmitted wavefield from the earth's surface until the datum in depth.

The classical interferometric expressions of convolutions and correlation-based have limitations when the overburden have inhomogeneities. To investigate the feasibility of the interferometric direct-wave redatuming, we have applied the method to synthetic surface data from a simple horizontally stratified model in order to construct redatumed data for sources and receivers at 500 m of depth. Our numerical example demonstrates that the redatumed reflections events are repositioned correctly and keep the correct amplitude proportions when compared with data obtained from seismic modeling at the datum level. In our numerical experiments, we have also investigated the consequences of inhomogeneities in the overburden. If the medium between the surface and the datum is free of scatterers, the redatumed wavefield is only perturbed by boundary effects. However, if the overburden contains strong reflectors, unphysical events are created in the redatumed data. We have analyzed the kinematics of all visible reflections in the redatumed data to discuss their origins and distinguish physical from unphysical events. In this way, we have seen that the unphysical events are the consequences of incorrectly redatumed overburden multiples.

By numerical examples, we have discussed the advantages and limitations of the classical correlation-based interferometric redatuming, particularly the quality of the recovered physical events and the origins of the generated nonphysical events. We demonstrated that even if the inhomogeneous overburden above the datum is fully known, using only the direct wave for redatuming is advantageous over using the full wave train. The full wave train generates much more artifacts, because, even the primaries can be incorrectly redatumed and rise more unphysical events in the redatumed data. This is a consequence of surface-seismic data which allows only single-sided redatuming rather than reda-

tuning from a closed boundary as required by the theory. In the other hand, when we discussed the limitations of the convolution-based interferometric redatuming, we demonstrated that the tendency of the non-physical events is to vanish as a consequence of the inversion properties when the inhomogeneous overburden above the datum is fully known.

In order to remove the artefacts that come from the inhomogeneities in the overburden when is used the classical interferometric expressions of convolution and correlation type in the redatuming process, we derived a new interferometric procedure to calculate the down- and upward Green's functions with sources at the earth's surface and receivers at a datum in depth, using the inverse wavefield extrapolation. With this methodology it is possible to retrieve only the down- and upward propagating constituents on an arbitrary focusing surface without anticausal events and without artifacts. Combining the down- and upward Green's function retrieved by wavefield inversion with the conventional version of convolution- based interferometric redatuming, we were able to retrieve the reflected wavefield at the datum, as demonstrated in many synthetic-data examples. As a major advantage, there is no influence of anticausal events in the final responses, which were removed with the inverse wavefield extrapolation in the first step of the redatuming process. To do this we only need the following input data if we know the overburden media: (a) transmitted wavefield from the earth's surface until the datum and its corresponding vertical derivative and (b) the full wavefield train above the datum with all seismic array over the earth's surface and its corresponding vertical derivative.

To solve the mathematical expressions that required inversion in this work, was necessary to consider the solution as an inverse problem. For that purpose, we used least-squares inversion to retrieve the desired wavefield constituents. We tested the behaviour of the inversion using different values for the regularization parameter. Though the problem is ill-posed, the numerical results for the retrieved up- and downgoing wavefield constituents showed a strong dependence on the regularization parameter. All recovered wavefields matched nicely with the simulated data at the datum. In this way, we have demonstrated that all retrieved events are kinematically correct. Moreover, in difference to purely correlation-based redatuming, the investigated technique has not produced non-physical events.

References

- Berryhill, J. R. (1979). Wave-equation datuming. *Geophysics*, 44:1329–1344.
- Berryhill, J. R. (1984). Wave equation datuming before stack. *Geophysics*, 49(11):2064–2067.
- Bevc, D. (1995). Imaging under rugged topography and complex velocity struture. *Ph.D. dissertation, Stanford University*.
- Bleistein, N., Cohen, J. K., and Jr., J. W. S. (2001). *Mathematics of Multidimensional Seismic Imaging, Migration, and Inversion*. Springer.
- Claerbout, J. (1968). Synthesis of a layered medium from its acoustic transmission response. *Geophysics*, 33:264–269.
- Curtis, A. (2009). Source-receiver seismic interferometry. *SEG meeting*, pages 3655–3659.
- Dong, S., Xiao, X., Luo, Y., and Schuster, G. (2007). 3D target-oriented reverse time datuming. *SEG Expanded Abstracts*, 26:2442–2445.
- Hansen, P. C., Nagy, J. G., and O’Leary, D. (2006). *Deblurring Images*. Siam.
- Kosloff, D. and Baysal, E. (1983). Migration with the full acoustic wave equation. *Geophysics*, 48:677–687.
- Li, S. and Fomel, S. (2013). Kirchhoff migration using eikonal-based computation of travelttime source-derivatives. *Geophysics*, 78:S211–S219.
- Lu, R., Willis, M., Chapman, X., Ajo-Franklin, J., and Toksöz, M. N. (2008). Redatuming through a salt canopy and target-oriented salt-flank imaging. *Geophysics*, 73:S63–S71.
- Rodberg, L. S. and Thaler, R. M. (1967). Introduction to the quantum theory of scattering. *Academic Press*.

- Scherbaum, F. (1978). Seismic imaging of the site response using microearthquake recordings. Part II. Application to the Swabian Jura, southwest Germany, seismic network. *Bulletin of Seismological Society of America*, 77:1924–1944.
- Schneider, W. A., Phillip, L. D., and Paal, E. F. (1995). Wave-equation velocity replacement of the low-velocity layer for overthrust-belt data. *Geophysics*, 60:573–580.
- Schuster, G. (2009). *Seismic interferometry*. Cambridge.
- Schuster, G. and Zhou, M. (2006). A theoretical overview of model-based and correlation-based redatuming methods. *Geophysics*, 71:SI103–SI110.
- Slob, E., Draganov, D., and Wapenaar, K. (2007). Interferometric electromagnetic Green's functions representations using propagation invariants. *Geophysical Journal International*, 169:60–80.
- Slob, E. and Wapenaar, K. (2007). Electromagnetic green's functions retrieval by cross-correlation and cross-convolution in media with losses. *Geophysical Research Letters*, 4:L05307.
- Tegtmeier, S., Gisolf, A., and Verschuur, E. (2004). 3D sparse data Kirchhoff redatuming. *Geophysical Prospecting*, 52(6):509–521.
- van der Neut, J. (2012). *Interferometric redatuming by multidimensional deconvolution*. PhD thesis, Delft University of Technology.
- van der Neut, J. (2016). Green's function limits. *Internal notes*.
- van der Neut, J., Thorbecke, J., Mehta, K., Slob, E., and Wapenaar, K. (2011). Controlled-source interferometric redatuming by crosscorrelation and multidimensional deconvolution in elastic media. *Geophysics*, 76:SA63–SA76.
- van der Neut, J., Vasconcelos, I., and Wapenaar, K. (2015a). On Green's function retrieval by iterative substitution of the coupled Marchenko equations. *Geophysical Journal International*, 203:792–813.
- van der Neut, J. and Wapenaar, K. (2015). Point-spread functions for interferometric imaging. *Geophysical prospecting*, 63:1033–1049.
- van der Neut, J., Wapenaar, K., Thorbecke, J., Slob, E., and Vanconcelos, I. (2015b). An illustration of adaptative Marchenko imaging. *The Leading Edge*, pages 818–822.
- Vasconcelos, I., Snieder, R., and Douma, H. (2009). Representation theorems and green's function retrieval for scattering in acoustic media. *Physical Review*, 80:036605–1 – 036605–14.

- Wapenaar, C. P. A. (1993). Kirchhoff-helmholtz downward extrapolation in a layered medium with curved interfaces. *Geophys J. Int.*, 115:445–455.
- Wapenaar, C. P. A. and Berkhout, A. J. (1989). *Elastic Wave Field Extrapolation: Redatuming of Single- and Multi-Component Seismic Data*. Elsevier.
- Wapenaar, C. P. A., Cox, H. L. H., and Berkhout, A. J. (1992). Elastic redatuming of multicomponent seismic data. *Geophysical Prospecting*, 40(04):465–482.
- Wapenaar, K., Draganov, D., Snieder, R., Campman, X., and Verdel, A. (2010a). Tutorial on seismic interferometry: Part 1 - basic principles and applications. *Geophysics*, 75:75A195–75A209.
- Wapenaar, K. and Fokkema, J. (1997). Inverse wavefield extrapolation revisited: limitations of single- and multi-valued operators. *67th annual SEG meeting*, pages 1509–1512.
- Wapenaar, K. and Fokkema, J. (2006). Green's function representations for seismic interferometry. *Geophysics*, 71:SI33–SI46.
- Wapenaar, K., Ruigrok, E., van der Neut, J., Draganov, D., Hunziker, J., Slob, E., and Thorbecke, J. (2010b). Green's function representation for seismic interferometry by deconvolution. *SEG meeting*, pages 3972–3978.
- Wapenaar, K., Slob, E., and Snieder, R. (2008). Seismic and electromagnetic controlled-source interferometry in dissipative media. *Geophysical prospecting*, 56:419 – 434.
- Wapenaar, K., Thorbecke, J., van der Neut, J., Broggini, F., Slob, E., and Snieder, R. (2014). Marchenko imaging. *Geophysics*, 79:WA39–WA57.
- Watkins, D. (2010). *Fundamentals of matrix computations*. Wiley.
- Wiggins, J. W. (1984). Kirchhoff integral extrapolation and migration of nonplanar data. *Geophysics*, 49:1239–1248.
- Xiao, X. and Schuster, G. (2006). Redatuming CDP data below salt with VSP Green's function. *SEG Expanded Abstracts*, 25:3511–3515.
- Yilmaz, O. and Lucas, D. (1986). Prestack layer replacement. *Geophysics*, 51:1355–1369.

A. Appendix A

Integral surfaces analysis in the correlation-based interferometric redatuming

Integral over the surface S_1

In this section we analyze the Green' functions, following the methodology of Wapenaar and Berkhout (1989). The analysis is carried out in the wavenumber domain. Also we will make decomposition of the incident and scattering wavefield in up- and down-ward constituents. We denote surface S_1 by lateral coordinates (x_1^1, x_2^1) , at a fixed x_3^1 .

In the cylindrical geometry that we showed in the Figure 3.4, the versor of surface S_1 is given by $\hat{n}_1 = (0, 0, -1)$. Substitution of the integral of expression (3.40), yields

$$\hat{I}_1 = - \iint_{S_1} \frac{1}{\rho_A(x)} \left[\hat{G}^{A*}(x, \omega; x') \partial_3 \hat{G}^s(x, \omega; x^B) - \hat{G}^s(x, \omega; x^B) \partial_3 \hat{G}^{A*}(x, \omega; x') \right] dx_1 dx_2. \quad (\text{A.1})$$

According to Wapenaar and Berkhout (1989), we can divide the Green's function in two parts, representing upward and downward wave fields. In this case, the unperturbed complex conjugate and scattered wavefields can be written as

$$\hat{G}^{A*}(x, \omega; x') = \hat{G}_+^{A*} + \hat{G}_-^{A*}, \quad (\text{A.2})$$

$$\hat{G}^s(x, \omega; x^B) = \hat{G}_+^s + \hat{G}_-^s. \quad (\text{A.3})$$

Subscripts (+) and (−) refer to down- and up-ward wavefield propagation, respectively. Replacing

equations (A.2) and (A.3) in equation (A.1), we have

$$\hat{I}_1 = - \iint_{S_1} \frac{1}{\rho_A(x)} \left[\left(\hat{G}_+^{A*} + \hat{G}_-^{A*} \right) \partial_3 \left(\hat{G}_+^s + \hat{G}_-^s \right) - \left(\hat{G}_+^s + \hat{G}_-^s \right) \partial_3 \left(\hat{G}_+^{A*} + \hat{G}_-^{A*} \right) \right] dx_1 dx_2. \quad (\text{A.4})$$

We now make use of the Parseval's theorem (Wapenaar and Berkhout, 1989), defining the wavenumber vector as $K = (k_1, k_2)$

$$\iint_{-\infty}^{\infty} \hat{A}^*(x, \omega) \hat{B}(x, \omega) dx_1 dx_2 = \left(\frac{1}{2\pi} \right)^2 \iint_{-\infty}^{\infty} \tilde{A}^*(K, \omega) \tilde{B}(K, \omega) dk_1 dk_2, \quad (\text{A.5})$$

where $\hat{A}(x, \omega)$ and $\hat{B}(x, \omega)$ are space-dependent functions and $\tilde{A}(K, \omega)$ and $\tilde{B}(K, \omega)$ are their 2D spatial Fourier transforms. We denoted that the Green's functions and the density after applied the Parseval's theorem have the following configuration $\tilde{G}_+^{A*} = \tilde{G}_+^{*}(K, x_3^1, \omega; x^A)$, $\tilde{G}_+^s = \tilde{G}_+(K, x_3^1, \omega; x^s)$ and $\tilde{\rho}_A = \tilde{\rho}_A(K, x_3^1)$, respectively. The same configuration is valid to the upward wavefield constituents. Applying theorem (A.5) in equation (A.4), we have

$$\begin{aligned} \tilde{I}_1 = - \left(\frac{1}{2\pi} \right)^2 \iint_{\tilde{S}_1} \frac{1}{\tilde{\rho}_A} \left[\left(\tilde{G}_+^{A*} + \tilde{G}_-^{A*} \right) \partial_3 \left(\tilde{G}_+^s + \tilde{G}_-^s \right) - \right. \\ \left. \left(\tilde{G}_+^s + \tilde{G}_-^s \right) \partial_3 \left(\tilde{G}_+^{A*} + \tilde{G}_-^{A*} \right) \right] dk_1 dk_2. \end{aligned} \quad (\text{A.6})$$

where x_3^1 just indicate the position in x_3 at surface S_1 , as we mentioned before. On the other hand we defined the surface in the wavenumber domain as $\tilde{S}_1 = \{(k_1, k_2) \in \mathbb{R}^2\}$. Similar to previous definitions, the Green' functions satisfy the following one-way wave equations in the wavenumber domain

$$\partial_3 \tilde{G}_\pm^s = \mp i k_3 \tilde{G}_\pm^s, \quad (\text{A.7})$$

The complex conjugate of the Green' function with source position in x^A , satisfies the following one-way wave equation:

$$\partial_3 \tilde{G}_\pm^{A*} = \pm i k_3 \tilde{G}_\pm^{A*}. \quad (\text{A.8})$$

If we define $\|k\|^2 = k_1^2 + k_2^2$, then for $k_1^2(x_3^1) \leq \|k(x_3^1)\|^2$, k_3 is defined

$$k_2(x_3^1) = \sqrt{\|k(x_3^1)\|^2 - k_1^2(x_3^1)}, \quad (\text{A.9})$$

where $k_3^* = k_3$. For $k_1^2(x_3^1) > \|k(x_3^1)\|^2$, k_3 is defined as

$$k_2(x_3^1) = -i\sqrt{\|k(x_3^1)\|^2 - k_1^2(x_3^1)}, \quad (\text{A.10})$$

where $k_3^* = -k_3$. According to Wapenaar and Berkhout (1989), equation (A.9) corresponds to the propagating wavenumber area and the expression (A.10) corresponds to the evanescent-wavenumber area. Substituting the one-way equations (A.7) and (A.8) in equation (A.6), we have:

$$\begin{aligned} \tilde{I}_1 = & - \left(\frac{1}{2\pi} \right)^2 \left\{ \iint_{\tilde{S}_1^1} \frac{1}{\tilde{\rho}_A} \left[\left(\tilde{G}_+^{A*} + \tilde{G}_-^{A*} \right) i k_3 \left(-\tilde{G}_+^s + \tilde{G}_-^s \right) \right. \right. \\ & \left. \left. - \left(\tilde{G}_+^s + \tilde{G}_-^s \right) i k_3 \left(\tilde{G}_+^{A*} - \tilde{G}_-^{A*} \right) \right] dk_1 dk_2 \right. \\ & + \iint_{\tilde{S}_1^2} \frac{1}{\tilde{\rho}_A} \left[\left(\tilde{G}_+^{A*} + \tilde{G}_-^{A*} \right) i k_3 \left(-\tilde{G}_+^s + \tilde{G}_-^s \right) \right. \\ & \left. \left. - \left(\tilde{G}_+^s + \tilde{G}_-^s \right) i k_3 \left(\tilde{G}_-^{A*} - \tilde{G}_+^{A*} \right) \right] dk_1 dk_2 \right\}. \end{aligned} \quad (\text{A.11})$$

Surfaces in equation (A.11) are defined as $\tilde{S}_1^1 = \left\{ (k_1, k_2) \in \tilde{S}_1 \mid k_1^2(x_3^1) \leq \|k(x_3^1)\|^2 \right\}$ and $\tilde{S}_1^2 = \left\{ (k_1, k_2) \in \tilde{S}_1 \mid k_1^2(x_3^1) > \|k(x_3^1)\|^2 \right\}$. Equation (A.11) can be written as

$$\begin{aligned} \tilde{I}_1 = & -2 \left(\frac{1}{2\pi} \right)^2 \left[\iint_{\tilde{S}_1^1} \frac{1}{\tilde{\rho}_A} \left(\tilde{G}_-^s i k_3 \tilde{G}_-^{A*} - \tilde{G}_+^s i k_3 \tilde{G}_+^{A*} \right) + \right. \\ & \left. \iint_{\tilde{S}_1^2} \frac{1}{\tilde{\rho}_A} \left(\tilde{G}_-^s i k_3 \tilde{G}_+^{A*} - \tilde{G}_+^s i k_3 \tilde{G}_-^{A*} \right) \right]. \end{aligned} \quad (\text{A.12})$$

According to Wapenaar and Berkhout (1989), in the equation (A.12), the second integral over the evanescent wavenumber area is negligible when both of the sources in x^A and x^B are not in the direct vicinity of $k(x_3^1)$. The main contributions to the integral in equation (A.11) come from the stationary points of the surface \tilde{S}_1^1 . This implies, for example that the terms $\tilde{G}_-^s i k_3 \tilde{G}_-^{A*}$ and $-\tilde{G}_-^{A*} i k_3 \tilde{G}_-^s$ give

equal contribution to the integral, whereas the contributions $\tilde{G}_+^s ik_3 \tilde{G}_-^{A*}$ and $-\tilde{G}_-^{A*} ik_3 \tilde{G}_+^s$ cancel each other (Wapenaar and Fokkema, 2006). Hence, equation (A.11) can be written as

$$\tilde{I}_1 \approx -2 \left(\frac{1}{2\pi} \right)^2 \iint_{\tilde{S}_1} \frac{1}{\tilde{\rho}_A} \left(\tilde{G}_-^s ik_3 \tilde{G}_-^{A*} - \tilde{G}_+^s ik_3 \tilde{G}_+^{A*} \right) dk_1 dk_2. \quad (\text{A.13})$$

Using expressions (A.7) and (A.8), treating correctly the signs and applying the inverse Parseval's theorem in equation (A.13), yields

$$\hat{I}_1 \approx 2 \iint_{S_1} \frac{1}{\rho_A(x)} \left(\hat{G}_-^s \partial_3 \hat{G}_-^{A*} + \hat{G}_+^s \partial_3 \hat{G}_+^{A*} \right) dx_1 dx_2. \quad (\text{A.14})$$

Equation (A.14) is the integral evaluated over the surface S_1 , where the expression $\hat{G}_-^s \partial_3 \hat{G}_-^{A*}$ and $\hat{G}_+^s \partial_3 \hat{G}_+^{A*}$ represent crosscorrelations in the time domain.

Finally in the integral over the surface S_1 , the terms \hat{G}_+^s and \hat{G}_+^{A*} vanishes because in states A and B we not considered free-surface. The last assumption allows us to rewrite equation (A.14) as

$$\hat{I}_1 \approx 2 \iint_{S_1} \frac{1}{\rho_A(x)} \hat{G}_-^s \partial_3 \hat{G}_-^{A*} dx_1 dx_2. \quad (\text{A.15})$$

Integral over the surface S_2

The analysis of the integral over surface S_2 is analogous to the done for surface S_1 , but in this case the normal vector over surface S_2 is $\hat{n}_2 = (0, 0, 1)$. Therefore the integral has the same form as (A.14), but with opposite sign. Thus, we can rewrite this integral expression for surface S_2 as

$$\hat{I}_2 \approx -2 \iint_{S_2} \frac{1}{\rho_A(x)} \left(\hat{G}_-^s \partial_3 \hat{G}_-^{A*} + \hat{G}_+^s \partial_3 \hat{G}_+^{A*} \right) dx_1 dx_2 = 0. \quad (\text{A.16})$$

In equation (A.16) we look at each term evaluated in the integral over the surface S_2 . In term $\hat{G}_-^s \partial_3 \hat{G}_-^{A*}$ the factor \hat{G}_-^{A*} vanishes, because in state A the medium below the surface S_2 is homogeneous. Implying that there cannot be an upward propagating wavefield. Moreover in the second term in equation (A.16), $\hat{G}_+^s \partial_3 \hat{G}_+^{A*}$, the Green's function \hat{G}_+^s approximately vanishes, because \hat{G}_+^s represent only the wavefield from scatters below surface S_2 , implying that there are no downgoing constituents at surface S_2 .

Integral surfaces analysis in the convolution-based interferometric redatuming

Integral over the surface S_1

We will start the analysis of the integral over the surface S_1 , just like we did in previous sections. To do that we remind that at the surface S_1 , the versor $\hat{n}_1 = (0, 0, -1)$. Replacing it in equation (3.52), we have

$$\hat{J}_1 = - \iint_{S_1} \frac{1}{\rho_A(x)} \left[\hat{G}^A(x', \omega; x^A) \nabla \hat{G}^s(x', \omega; x^B) - \hat{G}^s(x', \omega; x^B) \nabla \hat{G}^A(x', \omega; x^A) \right] dx_1 dx_2. \quad (\text{A.17})$$

The wavefields in the above integral can be decomposed into the up- and downward propagating constituents, regarding expressions (A.2) and (A.3) in the previous section. Doing the wavefield decomposition in equation (A.17), we can rewrite this expression as

$$\hat{J}_1 = - \iint_{S_1} \frac{1}{\rho_A(x)} \left[\left(\hat{G}_+^A + \hat{G}_-^A \right) \partial_3 \left(\hat{G}_+^s + \hat{G}_-^s \right) - \left(\hat{G}_+^s + \hat{G}_-^s \right) \partial_3 \left(\hat{G}_+^A + \hat{G}_-^A \right) \right] dx_1 dx_2. \quad (\text{A.18})$$

We now make use of the following version of Parseval's theorem (Wapenaar and Berkhout, 1989)

$$\iint_{-\infty}^{\infty} A(x) B(x) dS = \left(\frac{1}{2\pi} \right)^2 \iint_{-\infty}^{\infty} \tilde{A}(-k) \tilde{B}(k) dK, \quad (\text{A.19})$$

where $A(x)$ and $B(x)$ are space-dependent functions and $\tilde{A}(-k)$ and $\tilde{B}(k)$ are their 2D spatial Fourier transforms, defining again $k = (k_1, k_2, k_3)$ as wave number vector. Applying the theorem (A.19) in the equation (A.18), we have

$$\begin{aligned} \tilde{J}_1 = - \left(\frac{1}{2\pi} \right)^2 \iint_{\tilde{S}_1} \frac{1}{\tilde{\rho}_A} & \left[\left(\tilde{G}_+^A + \tilde{G}_-^A \right) \partial_3 \left(\tilde{G}_+^s + \tilde{G}_-^s \right) - \right. \\ & \left. \left(\tilde{G}_+^s + \tilde{G}_-^s \right) \partial_3 \left(\tilde{G}_+^A + \tilde{G}_-^A \right) \right] dk_1 dk_2. \end{aligned} \quad (\text{A.20})$$

As we mentioned in previous section, the Green's functions satisfy the following one-way wave equations

$$\partial_3 \tilde{G}_\pm^A = \mp i k_3 \tilde{G}_\pm^A, \quad \text{and} \quad \partial_3 \tilde{G}_\pm^s = \mp i k_3 \tilde{G}_\pm^s. \quad (\text{A.21})$$

The one-way wave equations defined in the relations (A.21), we can apply all these in the equation (A.20), which yields

$$\begin{aligned} \tilde{J}_1 = - \left(\frac{1}{2\pi} \right)^2 \left\{ \iint_{\tilde{S}_1} \frac{1}{\tilde{\rho}_A} \left[\left(\tilde{G}_+^A + \tilde{G}_-^A \right) ik_3 \left(-\tilde{G}_+^s + \tilde{G}_-^s \right) - \right. \right. \\ \left. \left. \left(\tilde{G}_+^s + \tilde{G}_-^s \right) ik_3 \left(-\tilde{G}_+^A + \tilde{G}_-^A \right) \right] dk_1 dk_2 \right\}. \end{aligned} \quad (\text{A.22})$$

According to Wapenaar and Berkhout (1989), the main contributions to the integral in equation (A.22) come from the stationary points on the surface evaluated. This implies, for example that the terms $\tilde{G}_+^s ik_3 \tilde{G}_-^A$ and $-\tilde{G}_-^A ik_3 \tilde{G}_+^s$ give equal contribution to the integral, whereas the contributions $\tilde{G}_+^s ik_3 \tilde{G}_+^A$ and $-\tilde{G}_+^A ik_3 \tilde{G}_+^s$ cancel each other (Wapenaar and Fokkema, 2006). Hence, equation (A.22) can be written as

$$\tilde{J}_1 \approx -2 \left(\frac{1}{2\pi} \right)^2 \iint_{\tilde{S}_1} \frac{1}{\tilde{\rho}_A} \left(\tilde{G}_-^s ik_3 \tilde{G}_+^A - \tilde{G}_+^s ik_3 \tilde{G}_-^A \right) dk_1 dk_2. \quad (\text{A.23})$$

Using expressions (A.21) in equation (A.23) and applying the inverse Parseval's theorem in (A.19), yields

$$\hat{J}_1 \approx 2 \iint_{S_1} \frac{1}{\rho_A(x)} \left(\hat{G}_-^s \partial_3 \hat{G}_+^A + \hat{G}_+^s \partial_3 \hat{G}_-^A \right) dx_1 dx_2 = 0. \quad (\text{A.24})$$

Equation (A.24) is the integral evaluated over the surface S_1 , where the expression $\hat{G}_{s-}^B \partial_3 \hat{G}_{i+}^A$ and $\hat{G}_{s+}^B \partial_3 \hat{G}_{i-}^A$ represent crossconvolutions in the time domain. Looking in detail each one of the terms in the expression (A.24). Since we consider a homogeneous halfspace above the nonfree surface S_1 , the terms \hat{G}_+^A and \hat{G}_+^s vanish at the surface S_1 , then the integral over surface S_1 is zero.

Integral over the surface S_2

An integral expression to describe the surface S_2 can be found following the previous analysis, where it is possible to reach almost the same expression of (A.24), the unique difference will be the sign of the equation, because our versor at the surface S_2 is $\hat{n}_2 = (0, 0, 1)$. Then, the expression (A.24) at surface S_2 will be

$$\hat{J}_2 \approx -2 \iint_{S_2} \frac{1}{\rho_A(x)} \left(\hat{G}_-^s \partial_3 \hat{G}_+^A + \hat{G}_+^s \partial_3 \hat{G}_-^A \right) dx_1 dx_2. \quad (\text{A.25})$$

In the integral over the surface S_2 , \hat{G}_-^A also vanishes because in state A , the medium below S_2 is also homogeneous. Then, equation (A.25) is written as

$$\hat{J}_2 \approx -2 \iint_{S_2} \frac{1}{\rho_A(x)} \hat{G}_-^s \partial_3 \hat{G}_+^A dx_1 dx_2. \quad (\text{A.26})$$

The integral over the surface S_2 showed in the equation (A.26) evaluate the crossconvolution between the upward Green's function and the vertical derivative of the downward Green's function $\hat{G}_{s-}^B \partial_3 \hat{G}_{i+}^A$.

B. Appendix B

Green's function limits

We define that $x = \{(x_1, x_2, x_3) \in \mathbb{R}^3 | x_3 = x_3^s\}$. The Green's function is the solution of a wave equation with a punctual source, which can be written as

$$\rho(x) \nabla \cdot \left[\frac{1}{\rho(x)} \nabla \hat{G}(x, \omega; x^s) \right] + \frac{\omega^2}{c(x)^2} \hat{G}(x, \omega; x^s) = -\delta(x_1 - x_1^s) \delta(x_2 - x_2^s) \delta(x_3 - x_3^s) \quad (\text{B.1})$$

To evaluate the behavior of the Green's function near to the source location at the position x_3^s , we can integrate this expression between $x_3^s - \alpha$ and $x_3^s + \alpha$ as

$$\begin{aligned} \int_{x_3^s - \alpha}^{x_3^s + \alpha} \left\{ \rho(x) \nabla \cdot \left[\frac{1}{\rho(x)} \nabla \hat{G}(x, \omega; x^s) \right] + \frac{\omega^2}{c(x)^2} \hat{G}(x, \omega; x^s) \right\} dx_3 = \\ -\delta(x_1 - x_1^s) \delta(x_2 - x_2^s) \int_{x_3^s - \alpha}^{x_3^s + \alpha} \delta(x_3 - x_3^s) dx_3 = -\delta(x_1 - x_1^s) \delta(x_2 - x_2^s). \end{aligned} \quad (\text{B.2})$$

For small α , we can assume that ρ and c are constant in the interval $(x_3 - \alpha, x_3 + \alpha)$. Then, except for the vertical derivative of the Green's function, all terms on the left-hand side of equation (B.2) are continuous in x_3 . Thus, in the limit of very small α , only the terms involving $\partial_3 \hat{G}$ are different from zero. Thus, we can conclude that

$$\lim_{\alpha \rightarrow 0} \partial_3 \hat{G}(x, \omega; x^s) \Big|_{x_3^s + \alpha} - \lim_{\alpha \rightarrow 0} \partial_3 \hat{G}(x, \omega; x^s) \Big|_{x_3^s - \alpha} = -\delta(x_1 - x_1^s) \delta(x_2 - x_2^s). \quad (\text{B.3})$$

If we assume local homogeneity around the source, it follows that the first term in the left-side corresponds to the downgoing wavefield that is ignited by the source, while the second term corresponds

to the upgoing wavefield. Hence, this result can be written as

$$\partial_3 \hat{G}_+(x, \omega; x^s) \Big|_{x=x_3^s} - \partial_3 \hat{G}_-(x, \omega; x^s) \Big|_{x=x_3^s} = -\delta(x_1 - x_1^s) \delta(x_2 - x_2^s). \quad (\text{B.4})$$

Since the source radiates equally in both up- and downgoing directions, it can be reasoned that (van der Neut, 2016)

$$\partial_3 \hat{G}^+(x, \omega; x^s) \Big|_{x=x_3^s} = -\frac{1}{2} \delta(x_1 - x_1^s) \delta(x_2 - x_2^s), \quad (\text{B.5})$$

and

$$\partial_3 \hat{G}^-(x, \omega; x^s) \Big|_{x=x_3^s} = \frac{1}{2} \delta(x_1 - x_1^s) \delta(x_2 - x_2^s). \quad (\text{B.6})$$

C. Appendix C

Boundary effects of the redatuming methods

In this Appendix we will show the principal limitation of the redatuming methods with correlation and convolution-based. This topic is treated by Wapenaar and Fokkema (1997), where they explained the principal reasons of retrieve artifacts when is used complex conjugate inverse operators to make inversion. It is well known that the wavefield recorded in a finite aperture is not exact. The wavefield contains artefacts that can be kinematically explained as ghost wavefields radiated by secondary sources located at the endpoints of the aperture, see Figure (C.1a) (Wapenaar and Fokkema, 1997). On the other hand we can suppose that the data would be recorded on an infinite aperture. Then forward wavefield extrapolation would be exact, because the ghost wavefield of the secondary sources at the endpoints would vanish when these endpoints were moved towards infinity, see Figure (C.1c) (Wapenaar and Fokkema, 1997). Since the wave equation is symmetrical in time, one would expect a similar conclusion for inverse extrapolation from an infinite aperture, see Figures (C.1b) and (C.1d).

In the numerical examples of this thesis work we showed that the boundary effect appear because the real acquisition is discretized. According with van der Neut et al. (2015a) this kind of noise could be attenuated in the shot domain using FK filters. An alternative to attenuate this kind of noise could be done when is applied normal move-out (NMO) and stacking in each shot gather. Doing this, the tendency is make attenuation of the non coherent information.

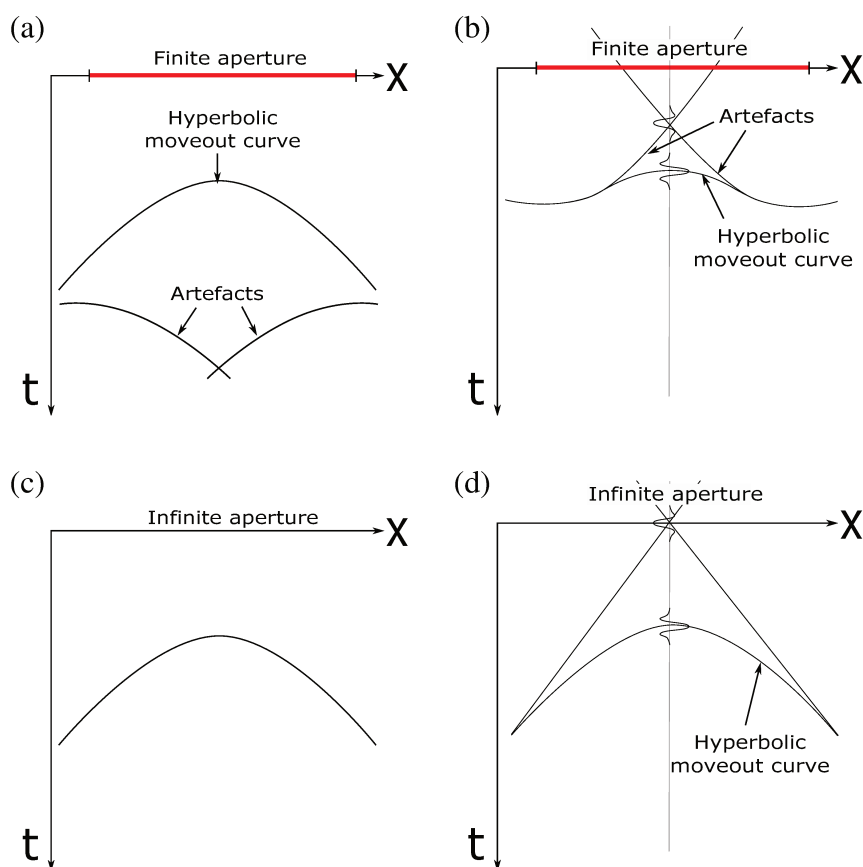


Figure C.1: Results of forward (a) and inverse (b) wavefield extrapolation of a point source response recorded on a finite aperture. On other hand we have the results of forward (c) and inverse (d) wavefield extrapolation of a point source response recorded on an infinite aperture. Note that the inverse extrapolation result contains artefacts, despite the infinite aperture (Wapenaar and Fokkema, 1997).